



ScuDo
Scuola di Dottorato ~ Doctoral School
WHAT YOU ARE, TAKES YOU FAR



Doctoral Dissertation
Doctoral Program in Aerospace Engineering (33.th cycle)

Shape sensing and load reconstruction for aerospace structures

Marco Esposito

* * * * *

Supervisors

Prof. Marco Gherlone
Prof. Pier Marzocca

Doctoral Examination Committee:

Prof. Prof. Daniel J. Inman, Referee, University of Michigan
Prof. Adnan Kefal, Referee, Sabanci University
Prof. E.F., University of ...
Prof. G.H., University of ...
Prof. I.J., University of ...

Politecnico di Torino
July 2, 2021



Shape sensing and load reconstruction for aerospace structures

A thesis submitted in fulfilment of the requirements for the degree of Doctor of
Philosophy

Marco Esposito

B.Eng (Aerospace), University of Naples Federico II
M.Eng (Aerospace), Politecnico di Torino

School of Engineering
College of Science, Technology, Engineering and Maths
RMIT University

July, 2021

This thesis is licensed under a Creative Commons License, Attribution - Noncommercial-NoDerivative Works 4.0 International: see www.creativecommons.org. The text may be reproduced for non-commercial purposes, provided that credit is given to the original author.

I certify that except where due acknowledgement has been made, the work is that of the author alone; the work has not been submitted previously, in whole or in part, to qualify for any other academic award; the content of the thesis is the result of work which has been carried out since the official commencement date of the approved research program; any editorial work, paid or unpaid, carried out by a third party is acknowledged; and, ethics procedures and guidelines have been followed.

I hereby declare that, the contents and organisation of this dissertation constitute my own original work and does not compromise in any way the rights of third parties, including those relating to the security of personal data.

.....

Marco Esposito
Turin, July 2, 2021

Acknowledgements

I would like to express my sincerest thanks and gratitude to my supervisors, Prof. Marco Gherlone and Prof. Pier Marzocca, for their guidance, support and inspiration.

I would also like to thank Dr. Massimiliano Mattone for his constant support during the experimental activities.

Contents

List of Tables	IX
List of Figures	XI
Summary	1
1 Introduction	5
1.1 Thesis outline	7
1.2 Thesis outcomes	8
2 Literature review	11
2.1 Shape sensing	11
2.2 Load reconstruction	13
2.2.1 Data driven loads reconstruction	14
2.2.2 Model based loads reconstruction	16
3 Shape sensing methods	19
3.1 Modal Method	19
3.1.1 Modal selection criterion	21
3.2 Ko's Displacement theory	22
3.2.1 Modal expansion	23
3.3 Inverse Finite Element Method	24
3.3.1 Tria formulation	28
3.3.2 Quad formulation	30
3.3.3 Incremental formulation	33
4 Numerical shape sensing	35
4.1 Preliminary study on the novel inverse QUAD element	35
4.2 Shape sensing on a composite wing box	42
4.2.1 The composite wing box	42
4.2.2 Strain sensors optimization	46
4.2.3 Deterministic analysis	49
4.2.4 Uncertainty quantification	56

4.3	Plate undergoing large displacements	66
5	Data driven methods for loads identification and reconstruction	69
5.1	Linear regression based algorithms	69
5.1.1	Search methods	70
5.1.2	Regularization	73
5.2	Artificial Neural Networks	73
5.2.1	Architectures	74
5.2.2	Training Algorithms	78
6	Internal wing loads reconstruction of a fighter aircraft	81
6.1	The dataset	81
6.2	Fatigue prediction assessment	84
6.3	Linear regression based analysis	87
6.4	Artificial Neural Networks analysis	89
6.5	Statistical Analysis and global best	90
7	External loads reconstruction and shape sensing on an aluminium wing box	93
7.1	An integrated approach	93
7.1.1	External loads identification (1 st step)	93
7.1.2	Shape sensing (2 nd step)	96
7.2	Application on an aluminium wing box	97
7.2.1	The wing box	97
7.2.2	Load cases	98
7.2.3	Numerical models	99
7.2.4	Matrices computations	103
7.2.5	Sensors optimization	104
7.2.6	From Tria to Quad	105
7.2.7	Results	107
7.2.8	Effect of measurement error	116
8	Experimental validation	121
8.1	Aluminium cantilevered C-beam	121
8.2	Aluminium stiffened panel	131
8.3	Swept aluminium wing box	137
9	Conclusions and future work	145
9.1	Conclusions	145
9.2	Future work	149
	Bibliography	151

A	Shape functions	165
B	Pressure distribution	167
C	Experimental strain measurements	169
C.1	C-Beam	170
C.2	Stiffened panel	172
C.3	Swept aluminium wing box	174
D	Swept wing box technical drawings	177

List of Tables

4.1	Lamina characteristics.	42
4.2	Optimization results.	49
4.3	Stochastic material characteristics.	58
4.4	Stochastic strain measurements.	62
4.5	Material strength characteristics.	64
6.1	m values for the considered aluminium alloys.	87
6.2	Highest performing results for linear regression based models with a 90% R^2 condition.	88
6.3	Highest performing results for ANNs with a 90% R^2 condition.	90
6.4	Global best performing System Identification Model.	92
7.1	Aluminium alloys mechanical properties.	98
7.2	Load Cases.	99
7.3	Quadrilateral and triangular meshes comparison	106
7.4	Load identification of Load Case 2 with only 1 sensing line - The positive directions and the identification numbers of the forces are the ones depicted in Figure 7.5.	116
7.5	Effect of measurement error for Load case 1	116
7.6	Effect of measurement error for Load case 2	117
8.1	6060 aluminium alloy mechanical properties.	121
8.2	Shape sensing and load identification results for Load case 1. In parenthesis, the percentage error with respect to the experimental values are reported.	127
8.3	Shape sensing and load identification results for Load case 2. In parenthesis, the percentage error with respect to the experimental values are reported.	130
8.4	AL-Li alloy mechanical properties.	131
8.5	Shape sensing and load identification results for the stiffened panel. In parenthesis, the percentage error with respect to the experimental values are reported.	136
8.6	Aluminium alloys mechanical properties.	137

8.7	Shape sensing and load identification results for the swept wing box. In parenthesis, the percentage error with respect to the experimental values are reported.	141
8.8	Updated model characteristics and resulting displacements.	144

List of Figures

3.1	Ko's Displacement theory - Geometry and sensors' location.	23
3.2	Plate notation.	25
3.3	Strain measure.	27
3.4	Triangular shell element (iMIN3).	29
3.5	Quadrilateral shell element (iQS4).	31
3.6	Incremental iFEM.	33
4.1	Plate - Benchmark plate for the validation of the novel integration scheme of the iFEM quad element.	36
4.2	iFEM mesh - The dots represent the location of the strain rosettes within each element.	37
4.3	In-plane shear load - In the figures, the displacements u along the x direction are reported for the in-plane shear load load case. The colour bar refers to the magnitude (in mm) of the u displacements.	38
4.4	Sensors' configuration proposed in [58].	39
4.5	In-plane shear load - Reconstruction of the u displacements along the x direction using the sensors' configuration reported in 4.4 and the old integration scheme.	40
4.6	Transverse load - In the figures, the displacements w along the z direction are reported for the transverse load case. The colour bar refers to the magnitude (in mm) of the w displacements.	41
4.7	Geometry and loading conditions for the unswept wing box. All the dimensions are expressed in [mm].	43
4.8	Numerical models of the wing box.	44
4.9	Reference deformed shape - The colour bar refers to the magnitude (in mm) of the resultant displacements, w_1 and w_2 represent, respectively, the vertical displacement of the top-left and top-right vertex of the tip cross section.	45
4.10	Selected mode shapes for the Modal Method and the Ko's Displacement theory.	46
4.11	Sensors' search space for the upper and lower panels.	47
4.12	Sensors' search space for the front and rear spars.	48

4.13	Sensor's configuration for the triangular elements on the top/bottom panels - The black square ($S_{1/2}$) represent the sensors location and the red dots (C_1, C_2) represent the location of the centroid for the two iTRIA3 elements.	48
4.14	iFEM Quad - In the panels (a) and (b) the optimized sensors' configuration is reported. In the panels (c) and (d) the reconstructed deformed shape is presented against the reference one.	52
4.15	iFEM Tria - In the panels (a), (b) and (c) the optimized sensors' configuration is reported. In the panels (d) and (e) the reconstructed deformed shape is presented against the reference one.	53
4.16	Ko's Displacement theory - In the panels (a) and (b) the optimized sensors' configuration is reported. In the panels (c) and (d) the reconstructed deformed shape is presented against the reference one.	54
4.17	Modal Method - In the panels (a) and (b) the optimized sensors' configuration is reported. In the panels (c) and (d) the reconstructed deformed shape is presented against the reference one.	55
4.18	Vertical displacement along the mid-chord line ($x = 363.18 \text{ mm}$) on the bottom panel.	56
4.19	Stacking sequences - The box is divided into seven zones. Each one has the same nominal stacking sequence but they are sampled separately in order to guarantee a higher degree of variability of the characteristics over the structure.	58
4.20	Material uncertainty simulation - The scheme illustrates the MCS with LHS procedure for the analysis of the material uncertainties.	59
4.21	PDFs - Material uncertainty - Probability density functions of the $\%ERMSw$ obtained for the three shape sensing approaches with 10000 input vectors of material characteristics sampled with LHS.	60
4.22	PDFs - Material uncertainty - Probability density functions of the $\%ERMSw$ obtained for the iFEM with varying λ_{1-8} values from 10^{-3} to 10^{-6}	61
4.23	Measurements noise effect simulation - The scheme illustrates the MCS with LHS procedure for the analysis of the measurement uncertainties.	62
4.24	PDFs - Strain error 5% - Probability density functions of the $ERMSw$ obtained for the three shape sensing approaches with 30000 input vectors of strains affected by a normal error of 5%.	63
4.25	PDFs - Strain error 10% - Probability density functions of the $ERMSw$ obtained for the three shape sensing approaches with 30000 input vectors of strains affected by a normal error of 10%.	63
4.26	PDFs - Strain error 5% - Probability density functions of the percentage error ($\%Err$ Tsai-Hill) in the reconstruction of the maximum Tsai-Hill failure index.	65

4.27	PDFs - Strain error 10% - Probability density functions of the percentage error (%Err Tsai-Hill) in the reconstruction of the maximum Tsai-Hill failure index.	65
4.28	Wing-shaped plate	66
4.29	Wing-shaped plate - Shape sensing at the maximum load level. . . .	67
4.30	Maximum transverse displacement.	67
4.31	% $ERMS_w$ error corresponding to linear iFEM and incremental iFEM solutions as a function of the load range	68
5.1	ANN node considering 4 inputs	74
5.2	A MISO neural network - The circles represent the nodes of the network and the lines the weighted connections. The \mathcal{S} symbol is related to nodes with a sigmoid activation function, whereas the \mathcal{L} symbol denotes a linear activation function.	74
5.3	Feedforward Network - The scheme is reported for a network with one time series input and one node in the hidden layer, but it can be easily extended to consider n time series inputs and n_{HL} nodes in the hidden layer. The activation function in the hidden layer is the sigmoid function (\mathcal{S}), whereas it is the linear function (\mathcal{L}) in the output layer.	75
5.4	Cascade Forward Network - The scheme is reported for a network with one time series input and one node in the hidden layer, but it can be easily extended to consider n time series inputs and n_{HL} nodes in the hidden layer. The activation function in the hidden layer is the sigmoid function (\mathcal{S}), whereas it is the linear function (\mathcal{L}) in the output layer.	75
5.5	Time-delay Neural Networks - The scheme is reported for a network with one time series input and one node in the hidden layer, but it can be easily extended to consider n time series inputs and n_{HL} nodes in the hidden layer. The scheme considers n_{IDL} input delays for every input. The activation function in the hidden layer is the sigmoid function (\mathcal{S}), whereas it is the linear function (\mathcal{L}) in the output layer. Every connection has a weight (w) and every node a bias (b).	76
5.6	Distributed Delay Network - The scheme is reported for a network with one time series input and one node in the hidden layer, but it can be easily extended to consider n time series inputs and n_{HL} nodes in the hidden layer. The scheme considers n_{DDL1} input delays and n_{DDL2} output delays. The activation function in the hidden layer is the sigmoid function (\mathcal{S}), whereas it is the linear function (\mathcal{L}) in the output layer. Every connection has a weight (w) and every node a bias (b).	76

5.7	Layer Recurrent Network - The scheme is reported for a network with one time series input and one node in the hidden layer, but it can be easily extended to consider n time series inputs and n_{HL} nodes in the hidden layer. The scheme considers n_{LDL} layer delays. The activation function in the hidden layer is the sigmoid function (\mathcal{S}), whereas it is the linear function (\mathcal{L}) in the output layer. Every connection has a weight (w) and every node a bias (b).	77
5.8	Non-linear Auto-regressive Network - The scheme is reported for a network with one time series input and one node in the hidden layer, but it can be easily extended to consider n time series inputs and n_{HL} nodes in the hidden layer. The scheme considers n_{IDL} input delays and n_{FDL} feedback delays. The activation function in the hidden layer is the sigmoid function (\mathcal{S}), whereas it is the linear function (\mathcal{L}) in the output layer. Every connection has a weight (w) and every node a bias (b).	77
6.1	Example of available load data and filtering	82
6.2	Input-output magnitude-squared coherence for a) Section 1 bending and b) Section 3 torsion	83
6.3	Miner's rule from the load cycles exceedance curve - The n_i are directly derived from the Load cycles exceedance curve. The stress ranges (S_i) are computed from the load ranges (L_i) through a structural model ($f(L_i)$). The cycles to failure (N_i) are computed from the stress ranges through the S/N curve of the material ($g(S_i)$). . . .	85
6.4	Box and whisker plots for R^2 - a) presents the linear regression based predictions and b) presents the ANN based predictions.	91
6.5	Best results comparison - a) presents the comparison between the best linear regression based models (ARMAX only) and the best ANNs in terms of R^2 b) presents the comparison between the best linear regression based models (ARMAX only) and the best ANNs in terms of $\%Fdf$	91
7.1	2-step integrated approach - The inputs of the process are highlighted in blue. The load identification step is highlighted in green and the shape sensing step is highlighted in orange.	96
7.2	Wing box geometry - In the figure, the panel and the spars are indicated by ①, the stiffeners that connect the skin panels to the spars are indicated by ②, the stringers are indicated by ③ and the ribs are indicated by ④. All dimensions are expressed in $[mm]$. . .	98
7.3	Load Case 1 - The figure shows the pressure distribution applied on the refined FE model of the wing box. The pressure is expressed in $[N/mm^2]$	100

7.4	Deformed shape for the Load Case 1 - The figure shows the refined Fe model of the wing box deformed under the pressure distribution of the Load Case 1. The color bar refers to the magnitude (in mm) of the resultant displacements.	100
7.5	Load Case 2 - The figure shows the distributed load applied on the wing tip section, discretized to nodal forces according to the FEM. The value of the nodal forces are reported in Table 7.2.	101
7.6	Deformed shape for the Load Case 2 - The figure shows the refined FE model of the wing box deformed under the distributed load of the Load Case 2. The color bar refers to the magnitude (in mm) of the resultant displacements.	101
7.7	Models - In (a), the refined mesh is presented. In (b), the elements whose contours are shown in red belong to the iFEM mesh and the pressure mesh. The elements whose contours are shown in black belong to the iFEM mesh only	102
7.8	Sensing lines - In the figure, the sensing lines and the sensing locations within each line are showed only for one panel and one spar. The same configurations should be considered for the other components.	104
7.9	Triangular meshes - In the figure are illustrated the four triangular meshes used to compare the accuracy of the newly introduced quad element.	106
7.10	Pressure field reconstruction of Load Case 1 - The $\%ERMS_p$ for the best sensors configuration, with the number of sensing lines varying from 1 to 10, are reported.	107
7.11	Pressure field reconstructions for Load Case 1.	109
7.12	Pressure reconstruction along the wing span for Load Case 1.	110
7.13	Shape sensing for Load Case 1 - The $\%ERMS_w$ for the best sensors configuration, with the number of sensing lines varying from 1 to 10, are reported for the two-step method (a) and the iFEM (b).	110
7.14	Vertical deflection along the wing span for Load Case 1.	111
7.15	Optimal sensors configurations for Load case 1 - The figures show the optimal sensors configurations for the two-step method (a) and the iFEM (b). In the legends, Upper and Lower refer to sensors located on the upper or lower panel, whereas Upper/lower refers to sensors located on both panels. Front and Rear refers to sensors that are located on the front or the rear spar, whereas Front/Rear refers to sensors located on both spars.	111
7.16	Nodal forces identification of Load Case 2 - The $\%ERMS_F$ for the best sensors configuration, with the number of sensing lines varying from 1 to 10, are reported.	112
7.17	Nodal forces identification along the wing tip chord for Load Case 2.	113

7.18	Shape sensing for Load Case 2 - The % $ERMS_w$ for the best sensors configuration, with the number of sensing lines varying from 1 to 10, are reported for the two-step method (a) and the iFEM (b).	113
7.19	Vertical deflection along the wing tip chord for Load Case 2.	114
7.20	Optimal sensors configurations for Load case 2 - The figures show the optimal sensors configurations for the two-step method (a) and the iFEM (b). In the legends, Upper and Lower refer to sensors located on the upper or lower panel, whereas Upper/lower refers to sensors located on both panels. Front and Rear refers to sensors that are located on the front or the rear spar, whereas Front/Rear refers to sensors located on both spars.	115
7.21	Pressure field reconstructions for Load Case 2 when strains are affected by a normal error of 1% (a) and 5% (b) and the Thikonov regularization is implemented. The results are showed for the 7 sensing lines configuration.	118
7.22	Vertical deflection along the wing span for Load Case 1 when strains are affected by a normal error of 1% and 5% and the Thikonov regularization is implemented. The results are showed for the 7 sensing lines configuration.	118
7.23	Nodal forces identification for Load Case 1 when strains are affected by a normal error of 1% (a) and 5% (b). The results are showed for the 7 sensing lines configuration.	119
7.24	Vertical deflection along the wing tip chord for Load Case 2 when strains are affected by a normal error of 1% and 5%. The results are showed for the 7 sensing lines configuration.	119
8.1	Aluminium C-Beam - The lateral view (a) and the cross section of the beam are shown. All the dimensions are expressed in [mm]. . .	122
8.2	Test configuration for the aluminium C-Beam.	123
8.3	Load and displacement sensing system at the tip section ($y = 1100\text{ mm}$). . .	123
8.4	LVDTs and fibre optics location on the C-Beam's cross section. . . .	124
8.5	Fibre optic installed on the beam.	125
8.6	Refined mesh.	125
8.7	C-Beam - iFEM mesh and strain sensors' configuration.	126
8.8	Load case 1 - Shear centre's location and loading condition.	128
8.9	Load case 2 - The forces and moments applied in the shear centre represent the unknown of the 2-step method; $F_{z(exp.)}$ represent the experimentally applied force. w_{1z} and w_{1z} are the investigated displacements.	129
8.10	Stiffened panel's lateral view.	131
8.11	Stiffened panel's geometry. All the dimensions are expressed in [mm]. . .	132
8.12	Stiffened panel - Test configuration	133
8.13	iFEM mesh and strain sensors' configuration.	134

8.14	Stiffened panel fibre's configuration - The six sensing lines, installed in a back-to-back configuration, are shown.	135
8.15	LVDTs' configuration - The location of the four LVDTs (v_{1-4}) on the surface of the panel are shown. All dimension are expressed in [mm]	135
8.16	Experimental wing box geometry - In the figure, the panel and the spars are indicated by ①, the stiffeners that connect the skin panels to the spars are indicated by ②, the stringers are indicated by ③ and the ribs are indicated by ④. All dimensions are expressed in [mm].	138
8.17	Swept wing box	139
8.18	Swept wing box -Test configuration on the wing span view	139
8.19	Swept wing box -Test configuration on the tip section view section	140
8.20	Swept wing box - iFEM mesh and strain sensor's configuration.	141
8.21	Swept wing box fibre's configuration - 8 sensing lines along the entire wing span (①-⑧) plus one sensing line along one half of wing span (⑨). All dimension are expressed in [mm].	142
8.22	Strain comparison between the experimental values and the simulated ones.	143
8.23	Strain comparison between the experimental values and the simulated ones from the updated model.	144
C.1	Experimental strains for Load case 1 - The strains from the fibres and the ones from the refined model are reported.	170
C.2	Experimental strains for Load case 2 - The strains from the fibres are reported. Since in this case no simulation has been performed, the strains from the high-fidelity model are not reported	171
C.3	Experimental strains from the stiffened panel - The numbering of the fibres is the one reported in Figure 8.14.	172
C.4	Experimental strains from the stiffened panel - The numbering of the fibres is the one reported in Figure 8.14.	173
C.5	Experimental strains from the upper panel of the swept aluminium wing box - The numbering of the fibres is the one reported in Figure 8.21 and s is the coordinate along the fibres' length.	174
C.6	Experimental strains from the lower panel of the swept aluminium wing box - The numbering of the fibres is the one reported in Figure 8.21 and s is the coordinate along the fibres' length.	175

Summary

The in-flight monitoring of the loads and of the induced displacement field is becoming essential in the development of next generation Structural Health Monitoring framework. To achieve the crucial change from its traditional formulation, based on pre-emptive maintenance, to a new philosophy, based on pro-active condition-based maintenance, the monitoring of these characteristics is paramount. The continuous tracking of the loads and the displacements generates information on the real status of the structure and can guide more accurate maintenance and sustainment practices. Moreover, anomalies in the monitored characteristics can also lead to the identification of critical conditions including the detection of structural damage.

Another recent progress in the design of aerospace structures has increased the demand for a more accurate monitoring system for loads and displacements, the development of smart structures. These structures are designed to adapt to the condition that they are exposed to. Therefore, the knowledge of the actual condition, in terms of deformed shape and of loading condition, is fundamental for the correct activation of their morphing capabilities, that allow the structure to obtain load alleviation and a higher aerodynamic efficiency.

Unfortunately, the direct measure of these characteristics, that prove to be so crucial for the development of the future aerospace structures, is usually hard to obtain. For this reason, shape sensing and load reconstruction/identification methods have been developed in the open literature. These techniques are designed to compute the displacement and the loads from easily measurable discrete strains. This research aims to give an important contribution to the further development of the shape sensing and load reconstruction methods, in particular for the specific application on aerospace structures.

The most widespread shape sensing methods emerged in the last few years are the inverse Finite Element Method (iFEM), the Modal Method (MM) and the Ko's Displacement theory. Although a lot of effort has been recently involved in the formulation of these methods, a comprehensive study, that specifically includes the analysis of the effect of the strain sensing configuration on the performances of the methods is missing. In this work, the three methods have been numerically and experimentally tested on the displacement reconstruction of several structures,

including a composite wing box, an aluminium swept wing box, an aluminium C-beam and an aluminium stiffened panel. For these analyses, the effect of the measurement error and of the number and location of the strain sensors have been widely investigated. The study has specifically focused on the optimization of the sensing technology for these methods. In particular, a more efficient approach to unequivocally determine the sensors locations for the iFEM quadrilateral elements has been introduced.

The comparative study shows the different scenarios that each method can be suitable for. The iFEM, also considering the introduced improvements, results as the most accurate shape sensing method for application, but a considerable amount of strain sensors is required to achieve this accuracy. The MM, on the other hand, is not able to reach the same level of accuracy, but can generate moderately accurate reconstruction of the displacements with fewer sensors. The Ko's Displacement theory, although can give a rough estimation of the deformed shape requiring very few sensors, is the less accurate of the three explored methods. Considering its impressive results, the iFEM has been selected for a further development and has been enriched with an incremental formulation for the analysis of structures undergoing large displacements.

The study on the load reconstruction methods has involved two different scenarios. The first one being the reconstruction of the internal loads, for the estimation of the fatigue life consumption, of a fighter aircraft's wing, whose physical characteristics were not provided. Only data of strain, loads and some flight parameters have been made available. For this problem data driven system identification methods have been explored. The recent progress in the field of these "black box" approaches has brought to life a vast amount of different model variants and formulations, with a broad landscape of functional parameters, that have never been explored under a single benchmark aircraft loads monitoring problem. For the application on the aircraft's wing, the investigation of this landscape of functional parameters for the linear regression based models and for the Artificial Neural Networks is considered. The broad exploration of these two families of system identification methods and of their functional parameters proves the superior capabilities of the ANNs with respect to the linear regression based models. Within the model variants of ANNs, the Distributed Delay architecture showed the best fatigue life consumption predictions.

The second scenario has concerned the identification of the external loads of a numerical aluminium swept wing box from discrete strain measurements. The loads have been computed using an existing approach, based on the discretization of the loads and on the computation of the coefficient of influence between the discretized loads and the discrete strain measurements. The discretization of distributed pressure fields is obtained using Finite Elements. In previous applications only triangular elements have been adopted, whereas, in this work, the method has been improved with the implementation of quadrilateral elements.

This activity has inspired the formulation of a novel and crucial tool for the progress of the monitoring systems analysed in this work. This is an innovative and integrated approach, able to simultaneously reconstruct the external loads and the displacement field of a structure from the same discrete strain measures. This 2-step approach uses the identified external loads to perform a standard FEM analysis and thus compute also the displacements of the structure. Therefore, the first step of the procedure includes the identification of the loads while the second one provides the application of these loads to the model of the structure to compute the displacement field. The method has been applied on the same structures analysed for the shape sensing campaign. The applications show that the 2-step procedure is able to simultaneously compute the external loads and the displacements with a remarkable accuracy, if a sufficient number of strain sensors are installed on the structure and they are not affected by significant measurement error. If the number of sensors is diminished or they are affected by measurement error, the first step of the procedure loses accuracy. Nevertheless, the method is still capable of impressive reconstruction of the deformed shape, making this a viable tool for the future of the aerospace structures monitoring.

Some of the research and results presented in this thesis have been published in:

A. Tessler, R. Roy, M. Esposito, C. Surace, and M. Gherlone. “Shape Sensing of Plate and Shell Structures Undergoing Large Displacements Using the Inverse Finite Element Method”. In: *Shock and Vibration* 8076085 (2018) [1].

M. Esposito and M. Gherlone. “Composite wing box deformed-shape reconstruction based on measured strains: Optimization and comparison of existing approaches”. In: *Aerospace Science and Technology* 99 (2020) [2].

M. Esposito and M. Gherlone. “Material and strain sensing uncertainties quantification for the shape sensing of a composite wing box”. In: *Mechanical Systems and Signal Processing* 160 (2021) [3].

M. Esposito, M. Gherlone, and P. Marzocca. “External loads identification and shape sensing on an aluminum wing box: An integrated approach”. In: *Aerospace Science and Technology* 114 (2021) [4].

Chapter 1

Introduction

Over the last years, Structural Health Monitoring (SHM) has seen a continuous increase in interest in aerospace applications. In particular, the SHM framework is rapidly changing its traditional formulation, based on the pre-emptive maintenance, to a new principle based on pro-active condition-based maintenance. This new concept requires the precise and in-flight monitoring of the structures. The monitoring of some crucial characteristics of a structure can lead to the optimization of the maintenance and sustainment practices, that can be guided by the knowledge of the actual status of the structure and not only by the design based programmed interventions. Moreover, in parallel with the development of the modern SHM framework, the birth and progress of the Smart structures has also increased the demand for a more intensive in-flight monitoring of the aerospace structures. As a consequence, the requests raised by these two new concepts have caused the simultaneous expansion of some monitoring techniques, designed to track the needed informations. The load reconstruction/identification and shape sensing methods have attracted considerable attention as crucial tools for the realization of an effective structural monitoring system. These two families of methods are designed to compute the loads and the displacement field of a structure from discrete strain measurements. The loads and the displacements are not easily measurable quantities, therefore, the use of easy measurable strains to indirectly compute these characteristics has emerged as a viable solution, also thanks to the progresses achieved by the strain sensing technology [5, 6].

The load identification framework is divided into external and internal load monitoring. The monitoring of the internal loads is crucial to guide condition-based maintenance, fatigue life estimation and critical load modelling for the SHM. In fact, the load spectra modelled during the design process do not always reflect the one really experienced during flight operation, therefore misleading the fatigue life prediction and the standard maintenance schedule. Moreover, unexpected highly impacting flight conditions can lead to the necessity of exceptional maintenance operation and they must be taken into account as they also strongly impact the

fatigue life of the structure. The monitoring of the external loads can serve the same purpose. In fact, the knowledge of the external loads can lead to the computation of the internal ones through the use of a structural model, able to relate the external load to the induced internal ones. On the other hand, the monitoring of the external loads can supply information about the health status of the structures through the detection of changes in the load paths caused by presence of damages [7]. Moreover, the knowledge of the in-flight load conditions is fundamental for the design of innovative smart structures that, thanks to their morphing capabilities, can optimize their shape to obtain load alleviation [8] and to improve the aerodynamic efficiency of the control surfaces [9].

The shape sensing techniques, starting from easily measurable in-situ characteristics, the strains, allow the reconstruction of the displacement field of a structure. The in-flight monitoring of the deformed shape also provides crucial information about the health status of a structure. The detection of anomalies in the displacement and strain field allows the individuation of damages [10, 11, 12, 13]. Moreover, the shape sensing can be easily expanded to perform stress sensing. In fact, once the displacement field is reconstructed, the use of the constitutive equation allows the computation of the stress field and, consequently, of the internal loads of the structure. These ones can be used for the same SHM operations already described. The world of morphing structure is also impacted by these monitoring methods. The morphing capabilities, to work properly, need to have a feedback on the actual shape of the structure, in order to modify it accordingly. The shape sensing can provide this fundamental information [14, 15, 16].

The highlighted importance of the simultaneous use of the shape sensing and the load reconstruction for the future of the SHM and of the smart structures inspired this work. In fact, as it will be pointed out in the literature review following this chapter, although the recent massive efforts, these methodologies still require a further development of some aspect that generated the following research questions:

- How can the shape sensing and load reconstruction be extended to analyse complex aerospace structures?
- How can strain sensing technology be optimized to fit requirements of the two techniques?
- How can the shape sensing be extended to reconstruct non-linear deformations?
- Can an integrated approach, including shape sensing and load reconstruction, be implemented?

To try to answer these questions this work has been developed into four main phases. The first phase is focused on the study of the shape sensing. In particular to its application on a complex aerospace structure and to the reconstruction of

the non-linear displacements. The second part is developed around the analysis of the internal and external load of aerospace structures. The third phase has seen the development of an integrated approach for the simultaneous monitoring of the loads and displacements. Finally, the results of these three phases have been experimentally evaluated on three different structures.

1.1 Thesis outline

The research phases have generated the following activities and the relative sections of this thesis.

An accurate literature review on the existing shape sensing methods and load reconstruction ones, focused on highlighting the strength and the weakness of the existing formulations has been carried on and it is reported in Chapter 2.

From this review, the Modal Method (MM), the Ko's Displacement theory and the inverse Finite Element Method (iFEM) have emerged as the most reliable and successful shape sensing methods in the open literature. Therefore, these methods have been selected for a comparative study on the displacement reconstruction of a composite wing box subject to torsion and bending deformation. The study involves the optimization of the strain sensors' configuration to fulfil the requirements of the three methods and the development of a novel formulation for the iFEM quadrilateral element. Although performed only numerically, the investigation also involves the evaluation of the effect of the uncertainties typical of the experimental environments. The shape sensing analysis has been continued with the introduction of an incremental iFEM formulation for the monitoring of structures undergoing large displacements. This proposed methodology has been numerically tested on the shape sensing of a wing-shaped plate. The detailed description of the shape sensing methods and of the introduced new formulations is reported in Chapter 3, whereas the numerical studies and their results are described in Chapter 4.

Two different problem have been considered for the study of the load reconstruction methods. The monitoring of the internal loads, with the purpose of assessing the fatigue life consumption due to these loads, and the reconstruction of the external aerodynamic loads. The identification of the internal loads induced on the wing of a fighter aircraft, without any knowledge of the airframe's characteristics, has been the focus of the first activity. For this problem, a broad investigation on the data driven system identification methods has been accomplished. The investigation involved a parametric study on the regression algorithms identified during the literature review, the linear regression based algorithms, ARX and ARMAX, and the Artificial Neural Networks. The scope of the parameters' exploration has been the evaluation of the best system identification architecture for the prediction of the loads from discrete strains. The system identification methods are introduced in Chapter 5 and their application to the wing monitoring is presented in Chapter

6.

The external loads identification has been implemented using an approach based on the coefficients of influence between the loads and the induced strains. A generic system of loads is discretized with concentrated loads or nodal pressures, according to the kind of load that the method has to reconstruct. In the case of nodal pressures, these are interpolated over the structural domains using finite elements, so that they can effectively simulate a continuously distributed pressure. The discrete loads are then identified by fitting the strain field caused by each discrete unit load to the measured ones. The detailed formulation of this method is reported in Chapter 7. This method inspired the formulation of the integrated approach for the simultaneous computation of the external loads and the displacement field of a structure, that, through the use of a structural model, can also lead to the reconstruction of the internal ones. The proposed 2-step method is simply based on the idea that the identified external loads can be used to run a standard FEM simulation to reconstruct the displacement field, the strain field and the stress field of the structure. The external loads reconstruction and the consequent 2-step approach have been tested on the numerical monitoring of a swept aluminium wing box and compared, in terms of the shape sensing, to the iFEM. Also in this case, a study on the optimization of the sensing technology and on the influence of the inputs' uncertainties has been considered. This investigation is described in Chapter 7.

The results of the above mentioned numerical activities have been finally tested on three different experimental scenarios. An aluminium cantilevered C-Beam, an aluminium stiffened panel and an aluminium wing box have been analysed. The results of the numerical investigation have guided the experimental activities and the introduced formulation have been evaluated on the monitoring of real structures. The experimental activities are presented in Chapter 8.

Finally, in Chapter 9, the concluding remarks and the suggestion for the future activities aimed at the further development of the load reconstruction and shape sensing frameworks are discussed.

1.2 Thesis outcomes

During this research project, several new considerations about already existing methods and new proposed formulations have been derived.

The study on the shape sensing of the composite wing box lead to the development of a new integration scheme for the inverse quadrilateral finite element IQS4. The new formulation is able to better adapt this element to the strain sensing technology. In fact, thanks to the novel formulation, the location of the strain sensors for the application of the method is univocally determined, making the process of sensors placement easier and more reliable. Moreover, the accuracy of this new element is proven to be higher on the reconstruction of the in-plane membrane

displacements.

The same study highlighted some original considerations on the capabilities of the MM, the Ko's Displacement theory and the iFEM to analyse complex structures. The three methods shows different characteristics that make them suitable for different scenarios, depending on the available strain sensors' setup. The iFEM is proven to be the most accurate shape sensing method, even when uncertainty is present in the system, when the structure is equipped with a high number of sensors. It also shows a considerable sensitivity to the specific sensors' locations. On the other hand, the MM shows more adaptability to the sensors' configuration and higher robustness with respect to the input's variability. Nevertheless, this method, although capable of moderate accuracy with a low number of sensors, it is not able to reach the accuracy shown by the iFEM. These results have been also confirmed by the experimental validation of the two methods. The Ko's Displacement theory showed the highest inaccuracy and the highest liability with respect to the input's uncertainties. However, this method is capable of a rough displacements reconstruction with a reduced number of strain sensors.

The internal loads study produced the following considerations on the analysed system identification methods. The Artificial Neural Networks show an overall higher accuracy than the ARX and ARMAX regression methods. Moreover, the Distributed Delay Neural Networks is the architecture that is capable of the better fatigue life prediction with respect to all the considered load spectra. For the evaluation of these performances, a new parameter for the fatigue life estimation, not dependent on the geometry of the structure, has been derived. In fact, the lack of physical informations for this problem needed the development of this parameter.

The identification of the external loads and the use of these to reconstruct the deformed shape of the structure generated impressive results. First of all the external load identification method has been enriched with the introduction of a quadrilateral element for the discretization of the pressure field, whereas only triangular elements have been used in the previous works. This element show an increased level of accuracy in the reconstruction of the pressure field. The external load can be predicted by the method if a sufficient amount of strain information is available. Moreover, the proposed 2-step method demonstrated an extreme accuracy in the reconstruction of the displacement field, even when the identified load are not accurate. This happens when the number of input strains is reduced or when they are affected by measurement errors. In fact, in this case, the method is still able to find an equivalent system of loads that, although different from the applied one, induce the same deformation to the structure and therefore, the shape sensing is still achievable.

Chapter 2

Literature review

In this chapter the current state-of-the-art on the shape sensing and load reconstruction methods is resumed. The different application and the results obtained by the methods in the past studies are highlighted and the shortcomings of the existing approaches, that need to be overcome in this work, are also pointed out.

2.1 Shape sensing

Shape sensing techniques have witnessed a rapid development during the last few decades. As already mentioned in the previous chapter, these techniques allow the reconstruction of the deformed shape of a structure from discrete strain measurements. These quantities are usually easily measurable through strain gauges. The technology related to the strain sensing has seen a simultaneous rapid progress. This has strongly enhanced the possibilities of the shape sensing methods and pushed the technology towards new horizons. In particular, the development of fibre optics distributed strain sensing systems [5, 6], based on Rayleigh scattering and Optical Frequency Domain Reflectometry (OFDR), allows the easy installation of a multitude of strain sensors in a more efficient way. These fibres present a high density of strain sensors, can be easily installed on a structure and, in the case of composite materials, can even be embedded in composite laminates during the layup phase.

Among the shape sensing methods that have benefited from the progress of these technologies and have attracted more attention, four main categories of methods have emerged: (1) methods based on numerical integration of experimental strains [17, 18, 19, 20, 21, 22]; (2) methods using global or piece-wise linear continuous basis functions to approximate the displacement field [23, 24, 25, 26, 27, 28, 29, 30, 31, 32, 33, 34, 35, 36]; (3) inverse Finite Element Methods (iFEM), based on a finite-element discretization and on a variational principle [37, 38, 39, 40, 41, 42, 43, 44, 45, 46, 47, 48, 49]; (4) method based on the use of the Artificial Neural Networks (ANNs) [50, 51]. Within these families of methods, three have emerged

as the more spread and successful for the shape sensing of aerospace structures, the Ko's Displacement theory, the Modal Method (MM) and the inverse Finite Element Method (iFEM). They belong to the first, the second and the third families, respectively.

The Ko's Displacement theory is based on the double integration of the curvature equation of the Bernoulli-Euler beam. In beam-like structure the curvature can be expressed in terms of a set of axial strains along the beam span and of the distance of these strain from the neutral axis of the beam. The double integration of the curvature can lead to the expression of the deflection of the beam in terms of the measured strain at the location where these are measured. As a consequence, the method allows the computation of the deflections along a strain sensing line. The method was introduced by Ko et al. in [19], numerically validated on the wing of the Ikhana Unmanned vehicle [20] and then experimentally applied on the Global Observer UAV [21]. Recently it has also been applied on the shape sensing of a cantilevered composite beam [52]. A crucial improvement for the method has been introduced by Pak [53]. In this work, the method is expanded in order to reconstruct the full displacement field of a beam-like structure, for components and location different from the ones reconstructable with the standard Ko's formulation. By means of a modal transformation [54, 55], the new formulation is able to expand the displacements reconstructed along the sensing lines to the displacements in locations outside of these lines, allowing the reconstruction of the full displacement field. The use of the modal transformation requires the computation of the modal characteristics of the structure.

The modal characteristics of the structure are also adopted by the Modal Method. This method has been simultaneously introduced in [26] and [27]. The method is based on the formulation of the strain field in terms of known spatial functions, the modal strain shapes, and unknown weights, the modal coordinates. The modal coordinates are computed by fitting the so formulated strain field to discrete measured strains. The displacement field is then computed from the derived strain field by means of the strain-displacements relations. The MM has been applied in [26] to reconstruct the displacement field of a cantilevered aluminium plate. In this application the modal strain shapes were experimentally computed. Since the experimental evaluation of the modal strain properties can be really difficult, in [24] they were numerically computed and then adopted to reconstruct the deformation of a real plate. Recently, in [56], the MM has been experimentally validated on the reconstruction of the static and dynamic displacements of a wing.

The inverse Finite Element Method (iFEM) has been developed by Tessler et al. in [57]. The iFEM is based on the standard discretization of the structural domain with finite elements. This discretization allows the formulation of the strain field in terms of the spacial derivatives of the shape functions and of the nodal values of the displacements. By minimizing the error between the interpolated strain field and the discrete strains, coming from sensors, the method is able to find the nodal

displacements that best fit the measured strains. This method has been widely and successfully applied to a broad variety of structures. Truss and beam structures has been studied in [41, 42]. Three nodes inverse shell elements have been widely used for the analysis of thin plates [1, 46, 49] and thin walled structures [39, 45]. Recently, a quadrilateral inverse shell element, the IQS4, has been developed and broadly applied to marine structures [43, 44, 58]. The quadrilateral element rises a complication in the attribution of the strain sensors to the inverse elements. In fact, differently from the triangular elements, where the location of sensors can be unequivocally determined, in the quad formulation adopted in these works the location of the sensors can not. The most recent development in the field of iFEM is represented by the introduction of an isogeometric formulation for variable cross-section beams [59] and curved shell structures [60]. The reduction in the number of strain sensors for the iFEM has been the focus of the study in [61]. A smoothing technique for the computation of the full strain field from discrete strain measures has been developed to enriched the capabilities of the iFEM. The a priori expansion of few strain measures, inputs of the method, allows an accurate shape sensing with fewer strain measurements.

Few comparative studies on the shape sensing methods have been performed. Devorkian et al. [62] compared the Ko's Displacement theory and the Modal Method on a swept cantilevered plate. The only comparison of the three methods have been performed by Gherlone et al. [63]. The three methods have been applied on a real swept wing-shaped aluminium plate.

An extensive comparison of the three main shape sensing methods on a structure that presents the level of complexity of a real aerospace structure is missing in the open literature. Moreover, the influence of the strain sensors' configuration on the three different techniques, in order to evaluate the pros and cons of each method in applications with different available strain information, has never been investigated. From the literature review, also emerged the lack of methods for the shape sensing of structures that experience large displacements, exceeding the limit of linear elastic behaviour. The possibility to achieve this capability is crucial to broaden the applicability of the shape sensing tools to real world aerospace structures.

2.2 Load reconstruction

In this work, two different approaches are adopted for the reconstruction of the loads, according to the problem's formulation they have to face. When no physical information on the structure but data of strain, flight parameters and loads were made available, the data driven methods have been implemented. On the other hand, when a model of the structure could be designed, the model based approach have been investigated.

2.2.1 Data driven loads reconstruction

The data driven system identification methods, adopting a "Black Box" approach, are able to create a regression between any inputs and outputs of a system, without any in-depth knowledge of the investigated system. Within the data driven system identification methods two families have been widely used in the prediction of loads from strain measures and other flight parameters, the auto regressive linear regression with external input models and the Artificial Neural Networks.

The auto regressive (AR) linear regression models are based on the concept that a value of a time series can be determined as a linear regression of the value of the time series in the previous time steps. The addition of an external input in the regression models generates the Auto-regressive with eXtra inputs model, ARX [64]. Moreover, the inclusion of a Moving Average (MA) term for better modelling the noise of the system produces the Auto-regressive Moving Average with eXtra input model, ARMAX [64]. These two System Identification Models have been used in several application related to the load monitoring and fatigue life prediction of structures. Mustapha et al. [65] used AR-ARX based regression models to detect and predict crack in steel reinforced concrete structures (validated by data from Sydney Harbour Bridge). Yi et al. [66] used system identification to develop models for failure prediction of composite pipes. Two models based on ARX and ARMAX were developed based on strain gauge data. Moreover, Ahsan and Lemma [67] studied the capability of AR models to predict useful life of gas turbine engines.

The Artificial Neural Networks are non-linear parametric function whose parameters are learned from the data through a process defined as training. They can be used to approximate highly non-linear functions that relate the outputs to the inputs of a system [68]. ANNs have been applied in aerospace applications since the late 1980s when they emerged as a powerful means of dealing with complex non-linear systems such as parameter estimation during manoeuvres. The US Naval Air Warfare centre is one of the pioneers of applying artificial neural networks for aircraft load prediction. In particular, Hoffman's report [69] is the first study to implement ANNs to predict airframe strains.

Artificial Neural Networks were firstly applied to solve the inverse problem of establishing the external loads-strain relationship by Cao et al. In [70] a simplified structural model of a wing is analysed. The study is able to successfully reconstruct a set of concentrated forces applied to a cantilevered beam by means of ANN using structural strains as an input. An ANN has been developed and trained from in-flight data to indirectly predict fatigue damage for a Lynx M9 helicopter in [71]. The predicted stresses are found to be highly accurate. Levinski [72] demonstrated the viability of ANNs for buffet prediction by developing ANN models for F/A-18 based on experimental data. The work shows Radial basis function (RBF) based ANNs to be more accurate than Multi-Layer Perceptron (MLP) based ANNs trained with backpropagation with orthogonal least square algorithm. Furthermore,

RMS values and frequency content of tail buffet pressures are accurately predicted using a full-scale F/A-18 tail buffet test by Levinski [73]. Levinski also considered a RBF-NN trained with an orthogonal least-squares algorithm and several transfer functions. It is concluded that a multi-quadratic transfer function is the most robust and accurate approach. In [74] Trivailo *et al.* tried multiple architecture of ANN to predict the manoeuvrer and buffet loads acting on the empennage of a F/A-18 fighter aircraft during a fatigue test. They have been able to obtain a good indication of the magnitude and frequency of the loads using only strain gauges as an input. They also demonstrated the applicability of neural networks to reconstruct loads at different stations from the ones where the loads were located during training. Wada and Sugimoto compared a Feed-forward Neural Network (FFN) and a structural based model for the prediction of distributed aerodynamic loads from discrete strains measures [75]. They applied the two methods to a cantilevered beam and studied the accuracy of the methods and the stability with respect to the number of available strain information. The FFN proves to outperform the structural based model when a reduction in the number of sensors occurs. On the other hand the structural based model results more reliable when the load distribution is highly different from the distribution used during the training of the network. Cooper et al. [76] used data generated from a calibrated Finite Elements model of a wing rib to train a FFN in order to establish a relation between the strains and static loads applied to the test article. The FFN is trained using the Lavemberg-Marquard algorithm. The network is then used to predict the load experimentally applied during a static test on the real rib. The experiment shows good correlation between the loads computed from the strains data and the measured ones. Recently, in [77], Niessen et al. propose the use of ANN for the static load calibration as an alternative to the standard multiple linear regression techniques. They use a FFN, trained with Levenberg-Marquardt algorithm, for the static strain-load calibration of a PC-9/A trainer aircraft. The neural network shows a smaller calibration error than the multiple linear regression models for a all the considered load components. In [78] they extend the application of the ground-calibrated neural network to the in-flight loads reconstruction. In this case the network shows poor accuracy in the evaluation of loads outside of the original training range, where extrapolation is needed.

To summarize the current state-of-the-art, a large number of research efforts within this space surround the use of standard ANN or regression based models for “black-box” predictive capabilities with generally good success. Both linear regression models and ANN architectures come with a broad landscape of functional parameters, variations in model adaptation, numerical optimization schemes, loss functions, *etc.*, hence, generally only one or two model variations are explored in any given communication. As a result, there is a clear requirement for a contribution to the body-of-knowledge that consolidates the extensive range of ANN and linear regression model variants, including the vast landscape of internal functionality

variations, under a single benchmark aircraft loads monitoring problem.

2.2.2 Model based loads reconstruction

The model based loads reconstruction methods are mainly focused on the identification of the external loads. In fact, the knowledge of the structural model allows the determination of the internal loads also from the external ones. Moreover, within the aerospace field, the research is mainly focused on the reconstruction of the pressure distribution resulting from a continuously distributed aerodynamic load. Shkarayev et al. [79] developed a method based on the parametric approximation of the aerodynamic loading. This method requires the formulation of the unknown pressure distribution as a linear combination of known pressure distributions multiplied by unknown coefficients. The coefficients are computed by studying the strain fields caused by each known pressure distribution and by fitting, in a least-square sense, the linear combination of these strain fields to the discrete measured strains. The method proved to be really accurate on the identification of two pressure distributions on a rectangular wing box, but it requires the a priori definition of a pressure distribution function as close as possible to the actually applied one. Following the same approach, Cameron *et al.* extended the method by adopting single Fourier cosine terms [80] and double Fourier series [81] to parametrize different two-variables pressure distributions over a square plate. In [82], Airolidi et al. parametrized the complex external loads acting on a composite spar with a set of concentrated loads. They used a least-square approach to identify the parametrized load set from discrete strains. They also used the reconstructed load to carry on a direct FEM analysis for the evaluation of the strain and of the displacement field. The study proved that, also in the case where the parametrized loads were poorly identified, the strain field could be accurately reconstructed. The main focus of the paper was on the accuracy of the reconstructed strains distribution and on how the strain sensors could be distributed on the structure. In [83], Nakamura et al. proposed a pressure distribution identification technique based on the discretization of the pressure field with Finite Elements. Triangular elements are used to discretize the spatial domain of a flat wing-shaped plate, where the pressure is applied. The pressure field is interpolated from its unknown nodal values using spatial shape functions. The unknown nodal values of the pressure are computed by fitting the strain field caused by each nodal value of the pressure to the discrete measured strains. This method does not need any a priori knowledge of the form of the unknown pressure distribution. In fact, when the method has been compared to a Neural Network based approach in [84], it has proven to be more effective when the unknown pressure form was different from the ones that the network was trained with.

Although the literature review shows a significant effort surrounding the development of the shape sensing and loads reconstruction methods, the most crucial

aspect that is missing in the existing literature is the realisation of an integrated framework that can allow the simultaneous reconstruction of the loads and of the displacement field from the same measured quantities.

Chapter 3

Shape sensing methods

In this chapter, the shape sensing methods, as they have been used throughout this research project, are described in details. In particular, the general formulation of the **Modal Method** and the **Ko's Displacement theory** for beam-like structures, with the most recent development that this method has witnessed, are presented. Moreover, the **inverse Finite Element Method** is introduced and a novel approach for the integration of the strain field over the area of the recently introduced inverse quad element is proposed. This method has been also expanded to reconstruct large displacements, therefore, the incremental formulation of the method, designed to face this challenge, is also presented.

3.1 Modal Method

The modal method is a shape sensing technique based on the expression of the displacement field through known spacial basis functions and unknown weight coefficients. The method uses the modal shape as basis function and computes the unknown weights by fitting the strain field to the measured discrete strains. The detailed formulation of the method, as firstly introduced by Foss and Haugse [26], is now described. Assuming that a FE discretization of the displacement field is adopted, the displacement and the strain field can be expressed, through the use of classical modal transformation, in terms of the \mathbf{M} modal coordinates \mathbf{q}

$$\mathbf{w} = \Phi_d \mathbf{q} \quad (3.1)$$

$$\boldsymbol{\varepsilon} = \Phi_s \mathbf{q} \quad (3.2)$$

where $\mathbf{w}_{D \times 1}$ is the nodal degrees-of-freedom (DOFs) vector and $\boldsymbol{\varepsilon}_{S \times 1}$ is the strains vector. The modal matrix $[\Phi_d]_{D \times M}$ is constituted by \mathbf{M} columns (the i -th column being the i -th modal eigenvector of the displacement degrees-of-freedom). The modal matrix $[\Phi_s]_{S \times M}$ is also constituted by \mathbf{M} columns (the i -th column being the i -th set of strains corresponding to the i -th mode shape of the FE model

of the structure). The inversion of 3.2 leads to the computation of the modal coordinates in terms of the strains

$$\mathbf{q} = \mathbf{\Phi}_s^{-1} \boldsymbol{\varepsilon} \quad (3.3)$$

and by substituting 3.3 into 3.1, the formulation of the DOFs in terms of the strains is easily obtained:

$$\mathbf{w} = \mathbf{\Phi}_d \mathbf{\Phi}_s^{-1} \boldsymbol{\varepsilon} \quad (3.4)$$

The inversion of $\mathbf{\Phi}_s$ is possible if the matrix is square and consequently this formulation is valid for $S = M$. The number of strains and the number of computed modes are generally different. Moreover, the method is based on the computation of the displacement field from discrete strain measures. Therefore, it is necessary to substitute $\boldsymbol{\varepsilon}$ with the vector of the S_m discretely measured strain components $\boldsymbol{\varepsilon}^m_{S_m \times 1}$. In addition, a finite number of retained modes, M_r , has to be selected. The modal matrix $\mathbf{\Phi}_s$ is modified accordingly, by retaining the rows correspondent to the actually measured strain components and the columns relative to the retained modes, thus obtaining $[\mathbf{\Phi}_{sr}^m]_{S_m \times M_r}$. The modal matrix $\mathbf{\Phi}_d$ is also modified by only selecting the columns relative to the selected modes, thus obtaining $[\mathbf{\Phi}_{dr}^m]_{D \times M_r}$. The Eq. 3.3 can be generalized for the cases where $S_m \neq M_r$, by means of the Moore-Penrose pseudo inverse matrix formulation, $\mathbf{\Phi}_s^{m+}$ [85]. The substitution of this generalized inverse matrix formulation into 3.3 and 3.4 leads to the general formulation that allows the computation of the DOFs of the structure from the discretely measured strains, using the modal characteristics of the structure:

$$\mathbf{w} = \mathbf{\Phi}_{dr} \mathbf{\Phi}_{sr}^{m+} \boldsymbol{\varepsilon}^m \quad (3.5)$$

In practical applications, the most common scenario is the one where the number of measured strain components is greater than the number of selected modes and, consequently, $S_m > M_r$. This implies that Eq. 3.2 usually describes an overdetermined system of linear equations and that the generalized inverse formulation of $\mathbf{\Phi}_{sr}^m$ is the following:

$$\mathbf{\Phi}_s^{m+} = (\mathbf{\Phi}_{sr}^T \mathbf{\Phi}_{sr})^{-1} \mathbf{\Phi}_{sr}^T \quad \text{if } S_m > M_r \quad (3.6)$$

The substitution of 3.6 into Eq. 3.3 represents the least-square solution of the overdetermined system of linear equation, thus allowing the computation of the modal coordinates that best-fit, in a least-square sense, the strain field. In the end, the most common formulation of the Modal Method, for $S_m > M_r$, is easily obtained substituting Eq. 3.6 into Eq. 3.5:

$$\mathbf{w} = \mathbf{\Phi}_{dr} (\mathbf{\Phi}_{sr}^T \mathbf{\Phi}_{sr})^{-1} \mathbf{\Phi}_{sr}^T \boldsymbol{\varepsilon}^m \quad \text{if } S_m > M_r \quad (3.7)$$

3.1.1 Modal selection criterion

The Modal Method's formulation requires the computation of the modal characteristics of the structure. Moreover, a finite number of modes and relative mode shapes need to be selected, so that the deformed shape investigated by the method could be represented by the combination of the retained modes shapes.

Following the procedure described by Bogert et al. [24], it is possible to calculate the least-square fit of the modal coordinates to the static solution with a limited number of retained modes (M_r) and consequently non-squared modal matrix, $[\Phi_{dr}]_{D \times M_r}$. Pseudo-inverting Φ_{dr} in Eq. 3.1, in the most common condition where $D > M_r$, gives the possibility to compute the approximated modal coordinates \mathbf{q}_r that can best represent, in a least-square sense, the static deformed shape \mathbf{w} using a limited number of modes:

$$\mathbf{q}_r = (\Phi_{dr}^T \Phi_{dr})^{-1} \Phi_{dr}^T \mathbf{w} \quad (3.8)$$

Using the least-square approximated modal coordinates \mathbf{q}_r in Eq. 3.1, it is possible to compute the approximated modal representation of the static solution, \mathbf{w}_r , using only the retained modes:

$$\mathbf{w}_r = \Phi_{dr} \mathbf{q}_r \quad (3.9)$$

This matrix expression can be written as the summation of the contribution of each mode:

$$\mathbf{w}_r = \sum_{i=1}^{M_r} \Phi_{dr_i} q_{r_i} \quad (3.10)$$

where Φ_{dr_i} is the column of the Φ_{dr} matrix relative to the i -th mode shape and q_{r_i} is the corresponding i -th modal coordinate.

Therefore, the contribution of the i -th mode shape to the representation of the displacement field is:

$$\mathbf{w}_{r_i} = \Phi_{dr_i} q_{r_i} \quad (3.11)$$

and consequently, the strain energy associated with this i -th contribution to the displacement field is:

$$E_{r_i} = \frac{1}{2} \mathbf{w}_{r_i}^T \mathbf{K} \mathbf{w}_{r_i} \quad (3.12)$$

where \mathbf{K} is the stiffness matrix.

Substituting Eq. 3.11 into Eq. 3.12 yields to:

$$E_{r_i} = \frac{1}{2} q_{r_i}^T \Phi_{dr_i}^T \mathbf{K} \Phi_{dr_i} q_{r_i} \quad (3.13)$$

If the modal shapes are then normalized with respect to mass matrix:

$$\Phi_{dr_i}^T \mathbf{K} \Phi_{dr_i} = \omega_i^2 \quad (3.14)$$

where ω_i is the natural angular frequency associated to the i -th mode, Eq. 3.13 becomes:

$$E_{r_i} = \frac{1}{2} \omega_i^2 q_{r_i}^2 \quad (3.15)$$

On the other hand, the total strain energy due to the static deformation is:

$$E = \frac{1}{2} \mathbf{w}^T \mathbf{K} \mathbf{w} \quad (3.16)$$

The comparison of the i -th contribution to the total strain energy and the total strain energy:

$$\frac{E_{r_i}}{E} \quad (3.17)$$

allows the quantification of the amount of the static deformation that the i -th mode is able to represent, thus allowing the selection of the modes that can most accurately reconstruct the investigated static deformation. To apply this selection criterion, the investigated static deformation has to be known a-priori to compute E .

3.2 Ko's Displacement theory

The Ko's Displacement [19] theory is a shape sensing method for beam-like structures. In fact, it is based on the Bernoulli-Euler's beam formulation. According to this beam theory, the curvature of the beam is expressed by the second derivative of the deflection w with respect to the axial coordinate of the beam. The curvature along the axis of the beam is related to the axial strain measured on top or bottom surfaces of the beam by the following expression:

$$w_{,pp}(p) = -\varepsilon(p)/z \quad (3.18)$$

where z is the distance between the neutral axis and the location where the strain is computed and ε is the strain measured along the p direction (Figure 3.1).

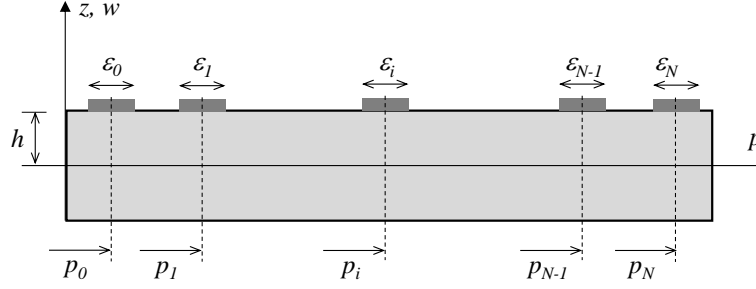


Figure 3.1: Ko's Displacement theory - Geometry and sensors' location.

If $N + 1$ strain measures are located along p at $p = p_0, p_1, \dots, p_N$ (Figure 3.1), respectively, and the strain is assumed to be linear within two consecutive strain measures, a function of ε in terms of the axial coordinate of the beam is easily obtained:

$$\varepsilon(p) = \varepsilon_{i-1} + \frac{(\varepsilon_i - \varepsilon_{i-1})}{(p_i - p_{i-1})}(p - p_{i-1}), \quad p_{i-1} \leq p \leq p_i \quad (i = 1, 2, \dots, N) \quad (3.19)$$

Eq. 3.19 can be substituted into Eq. 3.18 and, under the assumption that the distance of the strain measures from the neutral axis of the beam remains constant along p ($z = h$), the curvature can be integrated two times with respect to p , thus providing a formulation of the deflection of the beam in terms of the discretely measured $N + 1$ strains [63]:

$$w_i = -\frac{1}{6h} \left[\sum_{j=1}^i (2\varepsilon_{j-1} + \varepsilon_j)(p_j - p_{j-1})^2 + 3 \sum_{k=1}^{i-1} (\varepsilon_{k-1} + \varepsilon_k)(p_k - p_{k-1})(p_i - p_k) \right] \quad (i = 1, 2, \dots, N) \quad (3.20)$$

This expression is obtained by imposing the clamping boundary conditions ($w = 0$; $w_{,p} = 0$) to the section of the beam located at $p = p_0$. This configuration is the one that is more relevant for the study of wing structures, that resemble a clamped beam. In general, other formulations, considering different boundary conditions or a varying distance of the strain measures from the neutral axis have also been derived [19]. All the derived formulations, as the one reported here, are able to only compute the deflection of the beam at the specific locations where the axial strains are measured.

3.2.1 Modal expansion

To overcome the limitations on the displacements that the Ko's Displacement theory is able to reconstruct, a modal expansion approach has been developed by

Pak [53]. According to this procedure, the displacements along the strain sensing line are computed using the classic Ko's Displacement theory described in the previous section. These displacements are then used in a second analysis step to compute the whole displacement field of the structure, using only the axial strain measurements adopted in the previous step. The deflections reconstructed during the first step are defined as master degrees of freedom, \mathbf{w}_m and are used to derive the other degrees of freedom, that are called slave degrees of freedom, \mathbf{w}_s . The expansion from the master to slave degrees of freedom is obtained through the use of the modal shapes of the structure, according to the System Equivalent Reduction Expansion Process (SEREP) [54]. In fact, the master and slave DOFs can be expressed in terms of the modal shapes and the modal coordinates through Eq. 3.1:

$$\mathbf{w}_m = \Phi_{dm} \mathbf{q}_r \quad (3.21a)$$

$$\mathbf{w}_s = \Phi_{ds} \mathbf{q}_r \quad (3.21b)$$

where $[\Phi_{dm}]_{D_m \times M_r}$ and $[\Phi_{ds}]_{D_s \times M_r}$ are the modal matrices relative to the master and slave DOFs, respectively and $\mathbf{q}_r_{M_r \times 1}$ is the vector of the modal coordinates. The pseudo-inversion of Eq. 3.21a, for the most common case scenario, where the number of master DOFs, D_m , is higher than the number of retained modes, M_r , gives:

$$\mathbf{q}_r = (\Phi_{dm}^T \Phi_{dm})^{-1} \Phi_{dm}^T \mathbf{w}_m \quad (3.22)$$

that, substituted into Eq. 3.21b, allows the computation of the slave DOFs in terms of the master ones and the modal shapes of the structure:

$$\mathbf{w}_s = \Phi_{ds} (\Phi_{dm}^T \Phi_{dm})^{-1} \Phi_{dm}^T \mathbf{w}_m \quad (3.23)$$

This expression allows the expansion of the displacements calculated with the Ko's Displacement theory to the reconstruction of the whole displacement field. As can be noticed, this procedure requires the computation and the selection of the modal shapes that can best represent the investigated static deformation. Therefore, the selection criterion, illustrated for the Modal Method in section 3.1.1, can be also applied for this method. In the remaining of thesis, when referencing to Ko's Displacement theory, this extended formulation is considered.

3.3 Inverse Finite Element Method

The inverse Finite Element Method (iFEM) is a shape sensing method based on the discretization of the structural domain with Finite Elements [57]. As for the direct Finite Element method, the displacement field is expressed in terms of

the kinematic variables according to a specific structural model. In this work, only thin-walled structures are analysed and therefore the structural model considered has been the plate theory. Specifically, the First Order Shear Deformation Theory (FSDT) has been adopted for all the involved applications.

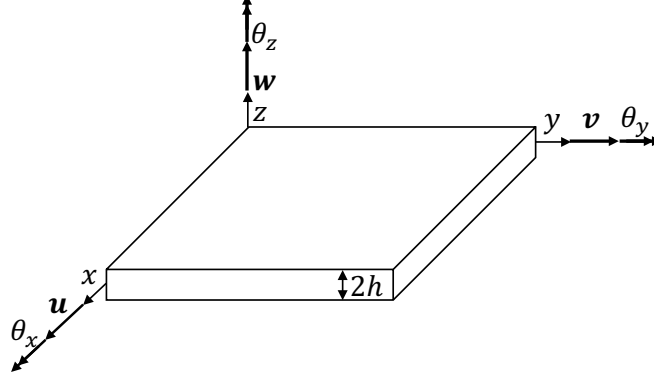


Figure 3.2: Plate notation.

Following the notation reported in Figure 3.2, the FSDT model of the displacement field of a plate can be expressed through the following equations:

$$u_x(x, y, z) \equiv u_x = u + z\theta_y \quad (3.24a)$$

$$u_y(x, y, z) \equiv u_y = v - z\theta_x \quad (3.24b)$$

$$u_z(x, y, z) \equiv u_z = w \quad (3.24c)$$

where u_x , u_y , u_z are the displacement's components along the coordinate axes (x, y, z) , u and v are the plate mid-surface in-plane displacements, w is the transverse deflection, θ_x and θ_y are the bending rotations. As a consequence, the strain field, derived from this formulation is:

$$\mathbf{e} = [u_{,x}, v_{,y}, v_{,x} + u_{,y}]^T = [\varepsilon_1, \varepsilon_2, \varepsilon_3]^T \quad (3.25a)$$

$$\mathbf{k} = [\theta_{y,x}, -\theta_{x,y}, \theta_{y,y} - \theta_{x,x}]^T = [\varepsilon_4, \varepsilon_5, \varepsilon_6]^T \quad (3.25b)$$

$$\mathbf{g} = [w_{,x} + \theta_y, w_{,y} - \theta_x]^T = [\varepsilon_7, \varepsilon_8]^T \quad (3.25c)$$

where \mathbf{e} , \mathbf{k} and \mathbf{g} represent the membrane strains, bending curvatures and transverse shear strains of the plate, respectively.

Once the kinematic model is established, the domain is discretized using FE and the displacement field inside each element is interpolated using shape functions:

$$[u, v, w, \theta_x, \theta_y]^T = \mathbf{N}\mathbf{u}^e \quad (3.26)$$

where \mathbf{N} is the shape functions matrix and \mathbf{u}^e is:

$$\begin{aligned}\mathbf{u}^e &= [\mathbf{u}_1^e \ \mathbf{u}_2^e \ \dots \ \mathbf{u}_S^e]^T \\ \mathbf{u}_i^e &= [u_i \ v_i \ w_i \ \theta_{xi} \ \theta_{yi}]^T \quad (i = 1, 2, \dots, S)\end{aligned}\tag{3.27}$$

\mathbf{u}_i^e is the vector of the DOFs relative to the i -th node of the element and S is the number of the element's nodes. \mathbf{N} and S depend on the chosen element formulation and will be described in details in the following sections. As a consequence, the i -th strain component defined in Eq. 3.25 can also be expressed in terms of the nodal values of the displacements and the spatial derivatives of the shape functions:

$$\varepsilon_k(\mathbf{u}^e) = \mathbf{B}_k \mathbf{u}^e \quad (k = 1, 2, \dots, 8)\tag{3.28}$$

where \mathbf{B}_k is the matrix containing the derivatives of the shape functions related to the k -th strain measure.

The iFEM is based on the minimization of the error between the strain field, expressed in terms of the nodal displacements of the discretized structural domain (Eq. 3.28), and the strain field actually measured on the structure at some discrete locations. This error is expressed through the following weighted functional:

$$\Psi^e(\mathbf{u}^e) = \sum_{k=1}^8 \lambda_k^e w_k^e \iint_{A_e} (\varepsilon_k(\mathbf{u}^e) - \varepsilon_k^\varepsilon)^2 dx dy\tag{3.29}$$

This functional takes into account for the eight strain components defined in Eqs. 3.25. The superscript ε denotes an experimentally measured value. The argument of the integral over the element's area, A_e , is the squared difference between the experimentally evaluated strain measure, $\varepsilon_k^\varepsilon$, and its analytical counterpart, $\varepsilon_k(\mathbf{u}^e)$, depending on the element nodal DOFs. In the case of sparse strain sensors, the absence of the k -th strain measure within an element is taken into account by setting the experimental strain measure to zero and by setting the penalization factor λ_k^e to a small value ($10^{-4}, 10^{-5}, 10^{-6}$). Otherwise, if the k -th strain measure has been experimentally evaluated in the element, the related λ_k^e is set to be equal to 1. The w_k^e are dimensional coefficients required to guarantee the physical units consistency of Eq. (3.29). They are set as follows: $w_k^e = 1$ for $k = 1, 2, 3, 7, 8$ and $w_k^e = (2h)^2$ for $k = 4, 5, 6$, where h is the half-thickness of the element.

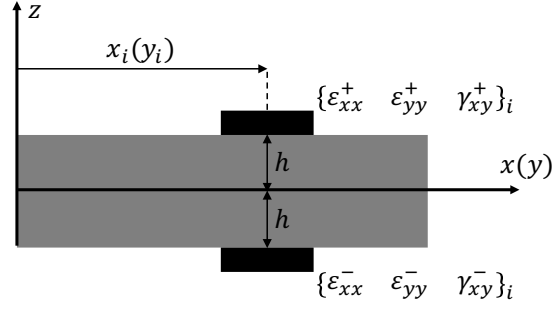


Figure 3.3: Strain measure.

The k -th integral in Eq. 3.29 is numerically computed using the Gaussian quadrature. Therefore, it is transformed into a summation of the integrand evaluated over the $n \times n$ Gauss points:

$$\iint_{A^e} (\varepsilon_k(\mathbf{u}^e) - \varepsilon_k^\varepsilon)^2 dx dy = \sum_{g=1}^{n \times n} J(g) \omega_g (\varepsilon_{k(g)}(\mathbf{u}^e) - \varepsilon_{k(g)}^\varepsilon)^2 \quad (k = 1, 2, \dots, 8) \quad (3.30)$$

where ω_g are the quadrature weights, $J(g)$ is the determinant of the Jacobian of the transformation from the physical coordinates to the natural ones of the element computed in the g -th quadrature point. The subscript g denotes the computation of the quantity in the g -th quadrature point.

The first six strain measures that appear in Eqs. 3.29 and 3.30 can be easily computed from experimentally measured strains on the bottom and top surfaces of the plate (Figure 3.3). In fact, at a generic i -th location, the membrane strains, $\mathbf{e}_{(g)}^\varepsilon$ and the bending curvatures $\mathbf{k}_{(g)}^\varepsilon$ can be evaluated as follows:

$$\mathbf{e}_{(g)}^\varepsilon = \begin{Bmatrix} \varepsilon_1 \\ \varepsilon_2 \\ \varepsilon_3 \end{Bmatrix}_{(g)} = \frac{1}{2} \begin{Bmatrix} \varepsilon_{xx}^+ + \varepsilon_{xx}^- \\ \varepsilon_{yy}^+ + \varepsilon_{yy}^- \\ \gamma_{xy}^+ + \gamma_{xy}^- \end{Bmatrix}_{(g)} \quad (3.31a)$$

$$\mathbf{k}_{(g)}^\varepsilon = \begin{Bmatrix} \varepsilon_4 \\ \varepsilon_5 \\ \varepsilon_6 \end{Bmatrix}_{(g)} = \frac{1}{2h} \begin{Bmatrix} \varepsilon_{xx}^+ - \varepsilon_{xx}^- \\ \varepsilon_{yy}^+ - \varepsilon_{yy}^- \\ \gamma_{xy}^+ - \gamma_{xy}^- \end{Bmatrix}_{(g)} \quad (3.31b)$$

On the other hand, since the transverse shear strains are not measurable, the $\lambda_{7,8}^\varepsilon$ are always set to a small value and the $\varepsilon_{7,8}^\varepsilon$ are equal to 0, in the functional.

The procedure is completed with the minimization of the error functional in (3.29) with respect to the DOFs, thus leading to a system of linear equations that can be solved to find the nodal DOFs of the element:

$$\frac{\partial \Psi_e(\mathbf{u}^e)}{\partial \mathbf{u}^e} = \mathbf{l}^e \mathbf{u}^e - \mathbf{f}^e = 0 \quad (3.32a)$$

$$\mathbf{u}^e = \mathbf{l}^{e-1} \mathbf{f}^e \quad (3.32b)$$

where:

$$\mathbf{l}^e = \sum_{k=1}^8 \sum_{g=1}^{n \times n} [J(g) \lambda_k^e w_k^e \omega_g \mathbf{B}_{k(g)}^T \mathbf{B}_{k(g)}] \quad (3.33a)$$

$$\mathbf{f}^e = \sum_{k=1}^6 \sum_{g=1}^{n \times n} [J(g) \lambda_k^e w_k^e \omega_g \mathbf{B}_{k(g)}^T \varepsilon_{k(g)}^e] \quad (3.33b)$$

The subscript g , related to the \mathbf{B}_k matrices, denotes the computation of the matrix in the g -th Gauss point. The summation in Eq. 3.33b is only extended to the first six strain components that are measurable on the plate, being $\varepsilon_{7,8}^e$ always equal to 0.

The extension of the procedure to all the elements of the domain, through the assembly process, leads to the system of linear equations for the global DOFs of the structure, \mathbf{U} :

$$\mathbf{U} = \mathbf{L}^{-1} \mathbf{F} \quad (3.34)$$

where \mathbf{L} is a matrix depending on the shape functions and strain-sensor locations, whereas \mathbf{F} is a vector incorporating the measured strains. The matrix \mathbf{L} is a well-conditioned square matrix that, upon enforcement of the displacement boundary conditions, can be inverted. Assuming that the strain-sensor locations is not changed, the inversion of \mathbf{L} is performed only once whereas the vector \mathbf{F} needs to be updated at each strain-data acquisition increment. Since only strain-displacement relations are invoked in the formulation, the method does not require the knowledge of the material properties or the applied loads. Thus, it is applicable for both static and dynamic loading conditions, without requiring inertial or damping material properties.

3.3.1 Tria formulation

The triangular shell elements are the ones that have been firstly developed for the iFEM formulation. In fact, these elements presents some characteristic that facilitate the computation of the required matrices with only one strain measure within the element, as it will be explained in the following.

The triangular element based on the FSDT, or Mindlin plate theory, is denoted as iMIN3 [49]. The formulation of the element is obtained by imposing that the number of nodes of the element, S , is equal to 3 and defining the shape functions matrix in Eq. 3.26. The displacement field, within the element, is expressed through C^0 continuous shape functions that interpolate the five nodal values of the displacement in each node, as they are shown in Figure 3.4.

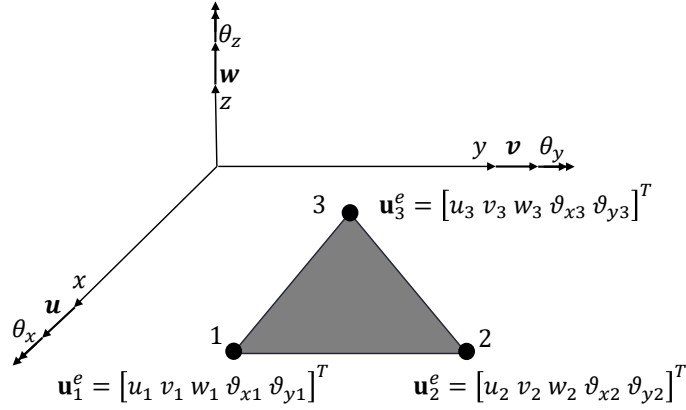


Figure 3.4: Triangular shell element (iMIN3).

Particularly, an anisoparametric interpolation is used. The deflection, w , is interpolated by a quadratic polynomial and the other four variables are interpolated linearly. Therefore, if the shape function matrix is written as follows:

$$\mathbf{N} = [\mathbf{N}^1 \ \mathbf{N}^2 \ \mathbf{N}^3] \quad (3.35)$$

then, the \mathbf{N}^i matrices are:

$$\mathbf{N}^i = \begin{bmatrix} L_i & 0 & 0 & 0 & 0 \\ 0 & L_i & 0 & 0 & 0 \\ 0 & 0 & L_i & L_{2i} & L_{1i} \\ 0 & 0 & 0 & L_i & 0 \\ 0 & 0 & 0 & 0 & L_i \end{bmatrix} \quad (i = 1, 2, 3) \quad (3.36)$$

where, L_i ($i = 1, 2, 3$) are the linear interpolation functions represented by the area-parametric coordinates of the triangle, whereas L_{1i} , L_{2i} ($i = 1, 2, 3$) are the following quadratic shape functions:

$$L_{1i} = \frac{L_i}{2}(a_l L_m - a_m L_l) \quad L_{2i} = \frac{L_i}{2}(b_m L_l - b_l L_m) \quad (3.37)$$

$$a_k = (x_m - x_l) \quad b_k = (y_l - y_m)$$

the $x_{m,l}$ and $y_{m,l}$ being the x and y coordinate of the (m,l) -th node of the triangle. The subscripts are obtained by the cyclic permutation of $k = 1, 2, 3$, $l = 2, 3, 1$ and $m = 3, 1, 2$.

From \mathbf{N} is easy to compute the eight \mathbf{B}_k matrices by differentiating the shape functions, according to Eqs. 3.25. Using the same notation adopted for the shape function matrix, the \mathbf{B}_k becomes:

$$\mathbf{B}_k = [\mathbf{B}_k^1 \ \mathbf{B}_k^2 \ \mathbf{B}_k^3] \quad (3.38)$$

and, consequently, the \mathbf{B}_k^i matrices can be expressed as it follows:

$$\begin{aligned}
 \mathbf{B}_1^i &= [L_{i,x} \ 0 \ 0 \ 0 \ 0] \\
 \mathbf{B}_2^i &= [0 \ L_{i,y} \ 0 \ 0 \ 0] \\
 \mathbf{B}_3^i &= [L_{i,y} \ L_{i,x} \ 0 \ 0 \ 0] \\
 \mathbf{B}_4^i &= [0 \ 0 \ 0 \ 0 \ L_{i,x}] \\
 \mathbf{B}_5^i &= [0 \ 0 \ 0 \ -L_{i,y} \ 0] \\
 \mathbf{B}_6^i &= [0 \ 0 \ 0 \ -L_{i,x} \ L_{i,y}] \\
 \mathbf{B}_7^i &= [0 \ 0 \ L_{i,x} \ L_{2i,x} \ (L_{1i,x} + L_i)] \\
 \mathbf{B}_8^i &= [0 \ 0 \ L_{i,y} \ (L_{2i,y} - L_i) \ L_{1i,y}] \quad (i = 1, 2, 3)
 \end{aligned} \tag{3.39}$$

The derivatives of the linear functions L_i are constant over the area of the triangle. Moreover, $J(g)$, for triangular element is constant and equal to the area of the triangle, A^e . Therefore, the computation of the integral in 3.30 and the consequent processing of the matrices \mathbf{l}^e and \mathbf{f}^e can be easily obtained. In fact, the first six strain components, that are the ones which are measurable, are constant over the element's area. The integrals relative to these components can be simply computed by multiplying the integrand by the area of the triangle. The matrices \mathbf{l}^e and \mathbf{f}^e are thus reduced to:

$$\mathbf{l}^e = \sum_{k=1}^6 A^e [\lambda_k^e w_k^e \mathbf{B}_k^T \mathbf{B}_k] + \sum_{k=7}^8 A^e \sum_{g=1}^{n \times n} [\lambda_k^e w_k^e \omega_g \mathbf{B}_{k(g)}^T \mathbf{B}_{k(g)}] \tag{3.40a}$$

$$\mathbf{f}^e = \sum_{k=1}^6 A^e [\lambda_k^e w_k^e \mathbf{B}_k^T \varepsilon_{k(centroid)}] \tag{3.40b}$$

The subscript (*centroid*) denotes the sensing of the experimentally measured strain in the centroid of the element. It is important to notice that, since the measurable strain field is constant over the area of the triangle, this triangular element only requires one strain measure within an element to compute \mathbf{f}^e . The unique experimentally measured strain is usually located in the centroid of the element, where the analytical evaluation of the strain is more accurate. Also in this case, $w_k^e = 1$ for $k = 1, 2, 3, 7, 8$ and $w_k^e = (2h)^2$ for $k = 4, 5, 6$, where h is the half-thickness of the element. λ_k^e is set to be equal to 1 when the related k-th strain component is actually measured on the element, whereas it is set to a small value if the measure is not available.

3.3.2 Quad formulation

The quadrilateral element based on the FSDT, defined as IQS4, has been developed in [58]. The formulation of this element introduced a higher level of complexity with respect to the integrations required by the iFEM. Moreover, this element

introduced the drilling degree of freedom [86], θ_z , and therefore, the six nodal displacements for each node are the ones presented in Figure 3.5.

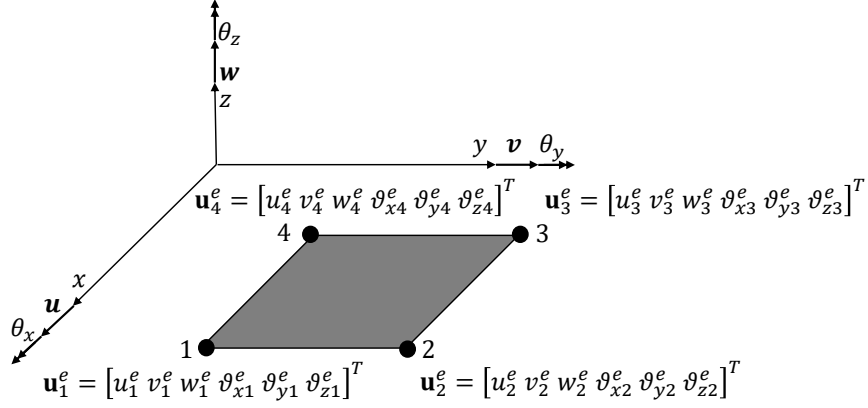


Figure 3.5: Quadrilateral shell element (iQS4).

As for the triangular element, the formulation uses an anisoparametric interpolation of the displacement field, selecting linear (N_i) and parabolic (L_i , M_i) shape functions. Once again, the shape function matrix can be expressed in the form:

$$\mathbf{N} = [\mathbf{N}^1 \quad \mathbf{N}^2 \quad \mathbf{N}^3 \quad \mathbf{N}^4] \quad (3.41)$$

where:

$$\mathbf{N}^i = \begin{bmatrix} N_i & 0 & 0 & 0 & 0 & L_i \\ 0 & N_i & 0 & 0 & 0 & M_i \\ 0 & 0 & N_i & -L_i & -M_i & 0 \\ 0 & 0 & 0 & N_i & 0 & 0 \\ 0 & 0 & 0 & 0 & N_i & 0 \\ 0 & 0 & 0 & 0 & 0 & N_i \end{bmatrix} \quad (i = 1, 2, 3, 4) \quad (3.42)$$

The detailed expressions of the shape functions N_i , L_i and M_i , as reported in [58, 87], can be found in Appendix A.

Using the strain-displacement relation in Eq. 3.25 it is possible to compute the \mathbf{B}_k matrices in the form:

$$\mathbf{B}_k = [\mathbf{B}_k^1 \quad \mathbf{B}_k^2 \quad \mathbf{B}_k^3 \quad \mathbf{B}_k^4] \quad (3.43)$$

where:

$$\begin{aligned}
 \mathbf{B}_1^i &= [N_{i,x} \ 0 \ 0 \ 0 \ 0 \ L_{i,x}] \\
 \mathbf{B}_2^i &= [0 \ N_{i,y} \ 0 \ 0 \ 0 \ M_{i,y}] \\
 \mathbf{B}_3^i &= [N_{i,y} \ N_{i,x} \ 0 \ 0 \ 0 \ (L_{i,y} + M_{i,x})] \\
 \mathbf{B}_4^i &= [0 \ 0 \ 0 \ 0 \ N_{i,x} \ 0] \\
 \mathbf{B}_5^i &= [0 \ 0 \ 0 \ -N_{i,y} \ 0 \ 0] \\
 \mathbf{B}_6^i &= [0 \ 0 \ 0 \ -N_{i,x} \ N_{i,y} \ 0] \\
 \mathbf{B}_7^i &= [0 \ 0 \ N_{i,x} \ -L_{i,x} \ (-M_{i,x} + N_{i,y}) \ 0] \\
 \mathbf{B}_8^i &= [0 \ 0 \ N_{i,y} \ (-L_{i,y} - N_{i,x}) \ -M_{i,y} \ 0] \quad (i = 1, 2, 3, 4)
 \end{aligned} \tag{3.44}$$

In this case, none of the eight strain component is constant over the element's area. Therefore, the integration in Eq. 3.30, and the consequent computation of \mathbf{l}^e and \mathbf{f}^e , can not be simplified. They remain the same expressed in Eqs. 3.33. Theoretically, the construction of \mathbf{f}^e requires the knowledge of the k -th strain measure in every $n \times n$ Gauss point of a sensorized element. In previous works [58, 88, 12], to avoid the excessive number of strain sensors required by the integration, the same strain measure, located in an arbitrary location within the the element ($\varepsilon_{k(element)}^e$), has been associated to all the quadrature points, thus obtaining the following formulation:

$$\mathbf{l}^e = \sum_{k=1}^8 \sum_{g=1}^{n \times n} [J(g) \lambda_k^e w_k^e \omega_g \mathbf{B}_{k(g)}^T \mathbf{B}_{k(g)}] \tag{3.45a}$$

$$\mathbf{f}^e = \sum_{k=1}^6 \sum_{g=1}^{n \times n} [J(g) \lambda_k^e w_k^e \omega_g \mathbf{B}_{k(g)}^T \varepsilon_{k(element)}^e] \tag{3.45b}$$

In this work, a novel integration scheme is proposed, to increase the accuracy in the attribution of the strain measure to a specific location within the element, namely the centroid of the quad. The procedure is inspired by the same penalization approach adopted in the formulation of the weighted functional. Using an odd number of Gauss points, there is always a quadrature point located in the centroid of the element. Therefore, another penalization factor, χ_g is introduced. This weight is set to 1 for the Gauss point that is located in the centroid of the element, where the strain measure is actually extracted, whereas is set to a small value for the remaining points of the quadrature. The formulation of the matrices is then modified as it follows:

$$\mathbf{l}^e = \sum_{k=1}^8 \sum_{g=1}^{n \times n} [J(g) \lambda_k^e w_k^e \omega_g \chi_g \mathbf{B}_{k(g)}^T \mathbf{B}_{k(g)}] \quad \begin{pmatrix} \chi_{g=\text{centroid}} = 1 \\ \chi_{g \neq \text{centroid}} = 10^{-4} \end{pmatrix} \quad (3.46a)$$

$$\mathbf{f}^e = \sum_{k=1}^6 \sum_{g=1}^{n \times n} [J(g) \lambda_k^e w_k^e \omega_g \chi_g \mathbf{B}_{k(g)}^T \varepsilon_{k(\text{centroid})}^e] \quad \begin{pmatrix} \chi_{g=\text{centroid}} = 1 \\ \chi_{g \neq \text{centroid}} = 10^{-4} \end{pmatrix} \quad (3.46b)$$

Since the χ_i weights are introduced to take into account for the exact location of the strain sensors, they are adopted only when a measure is present within the element. Therefore, for $k = 7, 8$ and for elements without sensors, only the penalization strategy introduced by λ_k^e is adopted.

3.3.3 Incremental formulation

To extend the capabilities of the iFEM, in this work, an incremental formulation of the method has been developed to allow the reconstruction of large displacements. This procedure is inspired by the standard incremental procedures used for geometrically non-linear analysis of the direct FEM. If the load (P), that induces the investigated large displacements and the consequent strains, is divided into N increments, the standard iFEM procedure can be applied for each load increment.

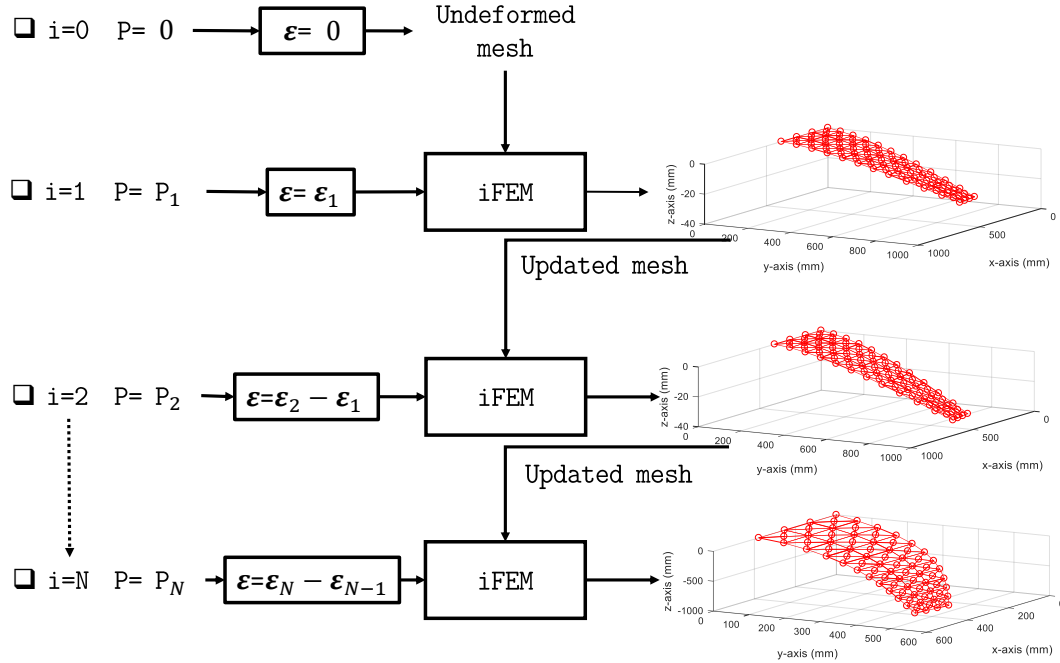


Figure 3.6: Incremental iFEM.

Particularly, the following procedure, schematized in Figure 3.6, is proposed:

- Starting from the undeformed structure, the load is divided into N load increments and for each one of them the strains' increments are also computed.
- For $i = 1$ the iFEM is applied on the undeformed mesh, using the strains' increment due to the P_1 load increment. The mesh is then updated by adding the reconstructed nodal displacements to the undeformed one.
- The i -th step, for $(i = 2, 3, \dots, N)$, is performed applying the standard iFEM procedure to the updated mesh from the previous step ($i = i - 1$) and considering the strains' increment relative to the i -th load's increment. The reconstructed displacements are then used to update the mesh for the next step ($i = i + 1$).
- The orientations of the measured strains are updated together with the mesh in every step, in order to be aligned with the updated geometry.
- The above-stated incremental procedure is repeated until the strain history is complete.

Chapter 4

Numerical shape sensing

The shape sensing methods described in the previous chapter are now numerically applied to different test cases. In particular, the proposed integration scheme for the quadrilateral iFEM elements is validated on the benchmark problem of a flat plate and its performances are compared with the ones from the previously developed integration procedure. Once the formulation is validated, the new iFEM quad formulation, the tria iFEM, the Modal Method and the Ko's Displacement's theory are all compared on the shape reconstruction of a composite Wing Box subject to torsion and bending deformations. The comparison involves the study of the optimal sensor's configuration for each method and the evaluation of the pros and cons that each method shows for the considered application. The shape sensing methods are also tested against the uncertainty of the inputs, related to real experimental scenarios. Finally, the proposed incremental iFEM is also validated on the sensing of a wing-shaped plate undergoing large displacements.

4.1 Preliminary study on the novel inverse QUAD element

The first study on the numerical application of the shape sensing methods involves the validation of the proposed inverse quad element's formulation. The new integration scheme of the strain field over the element's area, based on the penalization of the contribution from the gauss points where the strain is not measured (Section 3.3.2), is tested against the previous formulation that attributes the same value of the strain to all the gauss point within the element, without any penalization [58]. The two iFEM elements are compared on a benchmark problem. A thin plate is used to test the accuracy in the reconstruction of the in-plane and transverse displacements, when the plate is subject to an in-plane shear load or a transverse load, respectively.

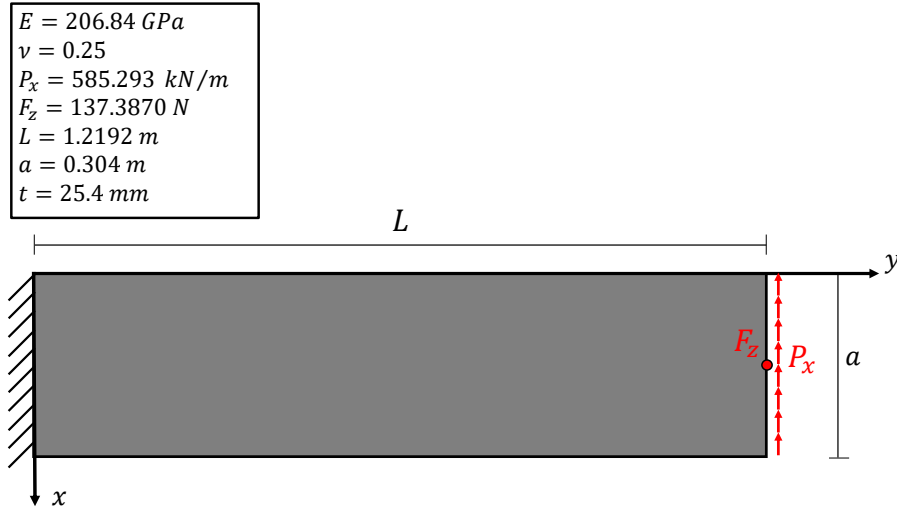


Figure 4.1: Plate - Benchmark plate for the validation of the novel integration scheme of the iFEM quad element.

The material properties and the geometry of the plate are illustrated in Figure 4.1, where E is the Young's Modulus, ν is the Poisson's ratio and t is the thickness of the plate. The plate is clamped on the left edge, at ($y = 0$), and two load cases are considered on the left edge, at ($y = L$). The first load case, designed to validate the membrane response of the new formulation, presents an in-plane shear distributed load, P_x , applied on the left edge. The load and its intensity are reported in Figure 4.1. The second load case, created to test the out-of-plane bending response of the element, is constituted by a nodal force, F_z , applied in the mid point of the right edge and directed along the negative direction of the z axis, as illustrated in Figure 4.1. For both the load cases the same inverse mesh and the same strain sensors' configuration are used. The iFEM mesh is constituted by 64 inverse quad elements and 85 nodes. Each element is sensorized with a strain rosette, located in the centroid, that measures the ε_{xx} , ε_{yy} and γ_{xy} strain components on the top (+) and bottom (-) surface of the plate. The inverse mesh and the sensors' configuration are shown in Figure 4.2.

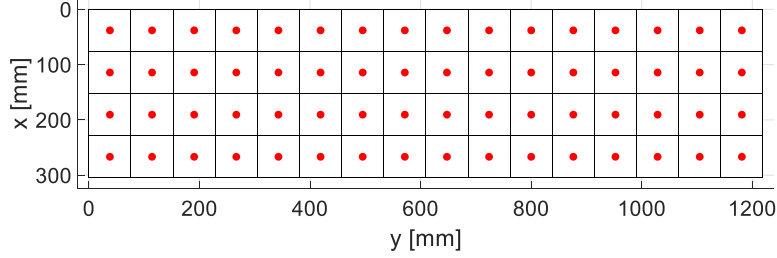
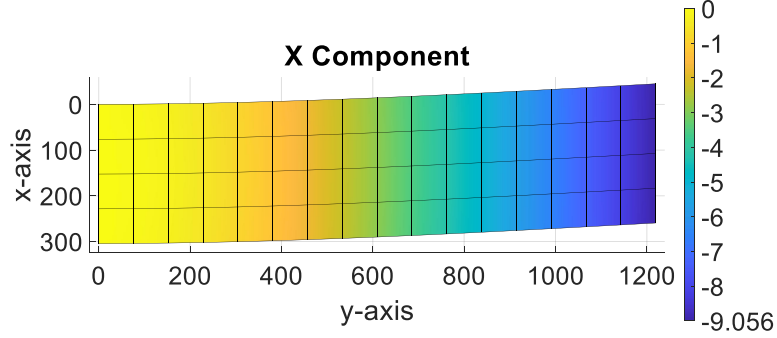


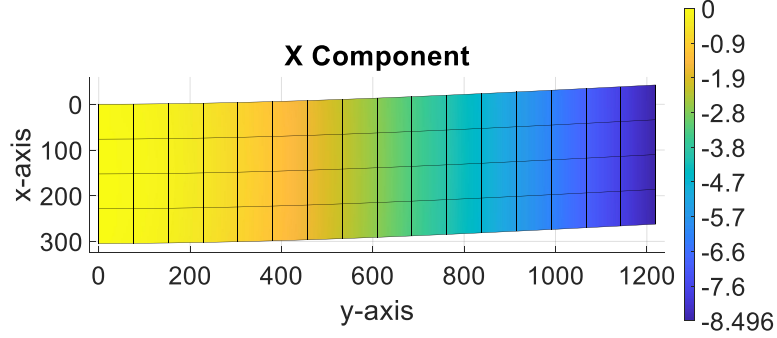
Figure 4.2: iFEM mesh - The dots represent the location of the strain rosettes within each element.

A high-fidelity mesh, used to compute the reference displacements and the input strains for the iFEM, is also realized using 1024 QUAD4 elements, and analysed through the commercial FEM solver MSC/NASTRAN®. The mesh is obtained by splitting the inverse mesh into 4×4 quads. By doing so, every node and every centroid of the inverse mesh has a corresponding node in the high-fidelity direct mesh.

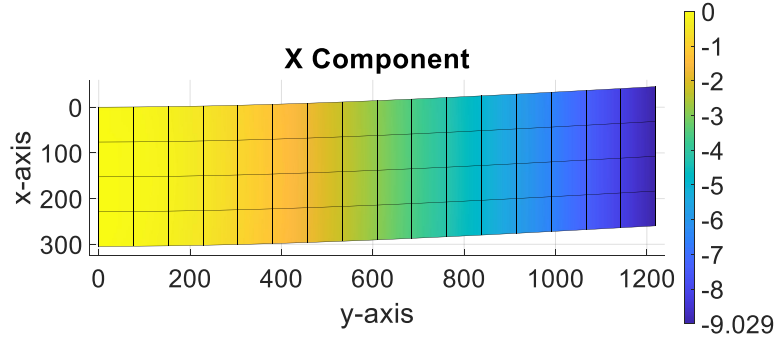
The reference displacements along x for the in-plane shear load, obtained with the refined model and reported on the nodes of the inverse mesh, are presented in Figure 4.3a.



(a) Reference u displacements



(b) Reconstructed u displacement - old integration scheme



(c) Reconstructed u displacement - new integration scheme

Figure 4.3: In-plane shear load - In the figures, the displacements u along the x direction are reported for the in-plane shear load load case. The colour bar refers to the magnitude (in mm) of the u displacements.

Along with the reference deformed shape along x , in Figure 4.3 are reported the reconstructed displacements with the iFEM, using the old integration scheme (4.3b) and the newly proposed one (4.3c). The percentage error on the reconstruction of the maximum vertical displacement, adopting the old integration scheme, is 6.2%. The same reconstruction, computed with the proposed integration scheme, generates a more accurate result, being the same percentage error equal to only 0.3%. These results are obtained using the same sensors configuration reported in Figure 4.2. A more accurate reconstruction can be achieved, using the old integration scheme, if a different strain sensors' configuration is chosen. Using the sensors' configuration proposed in [58] (Figure 4.4) and the old integration scheme, the reconstructed shape reported in Figure 4.5 is obtained. In this case, the error on the maximum vertical displacement is only 0.6%. This value is slightly higher than the one obtained with the novel integration scheme. Moreover, the sensors' locations are not unequivocally determined by the geometry of the elements, as it is for the other sensors' configuration where the centroid is used, and have to be somehow determined.

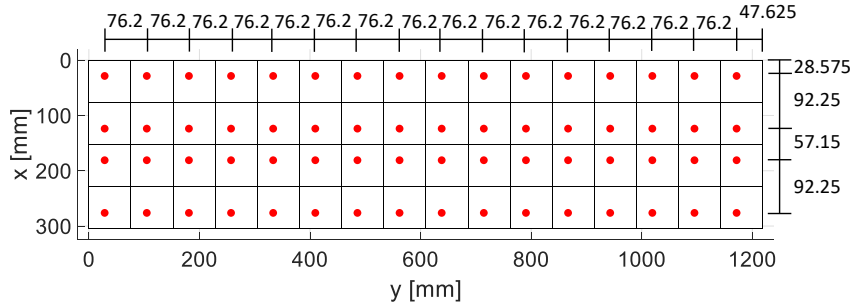


Figure 4.4: Sensors' configuration proposed in [58].

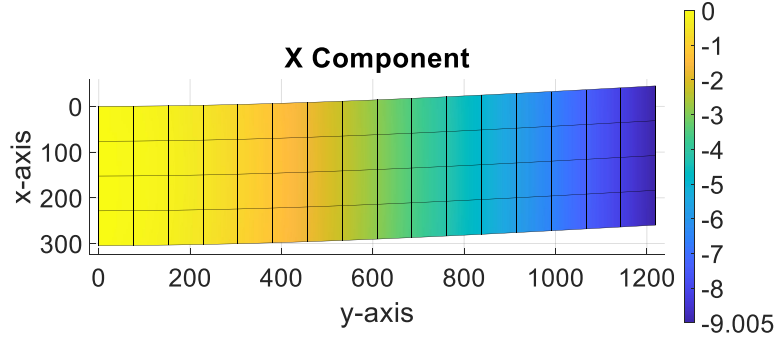
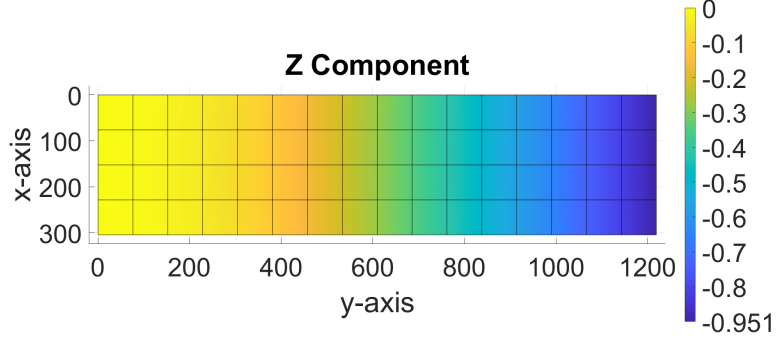


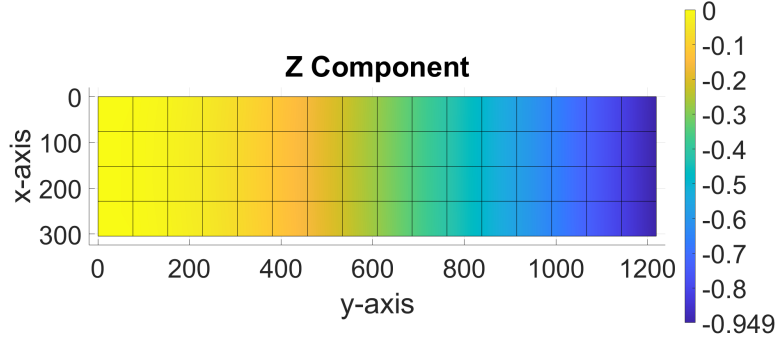
Figure 4.5: In-plane shear load - Reconstruction of the u displacements along the x direction using the sensors' configuration reported in 4.4 and the old integration scheme.

A Different behaviour is observed for the out-of-plane transverse load. The reference deformed shape along z and the reconstructed one are shown in Figure 4.6. In this case, the shape sensing using the old integration scheme (Figure 4.6b) and the one using the new scheme (Figure 4.6c) show the same level of accuracy. The value of the error in the reconstruction of the maximum displacement along z is 0.2% for both procedures. Therefore, for the bending behavior of the element, the introduced formulation does not provide measurable advantages.

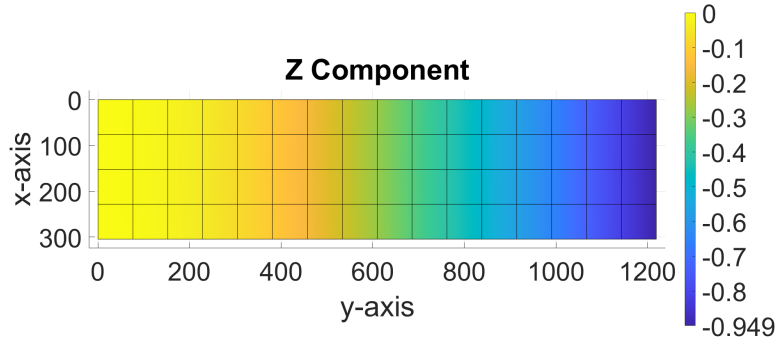
In conclusion, the proposed integration method, introduced in Section 3.3.2, is able to generally increase the accuracy of the membrane behaviour of the iQS4 inverse element. Although there are some sensors' configurations that are able to increase the accuracy of the old integration scheme, these configurations have to be determined. On the contrary, the novel formulation clearly identify the location of the strain sensor needed for the performance of the shape sensing and does not require the determination of the sensor's position within the element. In fact, this position is precisely prescribed to be in the centroid of the element. The bending behavior is not influenced by the proposed integration scheme.



(a) Reference w displacements



(b) Reconstructed w displacement - old integration scheme



(c) Reconstructed w displacement - new integration scheme

Figure 4.6: Transverse load - In the figures, the displacements w along the z direction are reported for the transverse load case. The colour bar refers to the magnitude (in mm) of the w displacements.

4.2 Shape sensing on a composite wing box

After the validation of the novel integration scheme for the iFEM quadrilateral element, the study on the shape sensing has been continued with the application of the three shape sensing methods described in Chapter 3 on a numerical model of a typical aerospace structure, a composite wing box. The three methods, namely the iFEM, the Modal Method and the Ko's Displacement theory, have been applied in the form and with the novelties introduced in the previous chapter. In particular, the iFEM has been implemented using both triangular and quadrilateral meshes. They have been firstly optimized, in terms of the strain sensors' configuration, and then compared in terms of the accuracy of the displacements' reconstructions. A further comparison on the performance of the three method has been conducted for the case where the uncertainties, typical of a real word scenario, have been introduced in the inputs of the shape sensing methods, namely the strains and the material properties.

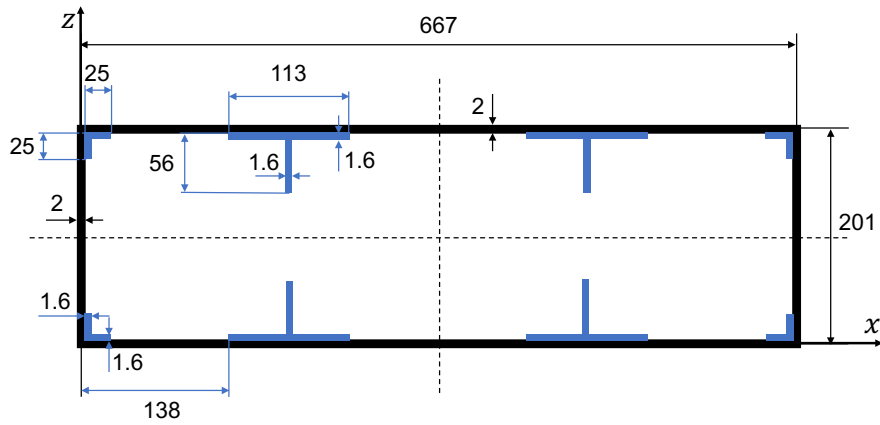
4.2.1 The composite wing box

The wing box, object of this analysis, is presented in Figure 4.7. It is composed of two panels connected by two spars. The connection are made possible by four L-shaped stringers located at the four corners of the cross section. The two panels are each one stiffened with two T-shaped stringers and the box is divided in two bays, along the wing span, by two ribs. The wing box is unswept and presents the constant cross section described in Figure 4.7a. All the structural components are composite laminates whose lamina characteristics are summarized in Table 4.1. A quasi-isotropic $(+45/-45/0/90)_s$ stacking sequence is assigned to all the components. The lamina thickness for the skin and spars is set to 0.25 mm while for the other components it is set to 0.2 mm.

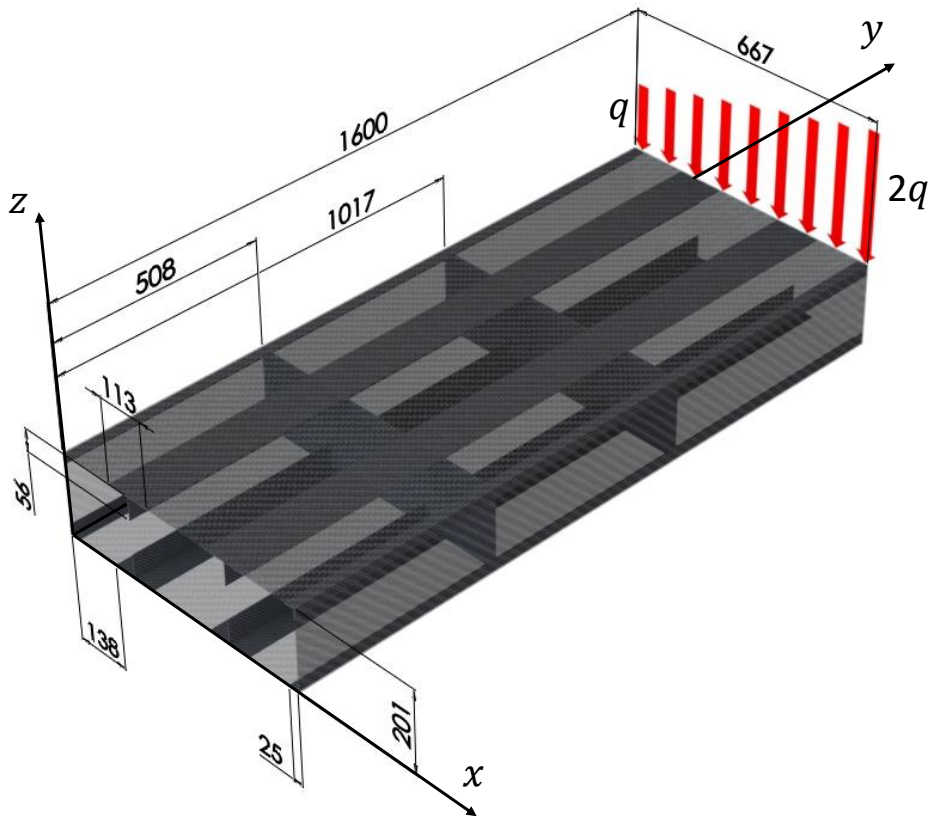
$E_{11}[GPa]$	$E_{22}[GPa]$	ν_{12}	$G_{12}[GPa]$	$G_{13}[GPa]$	$G_{23}[GPa]$
111	7.857	0.34	3.292	3.292	3.292

Table 4.1: Lamina characteristics.

The loading condition, considering the coordinate system shown in Figure 4.7b, is the following. The root section ($y = 0$) is clamped whereas the tip section ($y = 1600$) is loaded with a trapezoidal distributed load, with $q = 16 \text{ N/mm}$. This loading induces a deformation that shows both bending and torsional components and, therefore, represents a difficult challenge for the shape sensing algorithms object of this analysis.



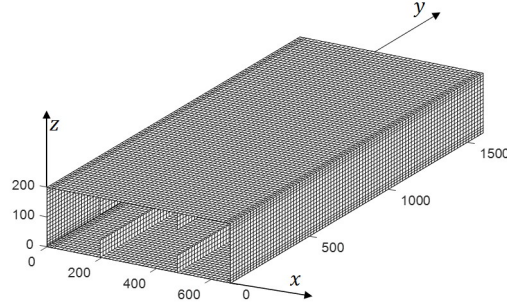
(a) Cross section



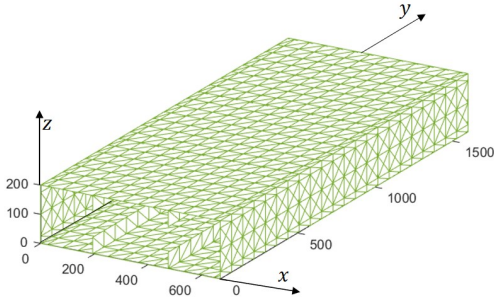
(b) Isometric view

Figure 4.7: Geometry and loading conditions for the unswept wing box. All the dimensions are expressed in [mm].

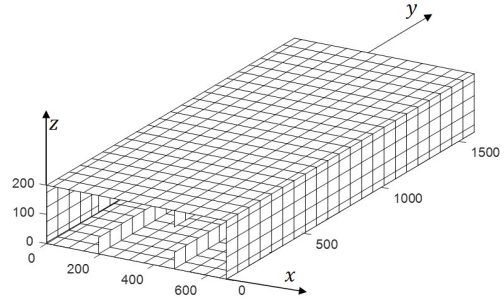
To numerically simulate the behaviour of the structure, a high-fidelity FE model has been realized (Figure 4.8a). This model, constituted of 21004 QUAD4 NASTRAN® elements and 16027 nodes, is used to generate the reference displacement and the strain's inputs for the shape sensing methods. A convergence study on the displacements resulting from this model proved that the mesh refinement is enough to capture the behavior of the structure.



(a) High-fidelity FEM



(b) iFEM Tria



(c) iFEM Quad

Figure 4.8: Numerical models of the wing box.

Two other meshes are necessary for the application of the the two formulation of the iFEM considered in this application. A triangular inverse mesh (Figure 4.8b) and a quadrilateral one (Figure 4.8c) have been realized for this purpose. These two models are coarser with respect to the hig-fidelity one. The requirement of a coarser mesh for iFEM is due to the fact that a good ratio between sensorized and unsensorized elements is necessary. A finer mesh, although capable of better

representing the deformation, would require a larger number of sensors. Therefore, the two meshes are composed of 2996 iTRIA3 (1136 nodes) and 1427 iQS4 (1064 nodes) elements, respectively. The formulations of the elements are the one described in Chapter 3. In particular, the iQS4's integration scheme is the newly proposed one (Section 3.3.2). All the nodes of the iFEM models have a corresponding node in the FE model, so that a comparison between the nodal displacements can be performed. Moreover, the possible locations of the strain sensors within the inverse elements are located where the FE mesh has a node, to guarantee an easy assignment of the strain measures.

The Modal Method and the Ko's Displacement theory, with the extension described in Section 3.2.1, need the computation of the modal shapes and the modal strain shapes of the structure. These characteristics are computed through the modal analysis of the high-fidelity model. The first 30 mode shapes have been calculated with the NASTRAN®'s SOL 103. According to the mode selection criteria reported in Section 3.1.1, these 30 modes are able to represent the 90.7% of the total deformation strain energy related to the investigated deformed shape. Within the selected range, the modes that contribute most to the total strain energy are the 1st, 3rd and 26th. The summation of these three modes contributes to the total strain energy for the 89.7%. Therefore, these modes are selected for the construction of the modal matrices necessary for the application of the Modal Method and for the extension of the Ko's Displacement theory.

In conclusion, the reference deformed shape, object of the shape sensing investigation, and the selected modal shapes, obtained with the high fidelity model are shown in Figures 4.9 and 4.10, respectively.

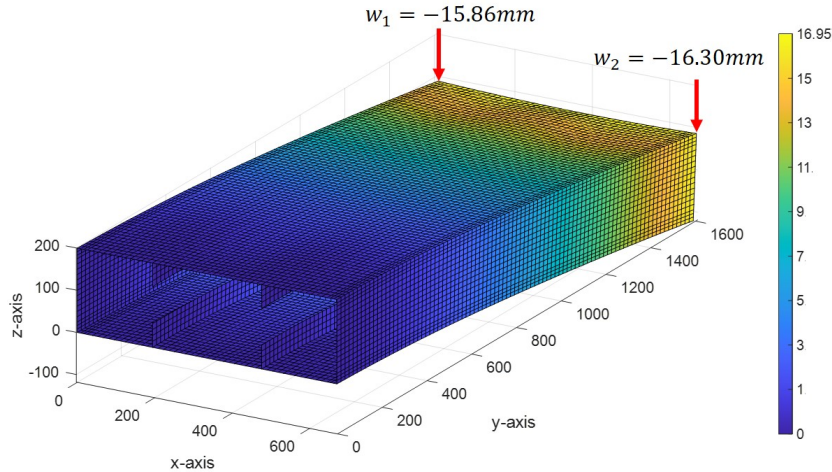


Figure 4.9: Reference deformed shape - The colour bar refers to the magnitude (in mm) of the resultant displacements, w_1 and w_2 represent, respectively, the vertical displacement of the top-left and top-right vertex of the tip cross section.

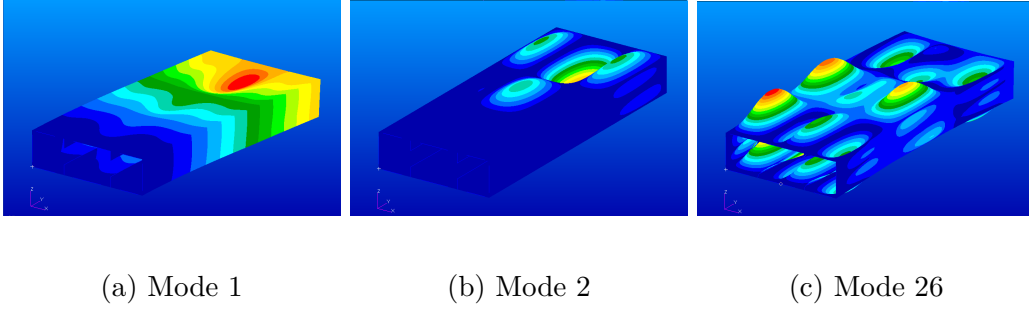


Figure 4.10: Selected mode shapes for the Modal Method and the Ko's Displacement theory.

4.2.2 Strain sensors optimization

The three methods' performance strongly depend on the number and position of the strains information that are provided to them. In order to make a consistent comparison of the three methods, it was chosen to compare them when performing in their optimum condition with a limited number of sensors. Therefore, the best strains sensors locations and directions, using a fixed number of sensors, were investigated for each technique.

The investigation over the best sensors configuration can be expressed as the search for the configuration that minimizes the value of the error between the reconstructed and the reference deformation. The solution landscape, that represents the different solutions for the different configurations, can result really complex and rugged, with multiple local minima values of the error. This kind of solution landscapes are particularly suited to be explored with a genetic algorithm optimizer. Moreover, genetic algorithms have been already successfully applied to the study of the sensors configuration for shape sensing by Foss and Haugse in [26]. As a consequence, also in this work, the sensors configuration investigation was carried on using a genetic algorithm optimizer.

The optimizer operated in two selection phases. During the first one, a selection criterion based on the individuals' fitness values was adopted. During the second one, a selection criterion based on the individuals' ranking was used. The first phase is capable of a broader search that helps to not get stuck in local optima whereas the second phase is capable of increasing the selective pressure towards the best configuration, only after the broader search is accomplished. Both phases were stopped when no significant increase in the objective function was observed over 10 generations. Each generation comprised a population of 500 individuals and within each generation, the one-point crossover, the two-points crossover, the mutation and the permutation genetic operators have been applied with a probability of 1, 0.9, 0.001 and 0.001 respectively.

The objective function, or fitness function, of the optimization is the $\%ERMS_w$,

formulated as it follows:

$$\%ERMS_w = 100 \times \sqrt{\frac{1}{n} \sum_{i=1}^n \left(\frac{w_i - w_i^{ref}}{w_{max}^{ref}} \right)^2} \quad (4.1)$$

where w_i^{ref} is the reference vertical displacement from the high-fidelity model in the i -th node's location, w_{max}^{ref} is the maximum reference vertical displacement and w_i is the reconstructed vertical displacement in the i -th node. The displacement are computed in the n nodes that all the three meshes have in common, in order to compare the three methods on the reconstruction of the same displacements. The vertical displacements are the most relevant one for the investigated deformation. Therefore, the minimization of the error relative to these displacement is chosen as the objective of the optimization.

The optimization is configured so that it can select different strain sensors' locations and different strain sensors' components. The possible sensors' locations are presented in Figures 4.11 and 4.12.

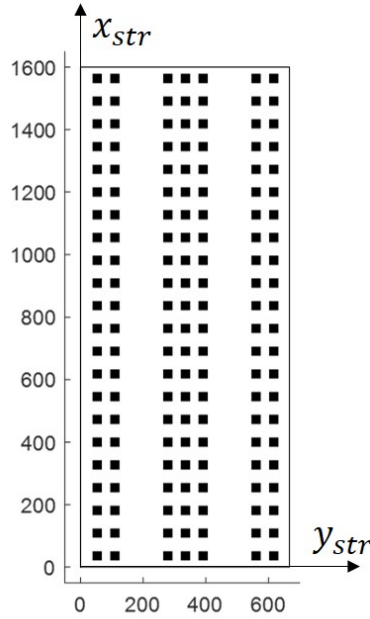


Figure 4.11: Sensors' search space for the upper and lower panels.

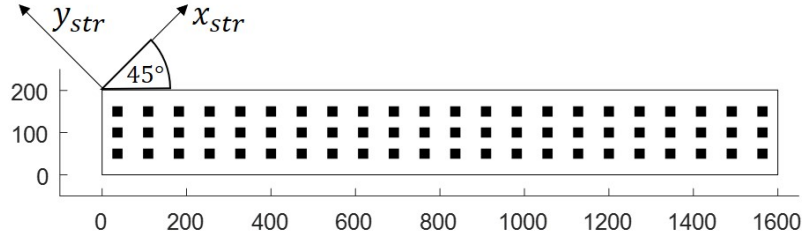


Figure 4.12: Sensors' search space for the front and rear spars.

The locations are selected on the top and bottom panel and on the front and rear spars. These locations coincide with the centroids of the inverse quadrilateral elements and with the centroid of the inverse triangular elements on the spars. This is not the case for the panels of the iTRIA3 mesh. In this case, an example of the location of a strain sensor is shown in Figure 4.13. Since the triangular mesh on the panels is obtained by splitting the quad elements along the diagonal, the centroid of the quad elements, where the sensors are located, lies on the mid-point of the side that the two triangles share. The strain measured at this location is associated with both the iTRIA3 that have the side in common. This strategy is adopted in order to have a triangular mesh that is refined enough to be able to represent the deformation of the wing box, but also to lower the ratio between sensorized and unsensorized elements with a reduced number of sensors.

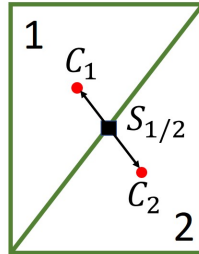


Figure 4.13: Sensor's configuration for the triangular elements on the top/bottom panels - The black square ($S_{1/2}$) represent the sensors location and the red dots (C_1, C_2) represent the location of the centroid for the two iTRIA3 elements.

Considering the practical difficulties connected to the application of sensors inside the wing box, only strains measured on the external surface are considered. Therefore, for the computation of the strain measures in Eqs. 3.31, constant values of the strains through the thickness of each plate are considered ($\varepsilon^+ = \varepsilon^-$). This approximation is admissible if the thickness of the skin panels is considerably smaller than the one of the entire wing box. In that case, the variation of the

strains through the plate thickness can be considered negligible with respect to the variation of the strains through the entire wing box. As a consequence, the areas where structural components overlap were not considered part of the sensors search space because of the resulting increase in the global plate thickness.

For the selected locations, two kinds of strain sensors are considered: the single strain gauge and the strain rosette. The single strain gauge measures the strain along the x_{str} direction, as identified in the Figures and 4.11 and 4.12. The strain rosette measures all the three membrane strain components along x_{str} , y_{str} and $x_{str}y_{str}$. The Ko Displacement's theory is applied considering the entire wing box as a beam-like structure. Consequently, the only considered strains for this method are the ones from the upper and lower skins. Moreover, according to the method's prescriptions, only the strains in the wingspan direction $\varepsilon_{x_{str}}$ have to be considered. Therefore, only single strain gauges on the top and bottom panels can be selected by the optimizer for this method.

The genetic optimizer is set to select 108 sensors for each shape sensing method. For the Ko's Displacement theory this results in a maximum of 108 single strain gauges. For the iFEM and MM it results in a minimum of 108 single axial strain gauges and maximum of 108 strain rosettes, accounting for a maximum of 324 single strain measures. Nevertheless, the optimizer has the possibility to select one sensor more than once, thus reducing the effective number of strain information adopted during the analysis. According to the working principle of the genetic algorithm, this reduction can be justified only if an increase in the performance of the objective function is experienced.

4.2.3 Deterministic analysis

In this section, the results of the shape sensing analysis of the wing box, using the nominal material properties and the strain inputs not affected by any uncertainty, are described and commented. The results of the strain sensors' optimization, in terms of the number of selected sensors and relative accuracy in the reconstruction of the vertical displacements, are summarized in Table 4.2.

	iFEM (Quad)	iFEM (Tria)	Ko	MM
$ERMS_w$ [%]	1.8	6.7	6.9	4.8
S_x		14	28	33
R_{xy}	108	94		40
S_{tot}	324	296	28	153

Table 4.2: Optimization results.

In the table are reported the number of single strain gauges (S_x), strain rosettes (R_{xy}) and total measured strain components (S_{tot}) necessary for each method to

reach the reported value of the $ERMS_w$. The selected sensors configurations and the consequently obtained deformed shapes, plotted against the reference one, are presented in the Figures 4.14 - 4.17 for the iFEM with the quadrilateral mesh, the iFEM with the triangular mesh, the Ko's Displacement theory and the Modal Method, respectively. Figure 4.18 shows the deflections, computed with the four methods and with the high-fidelity Finite Element reference model, of a line of nodes belonging to the lower panel and located close to the mid-chord position ($x = 363.18 \text{ mm}$).

The best accuracy is obtained by the **iFEM (Quad)**, i.e. the method formulated using quadrilateral elements. An $ERMS_w$ slightly below 2% is observed. The optimization process, in this case, selected the maximum number of sensors to reach this value of the error. As showed in Figs. 4.14a and 4.14b, the rosettes are all positioned on the spars of the wing box. The resulting reconstructed deformation does not show large discrepancy with respect to the reference one. The **iFEM (Tria)**, formulated using triangular elements, is not capable of such accuracy. In fact, the $ERMS_w$ reached in this case is close to 7%. From Figure 4.18 it is clear that this method underestimates the vertical displacements along the mid-chord line. The best sensors' configuration presents sensors located on the top and bottom panels and on the rear spar (Figs. 4.15a, 4.15b, 4.15c), the one that, due to torsion, experiences higher deformations. The majority of the selected sensors are strain rosettes, but few single strain gauges are also chosen. Therefore, the total amount of strains' components used by this formulation is slightly smaller than the one used by the quadrilateral one. Nevertheless, this small saving in terms of strain sensors does not justify the loss in the accuracy with respect to the quadrilateral formulation. In fact, the quadrilateral formulation is able to increase the accuracy of the shape sensing by 73%.

The **Ko's Displacement theory's** results are obtained with a low number of sensors selected by the optimizer to reach a modest 6.9% value of the $ERMS_w$. The few sensors are positioned on the lines located as close as possible to the leading and trailing edge of the wing (Figs. 4.16a, 4.16b). The low number of sensors is due to the fact that the optimizer selected many times the same sensors. This behaviour was studied in more details. A second optimization was performed, adding a penalization factor to all the solutions with repeated sensors, in order to force the optimizer to select the maximum number of sensors available. The results showed an even poorer $ERMS_w$ value for the optimal solution. A high number of sensors, for this test configuration, seemed to not have a beneficial effect on the evaluation of the vertical displacements in the application of the classical Ko's theory in the first step of the extended procedure. Therefore, a larger number of sensors resulted in a larger number of inaccurate vertical displacements used in the subsequent modal transformation. As a consequence, the transformation somehow amplified the errors from the master DOFs, leading to a higher value of the global error.

Looking at Fig. 4.16d it is possible to notice some discrepancy between the reconstructed and the reference deformation. Especially in the bay at the tip, it is possible to observe that the reconstructed displacement is strongly biased by the skins' deflection waves of the first mode shape of the structure (Fig. 4.10). From Fig. 4.18 it is easy to observe the inaccuracies of the method in the reconstruction of the deflection inside the last two bays and the tendency of the method to reproduce the modal shapes.

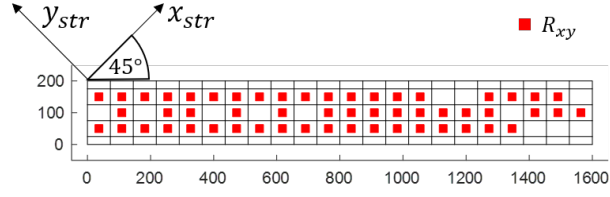
A trade-off between the methods previously described is provided by the **Modal Method**. The method is capable of reaching an acceptable accuracy with a modest number of sensors.

The optimizer selected both single strain sensors and strain rosettes and some repetitions occurred. The distribution of the sensors over the structure does not show a recognizable pattern (Figs. 4.17a, 4.17b). A study that avoided the repetition was performed for this method too. In this case, the use of all possible sensors did not affect the global error. The study suggested that the 4.8% $ERMS_w$ seems to be the maximum accuracy the method is capable to reach, regardless of how many strain measurements and modes are used. In fact, an analysis with the full set of strains measures and including all the 50 computed modes, resulted in the same $ERMS_w$ value of 4.8%, proving that the modes selection and the sensors optimization is capable to reach an asymptotic best value of the error.

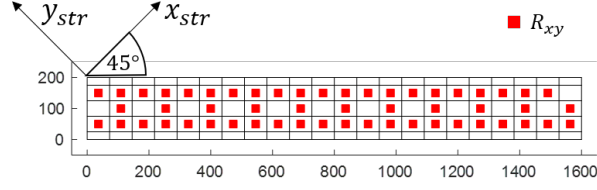
The shapes comparison (Figs. 4.17c, 4.17d) and the bottom mid-chord line deflection (Fig. 4.18) showed the same behaviour of the Ko's Displacements theory. Deflection waves in the second and third bays' lower and upper panels are observed. These waves are present in the 1st mode shape (Fig. 4.10) of the structure.

In conclusion, the methods show different characteristics that could be useful for different purposes and different requirements. The possibility to have a high number of sensors and the requirement for a high precision suggests the use of the more accurate iFEM (Quad) method whereas, a scarcity of sensors and the requirement of a first-approximation estimate suggests the use of the Ko's Displacement theory. The Modal Method represent a trade-off between these two methods, being capable of a decent accuracy with a medium number of sensors.

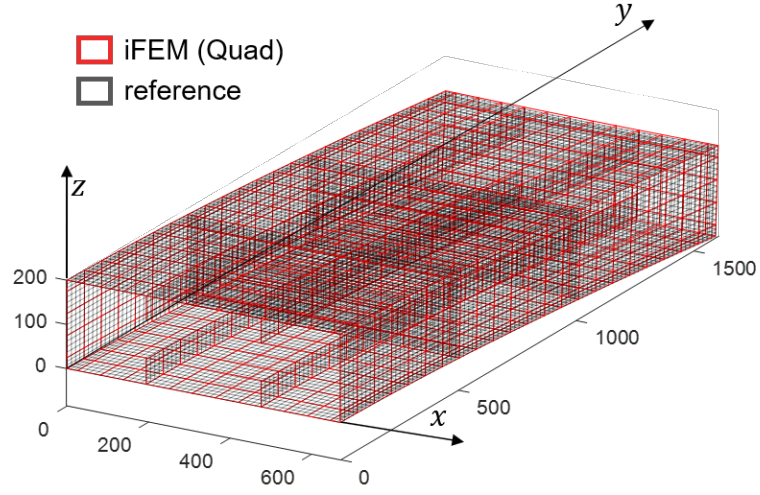
The Modal Method and the Ko's Displacement theory, as formulated in this work, require the knowledge of the modal characteristics of the structure whereas the iFEM does not have this requirement. Consequently, a further study on the robustness of the shape sensing methods with respect to uncertainties of the structural characteristics has been considered for a more complete comparison. Moreover, a study on the influence of noisy strain data has also been considered and will be discussed in the next section.



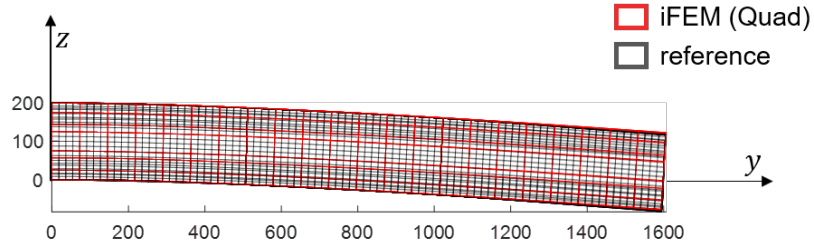
(a) Front spar ($x = 0 \text{ mm}$)



(b) Rear spar ($x = 667 \text{ mm}$)



(c) Deformed shape - Isometric view



(d) Deformed shape - Lateral view

Figure 4.14: iFEM Quad - In the panels (a) and (b) the optimized sensors' configuration is reported. In the panels (c) and (d) the reconstructed deformed shape is presented against the reference one.

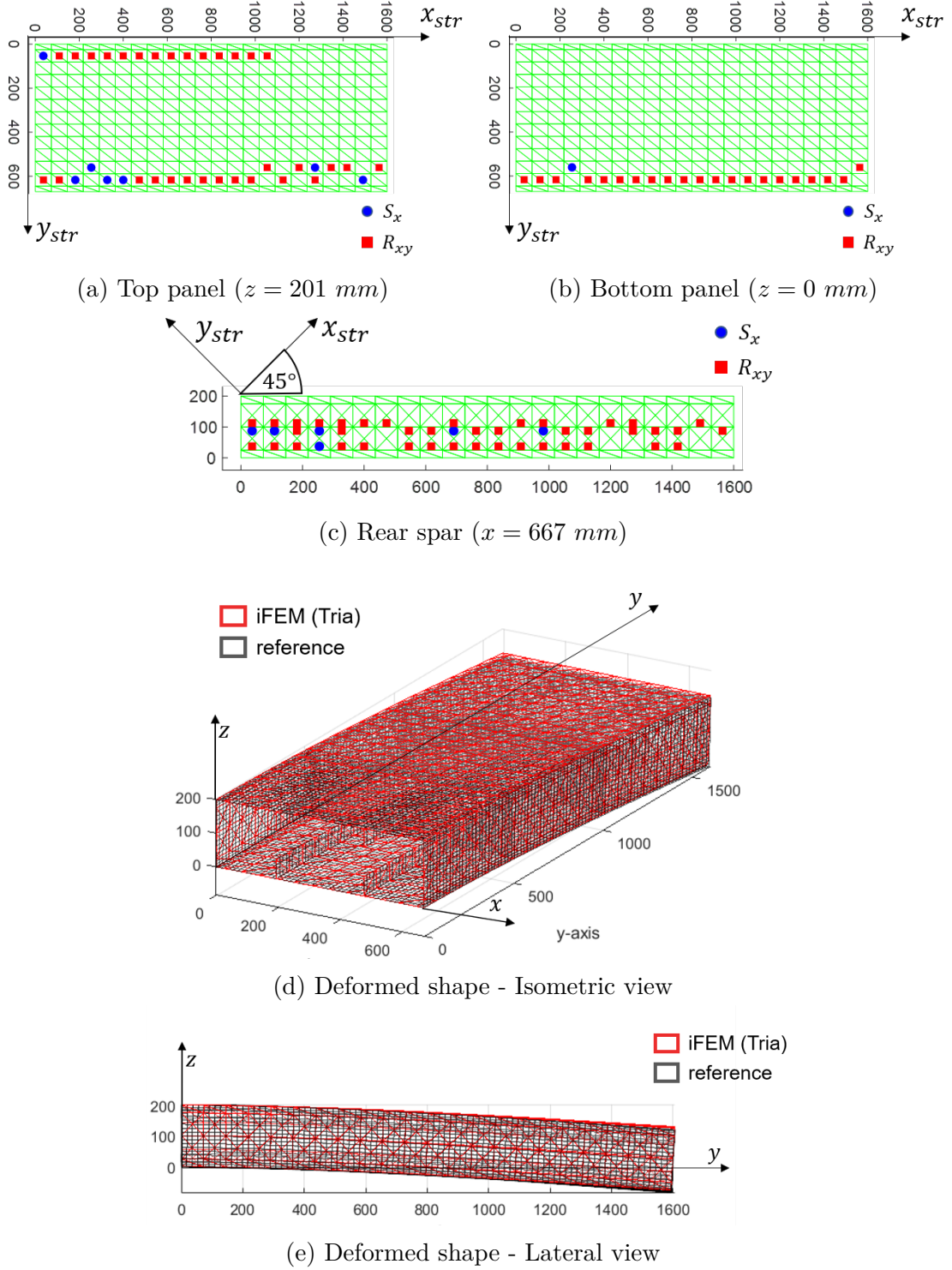
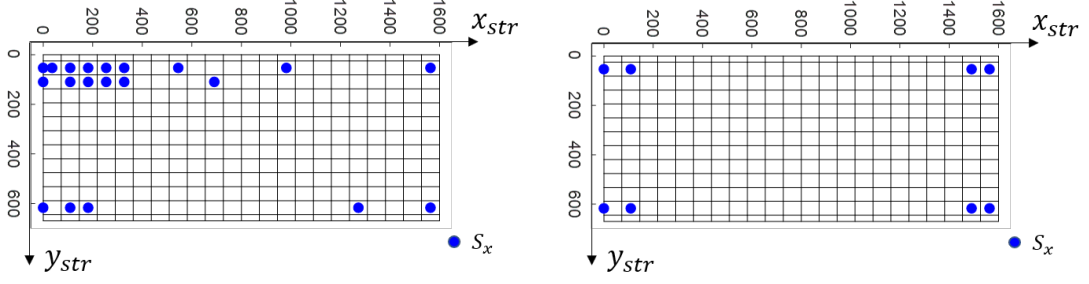
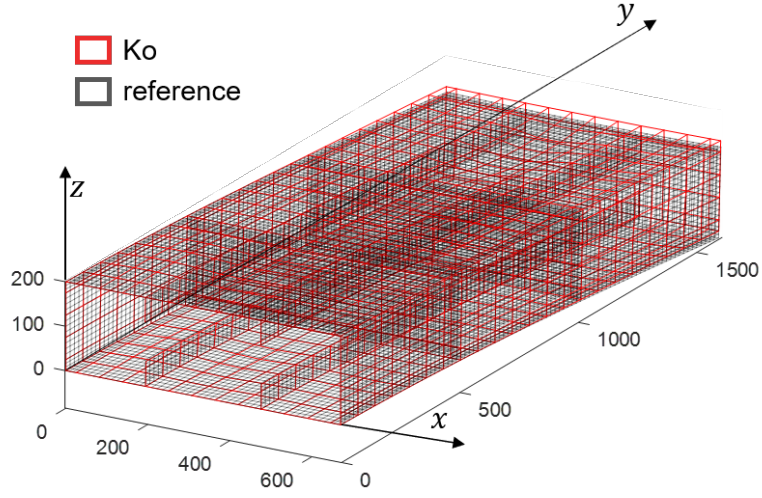
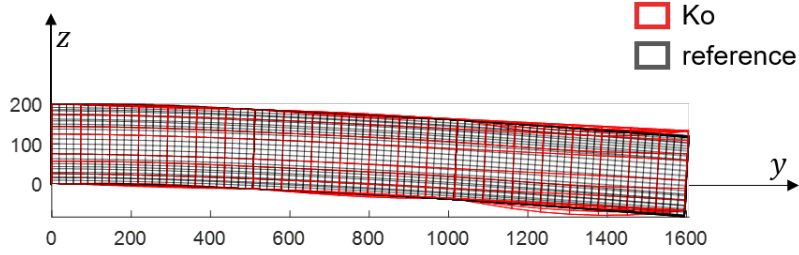


Figure 4.15: iFEM Tria - In the panels (a), (b) and (c) the optimized sensors' configuration is reported. In the panels (d) and (e) the reconstructed deformed shape is presented against the reference one.


 (a) Top panel ($z = 201 \text{ mm}$)

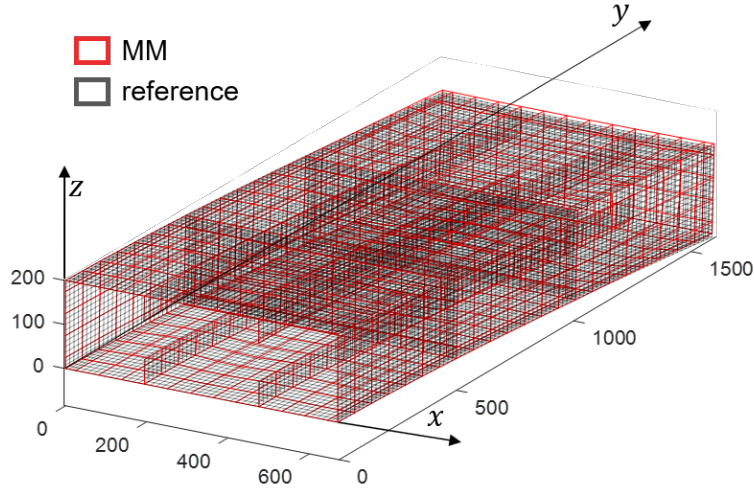
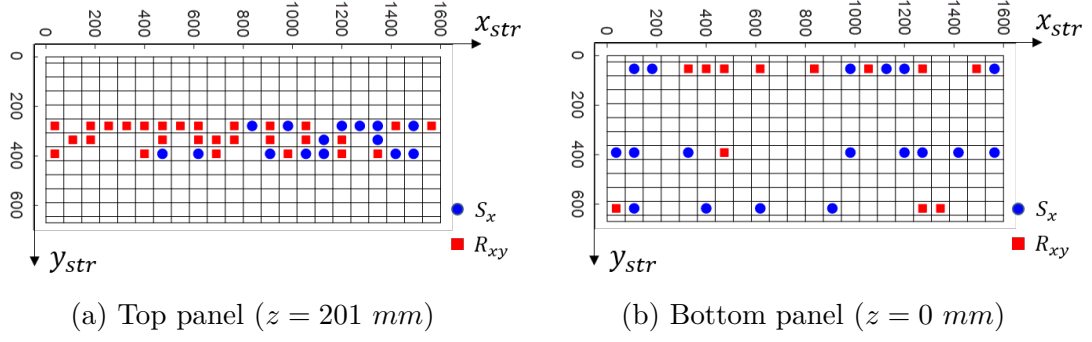
 (b) Bottom panel ($z = 0 \text{ mm}$)


(c) Deformed shape - Isometric view

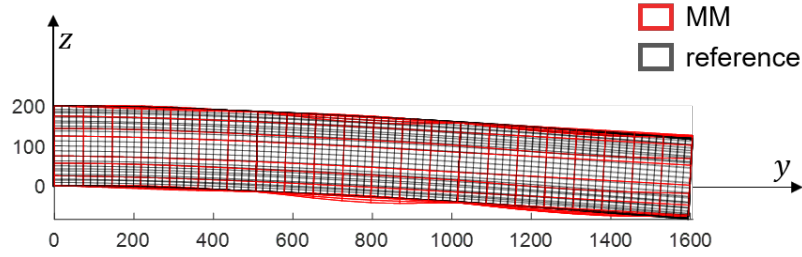


(d) Deformed shape - Lateral view

Figure 4.16: Ko's Displacement theory - In the panels (a) and (b) the optimized sensors' configuration is reported. In the panels (c) and (d) the reconstructed deformed shape is presented against the reference one.



(c) Deformed shape - Isometric view



(d) Deformed shape - Lateral view

Figure 4.17: Modal Method - In the panels (a) and (b) the optimized sensors' configuration is reported. In the panels (c) and (d) the reconstructed deformed shape is presented against the reference one.

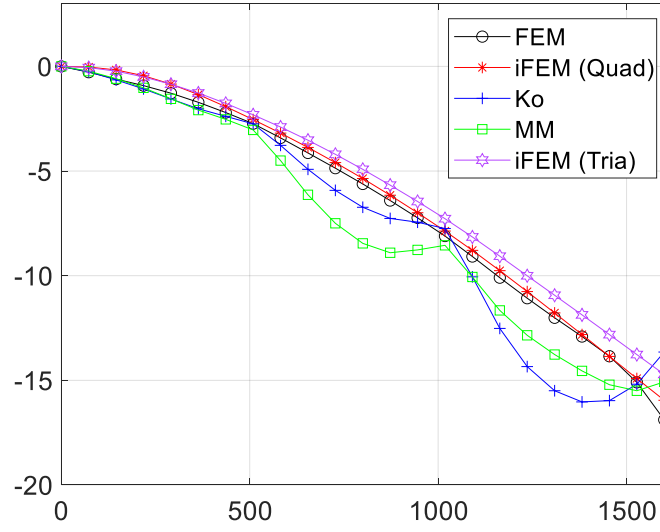


Figure 4.18: Vertical displacement along the mid-chord line ($x = 363.18 \text{ mm}$) on the bottom panel.

4.2.4 Uncertainty quantification

To perform a rigorous comparison between the shape sensing methods, the robustness of these methods to the variability of the inputs has to be considered. In real world scenario the strain measurement sampled on a structure can be affected by different sources of variability. The influence of temperature, transverse sensitivity of the sensor, misalignment, Wheatstone bridge's non-linearity and measurement noise, can all affect the accuracy of the measured strains [89, 90]. Moreover, the material properties and the geometry of a real structure may differ from the nominal ones. Specially the composite materials, whose manufacturing process is complex and difficult to control can present characteristics different from the nominal ones. Fibre-to-matrix volume ratio, alignment of the fibres, temperature effects during the curing process, porosity in the matrix, bonding between fibres and matrix are factors that depend on the manufacturing process and that can introduce variability in the material properties [91].

In this section, the influence of the aforementioned uncertainties on the outputs of the shape sensing methods is evaluated. The previous deterministic analysis, carried on the composite wing box, is therefore extended to take into account for the inputs' uncertainties. To perform this study, the same formulations and strain sensors' configurations previously investigated are adopted for the iFEM (Quad), the Ko's displacement's theory and the Modal Method. The iFEM (Tria) has been excluded because of its poor performance with respect to the iFEM(Quad).

The problem at stake is faced using a probabilistic approach. In fact, the uncertainty quantification process consists in studying the output's probability density function (PDF) and its statistical moments when the inputs are subjected to variability. The more widely used method to perform this kind of analysis is the Monte Carlo Simulation (MCS). According to this method, a probability distribution is associated to each input variable. Several values of each variable are sampled from the assumed probability distribution in order to obtain several input vectors (individuals) for the investigated model. The sampled input vector are then used to repetitively run the model, in this case the shape sensing methods, thus obtaining the PDF of the output. The number of input vectors influences the ability to obtain a PDF capable to fully describe the phenomenon. When simple random sampling is used, the required number of input vectors is large and, consequently, the computational time for the simulation is significant. The use of different sampling methods can increase the accuracy of the simulation with a smaller number of input vectors. Latin Hypercube Sampling (LHS) is a stratified sampling method that guarantees that all the portions of the distributions of each variable are represented in the sampling [92]. This guarantees a better accuracy with a small number of samples.

The input data for the shape sensing are the strain measurements. As already mentioned, these quantities can be affected by two kinds of uncertainties: uncertainties due to the material properties' variability and uncertainties affecting the experimental measurements. In this work, these two effects are treated separately.

Material uncertainties

The material uncertainties influence the strain field of the structure. In this work, the material uncertainties are analysed at the laminates' ply level, including the mechanical characteristics and the geometric ones. The ply mechanical properties' variability is modelled with normal distributions, having the mean values (μ) equal to the nominal ones and a Coefficient of Variation (CoV) of 7.5% [93]. The same distribution is used to represent the thickness of the plies. The fibre orientations are modelled with normal distributions with μ equal to the nominal ply angle and a standard deviations (σ) of 3° [94]. The statistical formulation of the material characteristics are resumed in Table 4.3. The variability represented by the distributions simulates the uncertainty that can originate from multiple sources. The deviation from the nominal values due to the complexity of the manufacturing process, the variation of the material properties due to the fluctuation in the ambient conditions and other sources that can influence the composite behaviour are all taken into account by the generous level of variability selected for the stochastic distributions of the variables.

Characteristic	Distribution	μ	σ
$E_{11}[GPa]$	Normal	111	7.5% μ
$E_{22}[GPa]$	Normal	7.857	7.5% μ
ν_{12}	Normal	0.34	7.5% μ
$G_{12}[GPa]$	Normal	3.292	7.5% μ
$G_{13}[GPa]$	Normal	3.292	7.5% μ
$G_{23}[GPa]$	Normal	3.292	7.5% μ
$St.seq.(StSeq\ 1-7)$	Normal	$[45/-45/0/90]_s$	3°
$t_{(StSeq\ 1)}[mm]$	Normal	$[0.25/0.25/0.25/0.25]_s$	7.5% μ
$t_{(StSeq\ 2-7)}[mm]$	Normal	$[0.20/0.20/0.20/0.20]_s$	7.5% μ

Table 4.3: Stochastic material characteristics.

The six lamina's mechanical properties are sampled from their normal distributions only once per individual and are associated to all the laminates of the wing box. On the other hand, to simulate a high variability of the composite lay-ups' characteristics over the wing box, seven different zones are identified (Figure 4.19). For each zone the values of the thickness and fibre orientations for each zone are sampled separately for each individual. To summarize, each input vector for the MCS is constituted by 62 input variables, namely 4 fibre orientations x 7 stacking sequences, 4 ply thicknesses x 7 stacking sequences and 6 mechanical properties. The sampling of the variables is obtained using a LHS from the multivariate normal distributions previously illustrated and summarized in Table 4.3.

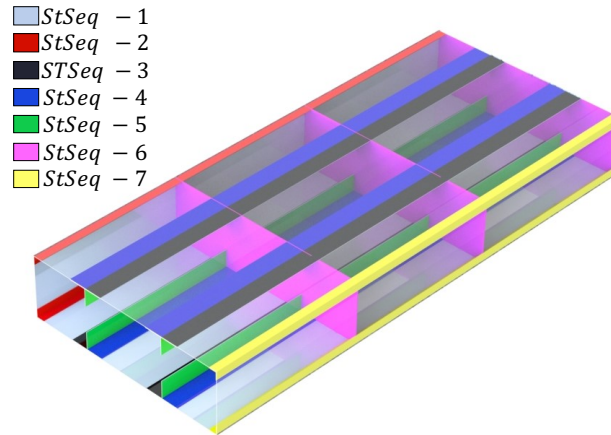


Figure 4.19: Stacking sequences - The box is divided into seven zones. Each one has the same nominal stacking sequence but they are sampled separately in order to guarantee a higher degree of variability of the characteristics over the structure.

Once a sufficient number of input vectors are sampled, the MCS's process is obtained as follows. For each individual, the sampled composites' characteristics are implemented into the high-fidelity FE model illustrated in section 4.2.1. From this model the strains, affected by the variability of the material properties, are computed for each individual. These strains are then used to perform the shape sensing with the three selected shape sensing methods in order to obtain a value of the $\%ERMS_w$ for each individual. The set of $\%ERMS_w$ s are then used to derive the PDFs of shape sensing's output. When computing the $ERMS_w$, the reference displacements are the one obtained from the FEM analysis of the correspondent individual. On the other hand, the Modal characteristics, necessary for the application of the MM and Ko's Displacement theory, are the ones obtained from the deterministic FE model (where all of the properties are set to the nominal values). This approach is based on the assumption that the modal properties, especially the one related to the strains, are really difficult to measure experimentally. Therefore, the idea is to simulate the most common case, i.e., the modal analysis is performed on the numeric model, whereas the strains and the displacements are measured experimentally and are affected by uncertainty. The entire process for n input vectors is schematized in Figure 4.20.

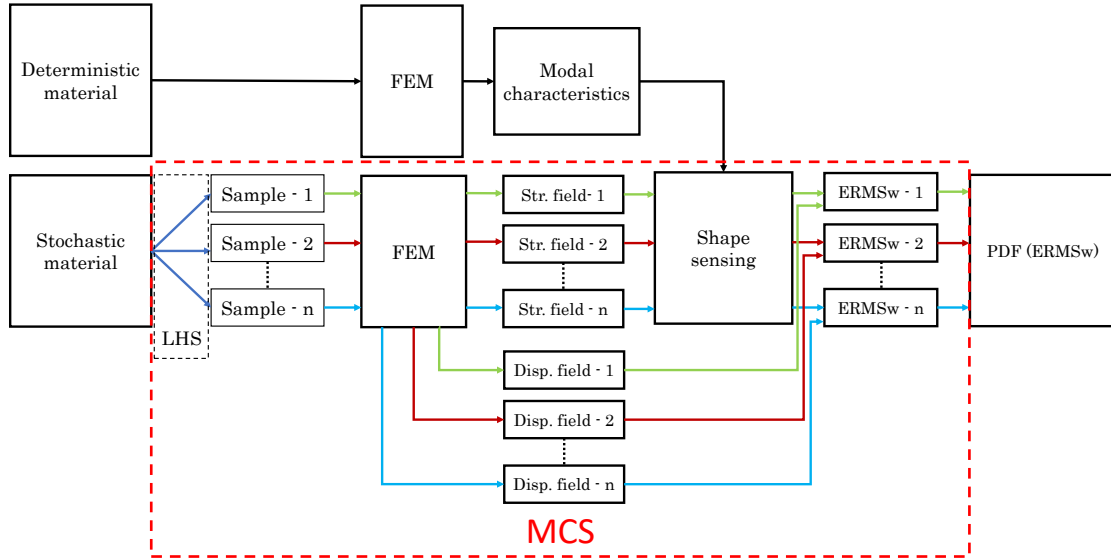


Figure 4.20: Material uncertainty simulation - The scheme illustrates the MCS with LHS procedure for the analysis of the material uncertainties.

The results of this analysis, for the wing box object of this study, are reported in Figure 4.21. The Figure shows the PDFs of the $\%ERMS_w$ obtained with the iFEM, the Modal Method and the Ko's displacement's theory as formulated during the deterministic analysis. The means, the standard deviations and the CoVs of the

distributions are also reported. The results are extracted using 10000 individuals. A convergence study to prove that this number of samples is able to characterize the output variability has been performed. The result of the study has shown that no variation for the value of the means and a maximum variation of 6% was observed for the CoV when increasing the number of samples to 20000 and 30000.

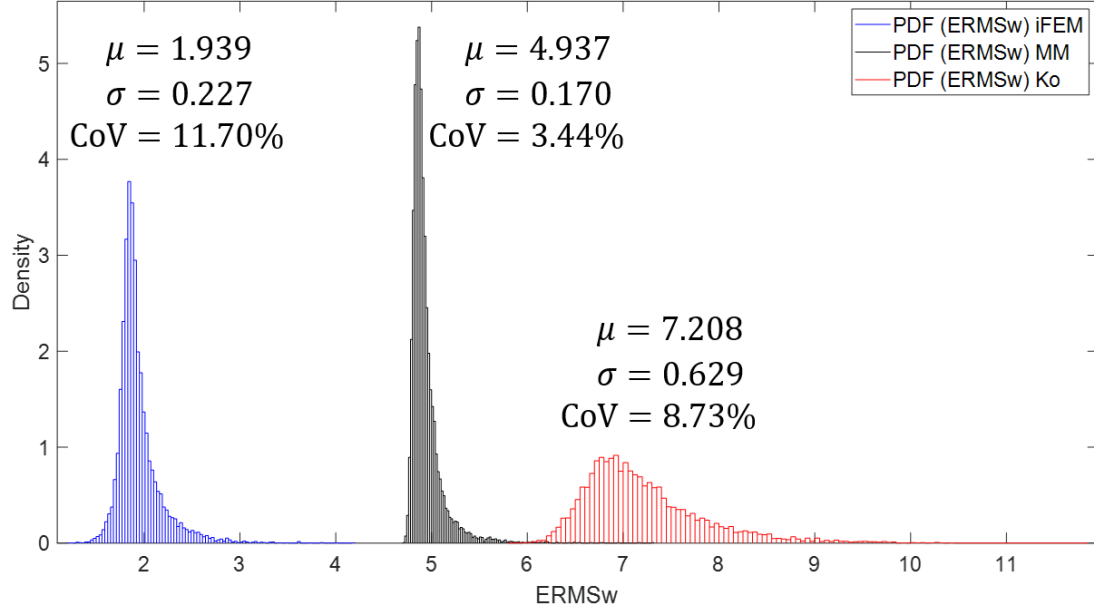


Figure 4.21: PDFs - Material uncertainty - Probability density functions of the %*ERMSw* obtained for the three shape sensing approaches with 10000 input vectors of material characteristics sampled with LHS.

The means of all the distributions are close to the deterministic results (Table 4.2), although they are slightly higher for all the three methods. The more peaked distribution is the one relative to the MM. The distribution corresponding to the iFEM is slightly less peaked, whereas the one relative to the Ko's Displacement theory is much flatter. Moreover, looking at the standard deviations, the same trend of variability for the three histograms can be inferred. The MM is found to be the less sensitive to the material uncertainty, exhibiting a really small influence of the input variability on the output. The iFEM shows a higher degree of variability, although it is important to notice that there is no overlapping between the worst result for the iFEM histogram and the best one for the MM one. Therefore, despite the fact that it is more affected by the material uncertainty, the iFEM is still able to perform better than the other two methods for any individual of the MCS. The Ko's displacement theory is strongly influenced by the variability in the material characteristics. It is interesting to notice that the right side of the MM's graph

extends so that it overlaps to the Ko's graph. It happens for a portion where the number of occurrences for the MM and the Ko's Displacement theory are really small. It means that, in some particular and rare conditions, the MM and the Ko's Displacement theory may perform with the same level of accuracy.

For the iFEM, an additional study on the influence of the penalization factors relative to the missing strain measurements (Section 3.3.2), λ_{1-8} , was performed. The results for values of λ_{1-8} varying from 10^{-3} to 10^{-6} are reported in Figure 4.22. The distributions show that the penalization factors have a significant influence on the mean value of the distribution, whereas they have almost no influence on the standard deviation and on the PDFs. They are very similar to each other in shape and are only translated according to the different mean values. Therefore, it is proven that the λ_{1-8} coefficients don't have an influence on the variability of the displacements reconstruction due to the material uncertainty, whereas they have an influence on the deterministic accuracy of the method.

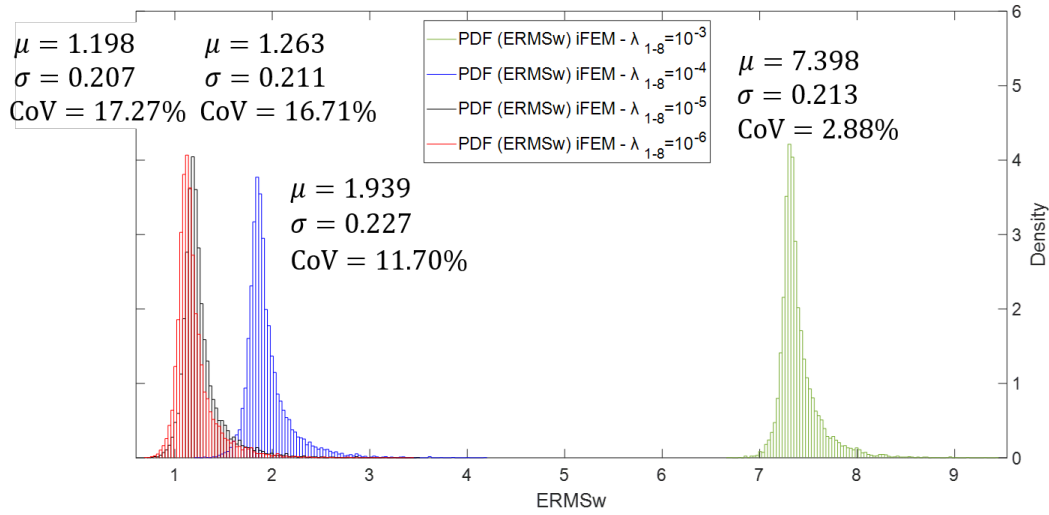


Figure 4.22: PDFs - Material uncertainty - Probability density functions of the $\%ERMSw$ obtained for the iFEM with varying λ_{1-8} values from 10^{-3} to 10^{-6} .

Measurement uncertainties

The uncertainties due to the measurement errors can also be evaluated with the same approach. To take into account for the various source of error that can affect the strain measurements, a normally distributed error is added to the strain measures obtained with the deterministic refined FE model. Two levels of the error are considered for this study, a 5% and a 10% error. Therefore, the statistic distribution of the strains for the measurement uncertainties evaluation are the one resumed in Table 4.4.

Characteristic	Distribution	μ	σ
ε	Normal	Deterministic value	$5 - 10\% \mu$

Table 4.4: Stochastic strain measurements.

From this distribution a certain number of individuals, represented by different strain input vectors, are sampled with the LHS and are used to repetitively run the shape sensing methods, thus generating the PDFs of the $\%ERMS_w$. In this case, the number of variables that constitute the input vectors depends on the number of strain sensors required by each of the shape sensing method. The modal characteristics are once again computed from the deterministic refined model and, this time, also the reference displacements are derived from this model. In fact, the scope is to evaluate the uncertainty that affects the strain measurements only. As a consequence, the simulated condition is the one where the real structure is supposed to behave like the deterministic one, but the experimental strains are affected by the measurement errors. The scheme of the simulation is reported in Figure 4.23.

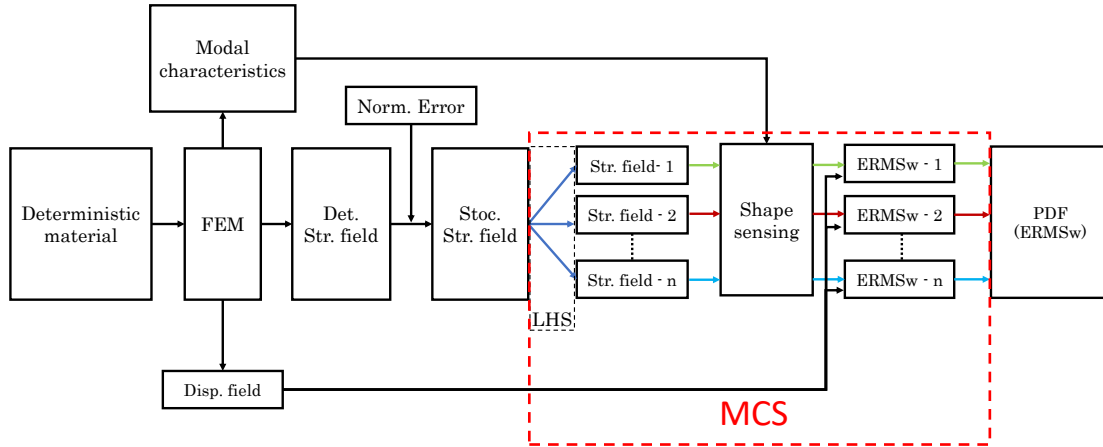


Figure 4.23: Measurements noise effect simulation - The scheme illustrates the MCS with LHS procedure for the analysis of the measurement uncertainties.

A sample size of 30000 individuals is chose for the LHS. In fact, the convergence study on the CoV of the outputs proved that the maximum variability in the CoV, when 50000 or 70000 samples are considered, is less than 2%.

The outputs' PDFs resulting from the analyses with 5% and 10% normal errors are reported in Figures 4.24 and 4.25, respectively. The peakedness of the distribution related to the MM is impressive. The 5% error has practically no effect in the $ERMS_w$ distribution and an almost negligible influence in the case of 10%

error. On the other hand, the iFEM and Ko's Displacement theory show a more significant variability.

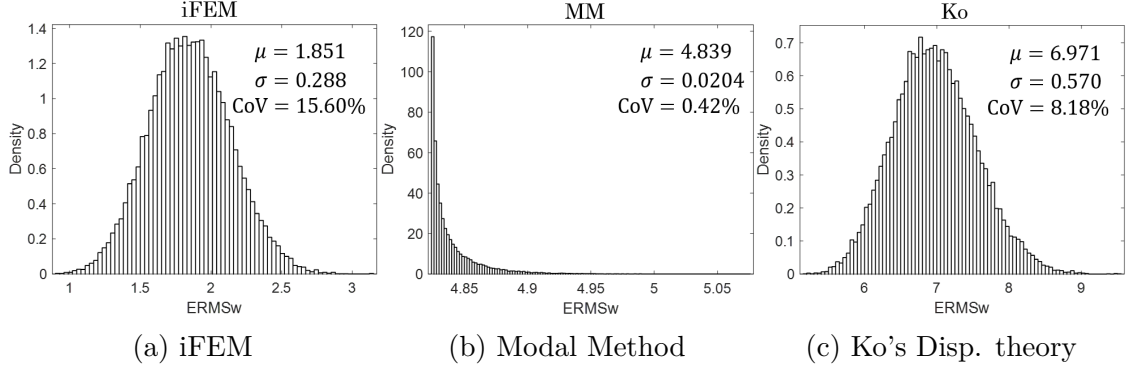


Figure 4.24: PDFs - Strain error 5% - Probability density functions of the $ERMSw$ obtained for the three shape sensing approaches with 30000 input vectors of strains affected by a normal error of 5%.

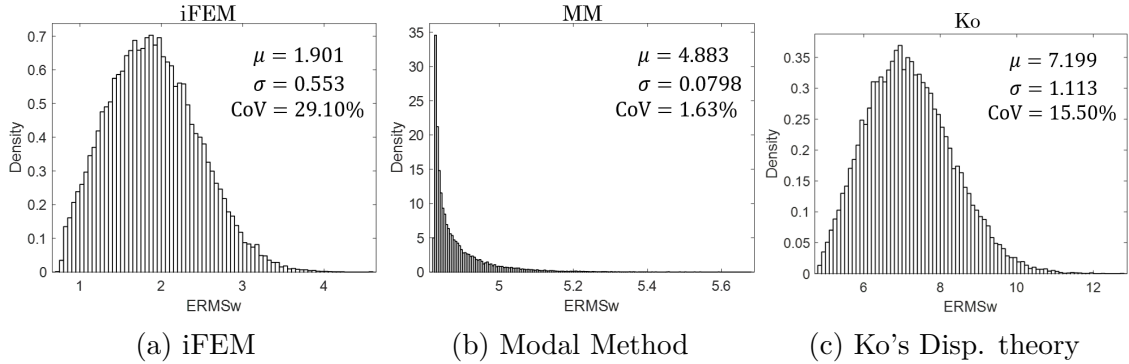


Figure 4.25: PDFs - Strain error 10% - Probability density functions of the $ERMSw$ obtained for the three shape sensing approaches with 30000 input vectors of strains affected by a normal error of 10%.

When a 5% error is present, the two methods exhibit values of the standard deviations comparable to the ones obtained during the material analysis. These values appear approximately twice as big in the case of 10% error. The iFEM shows less variability and, in the two error scenarios, its histograms still never overlaps to the other two, showing better results for any occurrence. The overlapping between the MM and the Ko's Displacement theory's histograms is noticed when the normal error reaches the 10%, but this happens in the area where really small occurrence bars are present. The iFEM and Ko's histograms share another common feature, a nearly symmetric distribution with respect to the mean value. This

feature indicates an equal possibility of having better or worst results with respect to the mean value. On the contrary, although with really lower variability, the MM's one is characterized by a highly positive skewness, only showing occurrences for solutions with a higher value of the $ERMS_w$ with respect to the mean one.

The present study on the effect of the measurement errors has also considered the effect that these have on the reconstruction of the stress field. The displacements computed with the shape sensing method can be used to reconstruct the stress field through the use of the constitutive equations. Therefore, the displacement fields that generated the distributions reported in Figs. 4.24 and 4.25 can be used to generate a distribution of the stress field reconstructions. For this particular application, taking into account the typical failure analysis relevant to multilayered composite structures, these displacement field are used to reconstruct the Tsai-Hill failure index's distributions. To compute the Tsai-Hill index, the material strength properties reported in Table 4.5 have been used. The deterministic value of the maximum Tsai-Hill index, computed using the reference displacements from the high-fidelity model without any uncertainty in the system, is 0.73.

Characteristic	Value
Longitudinal tensile strength	749 [MPa]
Longitudinal compressive strength	351 [MPa]
Transverse tensile strength	30 [MPa]
Transverse compressive strength	100 [MPa]
In-plane shear strength	25 [MPa]
Inter-laminar shear strength	14 [MPa]

Table 4.5: Material strength characteristics.

The distributions of the maximum values of the reconstructed Tsai-Hill index are plotted in Figures 4.26 and 4.27. The trend in the mean values of the error is the same noticed during the displacements analysis. The iFEM is the most accurate of the three method. Moreover, in this case, the advantage in the accuracy in favour of the iFEM is even more remarkable. The mean values of the estimations of the Tsai-Hill index for the MM and the Ko's Displacement theory are highly inaccurate. The standard deviations of the distributions relative to the three methods are comparable and also the CoVs are closer than in the shape sensing case. As a consequence, the higher robustness of the MM, in particular with respect to the iFEM, is still exhibited but less marked.

To sum up the results of the uncertainty quantification analysis, it has been observed that the Modal Method is the less influenced by any source of uncertainty present in the system. Therefore it represents an useful shape sensing tool when there is no confidence in the reliability of the material characteristics or the accuracy

of the strain sensing system. The iFEM is more influenced by the inputs' variability. Nevertheless, although requiring a higher number of sensors, its most negatively influenced reconstructions are still capable of a greater accuracy than the best one from MM. As a consequence, when more accuracy is required and more sensors are available, the iFEM is still to be preferred. Moreover, the advantages of the iFEM are even more remarkable when the reconstructions are extended to the stress field of the structure. In this case the iFEM is strongly recommended. The Ko's Displacement's theory is not suitable when uncertainty is present. The high variability in the output prevents from confidently rely on the obtained results.

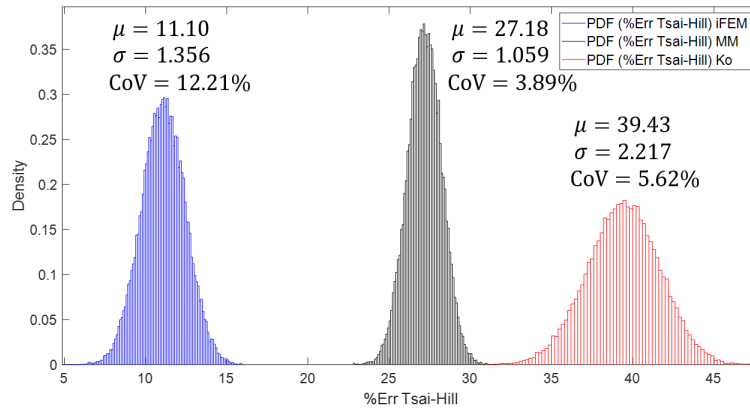


Figure 4.26: PDFs - Strain error 5% - Probability density functions of the percentage error (%Err Tsai-Hill) in the reconstruction of the maximum Tsai-Hill failure index.

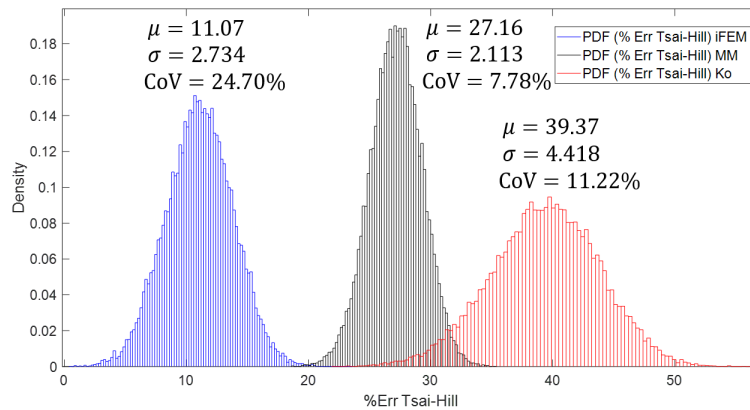
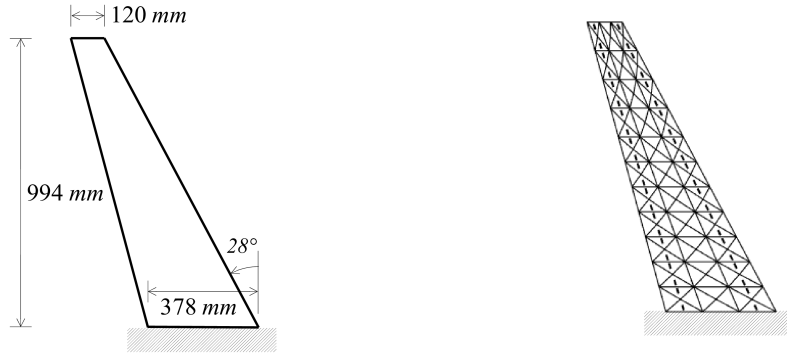


Figure 4.27: PDFs - Strain error 10% - Probability density functions of the percentage error (%Err Tsai-Hill) in the reconstruction of the maximum Tsai-Hill failure index.

4.3 Plate undergoing large displacements

The last numerical application related to the shape sensing is aimed at the validation of the incremental iFEM formulation introduced in Section 3.3.3. The proposed procedure is tested on the reconstructions of the traverse displacements of a wing-shaped aluminium cantilevered plate subject to a uniformly distributed transverse pressure of $2.466E-03 \text{ MPa}$. This level of load is able to induce highly non-linear deformation in the plate. The plate's geometry and boundary conditions



(a) Geometry and boundary conditions (b) Mesh and sensors' placement.

Figure 4.28: Wing-shaped plate

are presented in Figure 4.28a. The material is an aluminium alloy (Young's modulus $E = 72017 \text{ MPa}$, Poisson's ratio $\nu = 0.325$). The plate is meshed with triangular elements, as reported in Figure 4.28b. In the same figure are also reported the positions of the axial strain gauges used for the iFEM computation. They are denoted by the black lines running along the wing span. Every line represents a strain sensor that measure the strain on the upper and lower surfaces of the plate along the line's direction. The same triangular mesh is used for both the direct non-linear analysis and the inverse one. The direct non-linear analysis, that gives the reference values of the vertical displacements and the measured strain values, is carried on using 132 S3R shell elements in ABAQUS/Standard 6.13. The inverse mesh is constituted of the same amount of iMIN3 elements. The accuracy of the iFEM predictions is assessed by calculating the Root Mean Square Error ($\%ERMS_w$) of the nodal transverse deflections (w) with respect to the ones computed in the direct analysis (Eq. 4.1).

The direct non-linear analysis is obtained dividing the load into 32 increments. As prescribed by the iFEM incremental formulations, for each of these load increments the strains are collected, the displacements are computed with the iFEM and the mesh is updated for the next step of the procedure by adding the computed displacements to the inverse mesh's nodes. The reconstruction of the wing deformed

shape, against the reference one, is reported in Figure 4.29. A high accuracy of the shape reconstruction is observed.

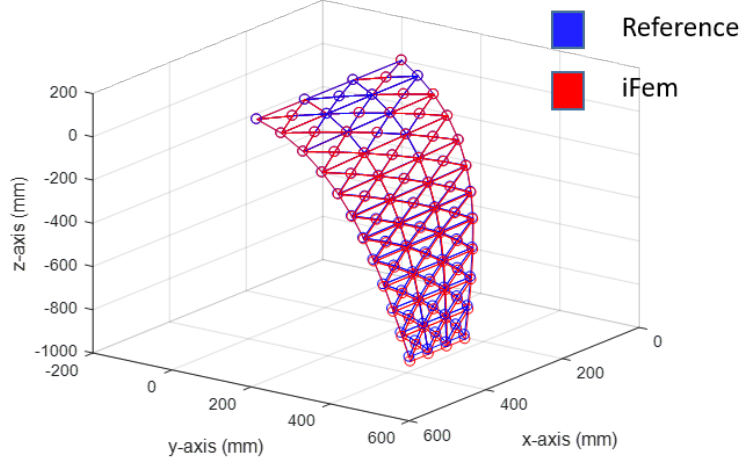


Figure 4.29: Wing-shaped plate - Shape sensing at the maximum load level.

A further inspection of the reconstructed maximum transverse displacement of the wing tip highlights the same significant level of accuracy. In Figure 4.29 the

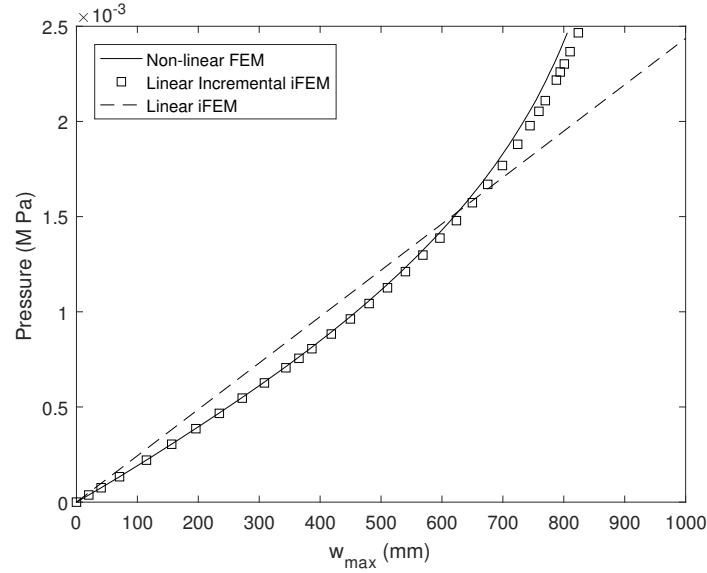


Figure 4.30: Maximum transverse displacement.

reference maximum vertical displacement and the reconstructed ones are plotted for every load increment. Moreover, the same displacement, reconstructed using

the strains from the last loading step and computed with the standard linear iFEM procedure, is reported. It can be notice that the incremental IFEM formulation is able to accurately reconstruct the displacements for every load increment and especially for the final value, whereas the standard formulation is not able to capture the non-linearity of the displacement. This is enforced by the trend observed for the $\%ERMS_w$ as a function of the load percentage (Figure 4.31). The $\%ERMS_w$, derived with the incremental iFEM, never exceeds 1%, whereas the one computed with the standard linear iFEM is always higher than 1% and reaches significant values for the final level of the load.

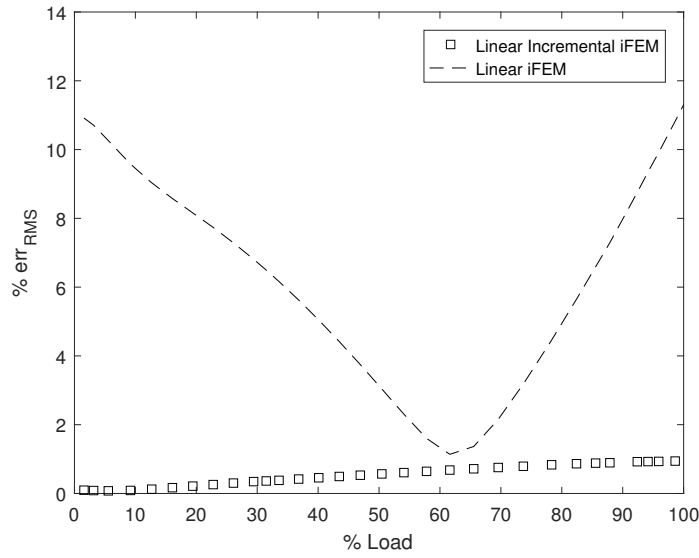


Figure 4.31: $\%ERMS_w$ error corresponding to linear iFEM and incremental iFEM solutions as a function of the load range

This numerical activity proves that the incremental iFEM formulation is accurate in reconstructing the non-linearities of the displacement field of a structure experiencing large displacements.

Chapter 5

Data driven methods for loads identification and reconstruction

After addressing the shape sensing of aerospace structures, the focus of this next step is another crucial aspect of the Structural Health Monitoring, the load reconstruction methods. Monitoring the loads that affect a structure is fundamental for several key aspects: the targeting of critical loading conditions during service; the evaluation of the load cycles for the assessment of the fatigue life consumption; the monitoring of the external loads as a feedback for the load alleviation mechanisms of the Smart/Morphing Structures.

In this chapter, data driven load identification/reconstruction methods, used in this research, are introduced. These are System Identification Methods that, adopting a "Black Box" approach, are able to create a regression between any inputs and the outputs of a system, without any in-depth knowledge of the investigated system. These methods will be applied to the reconstruction of the internal loads of a fighter aircraft's wing from flight parameters and strain inputs. The choice of this "Black Box" approach is driven by the lack of any knowledge of the physical characteristics that define the considered structure. For this application, two families of methods emerged from the literature review as the most widespread, linear regression based models and Artificial Neural Networks. These frameworks are described in details and a particular attention is dedicated to the description of the different parameters that characterize and define the models. These parameters will be object of a broad exploration during the investigation of the best System Identification Method for the monitoring of the fighter aircraft's wing internal loads.

5.1 Linear regression based algorithms

One of the most widespread System Identification Method, based on the linear regression, is the Auto-regressive with eXtra inputs model, ARX. This model is

based on the following linear difference equation [64]:

$$y(t) + a_1y(t-1) + \dots + a_{n_a}y(t-n_a) = b_1x(t-1) + \dots + b_{n_b}x(t-n_b) + e(t) \quad (5.1)$$

where $y(t)$ and $x(t)$ are the output and the input of the system at the time-step t , respectively, a_i are the n_a output's regressors, b_i are the n_b input's regressors and $e(t)$ is the white noise disturbance term. The equation express the concept that the output can be expressed as a linear regression of the previous time-steps values of the output (Auto-regression), plus the linear regression of the previous time-steps values of an external input (eXtra input), plus a disturbance white noise term. In fact, the next output's value, $y(t)_{pr}$ can be predicted as follows:

$$y(t)_{(pr)} = -a_1y(t-1) - \dots - a_{n_a}y(t-n_a) + b_1x(t-1) + \dots + b_{n_b}x(t-n_b) + e(t) \quad (5.2)$$

The regressors, a_i and b_i are the coefficients of this linear regression. If data of inputs and outputs of a system over a certain time interval are available, the regressors can be computed by fitting the output's values in Eq. 5.2 to the measured outputs through a process of minimization of the error between predicted and measured outputs of the system. Therefore, the numbers of the inputs and outputs' regressors are the parameters that define this model.

The limitation of the ARX model is the lack of adequate freedom in describing the properties of the disturbance term. It is possible to add flexibility to that by describing the equation error as a moving average of white noise, thus obtaining a different System Identification Method, the Auto-regressive Moving Average with eXtra input model, ARMAX. The formulation describing this model is:

$$\begin{aligned} y(t)_{(pr)} = & -a_1y(t-1) - \dots - a_{n_a}y(t-n_a) + b_1x(t-1) + \dots + b_{n_b}x(t-n_b) + \\ & + e(t) + c_1e(t-1) + \dots + c_{n_c}e(t-n_c) \end{aligned} \quad (5.3)$$

where c_i are the n_c regressors relative to the disturbance term. To the parameters that describe the ARX model, the number of disturbance term's regressors is added in the ARMAX model.

The expressions of the ARX and ARMAX models can be easily modified to describe a Multi-Input-Single-Output (MISO) system by expressing each $x(t-1) \dots x(t-m)$ and its relative regressors as vectors.

5.1.1 Search methods

Similar to the 'Training Algorithms' that will be analysed for ANNs, the regression search method is an iterative numerical optimization algorithm which is used to update the regressors values at each iteration to relate the system inputs to the output whilst minimizing the Mean Square Error (MSE) between the predicted

values from the regression algorithm ($y_{(pr)}$) and the measured ones (y). The MSE is a function of the parameters that appears in the formulation of $y_{(pr)}$:

$$MSE(\mathbf{p}) = \frac{1}{N_t} \sum_{i=1}^{N_t} (y(\mathbf{p})_{(pr)i} - y_i)^2 \quad (5.4)$$

where \mathbf{p} is the vector of the parameters of the model, i.e for ARX it contains the a_i and b_i regressors, N_t is the number of time steps of the time series and the subscript i denotes the computation of the quantity at the i -th time step.

Several optimization algorithms exist and some of them have been involved in the parametric exploration of the ARX and ARMAX models. The following minimization algorithms have been considered for these methods.

Gradient descent [95] is an unconstrained iterative minimization algorithm based on the computation of the gradient of the function that is the objective of the minimization. The function is minimized by moving in the direction of the negative gradient. In the context of regression algorithms, the gradient descent iterative procedure can be summarized as follows. It is started with a guess value of the parameters, \mathbf{p}_0 , and then the next values are computed by moving against the gradient:

$$\mathbf{p}_{n+1} = \mathbf{p}_n - \gamma_n \nabla MSE(\mathbf{p}_n)^T \quad (5.5)$$

so that the following monotonic sequence is obtained:

$$MSE(\mathbf{p}_0) \geq MSE(\mathbf{p}_1) \geq MSE(\mathbf{p}_2) \geq \dots MSE(\mathbf{p}_n) \quad (5.6)$$

The γ_n parameter defines the step size of the iteration. It influences the convergence speed. If increased, it can speed up the optimization process, but, if set too large, can cause the method to diverge. This minimization algorithm is really efficient and guarantees the convergence to the global minimum for convex function. On the other hand, for functions with a more complex and rugged solution landscape the method can often be able to only find a local minimum.

Newton's method [95] is another unconstrained iterative minimization method. It is based on the computation of the stationary point of the function through the minimization of the second-order Taylor approximation of the function around a candidate point. Starting from an initial set of guessed parameters, \mathbf{p}_0 , the method performs the iterations:

$$\mathbf{p}_{n+1} = \mathbf{p}_n - \gamma_n \frac{\nabla MSE(\mathbf{p}_n)}{\nabla^2 MSE(\mathbf{p}_n)} \quad (5.7)$$

where γ_n is the step size of the iteration. The Newton's method is more efficient than the Gradient descent algorithms and can converge in less iterations. However, it needs the computation of the second order derivatives for each iteration. Unfortunately, calculating this quantity is a formidable task from both CPU and

memory perspectives. To overcome this limitation, the **Gauss-Newton** method was introduced. It is derived from the Newton's method, but it is computationally more efficient because it does not require the computation of the second order derivatives. If the residuals of the regression are defined as:

$$\mathbf{r}(\mathbf{p}) = \mathbf{y} - \mathbf{y}(\mathbf{p})_{(pr)} \quad (5.8)$$

where \mathbf{y} is the vector of measured outputs and $\mathbf{y}(\mathbf{p})_{(pr)}$ is the vector of predicted outputs. The Gauss-Newton method iteratively minimizes the squared sum:

$$S(\mathbf{p}) = \sum_{i=1}^{N_t} r_i^2 \quad (5.9)$$

where r_i are the components of the residual vector and N_t is the total number of output's observations. The minimization is carried on iteratively updating the parameters' vector, starting from a trial value, in the following form:

$$\mathbf{p}_{n+1} = \mathbf{p}_n + (\mathbf{J}(\mathbf{p}_n)_{y(pr)}^T \mathbf{J}(\mathbf{p}_n)_{y(pr)})^{-1} \mathbf{J}(\mathbf{p}_n)_{y(pr)}^T \mathbf{r}(\mathbf{p}_n) \quad (5.10)$$

where $\mathbf{J}(\mathbf{p}_n)_{y(pr)}$ is the Jacobian matrix of the regression function $\mathbf{y}(\mathbf{p}_n)_{(pr)}$. The Jacobian matrix only includes first order derivatives of the function.

The third search method is the **Constrained non-linear programming solver based on trust-region**. Essentially, this algorithm searches for the minimum of a non-linear multi variable function, subject to constraints. The constraints can be described as mathematical rules that need to be considered as the algorithm searches for the minimum of an objective function (in the context of this work, MSE). The general constrained minimization problem can be described mathematically according to

$$\min MSE(\mathbf{r}) \quad for \quad \begin{cases} c(\mathbf{r}) > a \\ a < g(\mathbf{r}) < b \end{cases} \quad (5.11)$$

where $c(\mathbf{r})$ and $g(\mathbf{r})$ are constraint functions and, a and b are integers. This is different from the other unconstrained algorithms in which the algorithm searches for the minimum without having to adhere to constraints. In this work, the trust-region method is used, which means that to improve upon the current value of the objective function MSE , it is initially approximated with a simpler function q which reasonably represents MSE within a neighbourhood around the current value N_e , this is known as the trust-region. At each iteration the updated minimum is constrained to be within the trust-region, and furthermore at each iteration the trust-region gets decrease in size [96].

5.1.2 Regularization

Regularization is an mathematical process that reduces the effects of over-fitting in cases where the input-output time-series are heavily contaminated with noise. The regularization is obtained by penalizing some areas of the function space to improve generalization.

Regularization is implemented within the search method of the ARX model, the standard Gauss-Newton search method is used and regularization constants are calculated for the input and output regressors using the default 'tuned and correlated' regularization kernel [97].

5.2 Artificial Neural Networks

Artificial Neural Networks (ANNs) provide a method to approximate a non-linear function. A Neural Network can be interpreted as a non-linear parametric function whose parameters are learned from the data through a process defined as training. The network can continuously improve on its regressions based on the number of examples that it is trained with. ANNs do not need any inside knowledge of the system to build the input-output regression model.

The core of a Neural network are the nodes. Within the j -th node, the sum of weighted inputs (x_i) is summed with a bias (b_j) and a non-linear activation function (σ) is applied to obtain the output (y_j). The working scheme of a node is reported in Figure 5.1. A network is constituted of layers of nodes connected to each other. The input layer receive the inputs of the system, the middle layers (hidden layers) receive the output from the previous layers of nodes and finally the output layer, where a linear activation function is usually applied, return the output of the network. These allows the definition of a complex non-linear parametric function of the inputs. An example of the structure of simple Multi-Inputs-Single-Output (MISO) network is presented in Figure 5.2. Every connection of the network has its own weight and every neuron its own bias. The kind of connections between the layers, the number of hidden layers and the number of neurons defines the architecture of the network. The parameters of the networks, i.e., the weights and the biases, are determined through the training process. In practice, the input and output data of a system are given to the network, that, by fitting the data's outputs to the network's ones, is able to determine the best-fitting parameters. The reader is directed to [98] for a more detailed mathematical framework behind ANNs.

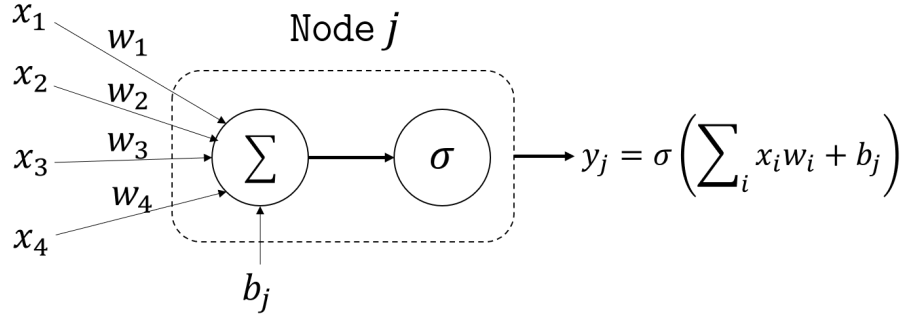
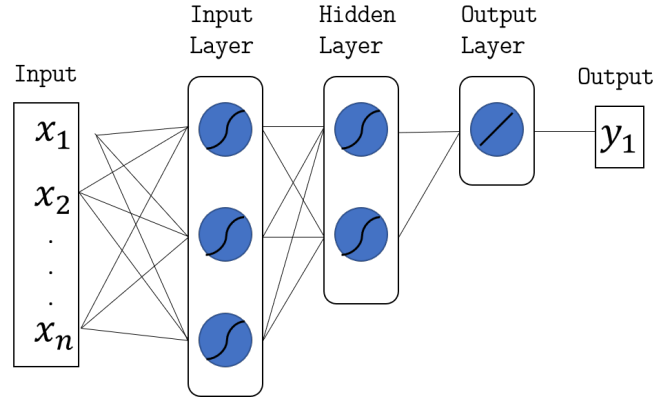


Figure 5.1: ANN node considering 4 inputs


 Figure 5.2: A MISO neural network - The circles represent the nodes of the network and the lines the weighted connections. The \mathcal{S} symbol is related to nodes with a sigmoid activation function, whereas the $/$ symbol denotes a linear activation function.

5.2.1 Architectures

The architecture of the neural network describes the pathway that the network follows between the input, hidden and output neurons. The simplest architecture, the feedforward, is presented in Figure 5.2. However, more complex architectures have been developed thanks to the recent advances within the field. Each architecture comes with pros and cons depending on the problem that the neural network is being designed to solve. The architectures which are investigated in this work are summarized in this section.

Feedforward neural networks [98] (FFN) are the original and simplest architectures of ANN. The data moves only in the forward direction and only the weights and biases of the forward connections need to be estimated in the training process. The working scheme of this architecture, as it will be used in this work, is reported in Figure 5.3.

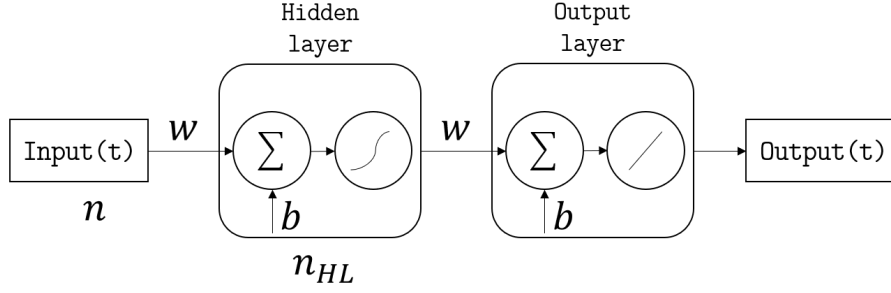


Figure 5.3: Feedforward Network - The scheme is reported for a network with one time series input and one node in the hidden layer, but it can be easily extended to consider n time series inputs and n_{HL} nodes in the hidden layer. The activation function in the hidden layer is the sigmoid function (\mathcal{S}), whereas it is the linear function (\mathcal{L}) in the output layer.

Cascade forward neural networks [99] are derived from FFN. However, they include connections between the input and each hidden layer. The weights of this connections are added to the parameters of the network. The CFN architecture, although introducing new parameters to be estimated, often shows better convergence performances than FFN. The CFN network is described in Figure 5.4

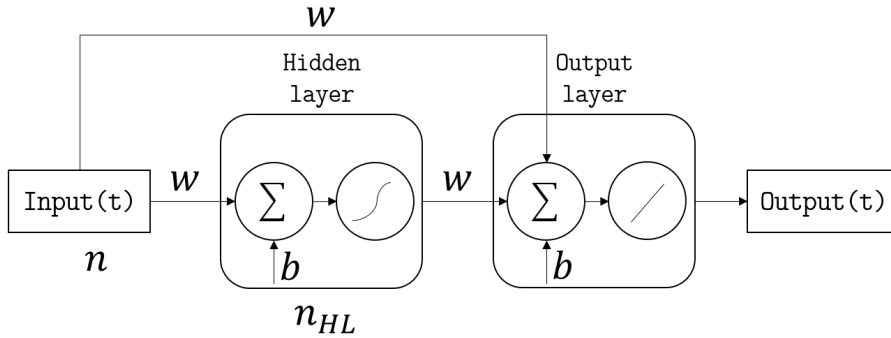


Figure 5.4: Cascade Forward Network - The scheme is reported for a network with one time series input and one node in the hidden layer, but it can be easily extended to consider n time series inputs and n_{HL} nodes in the hidden layer. The activation function in the hidden layer is the sigmoid function (\mathcal{S}), whereas it is the linear function (\mathcal{L}) in the output layer.

Time-delay neural networks [100] (TDN) introduce the concept of tap delay in the context of ANNs. With respect to the FFN architecture, a tap delay is associated to the input weights. That means that inputs from previous time steps are added to the inputs of the network and the relative weights are added to the parameters of the network. The lagged input variables in the input layer allow

TDNs to provide a finite dynamic response and hence the architecture is particularly applicable to time-series predictions [101].

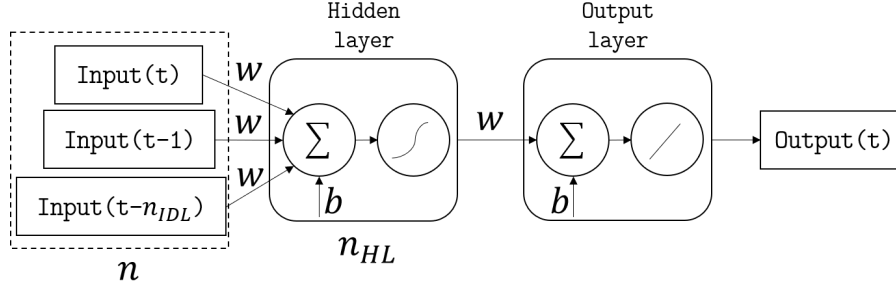


Figure 5.5: Time-delay Neural Networks - The scheme is reported for a network with one time series input and one node in the hidden layer, but it can be easily extended to consider n time series inputs and n_{HL} nodes in the hidden layer. The scheme considers n_{IDL} input delays for every input. The activation function in the hidden layer is the sigmoid function (\mathcal{S}), whereas it is the linear function (\mathcal{L}) in the output layer. Every connection has a weight (w) and every node a bias (b).

The **Distributed Delay Network** [99] (DDN) is similar to TDN, however, the tap delays are also added to the hidden layer's outputs (Figure 5.6). For this reason the DDN architecture provides higher fidelity with fewer iterations, however, the addition of the weights relative to the delayed outputs means that it is computationally less efficient.

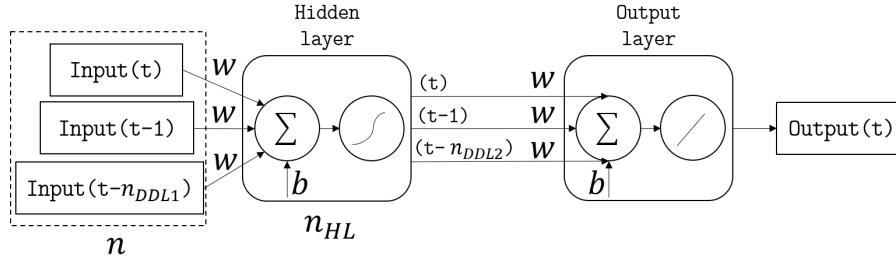


Figure 5.6: Distributed Delay Network - The scheme is reported for a network with one time series input and one node in the hidden layer, but it can be easily extended to consider n time series inputs and n_{HL} nodes in the hidden layer. The scheme considers n_{DDL1} input delays and n_{DDL2} output delays. The activation function in the hidden layer is the sigmoid function (\mathcal{S}), whereas it is the linear function (\mathcal{L}) in the output layer. Every connection has a weight (w) and every node a bias (b).

Layer Recurrent Networks [99] (LRN) introduce the concept of memory in the training/learning process. In fact, they use the delayed output from the hidden layer as an input for the layer itself (Figure 5.7). The advantage of the

LRNs is that they retain memory between iterations using their own output from the current iteration as an input for the next iteration.

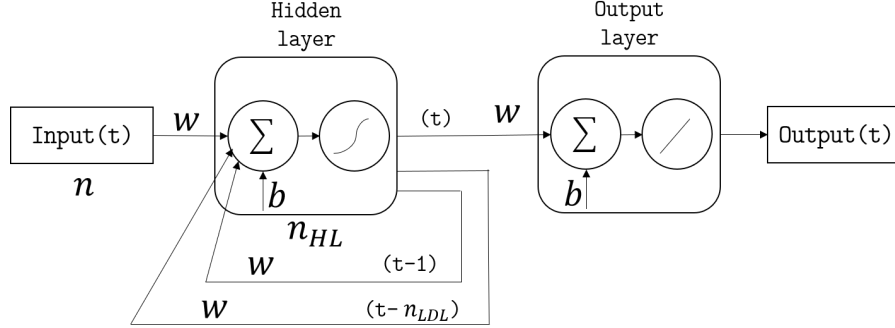


Figure 5.7: Layer Recurrent Network - The scheme is reported for a network with one time series input and one node in the hidden layer, but it can be easily extended to consider n time series inputs and n_{HL} nodes in the hidden layer. The scheme considers n_{LDL} layer delays. The activation function in the hidden layer is the sigmoid function (\mathcal{S}), whereas it is the linear function (\mathcal{L}) in the output layer. Every connection has a weight (w) and every node a bias (b).

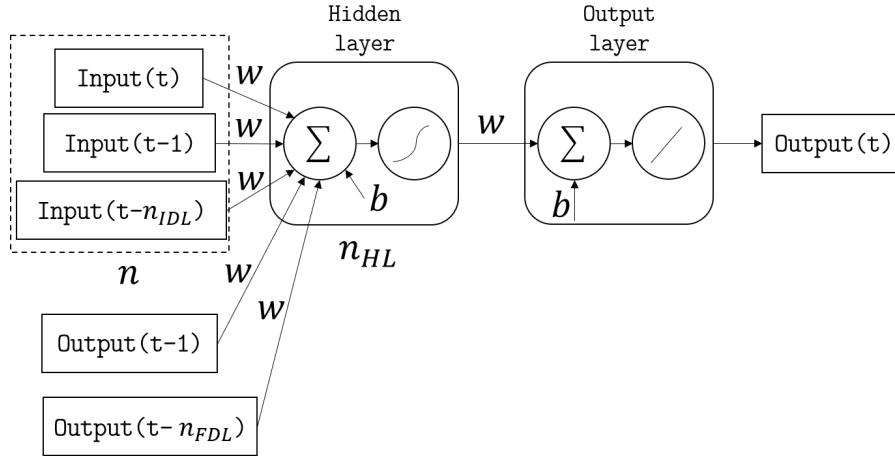


Figure 5.8: Non-linear Auto-regressive Network - The scheme is reported for a network with one time series input and one node in the hidden layer, but it can be easily extended to consider n time series inputs and n_{HL} nodes in the hidden layer. The scheme considers n_{IDL} input delays and n_{FDL} feedback delays. The activation function in the hidden layer is the sigmoid function (\mathcal{S}), whereas it is the linear function (\mathcal{L}) in the output layer. Every connection has a weight (w) and every node a bias (b).

Non-linear Auto-regressive Network [99] (NXN) is based on the auto-regression principle that inspired the ARX and ARMAX models, although introducing the non-linearity in the regression model. As a consequence, the outputs from the previous time steps are used as inputs from the current time step. As for the TDN, the inputs from the previous time steps are also considered as input for the current time step (Figure 5.8). The presence of multiple connections and the consequent high number of weights makes the approach suitable for highly non-linear dynamic systems but also makes it computationally expensive.

5.2.2 Training Algorithms

For all the different architectures the output predicted by the network at the i -th time step ($y_{(pr)i}$) can be expressed as a function of the inputs of the systems and of the weights and biases of the network:

$$y_{(pr)i} = f(x_i, \mathbf{p}) \quad (5.12)$$

where \mathbf{p} is the vector of the weights and biases of the network. Therefore, the same expressions of the MSE, reported in Eq. 5.1.1, and of the residual, included in Eq. 5.1.1, can be adopted to define the training of the networks. The training function is iteratively working to search for a set of weights and biases which can best relate the inputs to the output whilst minimizing the error. The Gradient descent and the quasi-Newton methods described in Paragraph 5.1.1 can be also used for the training of ANNs. They are, nevertheless, extremely memory intensive and, therefore they have been discarded from this study. The two following extremely efficient training algorithms have been considered:

Levenberg-Marquardt optimization is an iterative minimization algorithm that combines the features of the gradient decent and Gauss-Newton algorithms [102]. As for the Gauss-Newton optimizer, this algorithm works to minimize the squared sum in Eq. 5.1.1. Adopting the same notation of Eq. 5.1.1, the iteration process of this algorithm for the n -th+1 step is defined as:

$$\mathbf{p}_{n+1} = \mathbf{p}_n + (\mathbf{J}(\mathbf{p}_n)_{y(pr)}^T \mathbf{J}(\mathbf{p}_n)_{y(pr)} + \lambda_n \mathbf{I})^{-1} \mathbf{J}(\mathbf{p}_n)_{y(pr)}^T \mathbf{r}(\mathbf{p}_n) \quad (5.13)$$

where $\lambda_n > 0$ is a damping factor and \mathbf{I} is the identity matrix. The damping factor controls whether the method behave closely to the gradient descent or Gauss-Newton algorithms. In fact, if the reduction of the squared sum of the residuals (Eq. 5.1.1) is rapid, a smaller value can be used, bringing the algorithm closer to the Gauss-Newton algorithm, whereas if an iteration gives insufficient reduction, λ_n can be increased, giving a step closer to the gradient-descent direction. This method is widely used for the training of ANNs.

The second considered algorithm is the Levenberg-Marquardt method with **Bayesian regularization**. This method implements a regularization algorithm

within the standard Levenberg-Marquardt iterative procedure. For every iteration, the weights and biases computed by this algorithm are then further optimised to achieve a better generalisation and avoid over fitting, according to the Bayesian approach [103].

Chapter 6

Internal wing loads reconstruction of a fighter aircraft

This activity, undertaken in collaboration with Australian Defence Science & Technology (DST) Group, focuses on identifying the most appropriate strategy for the prediction of structural loading cases, where poorly calibrated and weakly coherent strain sensors and flight parameters data are used as an input to predict individual load spectra for a modern fighter air platform. The final goal is to estimate the fatigue life consumption of the airframe due to the monitored loads. The System Identification Methods described in Chapter 5 have been investigated to achieve this goal. For every method, a broad parameter exploration is performed and the best configurations are compared. The main difficulty arisen by the problem is the lack of physical information about the structure due to export restrictions. This poses a serious challenge for the evaluation on the fatigue life consumption. To overcome this limitation, a new parameter, independent from the geometry of the structure and able to statistically account for different possible materials is developed. This work is part of a broader investigation on the load monitoring of aircraft structures undertaken by RMIT and DST whose other outcomes are reported in [104, 105].

6.1 The dataset

Thanks to a collaborative research agreement between RMIT University and DST Group, surrogate data created from a normalised dataset and generated from defence fighter air platform flight test data, is provided by DST Group. The data consist of responses from N_{SG} strain sensors (the exact number not given to preserve data anonymity), the flight parameters (angle of attack and dynamic pressure) and six loading sensors on the main wing from 100 separate aircraft manoeuvres. The loading data is comprised of values for bending moment and torsion at three

sections of the wing. Therefore, the multi-input strain sensor information and flight parameters are used to predict the following load spectra: section one bending (S1B), section one torsion (S1T), section 2 bending (S2B), section two torsion (S2T), section three bending (S3B) and section three torsion (S3T). The increase in the numbering of the sections denotes an increase in the distance from the root section of the wing.

This activity focuses on the study of the low-frequency manoeuvrers loads. However, it is part of a broader study that includes also the analysis of the high-frequency buffet loads. These have been considered by Candon et. al in [104, 105]. Therefore, to analyse the low frequency manoeuvrer loads, a low-pass IIR zero-phase filter is applied to both the input strains and the output loads signals, whereas the data used to analyse the buffet is processed through a band-pass IIR zero-phase filter. The cut-off and band frequencies for the two filters are chosen according to consideration derived from the knowledge of the stiffness properties of the wing. These frequencies are not supplied to preserve data anonymity. An example of the filtered data for the manoeuvrer and buffet loads, along with the unfiltered data, is given in Fig. 6.1.

For this application, the 50% of the filtered data are used to train the investigated System Identification Methods, whereas the remaining 50% are used to verify the predictions of the methods.

It is important to highlight that no other information about the geometry and the material of the investigated structure is made available and, therefore, considered for the load identification process.

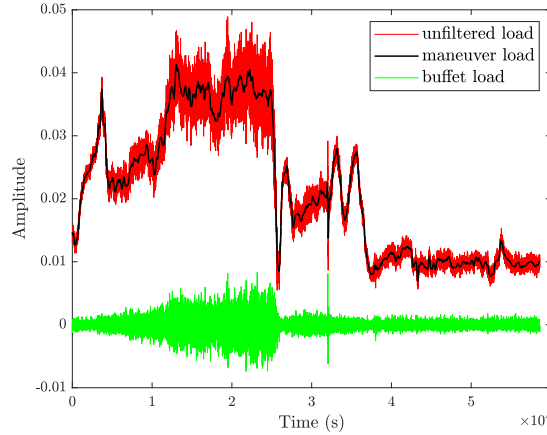


Figure 6.1: Example of available load data and filtering

Moreover, the challenging scenario posed by this application is highlighted by the analysis of the magnitude-squared coherence between a representative set of inputs (four wing strain sensors) and outputs (2 load spectra) data. The magnitude

squared coherence measures how well two signals correlate to each other for each frequency. For two signals $l(t)$ and $s(t)$, the magnitude-squared coherence is defined as it follows:

$$C_{ls}(f) = \frac{|P_{ls}(f)|^2}{P_{ll}(f)P_{ss}(f)} \quad (6.1)$$

where f is the frequency, $P_{ll}(f)$ and $P_{ss}(f)$ are the power spectral densities of $l(t)$ and $s(t)$, respectively, and $P_{ls}(f)$ is the cross power spectral density of $l(t)$ and $s(t)$. For each frequency, the perfect correlation between the signals generates $C_{ls}(f)$ equal to 1 and no correlation generates $C_{ls}(f)$ equal to 0.

Figure 6.2a presents the coherence analysis for S1B input-output problem which is the most coherent. There is reasonable correlation between the strain signal and the load (0.7 - 0.8) for the main peak at approximately 14.5 Hz, moderate correlation (0.3 - 0.6) from a single strain gauge (SG3) for the secondary peak, at approximately 5 Hz, and no correlation beyond 40 Hz.

Figure 6.2b shows the coherence for Section 3 torsion input-output problem which is the least coherent, hence, presents a significant challenge for the regression algorithms, as is shown in the remaining of this chapter. This load case is representative of all the torsion load spectra. In general, for the torsional loads, there is moderate correlation (0.5 - 0.6) for the main peak at approximately 15 Hz, a weaker correlation (0.2 - 0.4) for the peak between 20 Hz and 40 Hz and again no correlation above 40 Hz. These mostly poor coherences significantly increase the difficulty in obtaining accurate prediction of the load spectra. In fact, the regression models are trying to predict frequencies in the outputs which scarcely exist in the inputs.

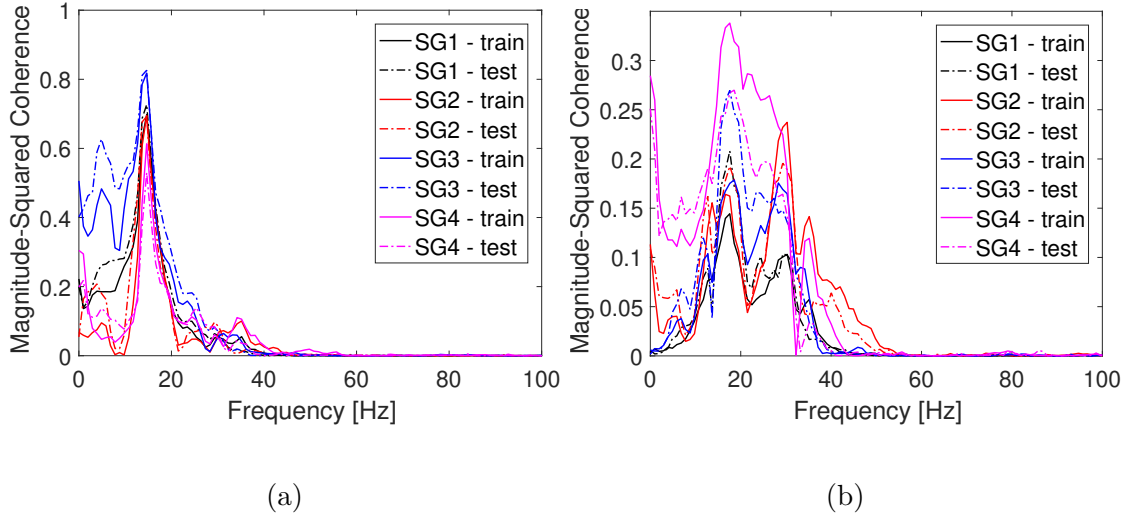


Figure 6.2: Input-output magnitude-squared coherence for a) Section 1 bending and b) Section 3 torsion

6.2 Fatigue prediction assessment

One of the main difficulties of this application, that inspired the use of data driven regression algorithms, is the lack of knowledge of a physical model and of the characteristics of the structure. Although this does not represent an obstacle for the application of the selected methods, it raises a significant challenge for the final goal of the project, the evaluation of the accuracy of the methods on the estimation of the fatigue life consumption.

A crucial tool for the fatigue life estimation is the rainflow-counting algorithm [106]. Essentially, a complex load spectrum can be reduced into a set of load reversals (peaks and troughs) which are grouped according to a set of pre-defined load cycle ranges, which represent the extent of fatigue cycles. These are then represented in what is known as a load cycle exceedance curve. From the measured and predicted load spectra of the section loads it is possible to easily compute the load cycle exceedance curves with the rainflow-counting approach [106]. These curves are typically used for the fatigue life analysis through the use of different fatigue models. One of the most simple method to estimate the number of cycles to failure is the Miner's rule. However, this rule is based on the stress levels induced by the load cycles and not on the load cycles themselves. Without the knowledge of the material of the structure and of the properties of the sections, the computation of the stress level induced by each load cycle is not measurable and consequently also fatigue life considerations are not derivable. The further analysis of the Miner's rule formulation and some hypothesis on the behaviour and modelisation of a wing structure led to the overcoming of this issue and to the consequent formulation of a parameter able to asses the accuracy of the fatigue life predictions.

The miner's rule is formulated as follows:

$$\sum_{i=1}^l \frac{n_i}{N_i} = D \quad (6.2)$$

where n_i are the number of cycles that exceed the i -th stress level, N_i is the number of cycles to failure for the i -th stress cycle range. The summation is performed over the l stress cycles ranges identified by the stress cycle exceedance curve. According to the rule, the failure due to fatigue happens when the value of D reaches 1. Therefore, D represents the percentage of consumed fatigue life for the load spectra that produced the considered stress cycle exceedance curve. The number of cycles to failure for a certain stress cycle range, N_i , is derived from the S/N curves. These are curves that report the values of these experimentally measured characteristics for a certain material. To sum up, the application of the Miner's rule, starting from the load cycle exceedance curve, requires the transformation of the load cycles into stress cycles, through the adoption of a structural model, and the knowledge of the S-N curve of the material (Figure 6.3).

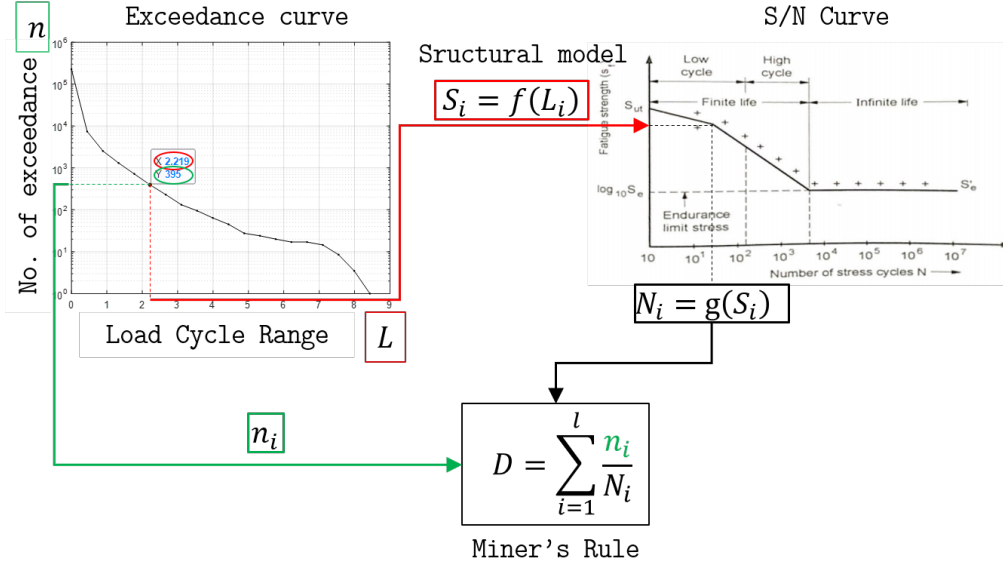


Figure 6.3: Miner's rule from the load cycles exceedance curve - The n_i are directly derived from the Load cycles exceedance curve. The stress ranges (S_i) are computed from the load ranges (L_i) through a structural model ($f(L_i)$). The cycles to failure (N_i) are computed from the stress ranges through the S/N curve of the material ($g(S_i)$).

On a first approximation, the wing of an aircraft can be modelled as a beam-like structure. Therefore, for this application a beam analytical structural model can be considered for the computation of the stresses. Following the scheme reported in Figure 6.3, the function, f , that express the stresses, S_i , in terms of the generic section loads, L_i , according to the beam model, can be expressed as it follows:

$$S_i = f(L_i) = \frac{L_i}{I} d \quad (6.3)$$

where I is an inertial characteristic of the section and d is a length that is also a characteristics of the section. These two parameters change according to considered load, a bending load or a torsion one, and are only dependent on the geometry of the beam section.

On the other hand, the relation ($g(S_i)$) between the stresses and the number of cycles to failure, N_i , given by the S/N curves of the material, has the following analytical formulation:

$$N_i = g(S_i) = k S_i^{-m} \quad (6.4)$$

where the k and m coefficient are evaluated experimentally and are a characteristic of the material. By combining Eq. 6.3 and Eq. 6.4 and substituting the derived expression of N_i into Eq. 6.2, the analytical formulation of the Miner's rule is

obtained:

$$D = \sum_{i=1}^l \frac{n_i}{N_i} = \sum_{i=1}^l \frac{n_i}{k \left(\frac{L_i}{I} d \right)^{-m}} \quad (6.5)$$

This expression depends on the geometry of the section through the characteristics I and d and on the material of the structure through the coefficients k and m . Following Eq. 6.5, the comparison of the consumed fatigue life, D , for the measured load cycles ranges and for the ones predicted through the investigated System Identification Methods, can be expressed mathematically in a fraction form:

$$\frac{(D)_{pr}}{(D)_{meas}} = \frac{\sum_{i=1}^l \frac{(n_i)_{pr}}{(N_i)_{pr}}}{\sum_{i=1}^l \frac{(n_i)_{meas}}{(N_i)_{meas}}} = \frac{\sum_{i=1}^l \frac{(n_i)_{pr}}{k \left(\frac{(L_i)_{pr}}{I} d \right)^{-m}}}{\sum_{i=1}^l \frac{(n_i)_{meas}}{k \left(\frac{(L_i)_{meas}}{I} d \right)^{-m}}} \quad (6.6)$$

where $(\cdot)_{meas}$ and $(\cdot)_{pr}$ denotes measured and predicted quantities, respectively. In the last expression of Eq. 6.6, some parameters can be simplified, leading to:

$$\frac{(D)_{pr}}{(D)_{meas}} = \frac{\sum_{i=1}^l \frac{(n_i)_{pr}}{(L_i)_{pr}^{-m}}}{\sum_{i=1}^l \frac{(n_i)_{meas}}{(L_i)_{meas}^{-m}}} \quad (6.7)$$

The percentage error in the predicted fatigue life consumption with respect to the measured one, $\%Edf$, can be computed as follows:

$$\%Edf = 100 \times \left(\frac{(D)_{pr}}{(D)_{meas}} - 1 \right) = 100 \times \left(\frac{\sum_{i=1}^l \frac{(n_i)_{pr}}{(L_i)_{pr}^{-m}}}{\sum_{i=1}^l \frac{(n_i)_{meas}}{(L_i)_{meas}^{-m}}} - 1 \right) \quad (6.8)$$

This parameter does not depend on the geometry of the section any more, however it still depends on the material through the m parameter of the S/N curve. To get rid of this dependency from an unknown characteristic of the investigated structure, a statistical approach is adopted. This error is computed for four aluminium alloys and then averaged to get a parameter able to provide a quantification of the error in the fatigue consumption not dependent on the unknown physical quantities of the problem. The fatigue life consumption error averaged with respect to the four materials, $\%Fdf$, is defined as:

$$\%Fdf = \sum_{j=1}^4 \frac{|\%Edf_j|}{4} \quad (6.9)$$

where the subscript j denotes the quantity computed for the j -th material. The four considered aluminium alloys are 7075, 2024, 7050 and 6061. The values of the m parameters for these materials are reported in Table 6.1.

Alloy	m	Source
7075-T6	5.80	MIL-HDBK-5H (fig. 3.7.6.1.8 (d))
2024-T4	9.09	MIL-HDBK-5H (fig. 3.2.3.1.8 (a))
7050-T7451	3.24	MIL-HDBK-5H (fig. 3.7.4.2.8 (a))
6061-T6	9.84	MIL-HDBK-5H (fig. 3.6.2.2.8)

Table 6.1: m values for the considered aluminium alloys.

Since very different load spectra can produce the same consumed fatigue life according to the Miner's rule, another parameter is considered, along with $\%Fdf$, to assess the accuracy of the predictions, the coefficient of determination. In this context, the coefficient of determination, R^2 , for a time series of N measured, $y_{(i=1,...,N)}$, and predicted, $y_{(pr)(i=1,...,N)}$ loads, is defined as:

$$R^2 = 1 - \frac{\sum_{i=1}^N (y_i - y_{(pr)i})^2}{\sum_{i=1}^N (y_i - \bar{y})^2} \quad (6.10)$$

where \bar{y} is the mean value of the time series $y_{(i=1,...,N)}$. R^2 gives a statistical evaluation of how well the observed data are fitted by the regression model. A value of $R^2 = 1$ indicates that the model explains all the variability of the observed data around their mean, whereas $R^2 = 0$ indicates that the model explains none of the variability of the observed data around their mean. The coefficient of determination, R^2 , with respect to the measured and predicted load spectra, is used to define an interval of confidence for the predictions of fatigue. In fact, it can be used as a reliability parameter to validate that the fatigue life consumption predictions are produced by a well predicted load spectrum and not by a different one able to produce similar fatigue life estimations. Within the parametric exploration of each System Identification Method, only predictions that show a value of the R^2 higher than the 90% of the maximum coefficient of determination measured for the selected method are considered. I.e., for the prediction of the S1T with ANNs, only prediction that resulted in a R^2 higher than 90% of the architecture that obtained the maximum value of R^2 for this load spectrum are considered.

6.3 Linear regression based analysis

In this section, the application of the linear regression based models on the loads and fatigue life prediction is described. The ARX and ARMAX models, as described in Paragraph 5.1, are applied using the strain gauges and the flight parameters as inputs to predict the loads and the fatigue life consumption error from the derived load cycles exceedance curves. Each load spectrum is analysed separately, thus considering six different Multi-Inputs-Single-Output models.

For the ARX model, Gauss–Newton (GN) search method, otherwise known as the quasi–Newton search method, is used. Within this framework, the default ‘tuned and correlated’ (TC) regularization kernel is also implemented. Hence, two ARX configurations are considered, ARX and ARX-reg. On the other hand, for the ARMAX model, the GN search method, the Gradient Descent (GD) and constrained non-linear programming (FMC) search methods are implemented in this section. This provides three frameworks, ARMAX-GN, ARMAX-GD and ARMAX-FMC.

For each one of the above mentioned frameworks, an intensive parametric exploration is performed. The parameters which are investigated for these regression models include:

- n_a (number of output regressors) = 2:2:10 – ARX and ARMAX
- n_b (number of input regressors) = 2:2:10 – ARX and ARMAX
- n_c (number of disturbance regressors) = 1:6 – ARMAX

In practice, 50 ARX architectures are considered: [2 configurations (ARX, ARX-reg)] x [5 output regressors’ configurations (2:2:10)] x [5 input regressors’ configurations (2:2:10)]. For the ARMAX, 450 architectures are considered: [3 configurations (ARMAX-GN, ARMAX-GD and ARMAX-FMC)] x [5 output regressors’ configurations (2:2:10)] x [5 input regressors’ configurations (2:2:10)] x [6 disturbance regressors’ configurations (1:6)].

The best performing configurations of this parametric exploration for each one of the six load spectra are reported in Table 6.2.

framework search meth.	Load spectrum					
	S1B	S1T	S2B	S2T	S3B	S3T
	ARMAX FMC	ARMAX GD	ARMAX FMC	ARMAX FMC	ARMAX GN	ARMAX FMC
n_a	10	4	4	4	8	4
n_b	8	4	6	10	4	6
n_c	1	1	4	6	1	6
$\%Fdf$	4.6	25.3	0.97	3.6	5.8	20.7
R^2	0.97	0.61	0.88	0.69	0.78	0.66

Table 6.2: Highest performing results for linear regression based models with a 90% R^2 condition.

It can be noticed that for all the six load spectra the ARMAX model produces the most accurate fatigue life consumption predictions. Nevertheless, this framework is able of accurate predictions only for the bending load spectra and for S2T, where the error in the predicted fatigue life never exceeds 6%. The torsion load

spectra, which according to the coherence analysis in Section 6.1 are the most difficult cases to predict, show a significant inaccuracy of the predictions. The same trend can be observed from the analysis of the values of R^2 .

6.4 Artificial Neural Networks analysis

The investigation is continued with the exploration of the Artificial Neural Networks. The architectures described in Paragraph 5.2.1 are tested on the reconstruction of the load spectra and the fatigue life consumption from strain and flight parameters inputs. Also in this case each load spectrum is treated separately through a Multi-Inputs-Single-Output system. Within each architecture two training algorithms are implemented, the Lavenberg-Marquardt optimization (LM) and the Lavenberg-Marquardt with Bayesian regularization algorithm (BR). Also in this case, a broad parameter exploration is performed for each architecture-training algorithm configuration. The functional parameter space investigated includes:

- n_{HL} (number of neurons in the hidden layer) = $1:N_{inputs}$
- n_{IDL} (number of input delays) = $1:[2:N_{inputs}]$ – TDN and NXN
- n_{FDL} (number of feedback delays) = $1:[2:N_{inputs}]$ – NXN
- n_{LDL} (number of layer delays) = $1:[2:N_{inputs}]$ – LRN
- n_{DDL1} (number of distributed delays) = $1:[2:N_{inputs}]$ – DDN
- n_{DDL2} (number of distributed delays) = $1:[2:N_{inputs}]$ – DDN

where N_{inputs} is the number of input parameters, that includes the angle of attack, the dynamic pressure and the strain sensors, whose quantity is not reported due to exportation restrictions. As for the ARX and ARMAX models the quantity of the tested network is obtained by multiplying each architecture by the number of tested training algorithms and the number of explored parameters.

The best performing configurations, resulting from this parametric study, are reported in Table 6.3. In this case, a unique best architecture can not be identified, although the DDN architecture, with the BR training algorithm, shows the highest accuracy in the fatigue evaluation for three out of six load spectra. The values of the error in the fatigue life consumption are smaller than 9% for all the load spectra. Nevertheless, once again, the torsion loads result as the most difficult to predict. The values of R^2 show a better overall accuracy than the linear regression based models.

	Load spectrum					
	S1B	S1T	S2B	S2T	S3B	S3T
Arch.	DDN	DDN	CFN	NXN	DDN	TDN
training alg.	BR	BR	LM	BR	BR	BR
n_{HL}	5	2	3	3	5	4
n_{IDL}	-	-	-	2	-	4
n_{DDL1}	3	6	-	-	5	-
n_{DDL2}	5	3	-	-	5	-
n_{FDL}	-	-	-	4	-	-
$\%Fdf$	0.84	8.3	1.1	3.3	0.93	4.3
R^2	0.97	0.72	0.99	0.72	0.84	0.75

Table 6.3: Highest performing results for ANNs with a 90% R^2 condition.

6.5 Statistical Analysis and global best

In this section, the assessment of the global best architecture is performed according to multiple considerations. The first evaluation involves a statistical analysis of the R^2 index, that is used as a primary condition to quantify the overall reliability for each explored System Identification Method. This statistical evaluation is performed via the box and whisker plots in Figure 6.4. The box are obtained considering all the R^2 values obtained by every tested architecture for the two families of methods. The plots for S1B, S2B, S3B, and S3T load spectra show a significantly higher consistency of the ANNs' predictions. In fact, the boxes (representing the first upper and lower quartiles) relative to ANNs are comparatively smaller than the linear regression based ones and the whiskers are within close range of the box. Moreover, the median lines within the boxes highlight the observation of a higher mean value of the ANNs for four out of six load spectra. On the contrary, for S1T and S2T, the statistical evaluation of the regression methods proves that these methods are more consistent than the ANNs, resulting in less dispersion and higher values of the first quartile and median values. Nevertheless, the majority of the load spectra suggests an overall better performance of the ANNs. Moreover it has to be mentioned that there is a large number of outliers (red crosses) for both ANN and regression results, indicating a significant dispersion of the results. This dispersion calls the attention to the importance of an accurate parameter optimization within each model, necessary to avoid these bad outliers.

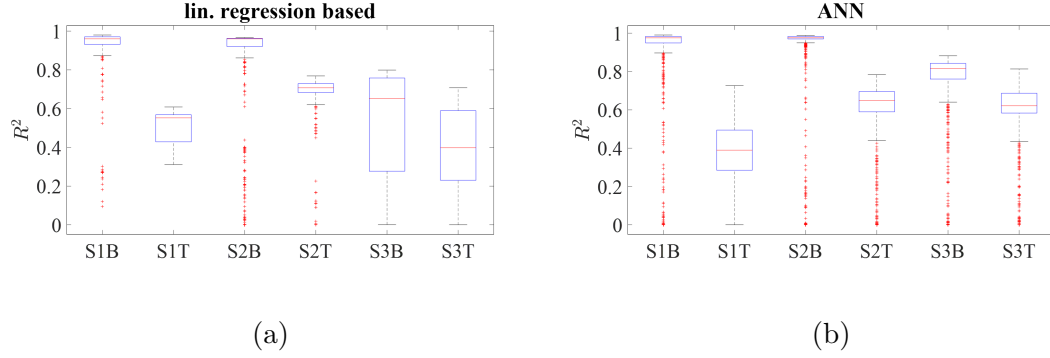


Figure 6.4: Box and whisker plots for R^2 - a) presents the linear regression based predictions and b) presents the ANN based predictions.

The overall better accuracy of the ANNs is further demonstrated by the comparison of the best fatigue life consumptions predictions reported in Table 6.2 and 6.3 for the linear regression based models and the ANNs, respectively. This comparison is graphically summarized in the bar plot of Figure 6.5. The better accuracy of the ANNs architectures is shown for all the load spectra and with respect to both R^2 and $\%Fdf$, with the only exception of the S2B load spectrum, that, anyway, shows a only trifling advantage in the $\%Fdf$. Moreover, for the load spectra S1T and S3T, that belong to the most difficult to predict torsion load spectra, the difference in the estimation of the fatigue life consumption is strongly in favour of the ANNs.

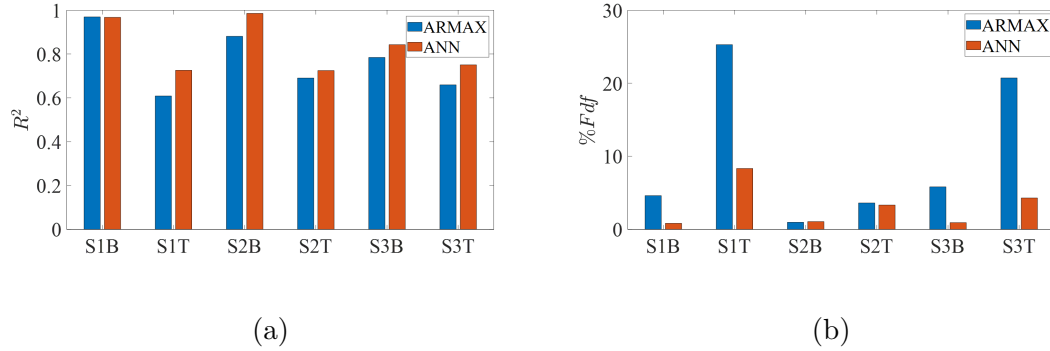


Figure 6.5: Best results comparison - a) presents the comparison between the best linear regression based models (ARMAX only) and the best ANNs in terms of R^2 b) presents the comparison between the best linear regression based models (ARMAX only) and the best ANNs in terms of $\%Fdf$.

These analysis restricted the search space for the unique best performing architecture to the ANN family. The further investigation on the best performing ANNs architectures highlights the prevalence of the Distributed Delays Network with the Bayesian regularization training algorithm. This architecture shows the

highest accuracy for four out of six load spectra, with the exception of the S2B, S2T, and S3T. Therefore, the DDL is selected as the global best candidate and the predictions of the three remaining load spectra are analysed. Table 6.4 shows the lowest fatigue life consumption errors obtained for all the six load spectra using the DDL-BR architecture. They are consistently under 9% for every load spectra, even for the ones that presented the best prediction from a different architecture. The DDL-BR is the only architecture that shows this level of consistency and accuracy for all the six load spectra and it is therefore selected as the global best System Identification Method for the selected problem.

	Load spectrum					
	S1B	S1T	S2B	S2T	S3B	S3T
Arch.	DDN	DDN	DDN	DDN	DDN	DDN
training alg.	BR	BR	BR	BR	BR	BR
n_{HL}	5	2	4	6	5	3
n_{DDL1}	3	6	5	2	5	6
n_{DDL2}	5	3	6	5	5	5
$\%Fdf$	0.84	8.3	3.2	6.3	0.93	5.0
R^2	0.97	0.72	0.98	0.72	0.84	0.75

Table 6.4: Global best performing System Identification Model.

To conclude, the study proves the overall superior capabilities of the ANNs based model with respect to the linear regression based ones on the prediction of the wing's load spectra of a fighter aircraft. In particular, the ANNs outperforms the other methods for the prediction of the torsion loads, that showed poor correlation with the strain inputs. In particular, the DDL-BR architecture shows the overall best prediction of the fatigue life consumption for the investigated application. Moreover, the statistical analysis of the parameter exploration for the different models, also highlights the importance of the parameters' calibration to find the best performing set of parameters within each model.

To generalise these conclusions and infer about the robustness of monitoring for the internal loads of a fighter aircraft, the future works should verify the obtained results for different data sets coming from different platforms.

Chapter 7

External loads reconstruction and shape sensing on an aluminium wing box

7.1 An integrated approach

In this section an integrated framework to simultaneously reconstruct the external loads and the deformed shape induced by the loads is proposed. The method is based on a 2 steps procedure. In the first step the external loads are identified from discrete strain measurements through the computation of the coefficients of influence between the discretized loads and the measured strains. The second step exploits the identified load to reconstruct the deformed shape through a standard FEM analysis. For simplicity, in the remaining of this thesis, this procedure will be defined as 2-step method.

The proposed 2-step procedure, once defined, is applied on the numerical monitoring of the external loads and the induced displacements of an aluminium swept wing box. Two load cases are considered, one constituted by a pressure distribution and one constituted by a set of concentrated forces. The pressure distribution is discretized with FE and, for the first time, quadrilateral elements are implemented for this discretization. The accuracy of the method to perform the shape sensing of the structure is compared with the well-established iFEM. Moreover, the effect of the measurement error, typical of experimental scenarios, is considered to assess the robustness of the method to this kind of uncertainty.

7.1.1 External loads identification (1st step)

The first step concerns the identification of the external loads. The external loads can be computed from discrete strain measurements through the computation of the coefficients of influence between the investigated loads and a set of

measured strains. To perform this task, the loads applied on a structure needs to be discretized in some way. Airolti et. al. [82] developed this concept for concentrated loads. If a load case can be modelled with a set of concentrated forces, the load identification problem is formulated as it follows.

If the hypothesis of linear elasticity is considered, the j -th measured strain component, ε_j^m , can be expressed as the superposition of the ε_{ji}^m strains induced by the m_f concentrated forces, F_i . Moreover, in the linear elastic regime, the i -th strain contribution, ε_{ji}^m , induced by the i -th F_i is linearly proportional to the i -th nodal force itself. These considerations lead to the following formulation of the j -th strain component:

$$\varepsilon_j^m = \sum_{i=1}^{m_f} \varepsilon_{ji}^m = \sum_{i=1}^{m_f} s_{f_{ji}} F_i \quad (7.1)$$

where $s_{f_{ji}}$ is the i -th unknown coefficient of linear combination that relates the j -th strain component to the i -th nodal values of the pressure. When m_s measured strain components are available, the Eq. 7.1, expressed in matrix form, becomes:

$$\{\varepsilon^m\}_{m_s \times 1} = [s_f]_{m_s \times m_f} \{F\}_{m_f \times 1} \quad (7.2)$$

If a detailed FE model of the structure is available, the matrix of the coefficients of influence, $[s_f]_{m_s \times m_f}$, can be easily computed through the iterative resolution of a standard direct FE problem. The i -th column of the matrix is computed by imposing that $F_i = 1$ and $F_k = 0$ ($k \neq i$). The i -th nodal force is then applied to the FE model of the structure and the desired m_s strain components are extracted. Iterating the procedure to the m_f columns, allows the computation of the entire matrix. The application of this procedure requires the construction of an accurate FE model of the structure. Therefore, the geometry, the material properties and the constraints of the structure have to be known.

Once the $[s_f]$ matrix is populated, the expression of the unknown nodal forces as a function of the measured strain is easily obtained by inverting Eq. 7.2. Since in practical applications $m_s \neq m_f$, the inversion of $[s_f]$ is obtained by means of Moore-Penrose pseudo inverse matrix formulation, $[s_f^+]$:

$$\{F\} = [s_f^+] \{\varepsilon^m\} \quad (7.3)$$

By substituting the actually measured values of the strains into $\{\varepsilon^m\}$, the expression gives the nodal values of the forces that best fit the actually applied loads that induced the measured strains.

This method has been expanded to identify pressure fields by Nakamura et al. in [83]. In order to adopt the same approach, a distributed pressure has to be discretized. The discretization of the pressure field is obtained through a Finite Element formulation. As for the classical FEM, the structural domain, where the pressure is applied, is discretized using Finite Elements. Within the element, the

pressure distribution is interpolated from the nodal values of the pressure using shape functions. Mathematically, it can be formulated as follows:

$$p^e(x, y) = \sum_{i=1}^n N_i^e(x, y) p_i^e \quad (7.4)$$

where $p^e(x, y)$ is the pressure distribution over the element's x-y plane, $N_i^e(x, y)$ are the shape functions dependent from the chosen element's formulation, n is the number of nodes of the element and p_i^e are the nodal values of the pressure.

If the domain is discretized with a mesh of pressure elements, the global $N_i(x, y)$ shape functions, related to the global m_p nodes of the pressure mesh, can be computed by means of the assembly procedure adopted by the standard FEM. Consequently, the pressure distribution over the entire domain, $p(x, y)$, can be expressed as follows:

$$p(x, y) = \sum_{i=1}^{m_p} N_i(x, y) p_i \quad (7.5)$$

where p_i is the nodal value in the i-th node of the mesh.

Therefore, in analogy with the classical structural FEM problem, in this case, the degrees of freedom (DOFs) of the system, that represents the unknowns of the problem, are the nodal values of the pressure, p_i . Once these values are computed, the full pressure distribution can be derived using the interpolation through the selected shape functions.

The nodal values of the pressure can be computed following the same scheme defined for the concentrated forces. In the same hypothesis of linear elasticity, m_s strain components can be expressed as a linear combination of the strains induced by the m_p nodal pressures, p_i :

$$\{\varepsilon^m\}_{m_s \times 1} = [s]_{m_s \times m_p} \{p\}_{m_p \times 1} \quad (7.6)$$

The matrix $[s]_{m_s \times m_p}$ can be easily computed through the iterative resolution of a direct FE problem. The i-th column of the matrix is computed by imposing that $p_i = 1$ and $p_k = 0$ ($k \neq i$) in Eq. 7.5. The resulting pressure field is then applied to a FE model of the structure and the desired strain components are measured. Iterating the procedure to the m_p nodal pressures, allows the computation of the entire matrix. The Pseudo-inversion of Eq. 7.6 leads to the formulation of the unknown nodal values of the pressure that fit the measured strains:

$$\{p\} = [s^+] \{\varepsilon^m\} \quad (7.7)$$

These nodal values of the pressure can then be used to compute the pressure distribution through the FE interpolation expressed in Eq. 7.5.

7.1.2 Shape sensing (2nd step)

The second step of the proposed procedure involves the shape sensing, i.e. the reconstruction of the displacement field. The 2-step procedure has been inspired by the standard direct structural analysis. The direct structural problem aims to compute the displacement field, and from it the stress and strain field of a structure, when the structure's geometry, material properties, constraints and external loads are known. The direct problem is usually solved by the application of the FEM. It is mathematically well-conditioned, that is, small perturbations in the inputs produce small perturbations in the outputs [107]. On the other hand, the shape sensing and the external loads identification are inverse problems and are often more difficult to solve. They are mathematically ill-posed and small perturbations in the inputs generally produce greater perturbations in the outputs [107]. In the previous section, a solution for the loads identification inverse problem has been presented. The objective of the proposed method is to use the results of the loads identification for the formulation of the shape sensing problem so that it could be reduced to a direct structural problem. By doing this, the resolution of only one inverse problem leads to the easy resolution of the other.

As already mentioned, the load identification step requires the design of a detailed FE model of the structure. Therefore, if this model is available and the loads can be identified with the described method, they can also be applied to the FE model of the structure and a direct FEM analysis performed. This method allows the integration of the two structural health monitoring tools in a unique procedure, as illustrated in the scheme in Fig. 7.1, where the first step is depicted in green colour and the second step is depicted in orange colour. The second step allows the computation of the displacement field and of the stress and strain fields of the whole structure.

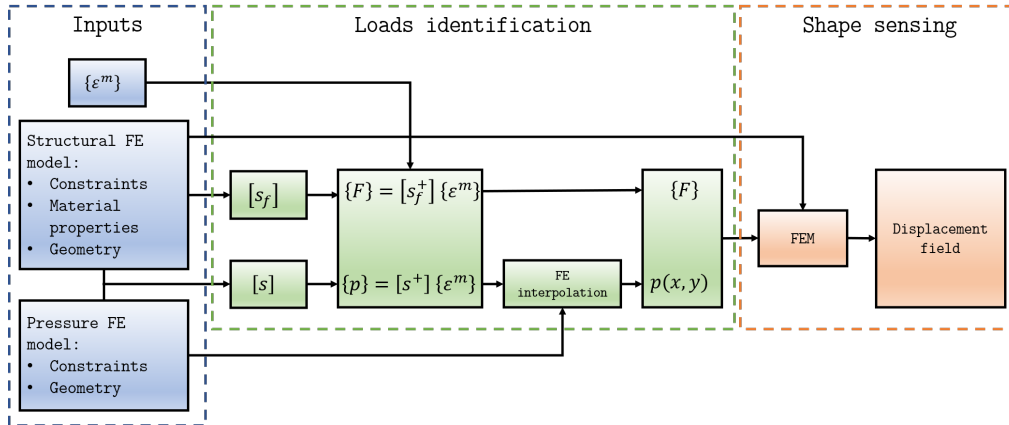


Figure 7.1: 2-step integrated approach - The inputs of the process are highlighted in blue. The load identification step is highlighted in green and the shape sensing step is highlighted in orange.

Although the procedure can seem complex and laborious, it is not. In fact, once the strain sensors configuration is established, the computationally intensive procedure is only represented by the preliminary computation of the $[s]$ or $[s_f]$ matrix, that requires the iterative solution of a FEM problem. Once this matrix is populated, and the FEM model of the structure established, the matrix of the coefficients of influence and the stiffness matrix ($[K]$) of the model need to be inverted or pseudo-inverted only once and don't need to be updated if the values of the measured strains are modified. Therefore, every different vector of measured strains is simply multiplied by $[s^+]$ or $[s_f^+]$ to derive $\{p\}$ or $\{F\}$, that are, in turn, multiplied by $[K^{-1}]$ to compute the displacements. In practice, the whole procedure of computing the loads and the displacements is reduced to two simple and fast to compute matrices multiplications.

7.2 Application on an aluminium wing box

The 2-step procedure is applied on the reconstruction of the external loads and the deformed shape of an aluminium swept wing box. This application is performed numerically. The study includes the analysis of two different load cases, one constituted by concentrated forces and one constituted by a pressure distribution. For the first time, quadrilateral elements are introduced for the discretization of this distribution. The results of the shape sensing part of the method are compared with the results from a iFEM analysis. The study is completed with the exploration of the influence of the strain configuration and of the effect of strain measurement error on the performance of the method.

7.2.1 The wing box

The structure object of this investigation has been inspired by and represent a preliminary study for an experimental campaign that will be presented in the next chapter. In fact, the wing box's geometry and material characteristics have been chosen according to considerations guided by the experiment conceptualization, considering the already available components and testing facilities.

The wing box is illustrated in Figure 7.2. The structure is composed of two swept panels and two spars. The panels are connected to the spars by four L-stiffeners and are reinforced with two L-stiffeners, one per each panel. The box is divided into seven bays by seven ribs. The spars and the stiffeners' sections are constant along the wing span, whereas the panels are swept. The selected configuration considers clamped boundary conditions at the root section.

The components of the structures are made of two different aluminium alloys, whose mechanical properties are reported in Table 7.1. The panels, the spars and the ribs are made of the 7075 alloy, whereas the stiffeners are made of the 6060

alloy.

Alloy	E [GPa]	ν	G [GPa]
6060	66	0.33	24.8
7075	72	0.32	27.2

Table 7.1: Aluminium alloys mechanical properties.

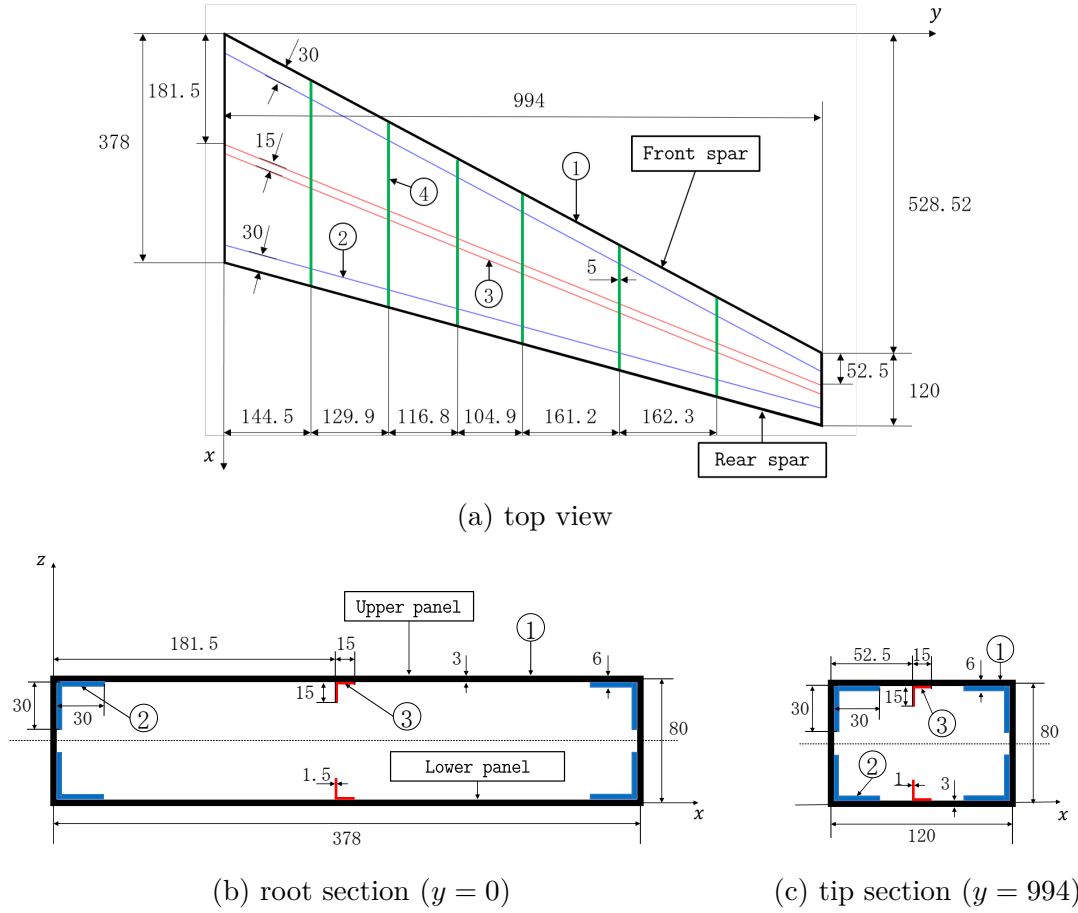


Figure 7.2: Wing box geometry - In the figure, the panel and the spars are indicated by ①, the stiffeners that connect the skin panels to the spars are indicated by ②, the stringers are indicated by ③ and the ribs are indicated by ④. All dimensions are expressed in [mm].

7.2.2 Load cases

Two load cases and the relative deformed shapes are considered for the described wing structure. The two different discretization approaches highlighted for the

load identification method (Section 7.1.1) are explored by these two load cases. Therefore a pressure distribution and a 2D distributed load are examined.

The Load case 1 considers a pressure distribution applied on the upper panel of the box and it is representative of an aerodynamic pressure distribution. The distribution is displayed in Figure 7.3. The distribution is a multiplication of a cubic polynomial function of x and a quadratic one of y . The structural domain, where the distribution is defined, and the relative x and y coordinates are illustrated in Figure 7.2a. The chosen distribution, along the wing span direction, has a maximum at the root section and vanishes at the tip section. Along the chord direction, it vanishes at the leading and trailing edge and has a maximum at one-third of the chord. As a consequence, mathematically, the polynomial function of y is constructed imposing that the function vanishes at the tip section, it has a maximum at the root section and this maximum is equal to 1. The cubic polynomial of x is defined by imposing that it vanishes at the trailing and leading edges, it has a maximum at one third of the chord and this maximum is equal to 1. The detailed mathematical expression of the pressure distribution $p(x, y)$ and of the aforementioned conditions can be found in Appendix B. The deformed shape of the wing box, when subjected to this pressure distribution, is reported in Figure 7.4.

The Load case 2 is intended to simulate the presence of a pod on the wing tip. This condition is simulated through a distributed load along the chord applied on the tip rib. The load has a constant value of of 100 N/mm . The discretization of this load is obtained through a set of concentrated forces applied in the nodes of the FE mesh. This discretization is shown in Figure 7.5. These concentrated forces are the unknowns of the load identification problem for this second load case and their values are reported in Table 7.2. The deformed shape induced by this load case and investigated by the second step of the procedure is shown in Figure 7.6.

To summarize, the two load cases, object of the load identification in the next sections, are summarized in Table 7.2 and the deformed shapes, object of the shape sensing investigation, are reported in Figures 7.4 and 7.6.

Load Case	Loads	Constraints
Load case 1	$p(x, y) = (a_x x^3 + b_x x^2 + c_x x + d_x) \cdot (a_y y^2 + b_y y + c_y)$	Clamped root section
Load case 2	$F_1 = F_{19} = 749N$; $F_2 = F_{18} = 1,499N$; $F_3 = F_{17} = 937N$; $F_{4-8} = F_{12-16} = 375N$; $F_9 = F_{11} = 562N$; $F_{10} = 749N$	Clamped root section

Table 7.2: Load Cases.

7.2.3 Numerical models

The application of the 2-step procedure requires the definition of two models. A detailed and refined FE model of the entire structure to compute the matrices for the application of the load identification step is required. Considering the

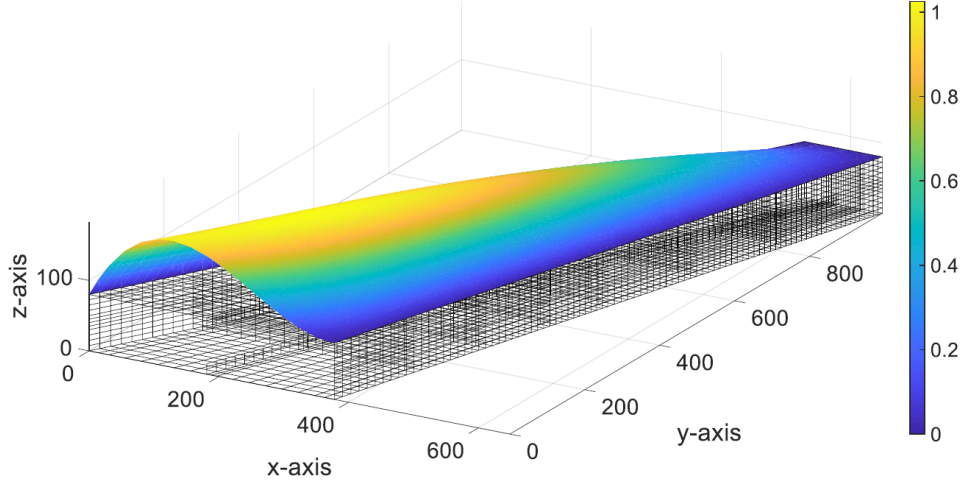


Figure 7.3: Load Case 1 - The figure shows the pressure distribution applied on the refined FE model of the wing box. The pressure is expressed in $[N/mm^2]$

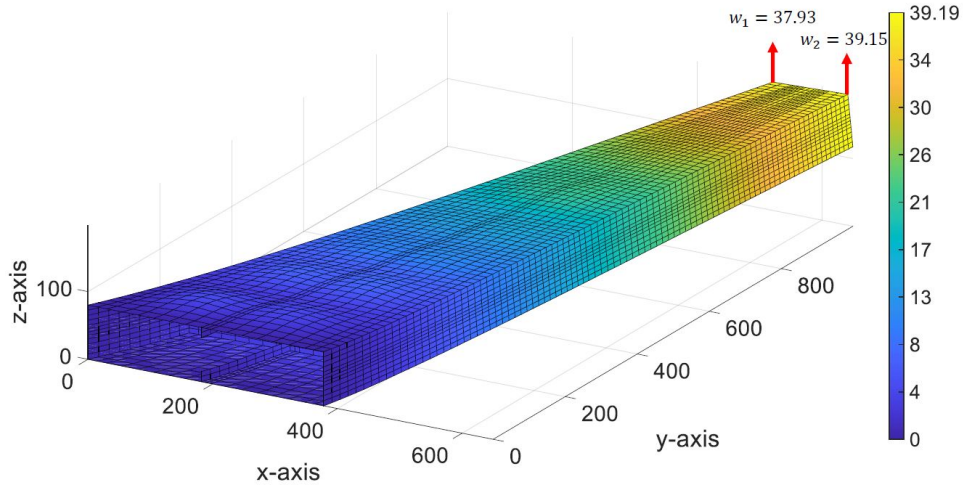


Figure 7.4: Deformed shape for the Load Case 1 - The figure shows the refined Fe model of the wing box deformed under the pressure distribution of the Load Case 1. The color bar refers to the magnitude (in mm) of the resultant displacements.

numerical nature of this study, this model is also used as a reference to model the real behaviour of wing box. On the other hand, a coarser FE model, limited to the domain where the pressure distribution is defined, is needed for the discretization of the distribution.

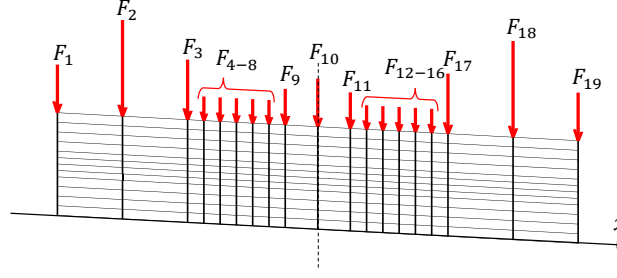


Figure 7.5: Load Case 2 - The figure shows the distributed load applied on the wing tip section, discretized to nodal forces according to the FEM. The value of the nodal forces are reported in Table 7.2.

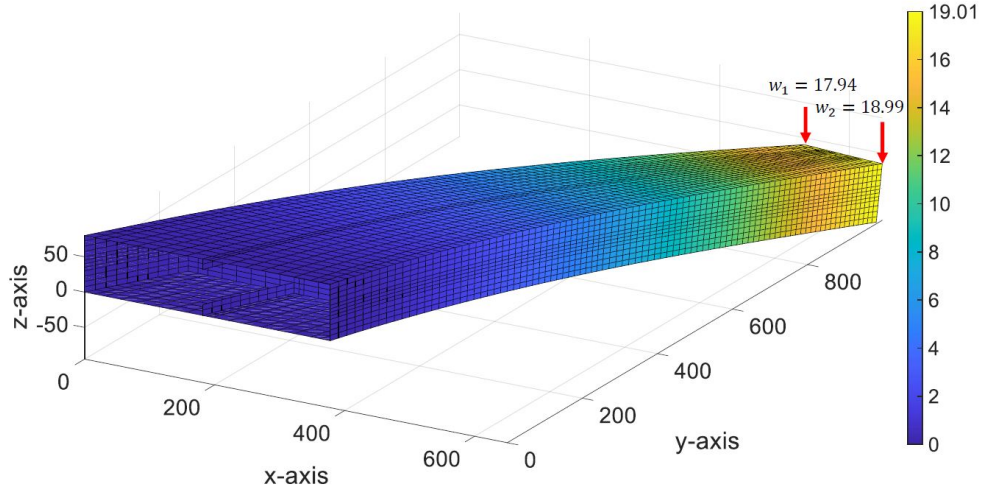
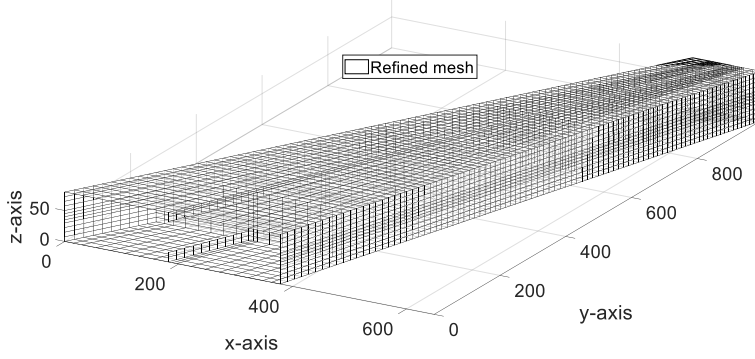


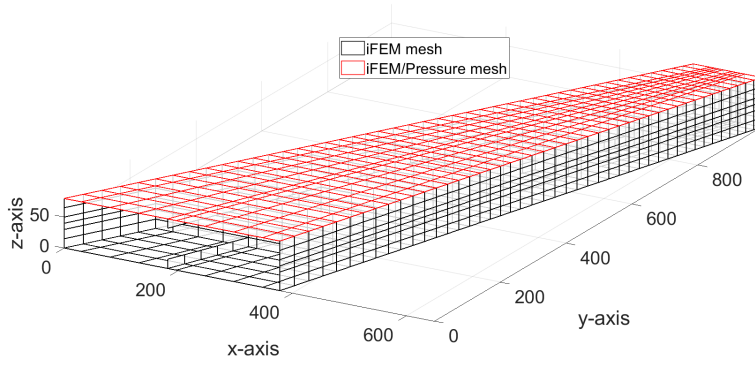
Figure 7.6: Deformed shape for the Load Case 2 - The figure shows the refined FE model of the wing box deformed under the distributed load of the Load Case 2. The color bar refers to the magnitude (in mm) of the resultant displacements.

The refined model is the one that appears in the Figures 7.3, 7.4 and 7.6. It is presented in details in Figure 7.7a. It is constituted of 9,792 QUAD4 NASTRAN® elements and of 7,129 nodes.

The pressure distribution for Load case 1 is defined on the top panel only. As a consequence, the pressure mesh is restricted to this domain. Differently from the previous application [83], where triangular elements were selected, in this work, for the first time, the pressure field is discretized with quadrilateral elements. Within each quadrilateral element the pressure is interpolated from its nodal values with the standard bilinear shape functions. Consequently, in Eq 7.4 $n = 4$ and $N_i^e =$



(a) Refined mesh



(b) iFEM/Pressure mesh

Figure 7.7: Models - In (a), the refined mesh is presented. In (b), the elements whose contours are shown in red belong to the iFEM mesh and the pressure mesh. The elements whose contours are shown in black belong to the iFEM mesh only

$(1 + \chi_i \chi)(1 + \eta_i \eta)$, where χ and η are the quadrilateral isoparametric coordinates and the subscript i denotes the computation relative to the i -th node. The pressure mesh is therefore composed of 405 quadrilateral elements and of 405 nodes and it is presented in Figure 7.7b.

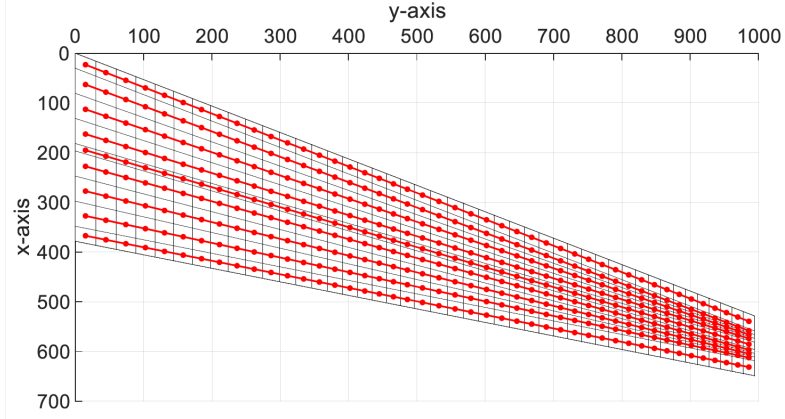
The application of the iFEM, used as a term of comparison to assess the accuracy of the shape sensing part of the procedure, requires the definition of a third mesh. To simplify this task, this mesh is developed starting from the discretization of the upper panel adopted for the pressure mesh. The model is composed of 1818 iQS4

formulated as described in Paragraph 3.3.2. This model is reported in Figure 7.7b, together with the pressure mesh. Since the formulation of the inverse quad elements prescribes the location of the strain sensors in the centroid of the elements, the mesh is designed so that the centroid of the inverse elements have a corresponding node in the refined mesh. This allows the easy association of the strains from the high-fidelity model to the iFEM elements.

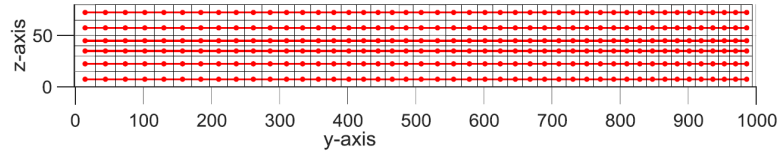
7.2.4 Matrices computations

Once the models are defined, the next step is the computation of the matrices necessary for the resolution of the load identification problem. To compute the $[s]$ and $[s_f]$ matrices, relative to the two load cases, it is necessary to identify all the strain components that can be used for the reconstructions of the discretized loads. Afterwards, it is possible to select a reduced set of sensors, among all the identified components, by selecting the row of the matrices correspondent to the selected components. The possible sensors' configurations, chosen for this application, have been inspired by the use of strain sensing systems based on optical fibres. This technology is in continuous development and it is establishing itself as one of the most effective for SHM applications. As a consequence, the eligible strain sensors are located on lines running from the root section to the tip section of the box, along the wing span. To allow the application of the iFEM, these lines pass through the centroid of the inverse elements. From these locations only the strain component along the lines' direction are considered, according to the sensing possibilities of the optical-fiber-based sensors. The sensing lines are distributed over the box as illustrated in Figure 7.8. As it can be observed, 9 sensing line for each panel and 6 for each spar are considered, accounting for a total of 30 lines. For each line 45 location are selected. A total of 1,350 strain components along the sensing lines represent the possible strain components. All the considered strain components are measured on the external surface of the box. This implies that, for the iFEM formulation, each measured strain is considered constant through the thickness of the plate.

Once the set of measurable strains is defined it is possible to populate the $[s]$ and $[s_f]$ matrices. The i -th column of the $[s]$ matrix is computed by imposing that $p_i = 1$ and computing the resulting pressure field through Eq. 7.5. This pressure field is then applied on the refined model and the induced 1,350 selected strains are computed and used to populate the i -th column of the matrix. To apply this pressure to the refined model it is necessary to compute the pressure values at the points, within the pressure elements, where nodes of the refined FE model are located. This can be done by mapping these nodes to the elements' natural coordinates [108] and by computing the values of the pressures at these locations. The iteration of this process to the 460 nodes of the pressure mesh allows the computation of the entire $[s]_{1,350 \times 460}$ matrix. The same procedure is adopted for



(a) Upper/Lower panels



(b) Front/Rear spar

Figure 7.8: Sensing lines - In the figure, the sensing lines and the sensing locations within each line are showed only for one panel and one spar. The same configurations should be considered for the other components.

the determination of the $[s_f]$ matrix. Although, in this case, the values of the i -th concentrated load do not need to be expanded through the shape functions and can be simply applied to the refined mesh in order to compute the 1,350 strain components. For the second load case, the iterative process needs to be extended to all the 19 concentrated forces to obtain the $[s_f]_{1,350 \times 19}$ matrix.

7.2.5 Sensors optimization

In this work, the influence of the sensors' configuration on the load identification and shape sensing steps is considered. This study is performed considering ten different sensors' configurations for each load case. Each configuration is obtained selecting an increasing number of lines among the candidate lines described in Figure 7.8. In practice, the first configuration considers a subset of 1 line, the second a subset of 2 lines and so on. As already mentioned, in the framework of the load identification, the selection of a subset of strain components is translated into considering only the correspondent rows of the $[s]/[s_f]$ matrices and discarding the others.

Each configuration is optimized so that the accuracy of the external load identification is the best that can be obtained with the correspondent finite number of sensing lines. More in details, the optimization is obtained by means of the Genetic Algorithm described in Section 4.2.2, whose objective is to minimize the root mean square percent error ($\%ERMS$) between the computed nodal value of the load and the actually applied one. The expression of the $\%ERMS$ for a generic quantity, g , is:

$$\%ERMS_g = 100 \times \sqrt{\frac{1}{k} \sum_{i=1}^k \left(\frac{g_i - g_i^{ref}}{g_{max}^{ref}} \right)^2} \quad (7.8)$$

where k is the number of nodes where the quantity is computed, g_i is the reconstructed quantity in the i -th node, g_i^{ref} is the reference value of the quantity in the i -th node and g_{max}^{ref} is the maximum value of the reference quantity. For the optimization of Load case 1 $g = p$, on the other hand, for Load case 2, $g = F$.

To summarize, the optimisation process generates 10 optimal sensors' configurations for each load case and, consequently, 10 sets of identified loads. These loads are then applied to the refined FEM model to perform the second step of the analysis and compute the displacements of the structure for the 10 configurations.

The iFEM, used to compare the results of the shape sensing, is also optimised in terms of sensors' configuration. The exact same approach is adopted to find the 10 best sensor's configurations for the method. The objective of the optimisation process for the 10 configurations is, in this case, the minimization of the $\%ERMS_w$, where w represents the transverse displacement along the z direction (Figure 7.7b) and it is selected because it is prevalent with respect to the displacements in the other directions. This parameter is also used to evaluate the shape sensing accuracy of the 2-step approach.

7.2.6 From Tria to Quad

Before the assessment of the accuracy of the 2-step approach in the solution of the double task and before the study on the influence of the sensors' configuration and of the effect of measurement error, a preliminary study is performed in order to validate the improvements in the pressure distribution identification introduced by the discretization of the pressure field with the newly proposed quadrilateral elements. To perform this task, the reconstruction of the pressure field from Load case 1, using the selected quad mesh, is compared with the one obtained with a set of triangular meshes. Four triangular meshes, with varying characteristics in terms of the number of DOFs and of the regularity of the mesh, are considered. The **Tria 1** mesh, showed in Figure 7.9a, has been obtained splitting the elements of the quad mesh along one diagonal and, consequently, presents the same number of nodes and unknown nodal values of the pressure (460) of the quad mesh. The **Tria 2** mesh (Figure 7.9b), on the other hand, has been constructed splitting the

quadrilateral elements of a different mesh along both diagonals. It has a slightly lower number of nodes (434). Finally, the **Tria 3** (Figure 7.9c) and **Tria 4** (Figure 7.9d) meshes are obtained by meshing the structural domain with a varying number of triangular elements. For this application the whole set of strain measurements

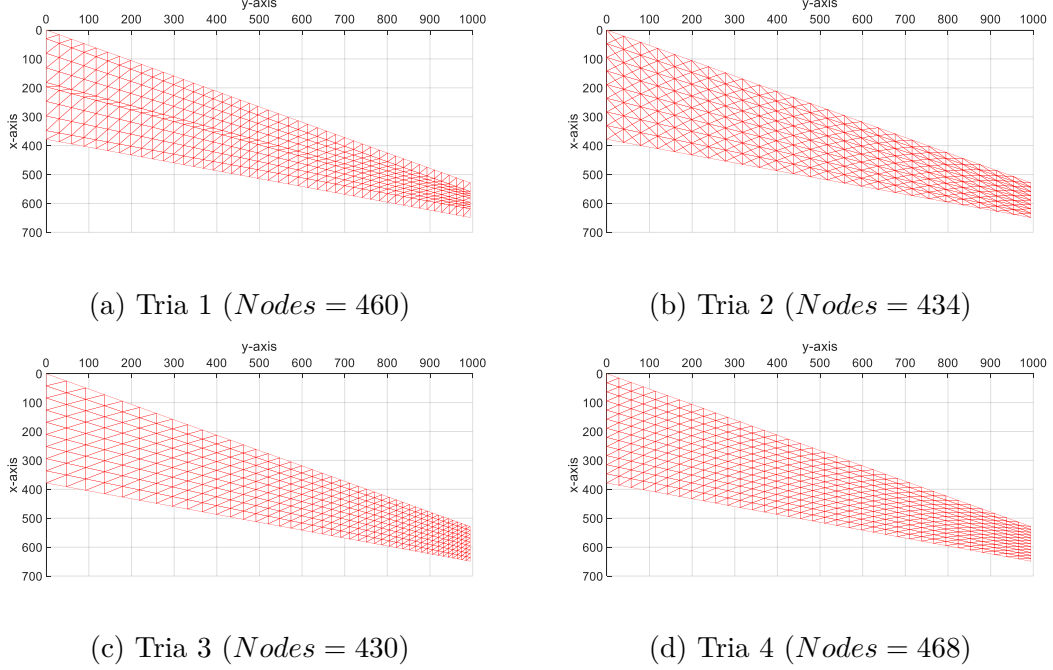


Figure 7.9: Triangular meshes - In the figure are illustrated the four triangular meshes used to compare the accuracy of the newly introduced quad element.

identified in Section 7.2.4 is considered.

In table 7.3 the results of this preliminary study are reported. The accuracy is assessed through the $\%ERMS_p$ parameter.

Mesh	#nodes	$\%ERMS_p$	$\%\text{Diff}$
Quad	460	0.732	-
Tria 1	460	0.768	+4.9%
Tria 2	434	2.564	+250.3%
Tria 3	430	0.984	+34.4%
Tria 4	464	1.021	+39.5%

Table 7.3: Quadrilateral and triangular meshes comparison .

The values of this parameter show that the quadrilateral mesh is able to reduce the error in the identification of the nodal values of the pressure with respect to all the considered triangular meshes. The reduction in the error is of 4.9% with respect

to the mesh presenting the same number of nodes and, therefore, the same number of DOFs. Moreover, the adoption of different meshing schemes for the triangular elements increases the advantage in the accuracy in favour of the quad mesh.

7.2.7 Results

In this section, the results of the sensors' optimisation for the two load cases are presented. The results include the analysis of the load identification step and of the shape sensing one for the 2-step method. The results of the last step are also compared with the displacements' reconstruction of the optimised iFEM. This application considers deterministic values of the strain measurements, not affected by any measurement error. These effects will be considered afterwards, in Section 7.2.8.

Load case 1

The results for the identification of the Load case 1 in terms of the $\%ERMS_p$ for the optimised 10 sensors' configurations are reported in Figure 7.10. Using only one sensing line produces an error of 16.05% in the identification of the nodal values of the pressure. This error rapidly decreases when increasing the number of selected lines from 2 to 7 where it reaches a value of 1.65%. Adding more sensing lines does not provide a significant increment in the accuracy. In fact, the best results, obtained with 10 sensing lines, is slightly better than the one obtained with 7, giving an $\%ERMS_p$ value of 1.24%.

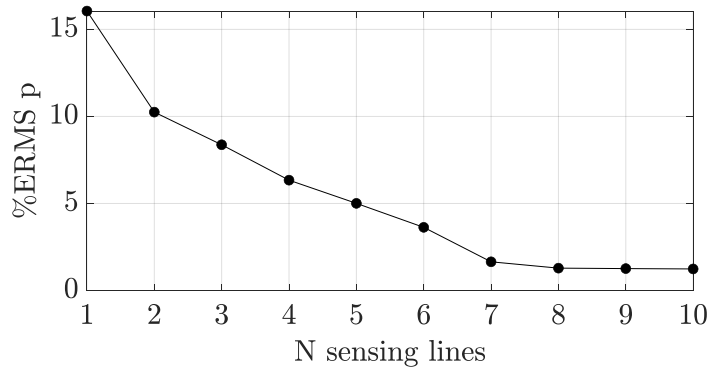


Figure 7.10: Pressure field reconstruction of Load Case 1 - The $\%ERMS_p$ for the best sensors configuration, with the number of sensing lines varying from 1 to 10, are reported.

The pressure distributions reconstructed from the optimized sets of strain sensors are reported for the configurations with 1 and 7 sensing lines in the Figure

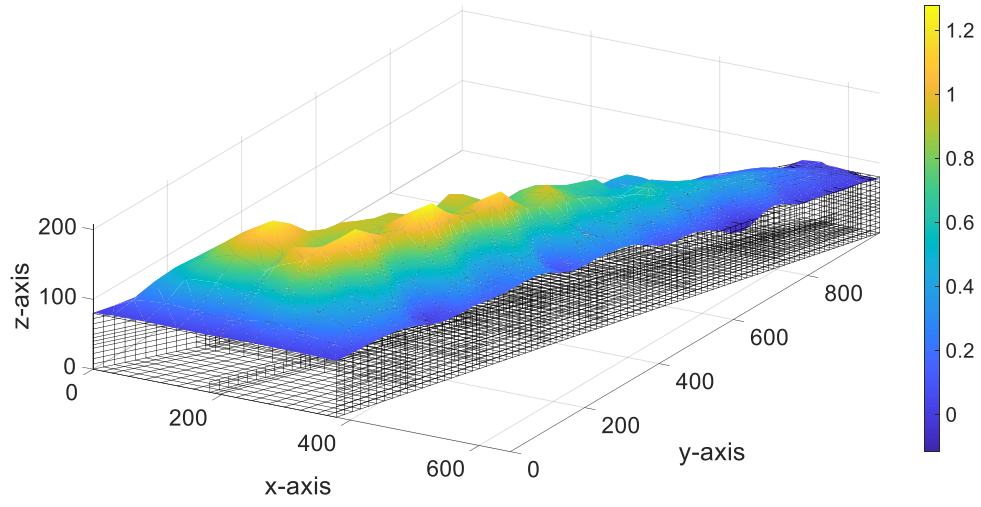
7.11. A more detailed analysis of the reconstructions is reported in Figure 7.12. The figure shows the identified values of the nodal pressures along the wing span for the sensors configurations with 1, 3, 5 and 7 sensing lines. The reconstructions are obtained along the line of nodes, from the pressure mesh, closest to points located at one-third of the chords. The analysis of the Figures 7.11 and 7.12 further highlights the loss of accuracy caused by the reduction in the strain information provided to the method.

The shape sensing is obtained applying these reconstructed pressure fields to the refined FE model and by performing a standard FEM analysis. The $\%ERMS_w$ obtained for the 10 considered configurations are shown in Figure 7.13. The errors are reported along with the ones derived with the iFEM for comparison. The comparison points out the extreme level of accuracy of the two-step method. Although the two methods show the same trend with respect to the variation in the number of sensing lines, the two-step method is able to reach an $\%ERMS_w$ that is, in the worst case (1 sensing line), equal to 0.19% and in the best one (10 sensing lines) $2.64 \times 10^{-4}\%$. On the other hand, the iFEM's error is comprised between the best value of 6.61% (10 sensing lines) and the worst of 38.80% (1 sensing line).

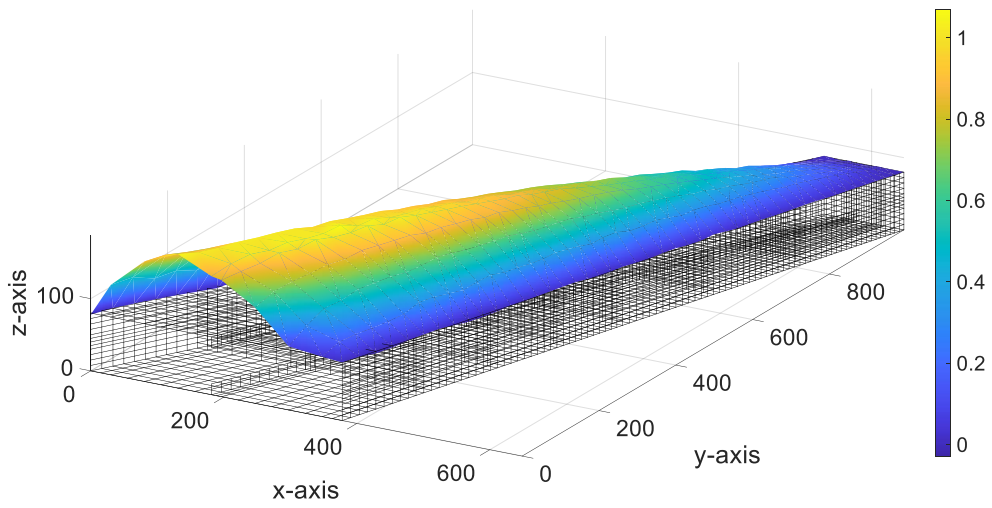
In addition, these results are supported by Figure 7.14. The figure shows the reconstructed and reference deflections along the wing span, on the same line of nodes considered in Figure 7.12. The deflections are reported for the best iFEM configuration and for the 2-step method considering 1, 3, 5 and 7 sensing lines. The deflections of the two-step method are superimposed to the reference one for every sensors' configuration and are significantly more accurate than the iFEM one. Only the configuration with 1 sensing line presents a slight deviation from the reference close to the root section of the wing.

It is important to notice that the 2-step approach is capable of extremely accurate reconstructions of the transverse displacements, even when the identification of the pressure field is not accurate. In fact, comparing Figure 7.3 and 7.11a, it is shown that the configuration with only one sensing line produces an identified pressure field that is highly inaccurate. Nevertheless, the method is able of an accurate shape sensing also with only one sensing line. This aspect will be examined more in deep when analysing the results of the second load case.

Finally, the two best sensors' configurations for the 2-step method, using 7 sensing lines, and for the iFEM, using 10 sensing lines, are reported in Figure 7.15. The optimisation process selected only lines on the spars for the iFEM, whereas only sensors on the panels for the 2-step method.



(a) 1 sensing line



(b) 7 sensing lines

Figure 7.11: Pressure field reconstructions for Load Case 1.

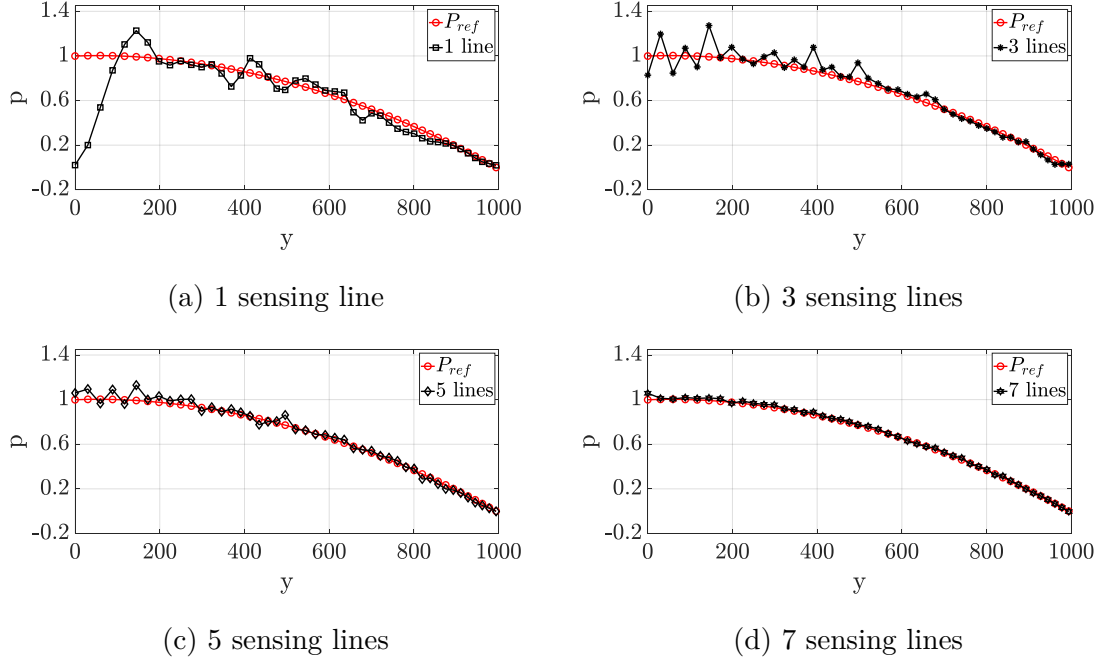


Figure 7.12: Pressure reconstruction along the wing span for Load Case 1.

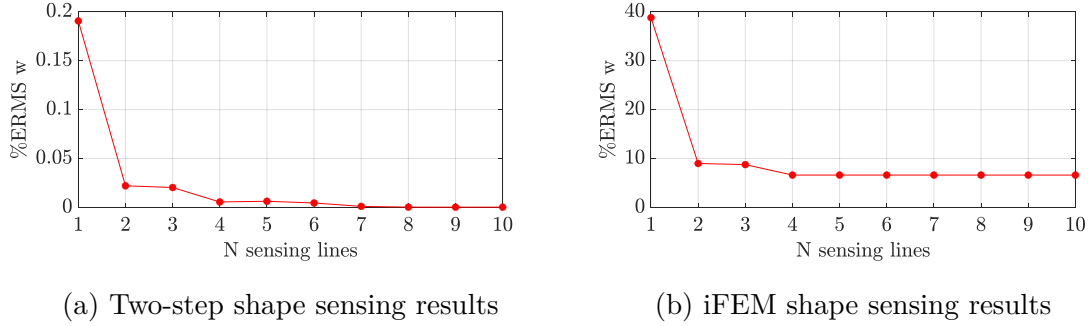


Figure 7.13: Shape sensing for Load Case 1 - The $\%ERMS_w$ for the best sensors configuration, with the number of sensing lines varying from 1 to 10, are reported for the two-step method (a) and the iFEM (b).

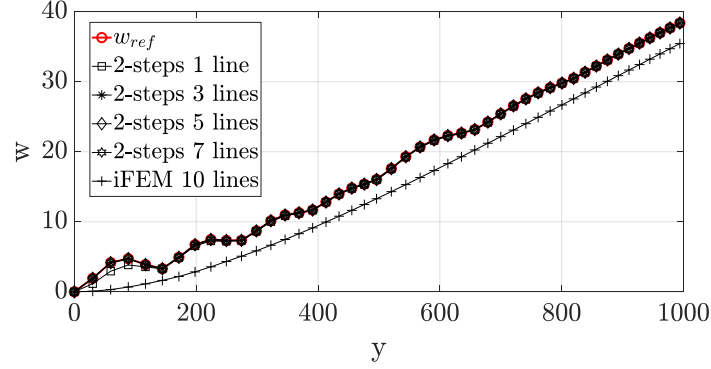
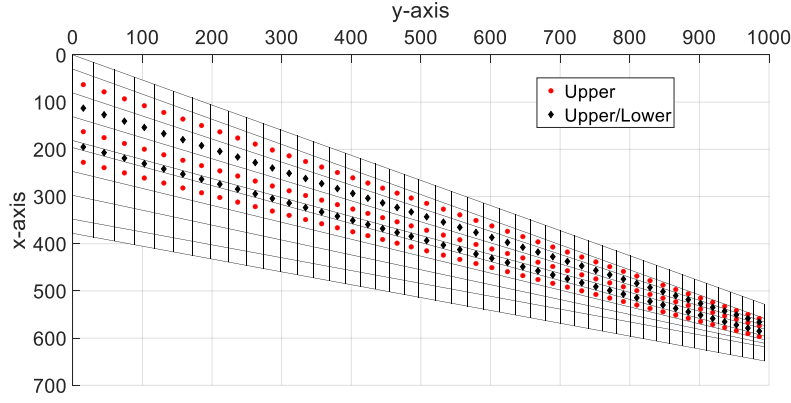
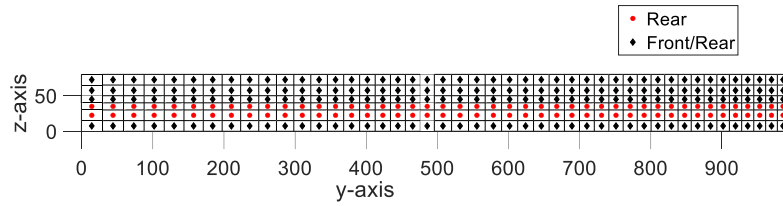


Figure 7.14: Vertical deflection along the wing span for Load Case 1.



(a) two-step method.



(b) iFEM

Figure 7.15: Optimal sensors configurations for Load case 1 - The figures show the optimal sensors configurations for the two-step method (a) and the iFEM (b). In the legends, Upper and Lower refer to sensors located on the upper or lower panel, whereas Upper/lower refers to sensors located on both panels. Front and Rear refers to sensors that are located on the front or the rear spar, whereas Front/Rear refers to sensors located on both spars.

Load case 2

The identification of Load case 2 generates the results summarized in Figure 7.16. The $\%ERMS_F$ has a worst maximum value of 50.10%, when only one line of sensors is available. The selection of 2 sensing lines does not increase the accuracy of the reconstruction. Therefore, the best configuration with only one line is still considered the best also for this configuration. On the other hand, including more lines in the analysis, from 3 to 7, continuously improves the accuracy of the method. The configuration with 7 sensing lines produces highly accurate identifications of the concentrated forces, showing a value of the error that is $\%ERMS_F = 0.49\%$. These relevant accuracy is further incremented for the configurations with 8 ($\%ERMS_f = 0.11\%$), 9 ($\%ERMS_f = 0.060\%$) and 10 ($\%ERMS_f = 0.034\%$) lines of sensors.

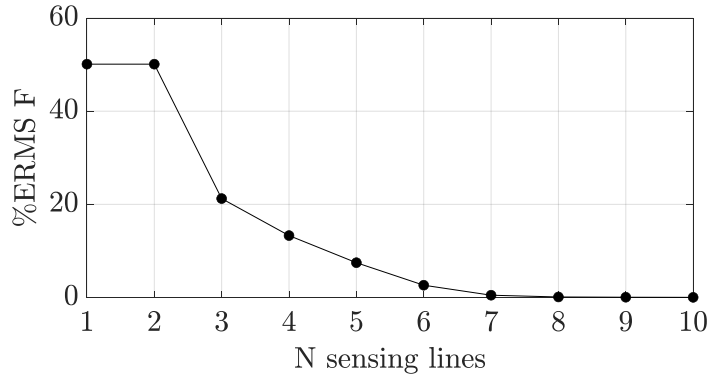


Figure 7.16: Nodal forces identification of Load Case 2 - The $\%ERMS_F$ for the best sensors configuration, with the number of sensing lines varying from 1 to 10, are reported.

The identified nodal values of the force, that generated the above mentioned errors, for the configurations with 1, 3, 5 and 7 sensing lines, along the wing tip chord, are reported in Figure 7.17.

The application of these identified loads to the refined model of the wing box allows the shape sensing of the structure. The results, in terms of the $\%ERMS_w$ and the number of optimized sensing lines, are illustrated in Figure 7.18a. Also in this case, they are compared with the best results from the 10 configurations obtained with the iFEM. For this load case, the iFEM shows a better accuracy. Nevertheless, the 2-step procedure is still consistently more accurate. The minimum value of the $\%ERMS_w$ for the iFEM is generated by the configuration with 4 sensing lines. This minimum error of 2.75% is not modified by adding more sensors and thus, the 4 lines configuration is considered the best one for this shape sensing method. The iFEM shows good reconstructions also for the configuration with only 3 and 4 sensing lines ($\%ERMS_w = 4.10$). On the other hand, for the 1 line configuration,

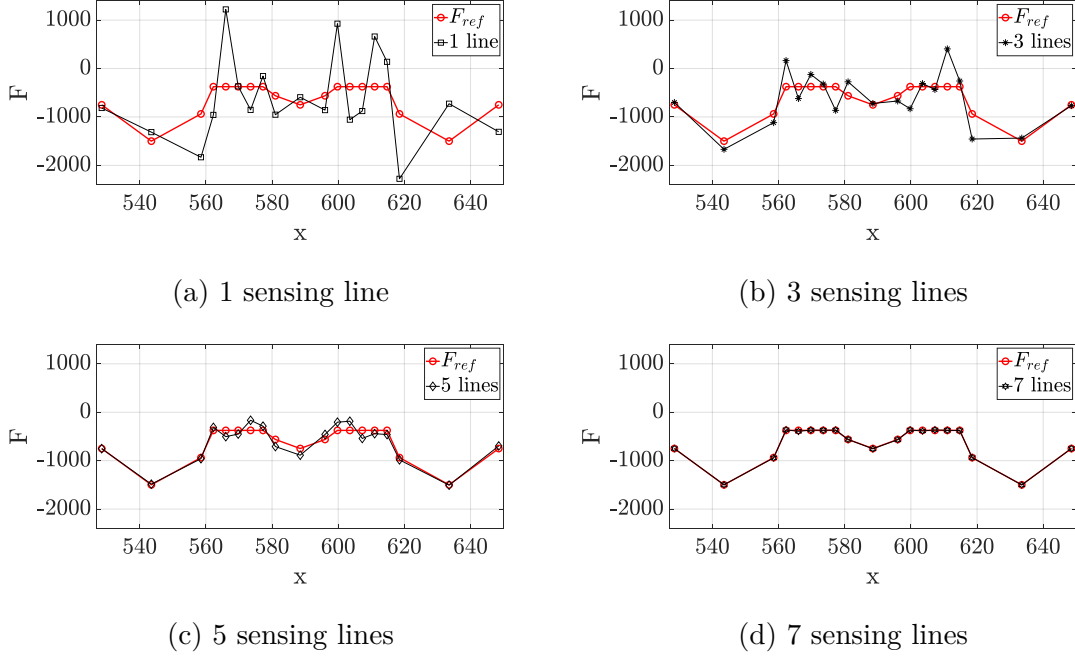


Figure 7.17: Nodal forces identification along the wing tip chord for Load Case 2.

the error rises to reach the value of 31.5%. The two-step technique sees a constant decreasing in the quality of the shape sensing with the decrease in the number of sensing lines too. Nevertheless, the values of the $\%ERMS_w$ are comprised between $4.13 \times 10^{-6}\%$, when 10 line are selected, and 0.015%, when 1 line is selected, thus resulting in an impressive accuracy for all the sensors configurations. The same

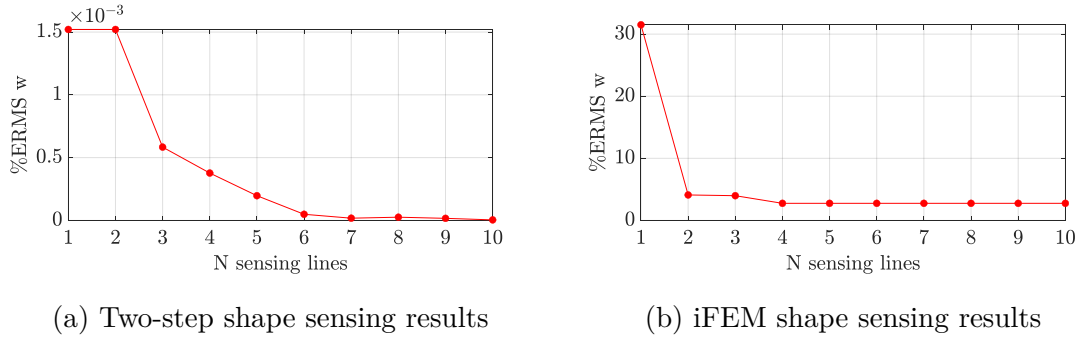


Figure 7.18: Shape sensing for Load Case 2 - The $\%ERMS_w$ for the best sensors configuration, with the number of sensing lines varying from 1 to 10, are reported for the two-step method (a) and the iFEM (b).

considerations can be inferred by looking at Figure 7.19. The graph shows the reconstructed and reference transverse deflections on the wing tip along the chord.

There is no visible deviation of the two-step solutions from the reference one for the reported sensors configurations. On the other hand, the best iFEM results, using 4 sensing lines, show an almost constant offset in the reconstruction of the vertical displacements along the chord.

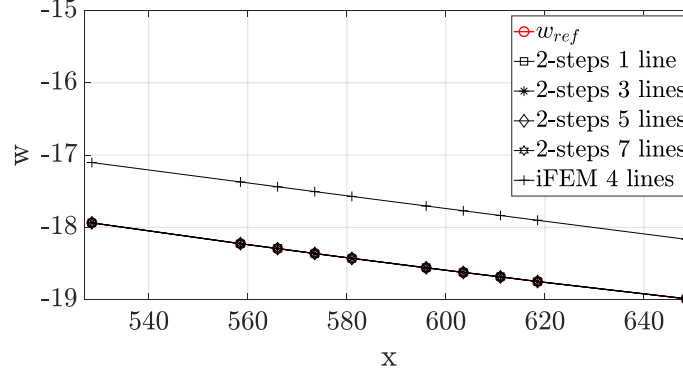
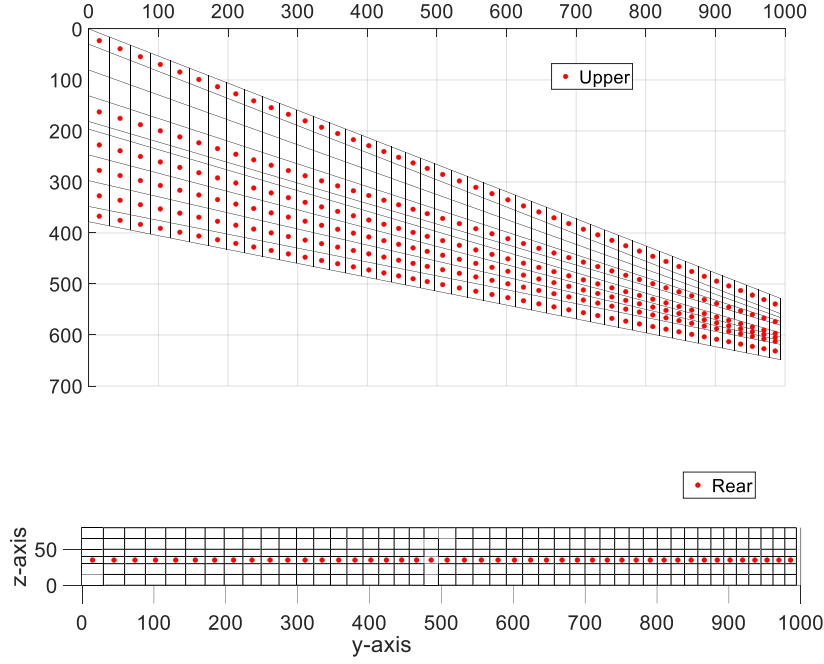


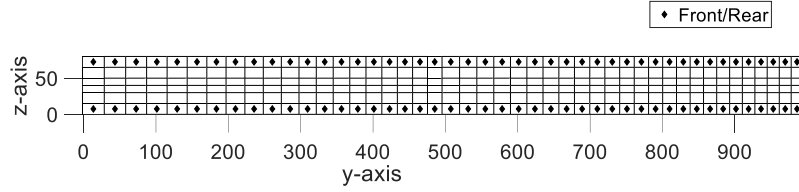
Figure 7.19: Vertical deflection along the wing tip chord for Load Case 2.

The best sensors' configurations for the two considered shape sensing methods are reported in Figure 7.20. The sensing schemes are reported for the 7 lines configuration for the 2-step method and for the 4 lines configurations for the iFEM. Also in this case the optimisation process selected sensors only on the spars for the iFEM. Differently, the best configuration for the 2-step approach comprises sensing lines mainly on the two panels, but it also includes one sensing line on the rear spar.

The configuration with only one sensing line deserves more attention, also to better explain the results from Load case 1. The identified forces and the actually applied ones for this configuration are reported in Table 7.4. The values of the $\%ERMS_F$ and also the comparison of the nodal forces highlights a relevant discrepancy of the reconstructions. Nevertheless, the resultants, R_z , of the two systems of loads, the reference and the reconstructed, show almost no discrepancy. Moreover, the computation of the resultant moment with respect to the centre of gravity of the tip section, M_z^G , also shows the same result for the two systems of loads. This results can explain the extreme accuracy of the novel shape sensing method for both the load cases, when few strain information is available and the external loads identification is not effective. The method is able to identify an equivalent system of loads that, although different from the applied one, induces the same deformation on the structure. In the end, it seems that the method, when few inputs are available, is able to find one of the infinite systems of loads that can generate the deformed shape, whose induced strains are used as inputs for the method.



(a) two-step method.



(b) iFEM

Figure 7.20: Optimal sensors configurations for Load case 2 - The figures show the optimal sensors configurations for the two-step method (a) and the iFEM (b). In the legends, Upper and Lower refer to sensors located on the upper or lower panel, whereas Upper/lower refers to sensors located on both panels. Front and Rear refers to sensors that are located on the front or the rear spar, whereas Front/Rear refers to sensors located on both spars.

	Loads	$\%ERMS_F$	R_z	M_y^G
Ref	$F_1 = F_{19} = 749N$; $F_2 = F_{18} = 1,499N$; $F_3 = F_{17} = 937N$; $F_{4-8} = F_{12-16} = 375N$; $F_9 = F_{11} = 562N$; $F_{10} = 749N$	-	11,993N	0N · mm
Rec	$F_1 = 814N$; $F_2 = 1,313N$; $F_3 = 1,832N$; $F_4 = 957N$; $F_5 = -1,221N$; $F_6 = 367N$; $F_7 = 853N$; $F_8 = 155N$; $F_9 = 953N$; $F_{10} = 592N$; $F_{11} = 858N$; $F_{12} = -926N$; $F_{13} = 1,056N$; $F_{14} = 878N$; $F_{15} = -661N$; $F_{16} = -139N$; $F_{17} = 2,276N$; $F_{18} = 726N$; $F_{19} = 1,307N$	50.10%	11,990N	0N · mm

Table 7.4: Load identification of Load Case 2 with only 1 sensing line - The positive directions and the identification numbers of the forces are the ones depicted in Figure 7.5.

7.2.8 Effect of measurement error

In this section the effect of the errors that can affect the measured strains is evaluated for the 2-step method. The best and worst configurations, namely the 7 sensing lines and the 1 sensing line configurations, considered in the previous analysis are analysed, but this time a random error is added to the strains computed from the refined FE model. Two cases of normally distributed errors with zero mean and a standard deviation of 1% and 5% of the nominal value are added to the strains. Moreover, the effect of the Tikhonov regularisation in smoothing the amplification of the error due to the ill-posedness of the problem is investigated. the Tikhonov regularization has been introduced in the solution of the inverse problem formulated in Eqs. 7.3 and 7.7. For each case, the Tikhonov regularization parameter (λ) has been computed empirically, searching for the value that maximized the accuracy in the reconstruction of the external loads. In Table 7.5 and 7.6, the results of this investigation are reported for the two load cases respectively. The results, in terms of $\%ERMS_p$, $\%ERMS_f$ and $\%ERMS_w$, are presented for the reconstructions obtained with and without the use of the Tikhonov regularization. In the tables, the values of the regularization parameters, λ , are also reported.

%Err	Sensors	NO regularization		Tikhonov regularization		
		$\%ERMS_p$	$\%ERMS_w$	$\%ERMS_p$	$\%ERMS_w$	λ
1%	1 line	934.6	9.9	23.1	0.5	7.0E-06
	7 lines	29478.4	13.6	15.5	0.06	8.0E-05
5%	1 line	2782.2	19.8	27.3	0.8	7.0E-05
	7 lines	247754.6	66.4	18.3	1.1	2.4E-04

Table 7.5: Effect of measurement error for **Load case 1**.

%Err	Sensors	NO regularization		Tikhonov regularization		
		% $ERMS_F$	% $ERMS_w$	% $ERMS_F$	% $ERMS_w$	λ
1%	1 line	21512113.2	448.7	22.1	3.5	2.0E-09
	7 lines	210209.8	32.0	23.3	0.04	3.0E-08
5%	1 line	130845922	2578.9	25.8	7.2	7.0E-09
	7 lines	4749253.5	58.5	23.5	0.2	2.0E-08

Table 7.6: Effect of measurement error for **Load case 2**.

The values of the errors show that the measurement error strongly influence the accuracy of the method in the application of both the steps. Even an error of 1% generates highly inaccurate reconstructions of the loads and, consequently, of the displacements. The introduction of the Thikonov regularization is able to reduce the negative effect of the measurement error. In fact, the regularization allows the reduction of the errors in the reconstruction of the loads (% $ERMS_p$, % $ERMS_f$) from values that reach, in the best case, almost 1000%, to values that, in the worst case, are close to 27%. However, the accuracy in the reconstruction of the loads is still not extremely accurate. On the other hand, the regularisation has a stronger positive effect on the shape sensing step of the procedure. Once again, the method generates accurate reconstructions of the displacement field, even with moderately accurate identified loads. As a matter of fact, the deformed shape is reconstructed with impressive accuracy for all the analysed configurations ($0.06 < \%ERMS_w < 1.2$), with the exception of the Load case 2 with only one sensing line ($\%ERMS_w > 3$).

The analysis of the configuration with 7 sensing lines helps to demonstrate the above mentioned behaviours. Figure 7.21 presents the identified pressure distributions obtained by the load identification step for the cases with 1% and 5% measurement error. The considered configuration is the one with 7 sensing line and with the regularisation implemented. The graphs, if compared with the reference pressure field in Figure 7.3, reveal the moderate level of accuracy reached by the method. However, the application of these identified distributions to the refined model of the structure produces the extremely accurate transverse displacements' reconstructions reported in Figure 7.22.

The same evaluation is performed for the Load case 2. The forces identified with the regularised configuration using 7 sensing lines are plotted in Figure 7.23, along with the resultant force, R_z , and the resultant moment with respect to the centre of gravity of the tip section, M_y^G . The accuracy in the prediction of the single values of the nodal forces is modest and, although R_z , compared with the reference one reported in Table 7.4, is well predicted, the values of the resultant moment, M_y^G , are far from the reference one, especially for the 5% error configuration. Nevertheless, the derived wing tip displacements, shown in Figure 7.24, prove once again the good

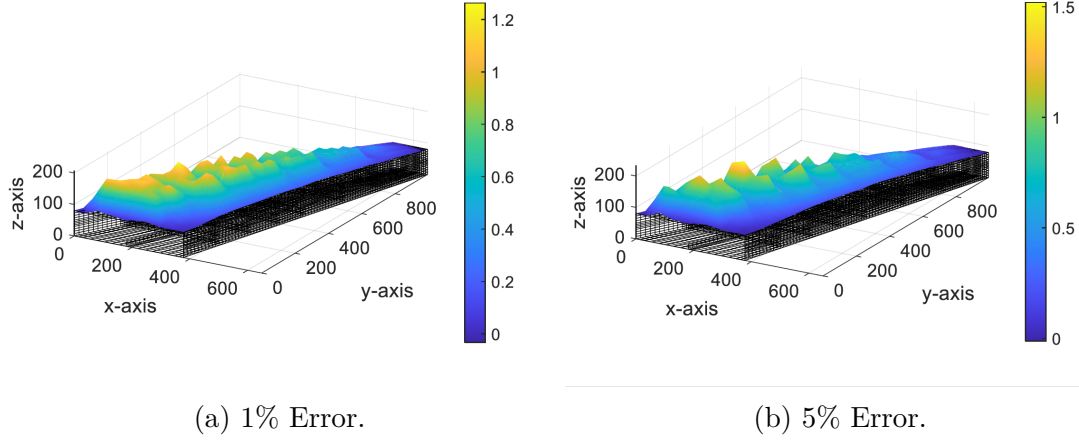


Figure 7.21: Pressure field reconstructions for Load Case 2 when strains are affected by a normal error of 1% (a) and 5% (b) and the Thikonov regularization is implemented. The results are showed for the 7 sensing lines configuration.

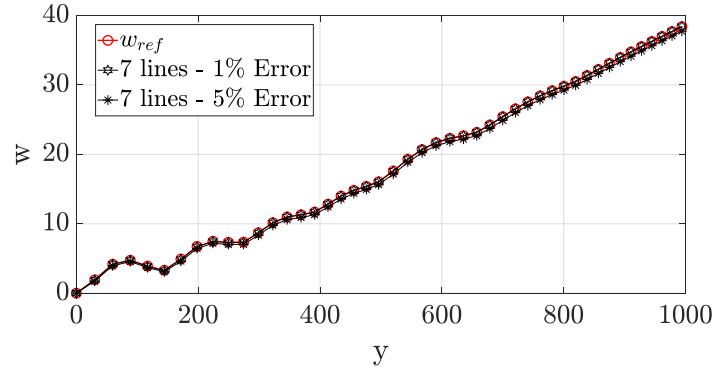


Figure 7.22: Vertical deflection along the wing span for Load Case 1 when strains are affected by a normal error of 1% and 5% and the Thikonov regularization is implemented. The results are showed for the 7 sensing lines configuration.

results obtained by the shape sensing step. As a consequence, it can be inferred that the magnitude of the discrepancy in the identified resultant moment is not so relevant to induce considerable effects on the deformation of the box.

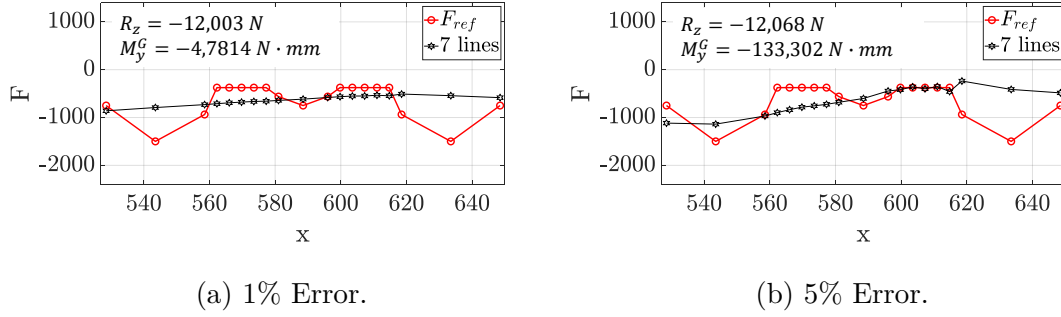


Figure 7.23: Nodal forces identification for Load Case 1 when strains are affected by a normal error of 1% (a) and 5% (b). The results are showed for the 7 sensing lines configuration.

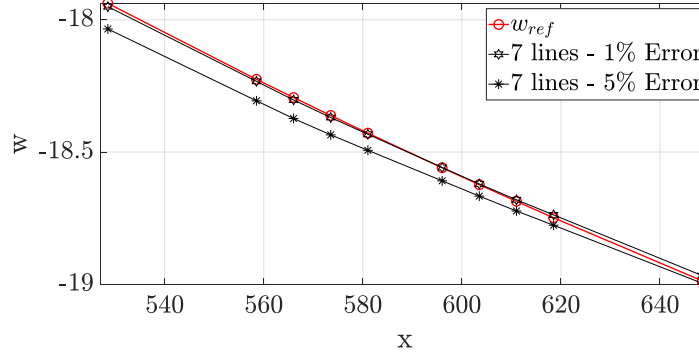


Figure 7.24: Vertical deflection along the wing tip chord for Load Case 2 when strains are affected by a normal error of 1% and 5%. The results are showed for the 7 sensing lines configuration.

In conclusion, an integrated procedure to simultaneously and efficiently compute the external loads and the induced displacements from discrete strain measures is proposed. The testing of this procedure on the numerical study of an aluminium wing box produced the following considerations. The method is proven to be accurate in the external loads identification, if a sufficient number of strain information is provided. In particular, the introduction of the quadrilateral elements for the discretization of the distributed loads helps to increment that accuracy. A reduction in the number of strain sensors and the presence of errors in the strain measurements significantly reduce the quality of these reconstructions. Nevertheless, the simultaneous reconstruction of the displacement field is impressively accurate, even when the number of strain sensors is strongly reduced. In this case, also the negative effect of the measurement error can be effectively smoothed with the use of the Thikonov regularisation. In the following chapter the results of this investigation

and of the previous ones will be validated on real structure in a broad experimental campaign.

Chapter 8

Experimental validation

The final part of this work regards the experimental validation of the methods firstly described and then numerically applied in the previous chapters. The considerations resulting from the numerical studies guided this experimental activity. The iFEM and the Modal Method are optimized and compared on the reconstruction of the displacement field of three structures, an aluminium cantilevered C-beam, a stiffened aluminium plate and an aluminium wing box. Along with these two shape sensing methods the two-step method is also applied on the same structures, allowing the simultaneous reconstruction of the displacements and the external loads. The Ko's Displacement theory has been discarded from the experimental activity because of its poor accuracy, especially when the uncertainties, typical of the experimental scenarios, are present in the system. In the following, the experimental configurations for the three test cases are presented and the results of the comparing activities are discussed.

8.1 Aluminium cantilevered C-beam

The test case for this activity is a C-beam. The geometry of the beam is presented in Figure 8.1, along with the reference coordinate system that will be used in the remaining of the discussion. The beam is made of a 6060 aluminium alloy, whose properties have been derived with a standard tensile test, conducted on three specimens made of the same material. The resulting Young's modulus (E) and Poisson's ratios (ν) from the three tests and the average values are reported in Table 8.1.

	Specimen 1	Specimen 2	Specimen 3	Averages
E [MPa]	68100	70000	66000	68033
ν	0.346	0.330	0.328	0.335

Table 8.1: 6060 aluminium alloy mechanical properties.

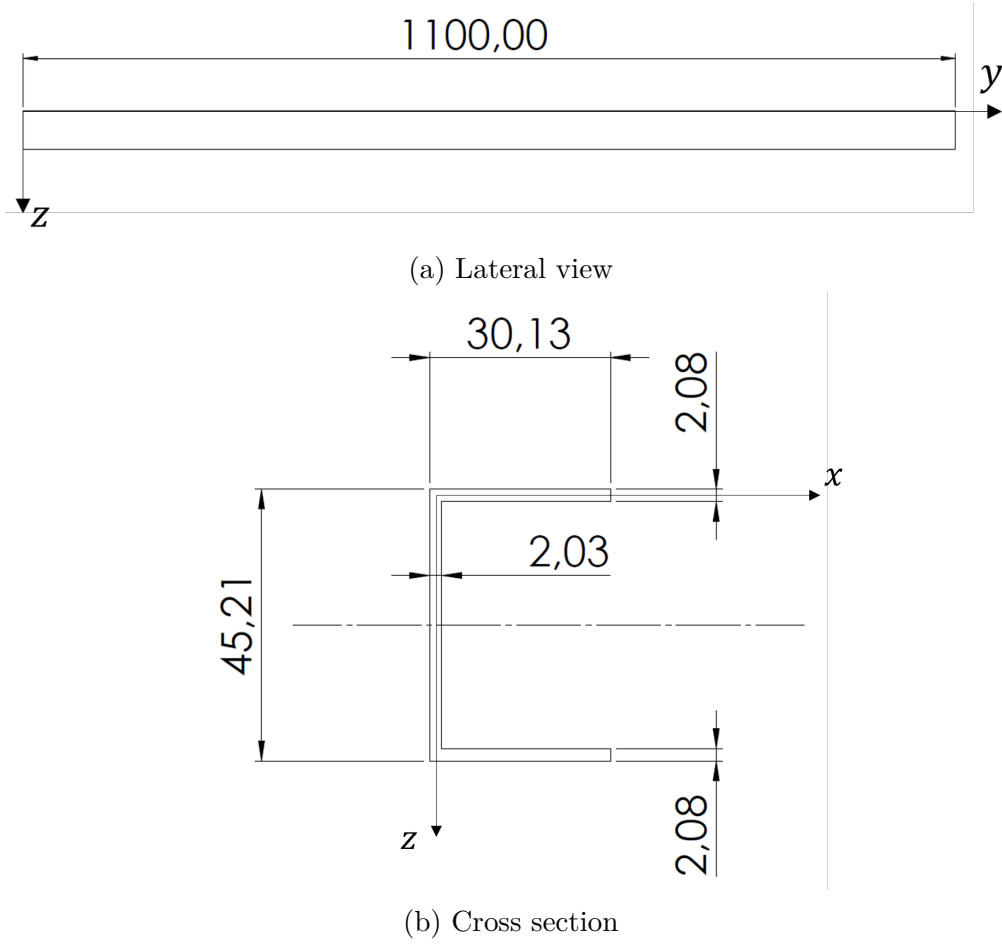


Figure 8.1: Aluminium C-Beam - The lateral view (a) and the cross section of the beam are shown. All the dimensions are expressed in [mm].

The root section of the beam ($y = 0$) is clamped. The clamping is obtained by holding a portion of the beam within two iron blocks. This portion of the beam is not considered in the length reported in Figure 8.1b. The tip end ($y = 1100 \text{ mm}$) is loaded with a concentrated force along the z axis (F_z). The test configuration is shown in Figure 8.2. The load is applied through a loading system that permits to move the load direction along the x axis (Figure 8.3). This allows to realize two loading conditions, one of pure bending, with the load aligned with the shear centre of the section, and one of bending+torsion, with the load not aligned with the shear centre. The load is applied through weights hanged on the load application system. The load application system is also equipped with two Linear Variable Differential Transformers (LVDTs), that measure the tip displacements along z at two different locations, ($x = -43.3 \text{ mm}$) and ($x = 47.2 \text{ mm}$) (Figure 8.3 and 8.4). These two measured displacements are the objective of the displacements reconstructions.

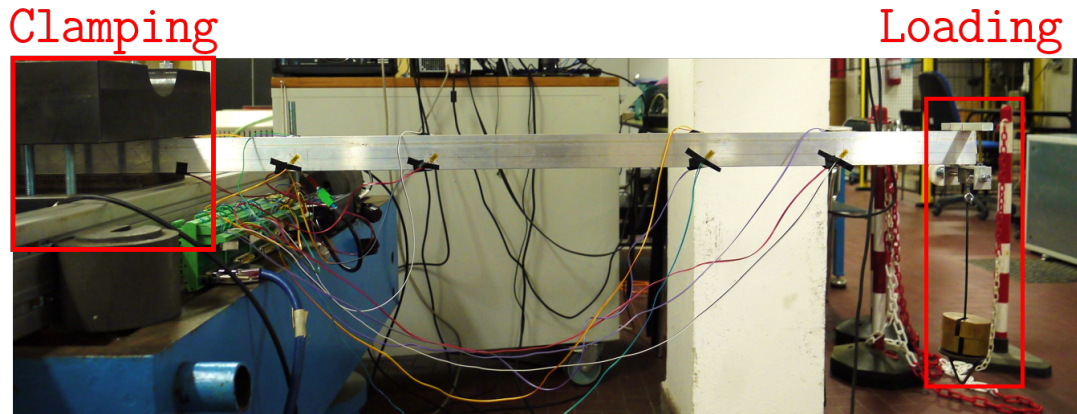


Figure 8.2: Test configuration for the aluminium C-Beam.

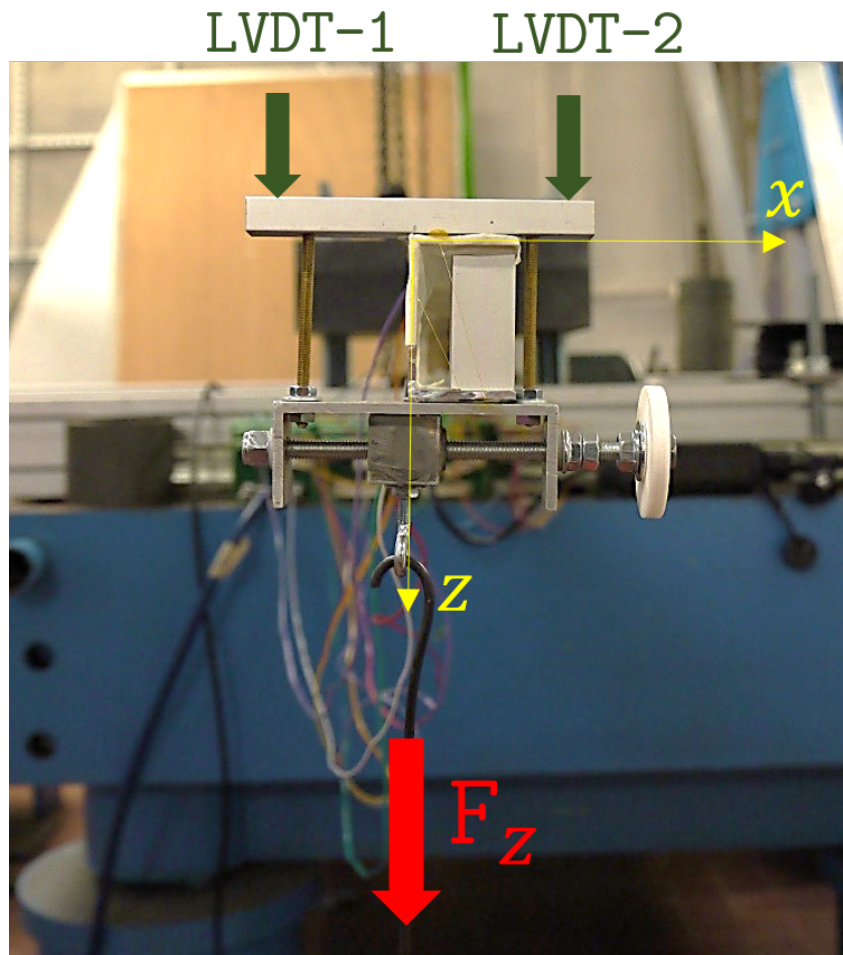


Figure 8.3: Load and displacement sensing system at the tip section ($y = 1100 \text{ mm}$).

Besides the displacements sensors, the strain sensors, necessary for the shape sensing, are also installed on the beam. The strain sensors' configuration for this experiment has not been specifically designed for the shape sensing methods that are going to be tested, but for another experimental application. This condition, although can negatively affect the performance of the investigated methods, can represent an interesting test. In fact, it can allow the study of the versatility of the methods to different sensing configurations not natively designed for them. The strains are measured with a LUNA® high-definition distributed fibre optic strain sensing system. This strain sensing system is able to measure the strains along the fibre's direction with a density of a measure every 0.65 mm. A 5 m long fibre is installed on the beam. The fibre is installed on the beam along the beam's length, making three loops, so that it defines three sensing lines: one on the top cap of the beam (Fibre Top), one on the lateral web (Fibre Lateral) and one on the bottom cap (Fibre Bottom). The sensor is only installed on the external surfaces of the structure. The fibre's locations on the section of the beam are illustrated in Figure 8.4. A detail on the installation of the fibre on the beam's bottom surface is presented in Figure 8.5.

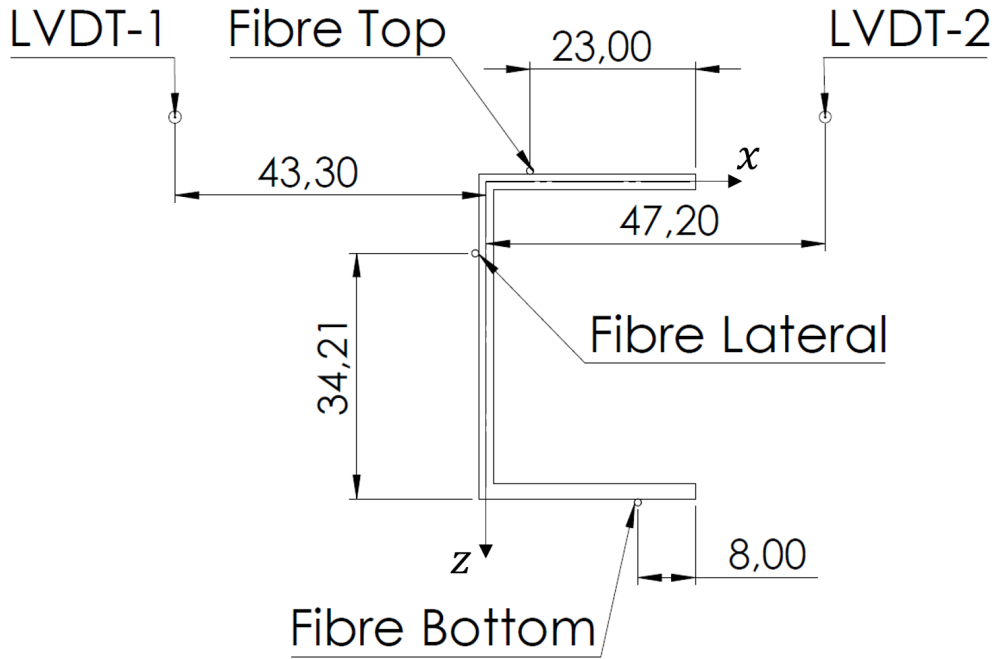


Figure 8.4: LVDTs and fibre optics location on the C-Beam's cross section.

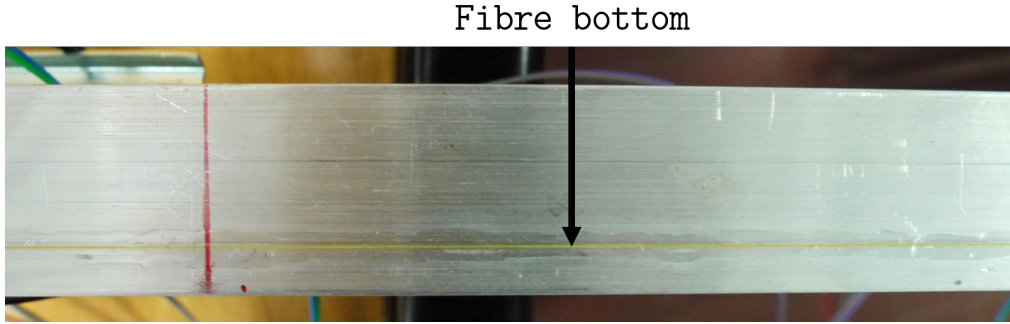


Figure 8.5: Fibre optic installed on the beam.

Once the experimental set-up has been defined, the numerical models can be designed. A refined shell FE model of the beam, constituted of 8712 MSC/NASTRAN® QUAD4 elements and 8992 nodes, is realized (Figure 8.6). This model is used to

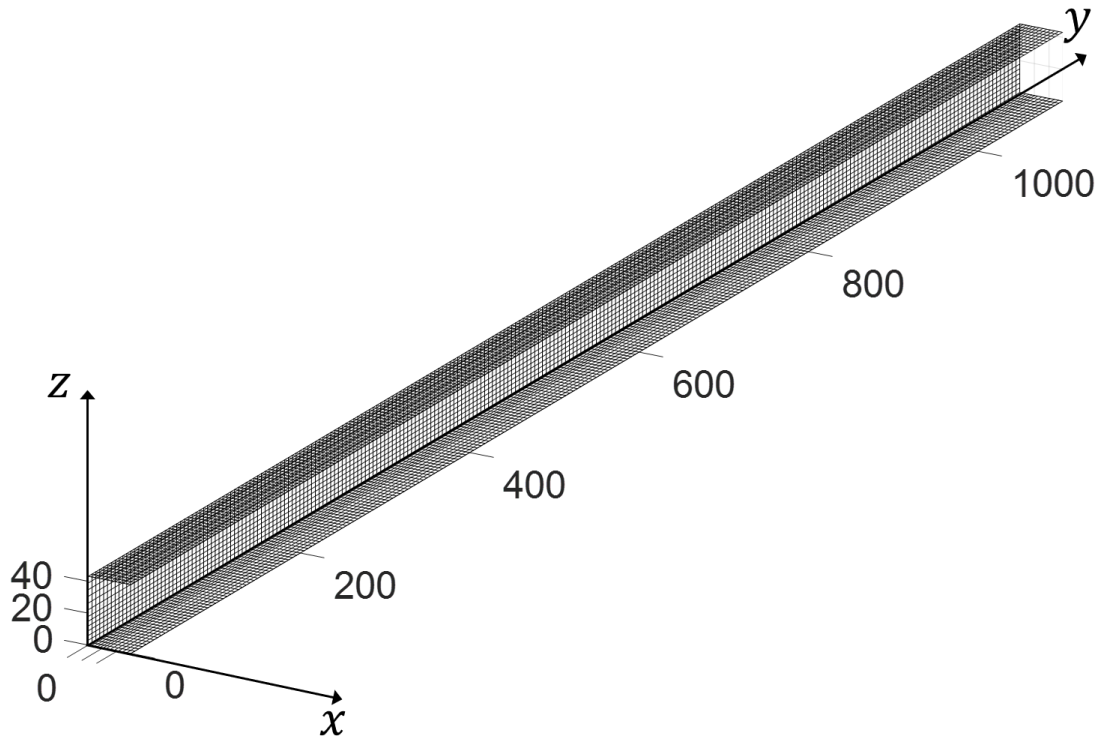


Figure 8.6: Refined mesh.

compute the modal characteristics of the structure, needed by the Modal Method, and to build the matrix of the coefficient of influence for the 2-step method. The modes selection criterion, illustrated in Section 3.1.1, has been used to select the

modes that could represent the bending deformation. The first twelve modes contribute to the total strain energy for the 99.8% and have been selected according to that criterion. The same modes are also considered for the bending+torsion load case, in order to verify the robustness of the modal method to the variation in the load configuration. An iFEM model is also designed with 2178 iQS4 elements and 2318 nodes. The nodes and the centroid of each element have a corresponding node in the refined mesh. The mesh is presented in Figure 8.7 along with the locations of the axial strain measurements (ε_y). These locations lay on the installed fibre and are located on the centroid of the inverse elements. These precise locations will be mapped to the several sensing locations on the fibre and the experimental strains in these positions will be extracted for the application of all the three monitoring methods. It can be noticed that the first elements, from ($y = 0$), of each sensing line do not have strain sensors. This is because of the impossibility to glue the fibre that close to the clamped end.

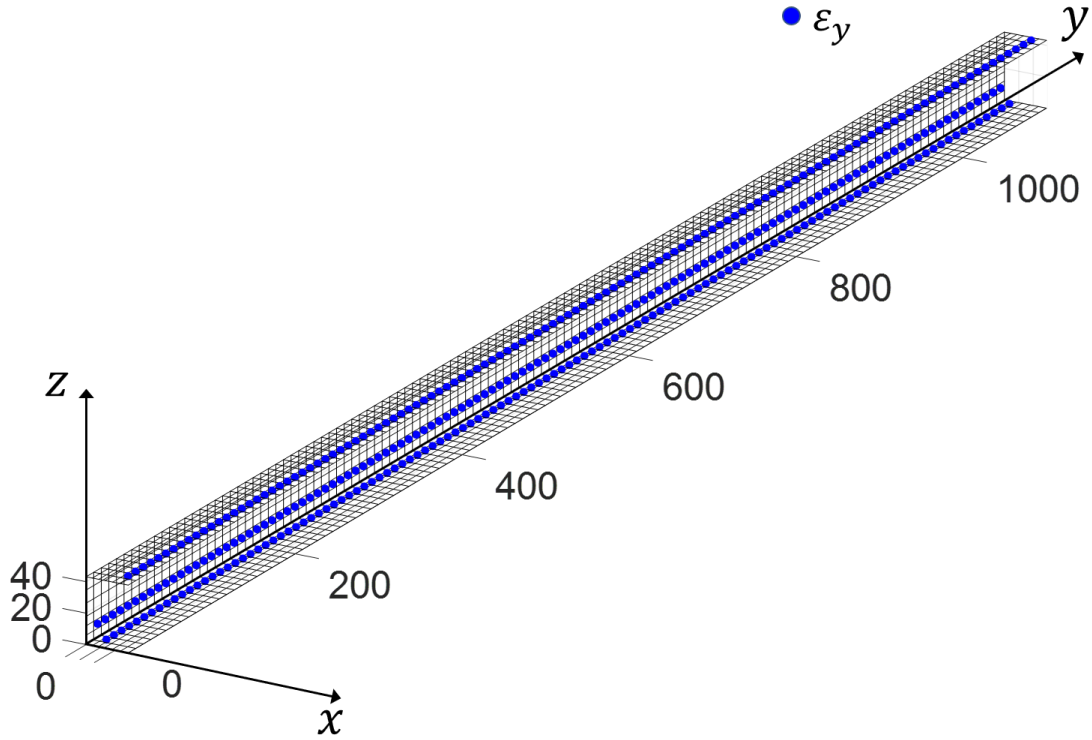


Figure 8.7: C-Beam - iFEM mesh and strain sensors' configuration.

Load case 1

The first load case consists of a concentrated transverse force passing through the shear centre, resulting in a pure bending deformation of the beam. To experimentally locate the shear centre, a load of 39.24 N has been applied to the loading system and the two LVDTs' measured displacements have been collected. Thanks to the mechanism of the load application system, the line of action of this load could be varied along x (Figure 8.3). The location for which a negligible difference ($< 1\%$) between the two LVDTs' measurements has been experienced has been defined as the experimental shear centre. The same procedure has been performed numerically on the high-fidelity model of the experiment. The shear centre's location is shown in Figure 8.8.

This preliminary test has been used to evaluate the accuracy of the refined model and to perform a model updating. The comparison between the vertical displacement recorded by the two LVDTs and the one from the refined FE model, initially implemented using the average values of the mechanical characteristics in Table 8.1, suggested an update of the Young's modulus of the model to $E = 60761 \text{ MPa}$.

The load system in Figure 8.8 is used to generate the matrix of coefficient for the 2-step method. Imposing ($F_z = 1$) and collecting the numerical axial strains (ε_y) from the updated refined model, the matrix can be easily populated. The F_z also represents the only unknown load for the load identification problem whereas the vertical displacement of the tip section represents the unknown of the shape sensing problem.

The collected strains from the fibre sensor, when a load of 39.24 N is applied through the shear centre of the experimental beam generated the reconstruction of the traverse displacement (w_z) and force (F_z) reported in Table 8.2 for the three investigated methods. In the Table, the reference experimentally measured values are also reported. The detailed strain data from this experiment are reported in Appendix C.1.

	Experimental	2-step	MM	iFEM
$F_z \text{ [N]}$	39.24	36.61		
$(\%Err_{F_z})$		(-6.7%)		
$w_z \text{ [mm]}$	4.127	3.856	3.924	3.478
$(\%Err_{w_z})$		(-6.7%)	(-4.9%)	(-15.7%)

Table 8.2: Shape sensing and load identification results for Load case 1. In parenthesis, the percentage error with respect to the experimental values are reported.

The Modal Method is the most accurate in the reconstruction of the vertical displacement, with an error in the reconstruction that is less than 5%. The 2-step

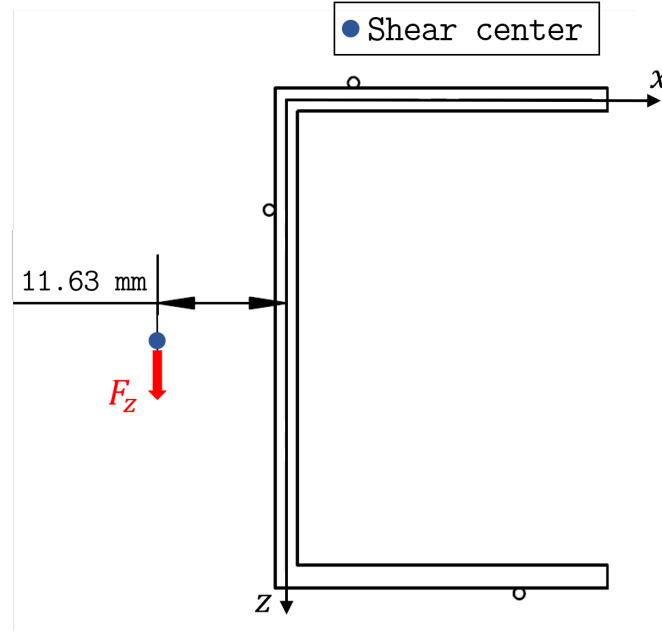


Figure 8.8: Load case 1 - Shear centre's location and loading condition.

method shows a moderate accuracy in the reconstruction of the load and of the vertical displacement, with an error close to 7%. On the other hand, the iFEM is significantly less accurate and the error reaches a value that is higher than 15%. These results will be further commented in the following section, together with the results from the study of the Load case 2.

Load case 2

The second load case is obtained by moving the line of action of the vertical load along the negative direction of the x axis, in order to get a deformation that combines bending and torsion. The magnitude of the translation is not measured and, therefore, the location of the force in the refined numerical model is not modified. This condition simulate a realistic and challenging scenario for the 2-step method for which the applied load system on the structure is unknown, not only in the intensity, but also in the general configuration of loads. Moreover, the knowledge of the real loading condition is not necessary for the application of the MM and the iFEM, that only rely on the strain measurements on the structure.

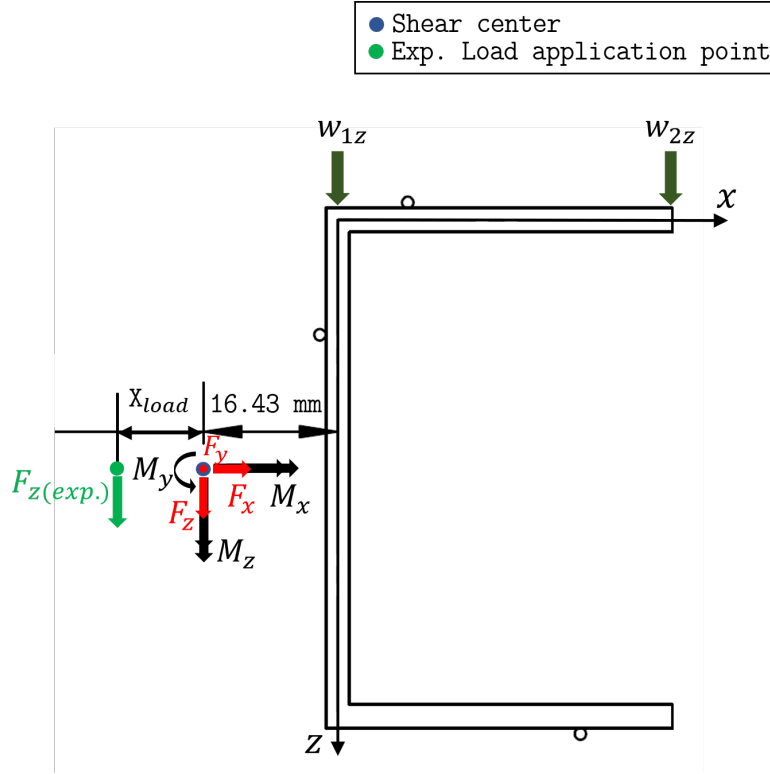


Figure 8.9: Load case 2 - The forces and moments applied in the shear centre represent the unknown of the 2-step method; $F_{z(exp.)}$ represent the experimentally applied force. w_{1z} and w_{2z} are the investigated displacements.

To take into account for the different scenario that the 2-step approach is confronted with, the other five components of the load, other than the vertical one, are added to the unknowns of the problem. Figure 8.9 shows the loading condition for both the experimental configuration and the numerical one, necessary for the application of the 2-step method. The inclusion of all the six load components allows the 2-step method to identify an equivalent, but different, load system from the one experimentally applied, without knowing the real loading condition a-priori. The matrix of the coefficients of influence is once again computed by iteratively imposing a unit value of the load for each load component and collecting the numerical strains in the sensors' locations.

The investigated displacements, this time, are the the ones identified in Figure 8.9 and denoted with the w_{1z} and w_{2z} symbols. The displacements measured by the two LVDTs can be easily transported in these desired locations using obvious geometrical considerations from Figure 8.4.

The beam is loaded with 34.33 N and the strains are collected to generate the reconstructions with the three methods. The strains collected from the fibres are reported in Appendix C.1. Since this load case have not been simulated, only the

experimental values are reported. The results of the experiment are listed in Table 8.3.

	Experimental	2-step	MM	iFEM
F_x [N]		-0.58		
F_y [N]		37.74		
F_z [N]	34.33	32.19		
(% Err_{F_z})		(-6.2%)		
M_x [N · mm]		483.23		
M_y [N · mm]		-60.08		
M_z [N · mm]		357.86		
w_{1z} [mm]	3.506	3.416	3.481	2.986
(% $Err_{w_{1z}}$)		(-2.6%)	(-0.71%)	(-14.8%)
w_{2z} [mm]	3.624	3.856	3.669	3.049
(% $Err_{w_{2z}}$)		(-5.2%)	(-4.1%)	(-20.3%)

Table 8.3: Shape sensing and load identification results for Load case 2. In parenthesis, the percentage error with respect to the experimental values are reported.

As expected, the 2-step approach identifies a different system of loads whose induced strains fit the strain field measured by the sensors and it is therefore capable of an accurate reconstruction of the two investigated displacements. Moreover, the identified vertical component of the load is also close to the applied one. Also for this case, the most accurate predictions for the displacements are the one produced by the MM and the less accurate are the ones generated by the iFEM.

In conclusion, the two experiments performed on the C-Beam confirm some of the considerations derived during the numerical studies. The experiment proves the extreme versatility of the MM to the sensors' configuration. In fact, the MM is able to provide good accuracy with a small number of strain sensors, not natively optimized for the application of the method. On the other hand, the investigation demonstrates that the iFEM requires a higher number of strain sensors and a specific sensors' configuration to reach the extreme level of accuracy showed in the numerical applications and in the experimental scenario that will be introduced next. The 2-step method also shows good level of adaptability to the unoptimized sensors' configuration and to the variation in the loading system. The method can reconstruct the displacements and the load with a good level of accuracy, when the applied load is coherent with the one hypothesized a-priori. On the other hand, if the applied load system is different from the defined one, the method is capable of finding a different load system that induces the same displacements and, therefore, the accuracy of the shape sensing is still preserved.

8.2 Aluminium stiffened panel

The second experimental activity involves the study of a typical aerospace component, an aluminium stiffened panel. The panel is made of an aluminium-lithium alloy whose characteristics have been previously computed through a tensile test and are reported in Table 8.4. The panel has been manufactured by RINA Consulting – CENTRO SVILUPPO MATERIALI SpA and has been courteously conceded for this activity.

Al-Li alloy	
E [MPa]	75958
ν	0.300

Table 8.4: AL-Li alloy mechanical properties.

The aluminium-lithium alloy has the peculiarity that can be welded. In fact, the three L-shaped stiffeners, that reinforce the panel, are directly welded to it and are of same material. The resulting geometry is presented in Figures 8.10 and 8.11, along with the reference coordinate frame. Besides the presence of the stiffeners, the panels also presents some other structural complexity. Between each bay, defined by the stiffeners, there are rectangular areas where the panel is thinner, as it can be observed in the figures.

The tested configuration considers simply supported boundary conditions for all the points located at ($y = 30\text{ mm}$) and ($y = 820\text{ mm}$). The plate is loaded in the centre point of the surface free of the stringers with a concentrated force. The test configuration is presented in Figure 8.12a. The supported boundary condition is obtained through the use of two iron half cylinder bars that constrain the plate so that the transverse displacements are not allowed but the bending rotations are (Figure 8.12c). The panel is loaded by tightening two nuts on two threaded rods. The nuts push down a iron half cylinder bar placed on top of the panel. An iron sphere is located between the bar and the panel. When the bar is pushed down, this sphere transmits the load to the centre point of the panel. The load generated by the nuts is measured by two load cells. The resultant concentrated force, applied in the centre of the plate, is the sum of these two measured loads.

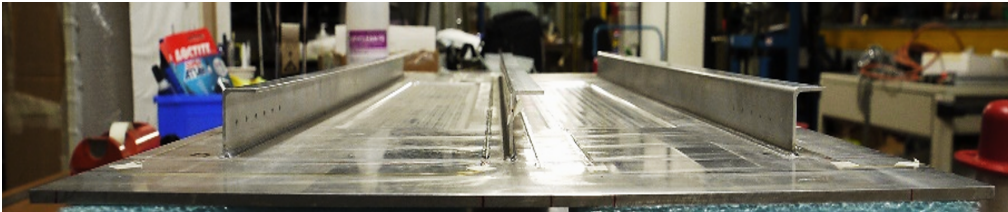
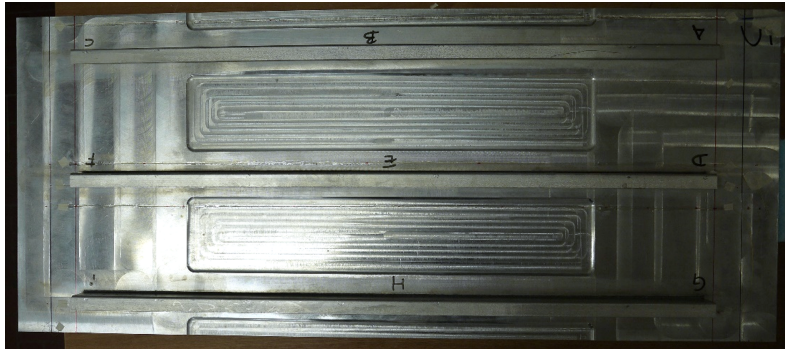
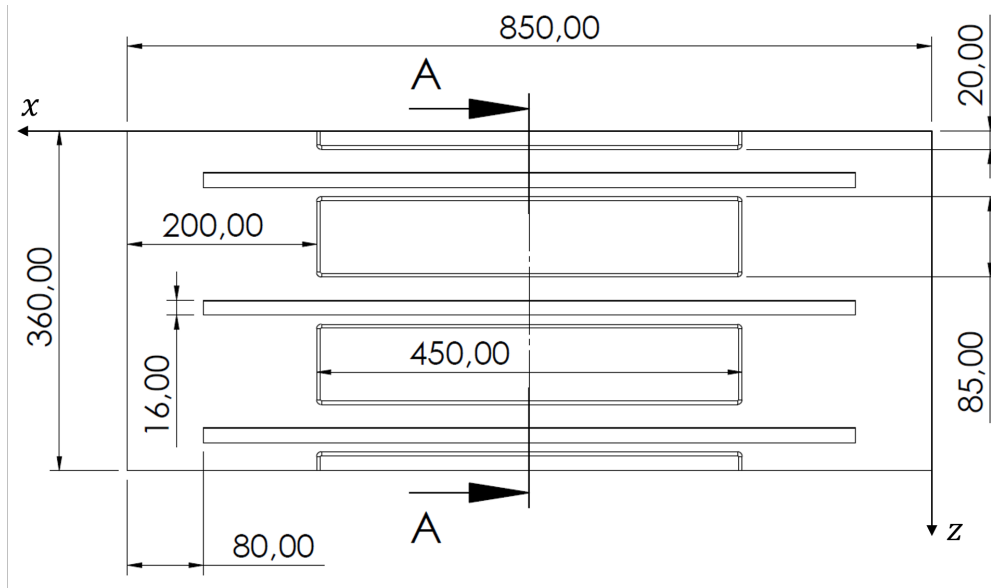


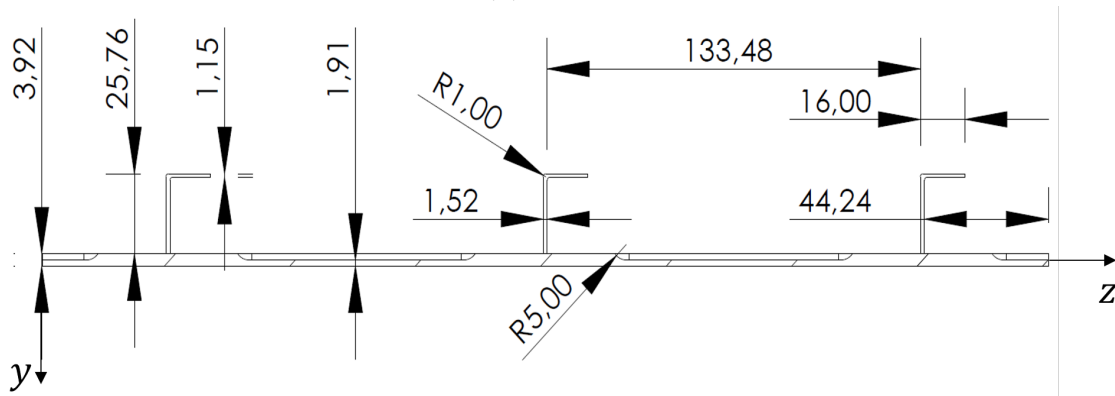
Figure 8.10: Stiffened panel's lateral view.



(a) Photo

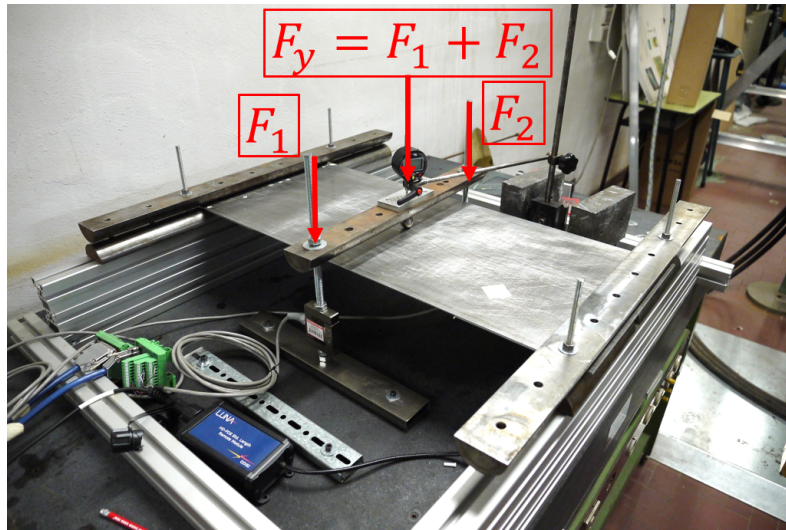


(b) Top view

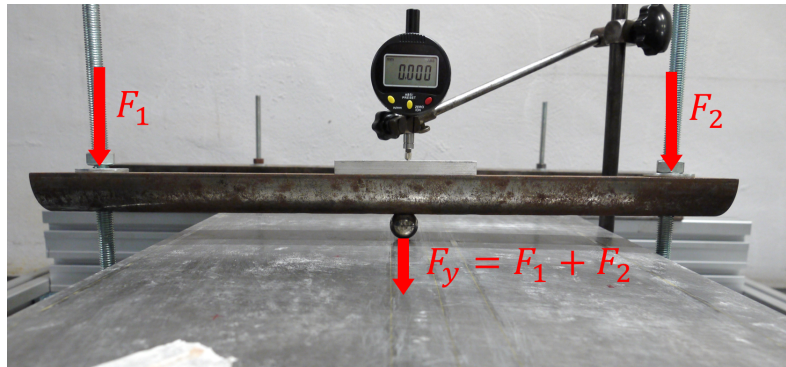


(c) Section A

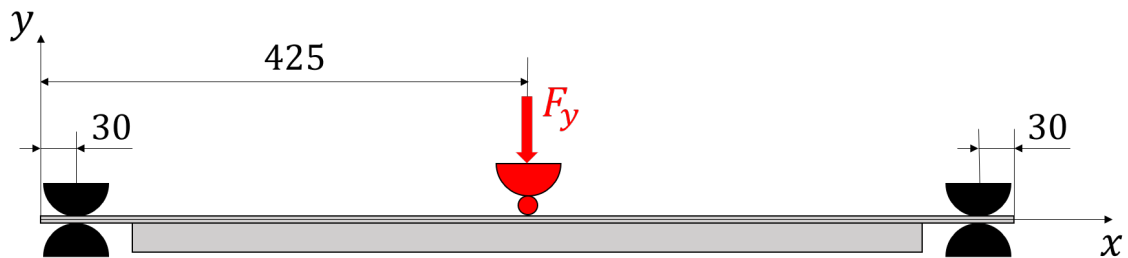
Figure 8.11: Stiffened panel's geometry. All the dimensions are expressed in [mm].



(a) Photo



(b) Detail of the load application system



(c) Scheme

Figure 8.12: Stiffened panel - Test configuration

From this test configuration the numerical models, necessary for the application of the iFEM, the MM and the 2-step approach, are designed. The iFEM mesh is constituted by 914 iQS4 elements and 978 nodes, not modelling the parts of the panel that exceed the supports (Figure 8.13). The refined one, used to compute the matrices for the Modal Method and the 2-step method, is obtained from the

inverse one by splitting each element into four elements. The modes selection criteria (3.1.1), suggested the use of the first 22 mode shapes, that account for the 97.6% of the total strain deformation energy.

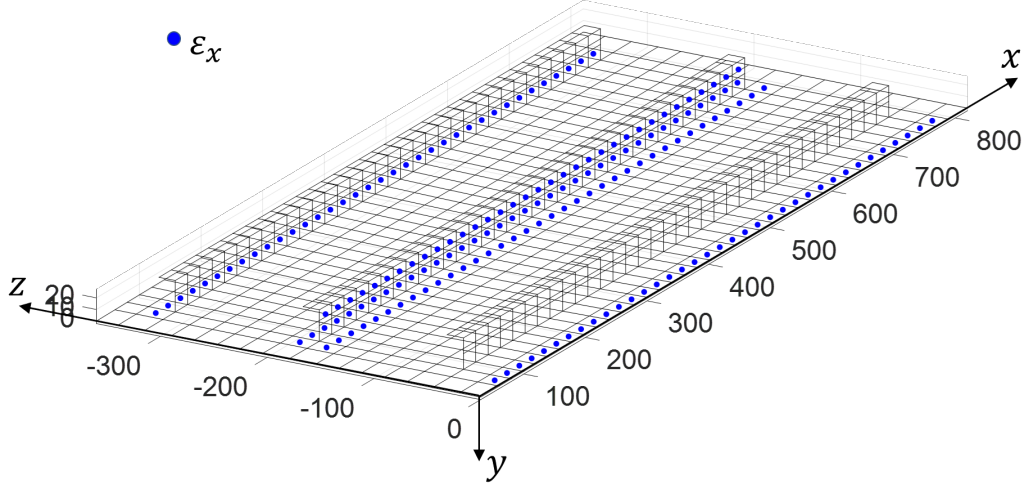


Figure 8.13: iFEM mesh and strain sensors' configuration.

Differently from the previous experiment, this time, a numerical study on the optimal sensors' configuration has been performed. Using the strain and the displacements extracted from the refined model of the experiment, an optimal sensors' configuration, that is able to guarantee a good level of accuracy for all the three methods, has been investigated. The optimization process has been performed considering the sensing technology that was intended to be used experimentally, the LUNA[®] high-definition distributed fibre optic strain sensing system. A 10 m long fibre has been considered. By making loops on the panels, the fibre is able to sense the strains on six lines along the panels' length in a back-to-back configuration, i.e. every sensor on the top surface of the panel has a corresponding one on the bottom surface of the panel. The optimal six back-to-back lines have been searched between the lines defined by the consecutive centroids' locations of the inverse elements along the x axis. As prescribed by the fibre optic sensing scheme, only strain measures along the x axis have been considered. The optimization has been carried on with the same genetic algorithm adopted in Section 4.2.2. The optimal trade-off configuration for the three shape/load reconstruction methods is reported in Figure 8.13 and the consequent fibre optic set-up is presented in Figure 8.14.

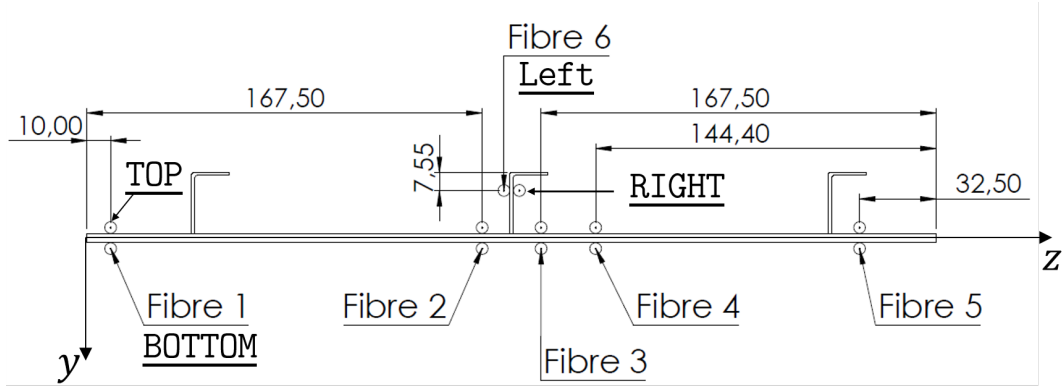


Figure 8.14: Stiffened panel fibre's configuration - The six sensing lines, installed in a back-to-back configuration, are shown.

For this configuration, the numerical $\%ERMS$, with respect to the transverse deflections of all the nodes of the inverse mesh, are 3.5, 3.7 and 5.9E-06 for the iFEM, the MM and the 2-step method respectively.

Once the strain sensors' configuration has been designed and installed on the panel, the displacements sensing system, necessary for the validation of the shape sensing methods, is also outlined. Four LVDTs have been located on the surface of the panel where the load is applied. These sensors measure the transverse displacements along y in the location where the concentrated force is applied (v_1) and in other three randomly distributed locations on one of the symmetric halves of the panel (v_{2-4}). The displacement sensors' configuration is illustrated in Figure 8.15.

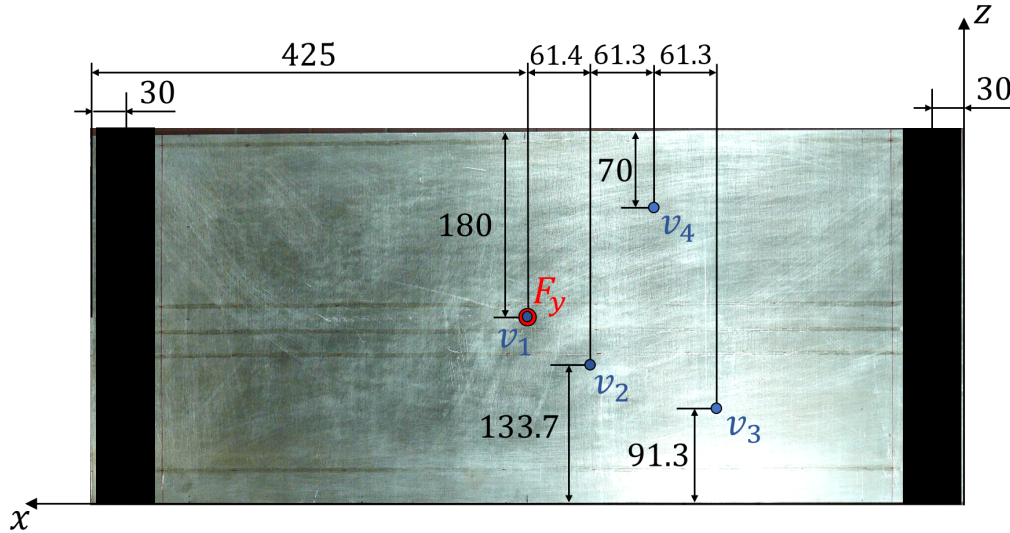


Figure 8.15: LVDTs' configuration - The location of the four LVDTs (v_{1-4}) on the surface of the panel are shown. All dimension are expressed in [mm]

Finally, the experiment is performed loading the panel with ($F_y = 882 \text{ N}$) and recording the outputs of the strain sensing system and of the LVDTs. The measured strains are reported in Appendix C.2. The measured displacements and the ones reconstructed with the three methods are reported in Table 8.5. The iFEM shows extremely accurate and consistent results, never exceeding an error of 2.5%, for every reconstructed displacement.

The Modal Method also shows a good overall accuracy except for the v_4 displacement. In this case, an error of -29.3% is observed. This phenomenon can be explained in the view of the results obtained during the numerical analysis in Paragraph 4.2.3. In that study it has been observed that, in some areas of the structure, the shape reconstruction from the Modal Method was strongly biased by the shape of some of the retained modes. Therefore, the method was able of an overall good accuracy but it lost that accuracy in some areas. The same behaviour can be observed in this experimental scenario.

The 2-step method is able to identify the applied load precisely. Nevertheless, the consequent displacements reconstruction show higher values of the errors. This is because, when applying the identified load to the FE model of the structure, the computed displacements also include the error due to the discrepancies between the real structure and the high-fidelity model. However, the sum of these errors never exceed the 8% and a good simultaneous reconstruction of the load and the displacement field can be obtained by the method.

	Experimental	2-step	MM	iFEM
$F_y \text{ [N]}$	-882	-899.7		
($\%Err_{F_y}$)		(+2.0%)		
$v_1 \text{ [mm]}$	-3.004	-3.201	-3.138	-3.034
($\%Err_{v_1}$)		(+6.6%)	(+4.5%)	(+1.0%)
$v_2 \text{ [mm]}$	-2.649	-2.862	-2.834	-2.701
($\%Err_{v_2}$)		(+8.0%)	(+7.0%)	(+2.0%)
$v_3 \text{ [mm]}$	-1.622	-1.727	-1.626	-1.644
($\%Err_{v_3}$)		(+6.5%)	(+0.2%)	(+1.3%)
$v_4 \text{ [mm]}$	-1.609	-1.664	-1.137	-1.649
($\%Err_{v_4}$)		(+3.4%)	(-29.3%)	(+2.5%)

Table 8.5: Shape sensing and load identification results for the stiffened panel. In parenthesis, the percentage error with respect to the experimental values are reported.

Once again, this activity proves the extreme accuracy of the iFEM when an optimized sensors' configuration, able to provide a sufficient number of strain information, is considered. It also proves that the Modal Method's performance can not exceed a certain level of accuracy even when a high number of strain sensors are

available. Moreover, it is confirmed that this method can generate highly inaccurate reconstructions in some areas of the structure. The 2-step method, although not able to reach the accuracy of the iFEM in the reconstruction of the displacement field, has the advantage of the simultaneous reconstruction of this characteristic and of the external load with a good average level of accuracy.

8.3 Swept aluminium wing box

The last experimental scenario is modelled on the aluminium wing box analysed in Chapter 7. However, from the initial design, studied in the previous analysis, and the experimental realization of the box, some differences have arisen. The necessity to reduce the stiffness of the box, in order to make it possible to easily obtain measurable displacements and strains in an experimental scenario, led to the installation of only three ribs instead of the eight previously considered. Moreover, the length of the web of the stiffeners that connect the skin panels to the spars has also been reduced from 30 mm to 15 mm. The modified geometry is presented in Figure 8.16.

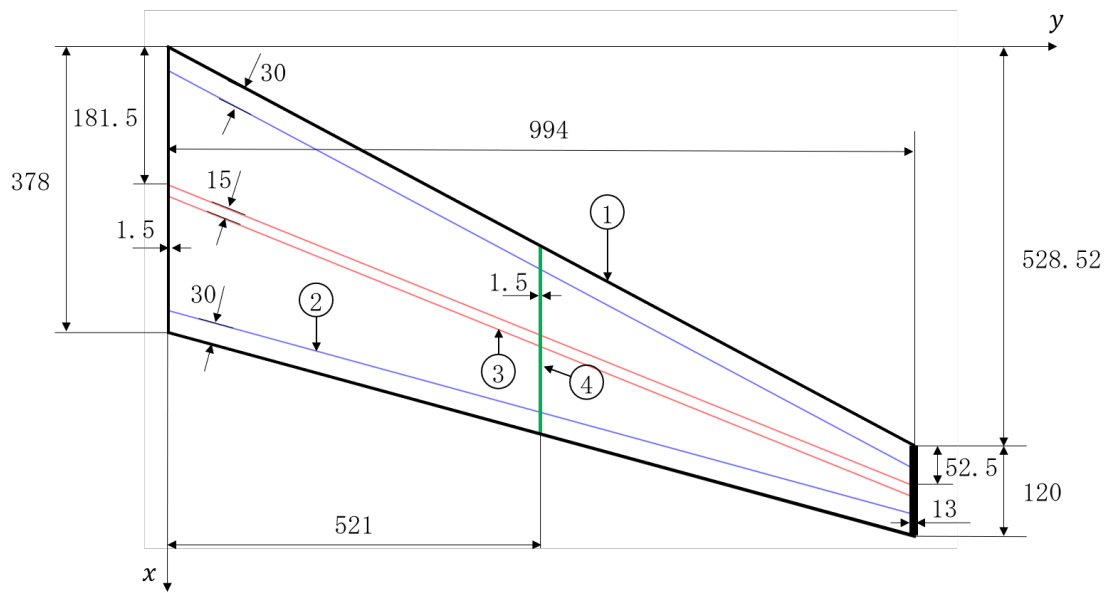
All the components of the box are jointed together by bolts. The two skin panels are connected to the root rib, the mid-span rib and the corners stiffeners by two rows of M4 bolts, each one separated by 10 mm. The spars are connected to the corner stiffeners by one row of M4 bolts, each one separated by 10 mm. Also the central stiffener is connected to the panels by one row of bolts. The tip rib presents threaded holes and it is fastened with the spars and skin panels by M4 screws. The pictures in Figure 8.17 show the wing box during the assembly process and the final assembled structure. For more details, the technical drawings of the wing box are reported in the Appendix D.

The skin panels and the spars of the box are made of a 7075 aluminium alloy, whereas the other components are made of the same 6060 alloy analysed in Section 8.1. The two aluminium alloys have been experimentally characterized with tensile tests and the resulting mechanical properties are reported in Table 8.6.

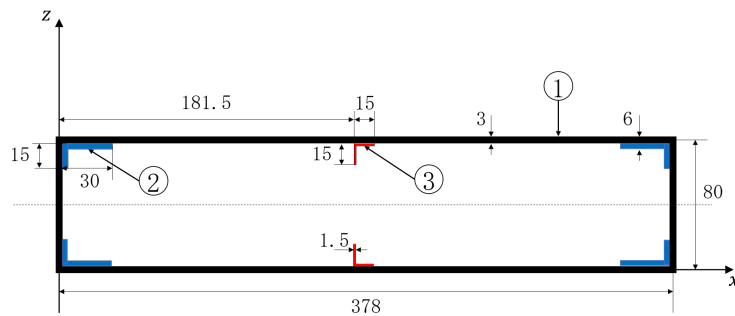
Alloy	E [MPa]	ν
6060	68033	0.335
7075	72017	0.325

Table 8.6: Aluminium alloys mechanical properties.

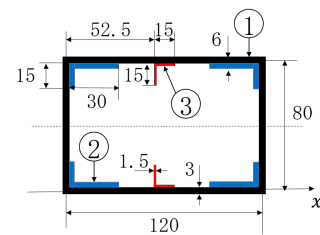
The designed experimental configuration considers a clamped root section and a concentrated traverse force at the tip section. This configuration is realized by clamping a 300 mm long portion of the wing box between two iron blocks, tighten together by bolts. The clamped portion of the wing box is not reported in Figure



(a) Top view ($z = 80$)



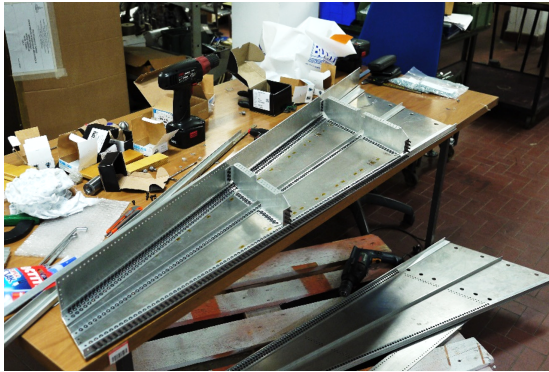
(b) Root section ($y = 0$)



(c) Tip section ($y = 994$)

Figure 8.16: Experimental wing box geometry - In the figure, the panel and the spars are indicated by ①, the stiffeners that connect the skin panels to the spars are indicated by ②, the stringers are indicated by ③ and the ribs are indicated by ④. All dimensions are expressed in $[mm]$.

8.16, where only the clear span is reported. The concentrated force is applied on the tip rib by a jack . The jack is equipped with an iron sphere that transmits the load to the wing box and a load cell able to measure the transmitted load. The loading system is suspended from the ground and directly connected to the test bed, that the wing box is clamped to, in order to avoid the rotation of the test bed due to applied load. At the tip section, two LVDTs, that measure the displacements in the same direction of the load, are installed on the leading edge and trailing edge corners, respectively. The test configuration is shown in Figures 8.18 and 8.19.

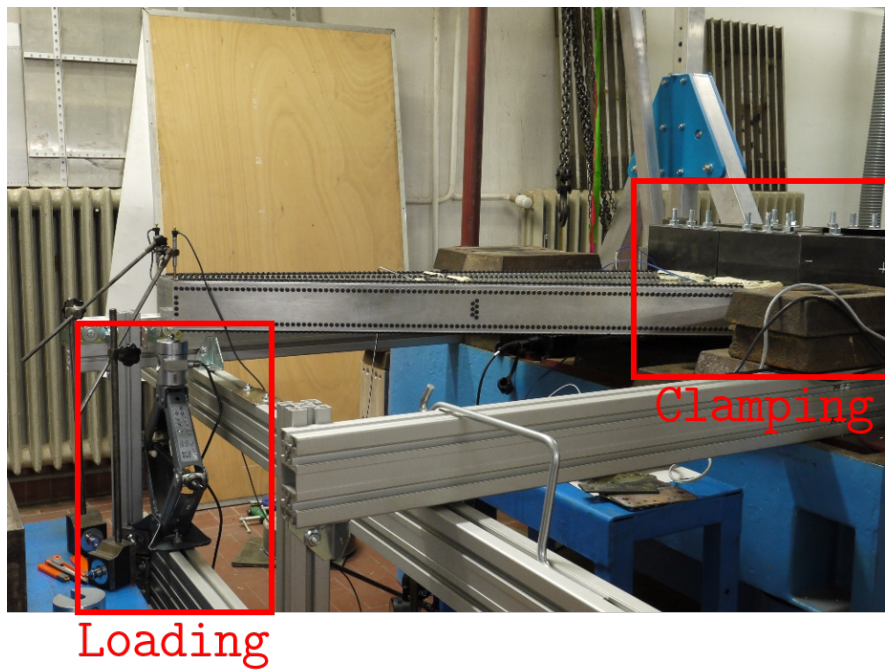


(a) Assembly process.

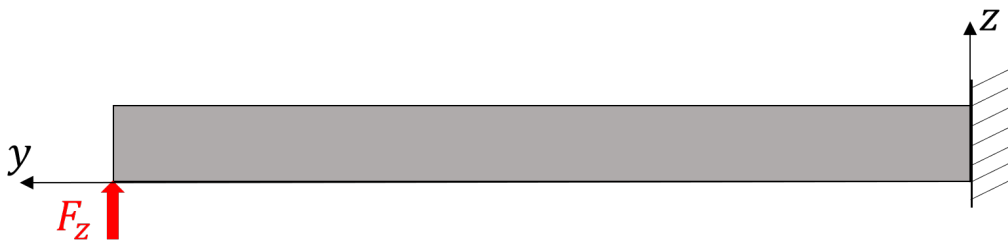


(b) Assembled wing box.

Figure 8.17: Swept wing box



(a) Photo.



(b) Scheme.

Figure 8.18: Swept wing box -Test configuration on the wing span view

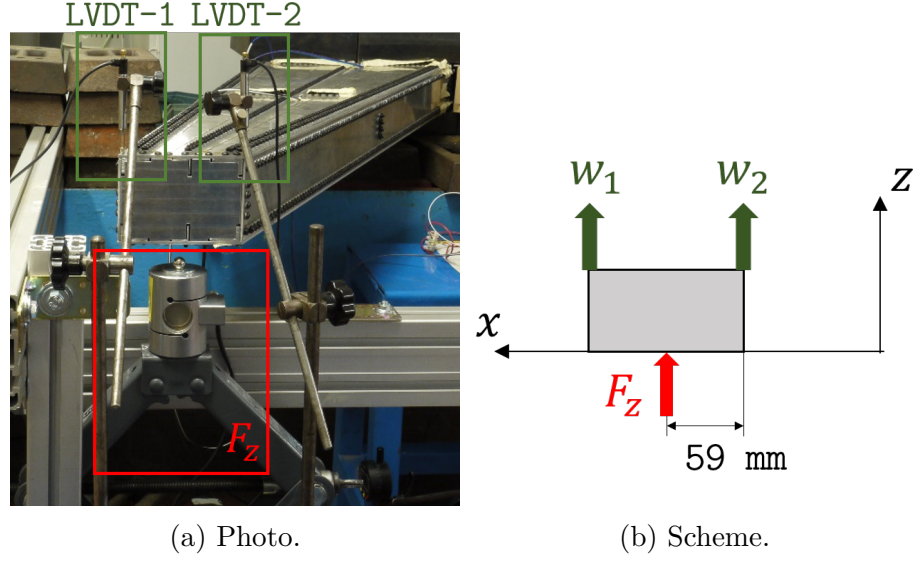


Figure 8.19: Swept wing box -Test configuration on the tip section view section

From this experimental set-up the inverse FE model and the high-fidelity FE model have been derived. The inverse model is constituted of 5842 iQS4 elements and 4528 nodes. The high-fidelity one has been derived from this model by splitting each quad element into four MSC/NASTRAN® QUAD4 elements. From this model, the first 22 mode shapes have been selected for the application of the MM and the matrices of the coefficient of influence have been extracted for the 2-step method. These modes are able to account for the 97.3% of the total strain energy of the investigated deformation. The bolted joints between the overlapped components of the structures have not been modelled in detail. These regions have been simulated with elements associated with the overlapped components having the reference plane off-setted and the nodes equivalenced, thus considering the bolted joint capable of a perfect connection. The inverse mesh is presented in Figure 8.20.

The same LUNA® high-definition distributed fibre optic strain sensing system has been adopted for this experimental activity. Therefore, the optimization of the sensors' placement has been performed according to the use of this technology. Considering a 10 m long fibre, eight optimal sensing lines along the entire wing span plus one sensing line along one half of the wing span have been searched between the ones defined by the centroid of the inverse elements. From this search, the portions of the structure where the bolts were located have been excluded. Only sensors on the external surface of the skin panels and the spars have been considered. The optimization, carried on with the usual genetic algorithm, was set to minimize the $\%ERMS_w$ error with respect to the transverse displacements along z of all the nodes of the inverse mesh. The optimized configuration is reported in Figure 8.20 and the relative fibre location is shown in Figure 8.21. The numerical $\%ERMS_w$,

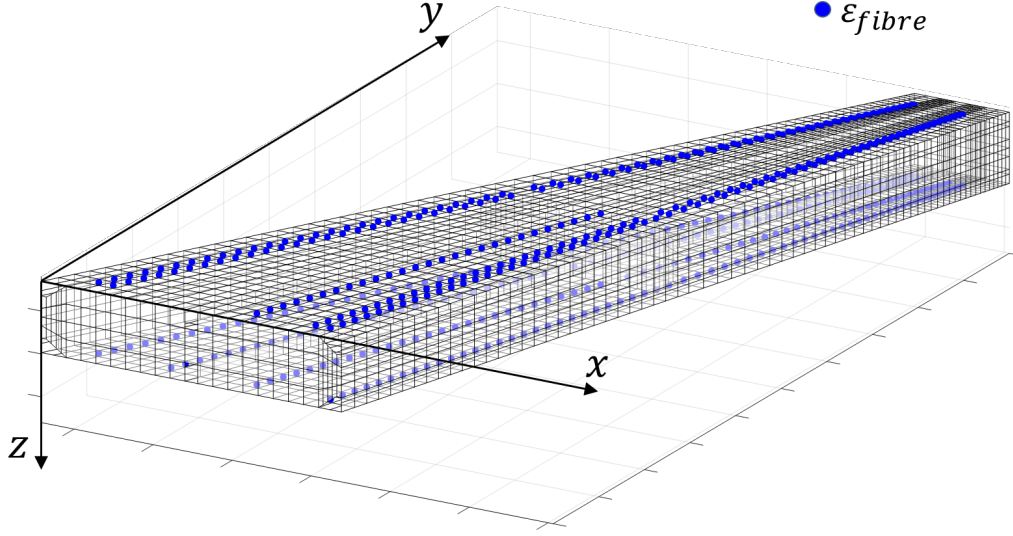


Figure 8.20: Swept wing box - iFEM mesh and strain sensor's configuration.

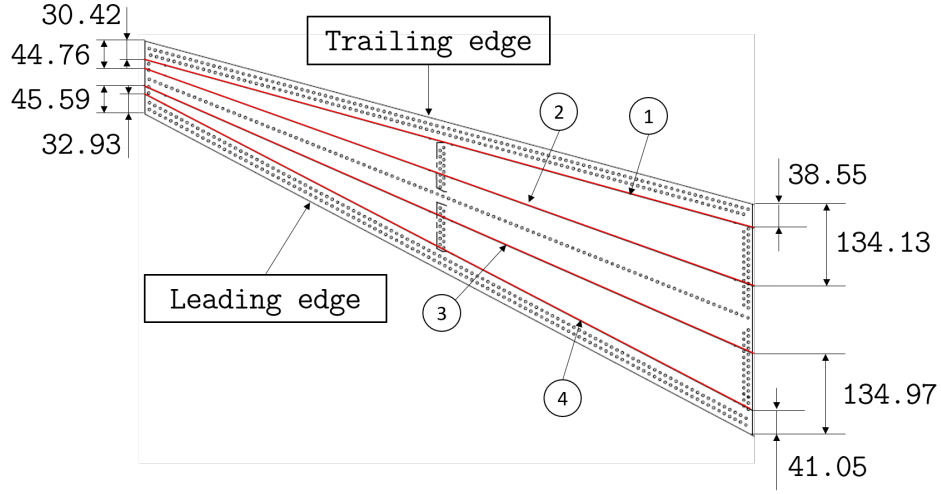
obtained with this configuration, are 4.2, 0.9 and $1.5\text{E-}06$ for the iFEM, the MM and the 2-step method respectively.

Finally, the experiment is performed applying a load of 1507 N to the wing box's tip and acquiring the induced strain and displacement. The results of this test are reported in Table 8.7. Along with the results from the load/displacements reconstructions, the resulting displacements from the high-fidelity model of the test are also reported.

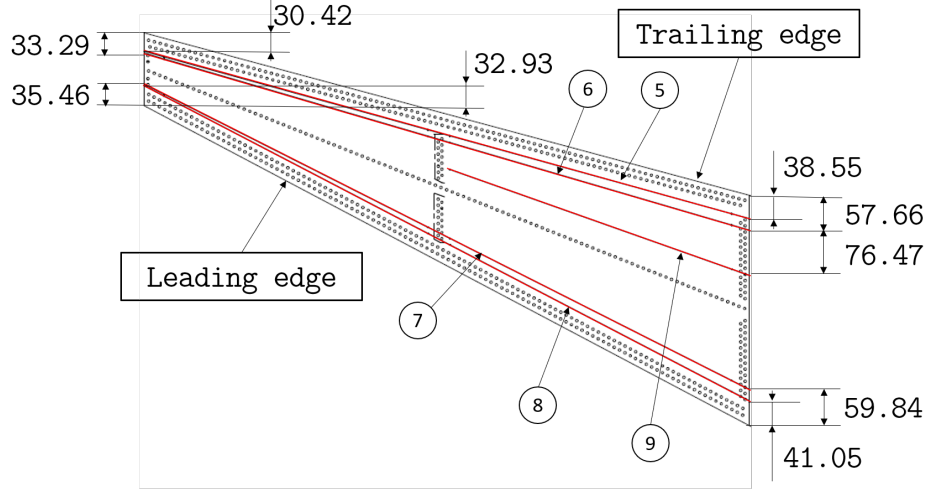
	Experimental	FEM	2-step	MM	iFEM
$F_z\text{ [N]}$	1507		1729		
$(\%Err_{F_z})$			(+14.7%)		
$w_1\text{ [mm]}$	3.54	2.26	2.59	2.58	2.19
$(\%Err_{w_1})$		(-36.31%)	(-26.28%)	(-27.1%)	(-38.1%)
$w_2\text{ [mm]}$	3.37	2.14	2.46	2.43	2.06
$(\%Err_{w_2})$		(-36.5%)	(-27.0%)	(-27.9%)	(-38.9%)

Table 8.7: Shape sensing and load identification results for the swept wing box. In parenthesis, the percentage error with respect to the experimental values are reported.

The results highlight a significant inaccuracy of all the three considered methods. The errors in the computation of the transverse displacements exceed 26% for



(a) Upper panel ($z = 80$).



(b) Lower panel ($z = 0$).

Figure 8.21: Swept wing box fibre's configuration - 8 sensing lines along the entire wing span (①-⑧) plus one sensing line along one half of wing span (⑨). All dimension are expressed in [mm].

all the methods. It is however important to notice that also the high fidelity FE model is not able to accurately simulate the behaviour of the wing box. In fact, the analysis of the measured strains, compared with the one extracted from the simulated experiment, also shows considerable discrepancies. This discrepancy increases when moving along the wing chord from the trailing to the leading edge, as shown in Figure 8.22 for Fibre 1 and 4. The lines closer to the trailing edge show a better correlation, whereas the lines closer to the leading edge show extremely

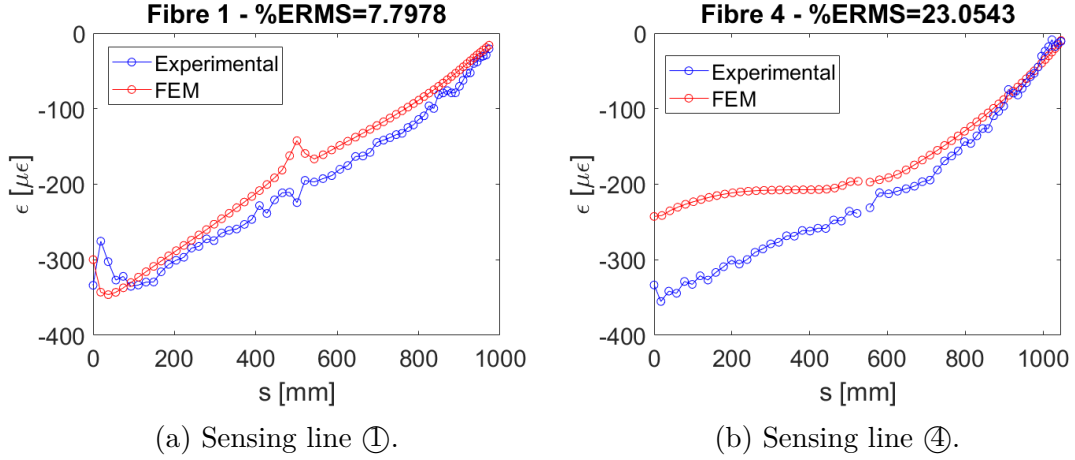


Figure 8.22: Strain comparison between the experimental values and the simulated ones.

poor correlation. These phenomena is observed on both the upper and the lower panel. The detailed distribution of the strains for all the fibres is reported in Appendix C.3. These considerations highlight the inadequacy of the considered numerical model to simulate the real behaviour of the structure. Therefore, it also explains the inaccuracy of the shape sensing and load identification algorithms, that is not to be attributed to some inadequate formulation, but to the inaccuracy of the numerical model that they rely on to simulate the experiment.

The modelisation of the bolted joints with equivalenced nodes is a strong claim and, therefore, this aspect of the model has been further investigated. A model updating has been tried in order to take into account the experienced reduction in the stiffness of the structure, probably caused by the presence of the joints. Two penalization factors have been attributed to the Young's modulus of the two alloys associated to the portions of the box where one row of bolts is present. Two different penalization factors have been adopted for the areas where two rows of bolts are installed. These four coefficients have been determined trough an optimization process aimed at simultaneously minimize the %ERMS error of the numerical strains and the displacements with respect to the experimentally measured ones. The minimization problem has been tackled with the same genetic algorithm adopted for the previous optimizations. Unfortunately, this model updating has not proven to be effective in the minimization of the observed discrepancies. The updated model, whose material properties and resulting displacements are resumed in Table 8.8, shows some reduction in the absolute value of the error on the displacements, that however remain highly inaccurate. Moreover, the update has not been able to significantly reduce the discrepancy observed for the sensing line close to the leading edge, as shown in Figure 8.23. Therefore, a more detailed model for the joint needs to be designed for this application in future work.

Updated FEM	
E_{6060} 1 row [Mpa]	55227
E_{6060} 2 rows [Mpa]	64565
E_{7075} 1 row [Mpa]	15533
E_{7075} 2 rows [Mpa]	48859
w_1 [mm]	3.94
(%Err $_{w_1}$)	(+11.3%)
w_2 [mm]	3.74
(%Err $_{w_2}$)	(+11.0%)

Table 8.8: Updated model characteristics and resulting displacements.

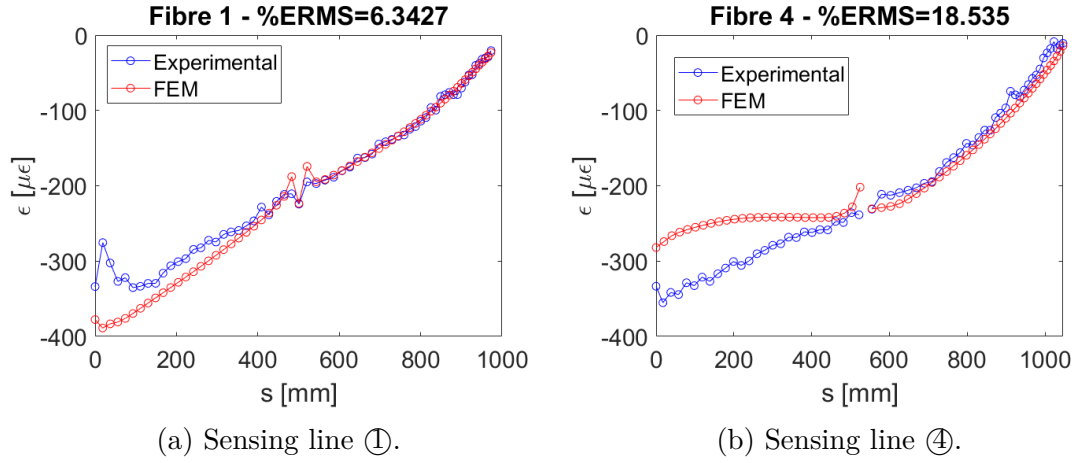


Figure 8.23: Strain comparison between the experimental values and the simulated ones from the updated model.

This experimental activity shows the inaccuracy of the shape sensing/load identification methods when a inadequate model is designed to simulate the real characteristics of the structure. In fact, being model based approaches, they strongly rely on the ability of the model to simulate the real structure's behaviour. Nevertheless, this activity does not highlight a limitation of the proposed methods' formulation, instead it points out some limitation about the general simulation of the structures with multiple bolted joints. In future works, a more detailed model of the joints should be taken into account and, consequently, the studied methods' formulations should be updated according to the new modelisation.

Chapter 9

Conclusions and future work

9.1 Conclusions

This work has focused on the analysis of two fundamental tools for the development of a modern Structural Health Monitoring framework and for the monitoring of the Smart structures, the shape sensing and load reconstruction/identification methods. These methods allow the reconstruction of the displacement field and of the loads of structure from discrete easily measurable strains. This research project started with the formulation of the following research questions:

- How can the shape sensing and load reconstruction be extended to analyse complex aerospace structures?
- How can strain sensing technology be optimized to fit requirements of the two techniques?
- How can the shape sensing be extended to reconstruct non-linear deformations?
- Can an integrated approach, including shape sensing and load reconstruction, be implemented?

This work has been developed around the answers to these research questions.

How can the shape sensing and load reconstruction be extended to analyse complex aerospace structures?

How can strain sensing technology be optimized to fit requirements of the two techniques?

To answer these two questions this research project has involved the use of already existing methods on complex aerospace structures, that these methods have

never been tested on, and also the implementation of new formulations able to push these technology toward the achievement of an accurate monitoring of aerospace structures. Moreover, an extreme consideration has also regarded the study of the adaptability of these methods to the available sensing technology. This part of the project has been developed on multiple activities, both numerical and experimental.

In particular, the most promising shape sensing methods, the Modal Method, the Ko's Displacement theory and the inverse Finite Element Method have been numerically tested on the displacements reconstruction of a composite wing box. From an applicability point of view, this activity has highlighted the different capabilities of the three methods and has provided useful information on how the methods can adapt to different scenarios. An evaluation of the influence of the strain configuration and of the material and sensors' uncertainties has showed that the iFEM is the most accurate shape sensing method. However, it requires a relevant amount of strain information to reach that significant accuracy. On the other hand, the Modal Method is able to generate accurate reconstructions with less strain sensors and it also proves to be less sensitive to the variability of the inputs, typical of the experimental scenarios. Nevertheless, it is not able to reach the accuracy of the iFEM, even using the same significant number of strain sensors. The Ko's displacement theory proved to be not accurate and strongly influenced by the inputs' variability. It is only able to provide a rough estimation of the displacement field of the structure, although with a really limited number of strain sensors.

The impressive accuracy demonstrated by the iFEM on the numerical and experimental activities has also been possible thanks to a new formulation developed in this work that extend the capabilities of the method to analyse complex structures and optimize the method for the strain sensing technology. The quadrilateral inverse element, iQS4, has been modified to better take into account for the effective locations of the strain sensors. The integration scheme of the measured strain field over the inverse element's area is modified according to a penalization approach, so that the location of the strain measurement is unequivocally identified in the centroid of the element. These allows an easier and more efficient allocation and association of the strain measurements for the application of the method and a better accuracy in the in-plane displacements' reconstruction.

Another research activity, aimed to provide a further contribution to the extension of the load reconstruction methods to complex aerospace structures, has been investigated. This activity has been developed around the monitoring of the internal loads of the wing of a fighter aircraft for the evaluation of the fatigue life consumption induced by these loads. For this case, the lack of knowledge of the structural characteristics of the investigated structure moved the research from model-based approaches to the exploration of the data driven system identification methods. Linear regression based ARX and ARMAX systems and several Artificial Neural Networks architectures have been studied in order to find the best system identification method to relate the strain inputs of the wing to the load outputs.

For each system a broad exploration of the parameters defining each architecture has been performed. The problem required the formulation of a parameter for the evaluation of the fatigue life estimation, without any knowledge on the material and the geometry of the structure. This problem has been solved with the definition of a new parameter, based on the Miner's rule formulation and on the beam structural model, that allowed the evaluation of the fatigue life consumption without these crucial information. The ANNs shows an overall best accuracy for this application and in particular, the Distributed Delay Artificial Neural Network generates the best predictions.

Following the analysis of the internal loads, the exploration of the load identification framework has been continued with the reconstruction of the external loads on a numerical swept wing box, subject to a distributed load and a pressure distribution. An already existing method has been applied for the first time on a 3D structure. This method is based on the discretization of the loads with concentrated nodal forces or nodal values of the pressure, according to the investigated type of load. The pressure field's domain is discretized with finite elements and, therefore, the nodal values of the pressure are interpolated over the elements' areas with shape functions. The computation of the strains induced by each discrete load allows the computation of the matrix of the coefficients of influence between the loads and the strains. The fitting of these coefficients to the measured discrete strains allows the computation of the unknown discrete loads. This method has been originally formulated with triangular elements for the discretization of the pressure field. In this work, the quadrilateral elements, that proved to be more accurate, have been introduced to extend the capabilities of the method.

How can the shape sensing be extended to reconstruct non-linear deformations?

The extension of the shape sensing to the reconstruction of non-linear deformations is fundamental for the monitoring of high-performance aerospace platforms whose structure often exceeds the limit of linear deformations. The study on large displacements has been performed considering the results of the investigation on the standard shape sensing methods. The promising results obtained by the iFEM on that application inspired the further development of this technology. The extension of the method to the analysis of large displacements has been achieved with a novel incremental formulation inspired by the direct FEM for geometrically non-linear analysis. The strains, inputs of the method, are divided into increments and for each increment the iFEM method is applied. At each iteration the inverse mesh, used for the application of the iFEM, needs to be updated by considering the reconstructed displacements from the previous step. The method has been tested on the analysis of a numerical wing-shaped plate subject to highly non-linear displacements. This application shows the extreme accuracy of the method in the

reconstruction of the large displacements and the highly superior performances of the novel formulation with respect to the standard iFEM for these kind of applications.

Can an integrated approach, including shape sensing and load reconstruction, be implemented?

A tool capable of simultaneously compute the loads and the displacement from the same discrete strain measurements has never been formulated in the existing literature, although it could be crucial for the progress of aerospace structural monitoring. In this research, a decisive attention has been dedicated to the design of this integrated framework.

The activity on the external load reconstruction inspired the formulation of an innovative 2-step approach for the simultaneous reconstruction of the external loads and of the displacement field. The 2-step procedure is easily obtained by identifying the loads with the above mentioned external loads reconstruction method and then using these load to perform a standard direct FEM analysis, thus computing the displacements induced by the loads. This integrated approach has shown promising results during the numerical analysis of a swept wing box. The external loads and the displacement field can be accurately reconstructed by the method when a sufficient number of strain sensors are installed on the structure and the measurements are not affected by errors. When the number of strains is reduced or measurement error is present in the system, the load predictions are poor. Nevertheless, the 2-step procedure is still capable of identifying an equivalent system of loads that, although different from the actually applied one, induces the same deformation on the structure. Therefore, in this case, the shape sensing from the proposed method is still impressively accurate.

Finally an experimental campaign, aimed at verifying the findings of the numerical study and validate the answers to the research questions, has been carried on. Three experiments have been designed to test the performances of the Modal Method, the iFEM and the 2-step approach. A cantilevered aluminium C-Beam, a stiffened aluminium panel and a swept aluminium wing box have been designed and tested. The experiments on the beam and on the stiffened panel confirmed some of the findings from the numerical analysis. In particular, the iFEM once again shows impressive accuracy, higher than the other methods, when the sensors' configuration provides a high amount of information and is optimized for the shape sensing. On the other hand, the MM and the 2-step method shows more versatility with respect to the sensor's configuration, being able to moderately accurate reconstructions of the displacements, even for sensors' configurations not optimized for the specific application. Moreover, the 2-step approach proves to be able to simultaneously identify the loads and the deformed shape when the applied system

of loads coincides with the one prescribed during the formulation of the method. But, more important, it is still able to compute the displacements even when the system of loads is different from the prescribed one, by identifying a system of loads that induces the same deformations.

The experiment on the swept wing box evidenced bad reconstruction of the load and of the deformed shape for all the three methods. A further analysis of the results showed that the inaccuracy of the methods was not to be attributed to their formulations or their inadequacy. In fact, the comparison of the experimental results, in terms of measured strains and displacements, with the one from a detailed standard FE model showed the same level of discrepancy. The investigation showed, therefore, the inadequacy of the numerical model that the methods were based on. The source of the error has been identified in the simulation of the bolted joints present on the wing box. These joints have been modelised with a perfect equivalence of the nodes associated with the jointed components.

9.2 Future work

Starting from this last mentioned results, there are still several aspect of the shape and load monitoring that should be addressed in future work. A more detailed modelisation of the bolted joints should be considered for the analysis of the swept wing box and of similar structures. In particular, the impact of this more detailed model on the formulation and accuracy of the considered monitoring methods should be examined in depth.

Moreover, the experimental campaign performed in this work only considered very simple load cases constituted by concentrated forces. Therefore, to validate the capabilities of the external load reconstruction method and of the consequent 2-step approach, more complex loading cases, including distributed pressures, should be analysed in a more advanced experimental campaign.

The prediction of the internal load through the use of data driven system identification systems should also be further investigated. The findings on the most appropriate Artificial Neural Network architecture should be validated through the study of the same problem on different platforms, to prove the robustness of the architecture to different scenarios.

In addition, the elevate accuracy of the iFEM, but its demanding requirements in terms of sensing technology, should inspire the study and development of techniques able to virtually expand few sensors, in order to make this method also exploitable for structures not equipped with many strain sensors.

Bibliography

- [1] A. Tessler, R. Roy, M. Esposito, C. Surace, and M. Gherlone. “Shape Sensing of Plate and Shell Structures Undergoing Large Displacements Using the Inverse Finite Element Method”. In: *Shock and Vibration* 8076085 (2018), 8 pages. DOI: [10.1155/2018/8076085](https://doi.org/10.1155/2018/8076085). URL: <https://www.hindawi.com/journals/sv/2018/8076085/>.
- [2] M. Esposito and M. Gherlone. “Composite wing box deformed-shape reconstruction based on measured strains: Optimization and comparison of existing approaches”. In: *Aerospace Science and Technology* 99 (2020), p. 105758. ISSN: 1270-9638. DOI: [10.1016/j.ast.2020.105758](https://doi.org/10.1016/j.ast.2020.105758). URL: <http://www.sciencedirect.com/science/article/pii/S1270963819324538>.
- [3] M. Esposito and M. Gherlone. “Material and strain sensing uncertainties quantification for the shape sensing of a composite wing box”. In: *Mechanical Systems and Signal Processing* 160 (2021), p. 107875. ISSN: 0888-3270. DOI: <https://doi.org/10.1016/j.ymssp.2021.107875>. URL: <https://www.sciencedirect.com/science/article/pii/S0888327021002703>.
- [4] M. Esposito, M. Gherlone, and P. Marzocca. “External loads identification and shape sensing on an aluminum wing box: An integrated approach”. In: *Aerospace Science and Technology* 114 (2021), p. 106743. ISSN: 1270-9638. DOI: <https://doi.org/10.1016/j.ast.2021.106743>. URL: <https://www.sciencedirect.com/science/article/pii/S1270963821002534>.
- [5] R. Di Sante. “Fibre Optic Sensors for Structural Health Monitoring of Aircraft Composite Structures: Recent Advances and Applications”. In: *Sensors* 15.8 (2015), pp. 18666–18713. ISSN: 1424-8220. DOI: [10.3390/s150818666](https://doi.org/10.3390/s150818666). URL: <https://www.mdpi.com/1424-8220/15/8/18666>.
- [6] B. J. Soller, D. K. Gifford, M. S. Wolfe, and M. E. Froggatt. “High resolution optical frequency domain reflectometry for characterization of components and assemblies”. In: *Opt. Express* 13.2 (Jan. 2005), pp. 666–674. DOI: [10.1364/OPEX.13.000666](https://doi.org/10.1364/OPEX.13.000666). URL: <http://www.opticsexpress.org/abstract.cfm?URI=oe-13-2-666>.

- [7] A. Airolidi, G. Sala, R. Evenblij, C. Koimtzoglou, T. Loutas, G. M. Carossa, P. Mastromauro, and T. Kanakis. “Load Monitoring by Means of Optical Fibres and Strain Gages”. In: *Smart Intelligent Aircraft Structures (SARISTU)*. Ed. by P. C. Wölcken and M. Papadopoulos. Cham: Springer International Publishing, 2016, pp. 433–469. ISBN: 978-3-319-22413-8. DOI: [10.1007/978-3-319-22413-8_20](https://doi.org/10.1007/978-3-319-22413-8_20).
- [8] T. de Souza Siqueira Versiani, F. J. Silvestre, A. B. Guimarães Neto, D. A. Rade, R. G. Annes da Silva, M. V. Donadon, R. M. Bertolin, and G. C. Silva. “Gust load alleviation in a flexible smart idealized wing”. In: *Aerospace Science and Technology* 86 (2019), pp. 762–774. ISSN: 1270-9638. DOI: <https://doi.org/10.1016/j.ast.2019.01.058>. URL: <http://www.sciencedirect.com/science/article/pii/S1270963818320868>.
- [9] S. Barbarino, O. Bilgen, R. M. Ajaj, M. I. Friswell, and D. J. Inman. “A Review of Morphing Aircraft”. In: *Journal of Intelligent Material Systems and Structures* 22.9 (2011), pp. 823–877. DOI: [10.1177/1045389X11414084](https://doi.org/10.1177/1045389X11414084). URL: <https://doi.org/10.1177/1045389X11414084>.
- [10] L. Colombo, C. Sbarufatti, and M. Giglio. “Definition of a load adaptive baseline by inverse finite element method for structural damage identification”. In: *Mechanical Systems and Signal Processing* 120 (2019), pp. 584–607. ISSN: 0888-3270. DOI: [10.1016/j.ymssp.2018.10.041](https://doi.org/10.1016/j.ymssp.2018.10.041). URL: <http://www.sciencedirect.com/science/article/pii/S0888327018307179>.
- [11] R. Roy, M. Gherlone, and C. Surace. “Damage Localisation in Thin Plates Using the Inverse Finite Element Method”. In: *Proceedings of the 13th International Conference on Damage Assessment of Structures*. Ed. by M. A. Wahab. Singapore: Springer Singapore, 2020, pp. 199–212. ISBN: 978-981-13-8331-1. DOI: [10.1007/978-981-13-8331-1_14](https://doi.org/10.1007/978-981-13-8331-1_14).
- [12] M. Li, A. Kefal, B. C. Cerik, and E. Oterkus. “Dent damage identification in stiffened cylindrical structures using inverse Finite Element Method”. In: *Ocean Engineering* 198 (2020), p. 106944. ISSN: 0029-8018. DOI: [10.1016/j.oceaneng.2020.106944](https://doi.org/10.1016/j.oceaneng.2020.106944). URL: <http://www.sciencedirect.com/science/article/pii/S0029801820300275>.
- [13] L. Colombo, D. Oboe, C. Sbarufatti, F. Cadini, S. Russo, and M. Giglio. “Shape sensing and damage identification with iFEM on a composite structure subjected to impact damage and non-trivial boundary conditions”. In: *Mechanical Systems and Signal Processing* 148 (2021), p. 107163. ISSN: 0888-3270. DOI: [10.1016/j.ymssp.2020.107163](https://doi.org/10.1016/j.ymssp.2020.107163). URL: <http://www.sciencedirect.com/science/article/pii/S0888327020305495>.
- [14] F. Austin, M. J. Rossi, W. Van Nostrand, G. Knowles, and A. Jameson. “Static shape control for adaptive wings”. In: *AIAA Journal* 32.9 (1994), pp. 1895–1901. DOI: [10.2514/3.12189](https://doi.org/10.2514/3.12189).

- [15] A. Koreanschi, O. S. Gabor, J. Acotto, G. Brianchon, G. Portier, R. M. Botez, M. Mamou, and Y. Mebarki. "Optimization and design of an aircraft's morphing wing-tip demonstrator for drag reduction at low speeds, Part II - Experimental validation using Infra-Red transition measurement from Wind Tunnel tests". In: *Chinese Journal of Aeronautics* 30.1 (2017), pp. 164–174. ISSN: 1000-9361. DOI: [10.1016/j.cja.2016.12.018](https://doi.org/10.1016/j.cja.2016.12.018).
- [16] M. Arena, F. Amoroso, R. Pecora, G. Amendola, I. Dimino, and A. Concilio. "Numerical and experimental validation of a full scale servo-actuated morphing aileron model". In: *Smart Materials and Structures* 27.10 (Sept. 2018), p. 105034. DOI: [10.1088/1361-665x/aad7d9](https://doi.org/10.1088/1361-665x/aad7d9).
- [17] W. Akl, S. Poh, and A. Baz. "Wireless and distributed sensing of the shape of morphing structures". In: *Sensors and Actuators A: Physical* 140.1 (2007), pp. 94–102. ISSN: 0924-4247. DOI: <https://doi.org/10.1016/j.sna.2007.06.026>. URL: <https://www.sciencedirect.com/science/article/pii/S092442470700502X>.
- [18] J. Bakalyar and C. Jutte. "Validation Tests of Fiber Optic Strain-Based Operational Shape and Load Measurements". In: *53rd AIAA/ASME/ASCE/AHS/ASC Structures, Structural Dynamics and Materials Conference*. DOI: [10.2514/6.2012-1904](https://doi.org/10.2514/6.2012-1904). URL: <https://arc.aiaa.org/doi/abs/10.2514/6.2012-1904>.
- [19] W. L. Ko, W. L. Richards, and V. T. Fleischer. *Displacement Theories for In-Flight Deformed Shape Predictions of Aerospace Structures*. Report NASA/TP-2007-214612. NASA Dryden Flight Research Center; Edwards, CA, United States, 2007.
- [20] W. L. Ko, W. L. Richards, and V. T. Fleischer. *Applications of the Ko displacement theory to the deformed shape predictions of the doubly-tapered Ikhana wing*. Report NASA/TP-2009-214652. NASA Dryden Flight Research Center; Edwards, CA, United States, 2009.
- [21] C. V. Jutte, W. L. Ko, C. A. Stephens, J. A. Bakalyar, and W. L. Richards. *Deformed Shape Calculation of a Full-Scale Wing Using Fiber Optic Strain Data from a Ground Loads Test*. Report NASA/TP-2011-215975. NASA Dryden Flight Research Center; Edwards, CA, United States, 2011.
- [22] J. Smoker and A. Baz. "Monitoring the bending and twist of morphing structures." In: *Sensors and Smart Structures Technologies for Civil, Mechanical, and Aerospace Systems 2008*. URL: <https://spie.org/Publications/Proceedings/Paper/10.1117/12.776433?SSO=1>.
- [23] H. Bang, S. Ko, M. Jang, and H. Kim. "Shape estimation and health monitoring of wind turbine tower using a FBG sensor array". In: *2012 IEEE International Instrumentation and Measurement Technology Conference Proceedings*. 2012, pp. 496–500. DOI: [10.1109/I2MTC.2012.6229407](https://doi.org/10.1109/I2MTC.2012.6229407).

- [24] P. Bogert, E. Haugse, and R. Gehrki. “Structural Shape Identification from Experimental Strains Using a Modal Transformation Technique”. In: *44th AIAA/ASME/ASCE/AHS/ASC Structures, Structural Dynamics, and Materials Conference*. Norfolk, 2012. DOI: [10.2514/6.2003-1626](https://doi.org/10.2514/6.2003-1626).
- [25] M. A. Davis, A. D. Kersey, J. Sirkis, and E. J. Friebele. “Shape and vibration mode sensing using a fiber optic Bragg grating array”. In: *Smart Materials and Structures* 5.6 (Dec. 1996), pp. 759–765. DOI: [10.1088/0964-1726/5/6/005](https://doi.org/10.1088/0964-1726/5/6/005). URL: <https://doi.org/10.1088/0964-1726/5/6/005>.
- [26] G. Foss and E. Haugse. “Using Modal Test Results to Develop Strain to Displacement Transformations”. In: *Proceedings of the 13th International Modal Analysis Conference*. Nashville, 1995.
- [27] A. C. Pisoni, C. Santolini, D. E. Hauf, and S. Dubowsky. “Displacements In A Vibrating Body By Strain Gauge Measurements”. In: *Proceedings of the 13th International Modal Analysis Conference*. Nashville, 1995.
- [28] R. T. Jones, D. G. Bellemore, T. A. Berkoff, J. S. Sirkis, M. A. Davis, M. A. Putnam, E. J. Friebele, and A. D. Kersey. “Determination of cantilever plate shapes using wavelength division multiplexed fiber Bragg grating sensors and a least-squares strain-fitting algorithm”. In: *Smart Materials and Structures* 7.2 (Apr. 1998), pp. 178–188. DOI: [10.1088/0964-1726/7/2/005](https://doi.org/10.1088/0964-1726/7/2/005). URL: <https://doi.org/10.1088/0964-1726/7/2/005>.
- [29] L.-H. Kang, D.-K. Kim, and J.-H. Han. “Estimation of dynamic structural displacements using fiber Bragg grating strain sensors”. In: *Journal of Sound and Vibration* 305.3 (2007), pp. 534–542. ISSN: 0022-460X. DOI: <https://doi.org/10.1016/j.jsv.2007.04.037>. URL: <https://www.sciencedirect.com/science/article/pii/S0022460X07003045>.
- [30] H.-I. Kim, L.-H. Kang, and J.-H. Han. “Shape estimation with distributed fiber Bragg grating sensors for rotating structures”. In: *Smart Materials and Structures* 20.3 (Feb. 2011), p. 035011. DOI: [10.1088/0964-1726/20/3/035011](https://doi.org/10.1088/0964-1726/20/3/035011). URL: <https://doi.org/10.1088/0964-1726/20/3/035011>.
- [31] N. S. Kim and N. S. Cho. “Estimating deflection of a simple beam model using fiber optic bragg-grating sensor”. In: *Experimental Mechanics* 44.4 (Aug. 2004), pp. 433–439. DOI: [10.1007/BF02428097](https://doi.org/10.1007/BF02428097). URL: <https://doi.org/10.1007/BF02428097>.
- [32] C.-J. Li and A. Ulsoy. “High-precision measurment of tool-tip displacement using strain gauges in precision flexible line boring”. In: *Mechanical Systems and Signal Processing* 13.4 (1999), pp. 531–546. ISSN: 0888-3270. DOI: <https://doi.org/10.1006/mssp.1999.1223>. URL: <https://www.sciencedirect.com/science/article/pii/S0888327099912232>.

- [33] L. Li, B. S. Zhong, Z. Y. Geng, and W. Sun. “Structural Shape Reconstruction of FBG Flexible Plate Using Modal Superposition Method”. In: vol. Volume 8: 29th Conference on Mechanical Vibration and Noise. International Design Engineering Technical Conferences and Computers and Information in Engineering Conference. V008T12A038. Aug. 2017. DOI: [10.1115/DETC2017-67316](https://doi.org/10.1115/DETC2017-67316). URL: <https://doi.org/10.1115/DETC2017-67316>.
- [34] P. S. Lively, M. J. Atalla, and N. W. Hagood. “Investigation of filtering techniques applied to the dynamic shape estimation problem”. In: *Smart Materials and Structures* 10.2 (Apr. 2001), pp. 264–272. DOI: [10.1088/0964-1726/10/2/311](https://doi.org/10.1088/0964-1726/10/2/311). URL: <https://doi.org/10.1088/0964-1726/10/2/311>.
- [35] S. Rapp, L.-H. Kang, J.-H. Han, U. C. Mueller, and H. Baier. “Displacement field estimation for a two-dimensional structure using fiber Bragg grating sensors”. In: *Smart Materials and Structures* 18.2 (Jan. 2009), p. 025006. DOI: [10.1088/0964-1726/18/2/025006](https://doi.org/10.1088/0964-1726/18/2/025006). URL: <https://doi.org/10.1088/0964-1726/18/2/025006>.
- [36] W. Yin, T. Fu, J. Liu, and J. Leng. “Structural shape sensing for variable camber wing using FBG sensors”. In: *Sensors and Smart Structures Technologies for Civil, Mechanical, and Aerospace Systems 2009*. Ed. by M. Tomizuka. Vol. 7292. International Society for Optics and Photonics. SPIE, 2009, pp. 517–526. URL: <https://doi.org/10.1117/12.812484>.
- [37] M. Alioli, P. Masarati, M. Morandini, T. Carpenter, N. B. Osterberg, and R. Albertani. “Membrane Shape and Load Reconstruction from Measurements Using Inverse Finite Element Analysis”. In: *AIAA Journal* 55.1 (2017), pp. 297–308. DOI: [10.2514/1.J055123](https://doi.org/10.2514/1.J055123). URL: <https://doi.org/10.2514/1.J055123>.
- [38] M. Gherlone, P. Cerracchio, M. Mattone, M. Di Sciuva, and A. Tessler. “Shape sensing of 3D frame structures using an inverse Finite Element Method”. In: *International Journal of Solids and Structures* 49.22 (2012), pp. 3100–3112. ISSN: 0020-7683. DOI: <https://doi.org/10.1016/j.ijsolstr.2012.06.009>. URL: <https://www.sciencedirect.com/science/article/pii/S0020768312002648>.
- [39] P. Cerracchio, M. Gherlone, and A. Tessler. “Real-time displacement monitoring of a composite stiffened panel subjected to mechanical and thermal loads”. In: *Meccanica* 50 (2015), pp. 2487–2496. DOI: [10.1007/s11012-015-0146-8](https://doi.org/10.1007/s11012-015-0146-8). URL: <http://www.sciencedirect.com/science/article/pii/S1270963817312397>.

- [40] P. Cerracchio, M. Gherlone, M. Di Sciuva, and A. Tessler. “A novel approach for displacement and stress monitoring of sandwich structures based on the inverse Finite Element Method”. In: *Composite Structures* 127 (2015), pp. 69–76. ISSN: 0263-8223. DOI: <https://doi.org/10.1016/j.compstruct.2015.02.081>. URL: <https://www.sciencedirect.com/science/article/pii/S0263822315001695>.
- [41] M. Gherlone, P. Cerracchio, M. Mattone, M. D. Sciuva, and A. Tessler. “Shape sensing of 3D frame structures using an inverse Finite Element Method”. In: *International Journal of Solids and Structures* 49.22 (2012), pp. 3100–3112. ISSN: 0020-7683. DOI: [10.1016/j.ijsolstr.2012.06.009](https://doi.org/10.1016/j.ijsolstr.2012.06.009). URL: <http://www.sciencedirect.com/science/article/pii/S0020768312002648>.
- [42] M. Gherlone, P. Cerracchio, M. Mattone, M. D. Sciuva, and A. Tessler. “An inverse finite element method for beam shape sensing: theoretical framework and experimental validation”. In: *Smart Materials and Structures* 23.4 (2014), p. 045027. DOI: [10.1088/0964-1726/23/4/045027](https://doi.org/10.1088/0964-1726/23/4/045027). URL: <https://doi.org/10.1088/0964-1726/23/4/045027>.
- [43] A. Kefal and E. Oterkus. “Displacement and stress monitoring of a chemical tanker based on inverse finite element method”. In: *Ocean Engineering* 112 (2016), pp. 33–46. ISSN: 0029-8018. DOI: [10.1016/j.oceaneng.2015.11.032](https://doi.org/10.1016/j.oceaneng.2015.11.032). URL: <http://www.sciencedirect.com/science/article/pii/S002980181500654X>.
- [44] A. Kefal and E. Oterkus. “Displacement and stress monitoring of a Panamax containership using inverse finite element method”. In: *Ocean Engineering* 119 (2016), pp. 16–29. ISSN: 0029-8018. DOI: [10.1016/j.oceaneng.2016.04.025](https://doi.org/10.1016/j.oceaneng.2016.04.025). URL: <http://www.sciencedirect.com/science/article/pii/S0029801816300919>.
- [45] E. J. Miller, R. Manalo, and A. Tessler. *Full-Field Reconstruction of Structural Deformations and Loads from Measured Strain Data on a Wing Using the Inverse Finite Element Method*. Report NASA/TM-2016-219407. NASA Dryden Flight Research Center; Edwards, CA United States, 2016.
- [46] U. Papa, S. Russo, A. Lamboglia, G. D. Core, and G. Iannuzzo. “Health structure monitoring for the design of an innovative UAS fixed wing through inverse finite element method (iFEM)”. In: *Aerospace Science and Technology* 69 (2017), pp. 439–448. ISSN: 1270-9638. DOI: [10.1016/j.ast.2017.07.005](https://doi.org/10.1016/j.ast.2017.07.005). URL: <http://www.sciencedirect.com/science/article/pii/S1270963817312397>.

- [47] C. Quach, S. Vazquez, A. Tessler, J. Moore, E. Cooper, and J. Spangler. “Structural Anomaly Detection Using Fiber Optic Sensors and Inverse Finite Element Method”. In: *AIAA Guidance, Navigation, and Control Conference and Exhibit*. DOI: [10.2514/6.2005-6357](https://doi.org/10.2514/6.2005-6357). URL: <https://arc.aiaa.org/doi/abs/10.2514/6.2005-6357>.
- [48] A. Tessler and J. Spangler. *A variational principal for reconstruction of elastic deformation of shear deformable plates and shells*. Report NASA/TM-2003-212445. NASA Langley Research Center, Hampton, VA, United States, 2003.
- [49] A. Tessler and J. L. Spangler. “Inverse FEM for Full-Field Reconstruction of Elastic Deformations in Shear Deformable Plates and Shells”. In: *Proceedings of the 2nd European Workshop on Structural Health Monitoring*. Munich, 2004.
- [50] R. Bruno, N. Toomarian, and M. Salama. “Shape estimation from incomplete measurements: a neural-net approach”. In: *Smart Materials and Structures* 3.2 (June 1994), pp. 92–97. DOI: [10.1088/0964-1726/3/2/002](https://doi.org/10.1088/0964-1726/3/2/002). URL: <https://doi.org/10.1088/0964-1726/3/2/002>.
- [51] Z. Mao and M. Todd. “Comparison of shape reconstruction strategies in a complex flexible structure”. In: *Sensors and Smart Structures Technologies for Civil, Mechanical, and Aerospace Systems 2008*. Ed. by M. Tomizuka. Vol. 6932. International Society for Optics and Photonics. SPIE, 2008, pp. 127–138. URL: <https://doi.org/10.1117/12.775931>.
- [52] G. Ding, S. Yue, S. Zhang, and W. Song. “Strain - deformation reconstruction of CFRP laminates based on Ko displacement theory”. In: *Nondestructive Testing and Evaluation* 0.0 (2020), pp. 1–13. DOI: [10.1080/10589759.2019.1707200](https://doi.org/10.1080/10589759.2019.1707200).
- [53] C. Pak. “Wing Shape Sensing from Measured Strain”. In: *AIAA Journal* 54.3 (2016), pp. 1068–1077. DOI: [10.2514/1.J053986](https://doi.org/10.2514/1.J053986).
- [54] J. C. O’Callahan, P. Avitabile, and R. Riemer. “System Equivalent Reduction Expansion Process”. In: *Proc. of the 7th Inter. Modal Analysis Conf.* Las Vegas, 1989. URL: <https://ci.nii.ac.jp/naid/10015640027/en/>.
- [55] C. Chipman and P. Avitabile. “Expansion of transient operating data”. In: *Mechanical Systems and Signal Processing* 31 (2012), pp. 1–12. ISSN: 0888-3270. DOI: [10.1016/j.ymssp.2012.04.013](https://doi.org/10.1016/j.ymssp.2012.04.013). URL: <http://www.sciencedirect.com/science/article/pii/S0888327012001409>.
- [56] M. Freydin, M. K. Rattner, D. E. Raveh, I. Kressel, R. Davidi, and M. Tur. “Fiber-Optics-Based Aeroelastic Shape Sensing”. In: *AIAA Journal* 57.12 (2019), pp. 5094–5103. DOI: [10.2514/1.J057944](https://doi.org/10.2514/1.J057944).

- [57] A. Tessler and J. L. Spangler. *Deformed Shape Calculation of a Full-Scale Wing Using Fiber Optic Strain Data from a Ground Loads Test*. Report NASA/TM-2003-212445. NASA Langley Research Center, Hampton, VA, United States, 2003.
- [58] A. Kefal, E. Oterkus, A. Tessler, and J. L. Spangler. “A quadrilateral inverse-shell element with drilling degrees of freedom for shape sensing and structural health monitoring”. In: *Engineering Science and Technology, an International Journal* 19.3 (2016), pp. 1299–1313. ISSN: 2215-0986. DOI: [10.1016/j.jestch.2016.03.006](https://doi.org/10.1016/j.jestch.2016.03.006). URL: <http://www.sciencedirect.com/science/article/pii/S221509861530118X>.
- [59] F. Zhao, L. Xu, H. Bao, and J. Du. “Shape sensing of variable cross-section beam using the inverse finite element method and isogeometric analysis”. In: *Measurement* 158 (2020), p. 107656. ISSN: 0263-2241. DOI: [10.1016/j.measurement.2020.107656](https://doi.org/10.1016/j.measurement.2020.107656). URL: <http://www.sciencedirect.com/science/article/pii/S0263224120301949>.
- [60] A. Kefal and E. Oterkus. “Isogeometric iFEM Analysis of Thin Shell Structures”. In: *Sensors* 20.9 (2020). ISSN: 1424-8220. DOI: [10.3390/s20092685](https://doi.org/10.3390/s20092685). URL: <https://www.mdpi.com/1424-8220/20/9/2685>.
- [61] A. Kefal, I. E. Tabrizi, M. Yildiz, and A. Tessler. “A smoothed iFEM approach for efficient shape-sensing applications: Numerical and experimental validation on composite structures”. In: *Mechanical Systems and Signal Processing* 152 (2021), p. 107486. ISSN: 0888-3270. DOI: [10.1016/j.ymssp.2020.107486](https://doi.org/10.1016/j.ymssp.2020.107486). URL: <http://www.sciencedirect.com/science/article/pii/S0888327020308724>.
- [62] A. Derkevorkian, S. F. Masri, J. Alvarenga, H. Boussalis, J. Bakalyar, and W. L. Richards. “Strain-Based Deformation Shape-Estimation Algorithm for Control and Monitoring Applications”. In: *AIAA Journal* 51.9 (2013), pp. 2231–2240. DOI: [10.2514/1.J052215](https://doi.org/10.2514/1.J052215). URL: <https://doi.org/10.2514/1.J052215>.
- [63] M. Gherlone, P. Cerracchio, and M. Mattone. “Shape sensing methods: Review and experimental comparison on a wing-shaped plate”. In: *Progress in Aerospace Sciences* 99 (2018), pp. 14–26. ISSN: 0376-0421. DOI: [10.1016/j.paerosci.2018.04.001](https://doi.org/10.1016/j.paerosci.2018.04.001). URL: <http://www.sciencedirect.com/science/article/pii/S037604211730221X>.
- [64] L. Ljung. *System Identification: Theory for the User*. Pearson Education, 1997. ISBN: 9780132440530. URL: <https://www.pearson.com/us/higher-education/program/Ljung-System-Identification-Theory-for-the-User-2nd-Edition/PGM168305.html>.

- [65] S. Mustapha, Y. Hu, K. Nguyen, M. Alamdari, P. Runcie, U. Dackermann, V. Nguyen, J. Li, and L. Ye. “Pattern Recognition based on Time series Analysis using Vibration Data for Structural Health Monitoring in Civil Structures”. In: *Electronic Journal of Structural Engineering* (2015). ISSN: 1443-9255.
- [66] A. J. Yi, M. S. A. Majid, A. M. Nor, M. J. M. Ridzuan, and S. Yaacob. “Failure prediction of $\pm 55^\circ$ glass/epoxy composite pipes using system identification modelling”. In: *Journal of Physics: Conference Series* 908 (Oct. 2017), p. 012012. DOI: [10.1088/1742-6596/908/1/012012](https://doi.org/10.1088/1742-6596/908/1/012012). URL: <https://doi.org/10.1088/1742-6596/908/1/012012>.
- [67] A. Shazaib and A. L. Tamiru. “Remaining Useful Life Prediction of Gas Turbine Engine using Autoregressive Model”. In: *MATEC Web Conf.* 131 (2017), p. 04014. DOI: [10.1051/mateconf/201713104014](https://doi.org/10.1051/mateconf/201713104014). URL: <https://doi.org/10.1051/mateconf/201713104014>.
- [68] S. S. Haykin. *Neural networks and learning machines*. Third. Upper Saddle River, NJ: Pearson Education, 2009.
- [69] M. Hoffman. *A Neural Network Prototype for Predicting F-14B Strains at the BL 10 Longeron*. Report. Naval Air Warfare Center Aircraft Div Warminster PA Air Vehicle and Crew Systems Technology Dept, 1992.
- [70] X. Cao, Y. Sugiyama, and Y. Mitsui. “Application of artificial neural networks to load identification”. In: *Computers & Structures* 69.1 (1998), pp. 63–78. ISSN: 0045-7949. DOI: [https://doi.org/10.1016/S0045-7949\(98\)00085-6](https://doi.org/10.1016/S0045-7949(98)00085-6). URL: <https://www.sciencedirect.com/science/article/pii/S0045794998000856>.
- [71] H. Azzam. “A practical approach for the indirect prediction of structural fatigue from measured flight parameters”. In: *Proceedings of the Institution of Mechanical Engineers, Part G: Journal of Aerospace Engineering* 211.1 (1997), pp. 29–38. DOI: [10.1243/0954410971532479](https://doi.org/10.1243/0954410971532479). URL: <https://doi.org/10.1243/0954410971532479>.
- [72] O. Levinski. “Prediction of Buffet Loads on Twin Vertical Tail Using Vortex Method”. In: *Australian Department of Defence, Defence Science and Technology Organisation* (DSTO-RR-0217, 2001).
- [73] O. Levinski. “Use of Artificial Neural Networks for Buffet Loads Prediction”. English. In: *15th International Conference on Industrial and Engineering Applications of Artificial Intelligence and Expert Systems*. Cairns, Australia, June 2002.

- [74] P. M. Trivailo and C. L. Carn. “The inverse determination of aerodynamic loading from structural response data using neural networks”. In: *Inverse Problems in Science and Engineering* 14.4 (2006), pp. 379–395. DOI: [10.1080/17415970600573692](https://doi.org/10.1080/17415970600573692).
- [75] D. Wada and Y. Sugimoto. “Inverse analysis of aerodynamic loads from strain information using structural models and neural networks”. In: *Sensors and Smart Structures Technologies for Civil, Mechanical, and Aerospace Systems 2017*. Ed. by J. P. Lynch. Vol. 10168. International Society for Optics and Photonics. SPIE, 2017, pp. 227–233. URL: <https://doi.org/10.1117/12.2258583>.
- [76] S. B. Cooper and D. DiMaio. “Static load estimation using artificial neural network: Application on a wing rib”. In: *Advances in Engineering Software* 125 (2018), pp. 113–125. ISSN: 0965-9978. DOI: [10.1016/j.advengsoft.2018.01.007](https://doi.org/10.1016/j.advengsoft.2018.01.007). URL: <http://www.sciencedirect.com/science/article/pii/S0965997817301916>.
- [77] K. E. Niessen, D. O. Franke, and M. T. Corneliusen. “Analysis of static load calibration data using neural networks : case study”. In: *Proceedings of the AIAC18: 18th Australian International Aerospace Congress* (2019).
- [78] K. E. Niessen, D. O. Franke, and M. T. Corneliusen. “Prediction of in-flight loading using neural networks : case study”. In: *Proceedings of the AIAC18: 18th Australian International Aerospace Congress* (2019).
- [79] S. Shkarayev, R. Krashanitsa, and A. Tessler. “An Inverse Interpolation Method Utilizing In-Flight Strain Measurements for Determining Loads and Structural Response of Aerospace Vehicles”. In: *Proc. Third Int. Workshop on Structural Health Monitoring*. Stanford, 2001. URL: <https://ntrs.nasa.gov/api/citations/20040086071/downloads/20040086071.pdf>.
- [80] C. Coates, P. Thamburaj, and C. Kim. “An Inverse Method for Selection of Fourier Coefficients for Flight Load Identification”. In: *46th AIAA/ASME/ASCE/AHS/ASC Structures, Structural Dynamics and Materials Conference*. Austin, 2005. DOI: [10.2514/6.2005-2183](https://doi.org/10.2514/6.2005-2183). URL: <https://arc.aiaa.org/doi/abs/10.2514/6.2005-2183>.
- [81] C. W. Coates and P. Thamburaj. “Inverse Method Using Finite Strain Measurements to Determine Flight Load Distribution Functions”. In: *Journal of Aircraft* 45.2 (2008), pp. 366–370. DOI: [10.2514/1.21905](https://doi.org/10.2514/1.21905). URL: <https://doi.org/10.2514/1.21905>.
- [82] A. Airolidi, L. Marelli, P. Bettini, G. Sala, and A. Apicella. “Strain field reconstruction on composite spars based on the identification of equivalent load conditions”. In: *Sensors and Smart Structures Technologies for Civil, Mechanical, and Aerospace Systems 2017*. Ed. by J. P. Lynch. Vol. 10168.

- International Society for Optics and Photonics. SPIE, 2017, pp. 207–226. DOI: [10.1117/12.2260161](https://doi.org/10.1117/12.2260161). URL: <https://doi.org/10.1117/12.2260161>.
- [83] T. Nakamura, H. Igawa, and A. Kanda. “Inverse identification of continuously distributed loads using strain data”. In: *Aerospace Science and Technology* 23.1 (2012), pp. 75–84. ISSN: 1270-9638. DOI: <https://doi.org/10.1016/j.ast.2011.06.012>. URL: <http://www.sciencedirect.com/science/article/pii/S1270963811001052>.
- [84] D. Wada and Y. Sugimoto. “Inverse analysis of aerodynamic loads from strain information using structural models and neural networks”. In: *Sensors and Smart Structures Technologies for Civil, Mechanical, and Aerospace Systems 2017*. Ed. by J. P. Lynch. Vol. 10168. International Society for Optics and Photonics. SPIE, 2017, pp. 227–233. DOI: [10.1117/12.2258583](https://doi.org/10.1117/12.2258583). URL: <https://doi.org/10.1117/12.2258583>.
- [85] R. Penrose. “On best approximate solutions of linear matrix equations”. In: *Mathematical Proceedings of the Cambridge Philosophical Society* 52.1 (1956), pp. 17–19. DOI: [10.1017/S0305004100030929](https://doi.org/10.1017/S0305004100030929).
- [86] R. Cook. “Four-node ‘flat’ shell element: Drilling degrees of freedom, membrane-bending coupling, warped geometry, and behavior”. In: *Computers & Structures* 50.4 (1994), pp. 549–555. ISSN: 0045-7949. DOI: [10.1016/0045-7949\(94\)90025-6](https://doi.org/10.1016/0045-7949(94)90025-6). URL: <http://www.sciencedirect.com/science/article/pii/0045794994900256>.
- [87] A. Tessler and T. J. Hughes. “An improved treatment of transverse shear in the mindlin-type four-node quadrilateral element”. In: *Computer Methods in Applied Mechanics and Engineering* 39.3 (1983), pp. 311–335. ISSN: 0045-7825. DOI: [10.1016/0045-7825\(83\)90096-8](https://doi.org/10.1016/0045-7825(83)90096-8). URL: <https://www.sciencedirect.com/science/article/pii/0045782583900968>.
- [88] M. Li, Z. Wu, H. Yang, and H. Huang. “Direct damage index based on inverse finite element method for structural damage identification”. In: *Ocean Engineering* 221 (2021), p. 108545. ISSN: 0029-8018. DOI: [10.1016/j.oceaneng.2020.108545](https://doi.org/10.1016/j.oceaneng.2020.108545). URL: <https://www.sciencedirect.com/science/article/pii/S0029801820314530>.
- [89] J. Arpin-Pont, M. Gagnon, A. S. Tahan, A. Coutu, and D. Thibault. “Methodology for estimating strain gauge measurement biases and uncertainties on isotropic materials”. In: *The Journal of Strain Analysis for Engineering Design* 50.1 (2015), pp. 40–50. DOI: [10.1177/0309324714550116](https://doi.org/10.1177/0309324714550116).
- [90] W. Montero, R. Farag, V. Díaz, M. Ramirez, and B. L. Boada. “Uncertainties Associated with Strain-Measuring Systems Using Resistance Strain Gauges”. In: *The Journal of Strain Analysis for Engineering Design* 46.1 (2011), pp. 1–13. DOI: [10.1243/03093247JSA661](https://doi.org/10.1243/03093247JSA661).

- [91] S. Sriramula and M. K. Chryssanthopoulos. “Quantification of uncertainty modelling in stochastic analysis of FRP composites”. In: *Composites Part A: Applied Science and Manufacturing* 40.11 (2009), pp. 1673–1684. ISSN: 1359-835X. DOI: <https://doi.org/10.1016/j.compositesa.2009.08.020>. URL: <http://www.sciencedirect.com/science/article/pii/S1359835X09002577>.
- [92] M. D. McKay, R. J. Beckman, and W. J. Conover. “A Comparison of Three Methods for Selecting Values of Input Variables in the Analysis of Output from a Computer Code”. In: *Technometrics* 42.1 (2000), pp. 55–61. ISSN: 00401706. URL: <http://www.jstor.org/stable/1271432>.
- [93] A. Carvalho, T. A. Silva, and M. A. Loja. “Assessing Static and Dynamic Response Variability due to Parametric Uncertainty on Fibre-Reinforced Composites”. In: *Journal of Composites Science* 2.1 (2018). ISSN: 2504-477X. DOI: [10.3390/jcs2010006](https://doi.org/10.3390/jcs2010006). URL: <https://www.mdpi.com/2504-477X/2/1/6>.
- [94] M. Corradi, M. Gherlone, M. Mattone, and M. Di Sciuva. “A Comparative Study of Uncertainty Propagation Methods in Structural Problems”. In: *Computational Methods in Stochastic Dynamics: Volume 2*. Ed. by M. Papadrakakis, G. Stefanou, and V. Papadopoulos. Dordrecht: Springer Netherlands, 2013, pp. 87–111. ISBN: 978-94-007-5134-7. DOI: [10.1007/978-94-007-5134-7_6](https://doi.org/10.1007/978-94-007-5134-7_6). URL: https://doi.org/10.1007/978-94-007-5134-7_6.
- [95] S. Boyd and L. Vandenberghe. *Convex Optimization*. Cambridge University Press, 2004. DOI: [10.1017/CB09780511804441](https://doi.org/10.1017/CB09780511804441).
- [96] J. J. Moré and D. C. Sorensen. “Computing a Trust Region Step”. In: *SIAM Journal on Scientific and Statistical Computing* 4.3 (1983), pp. 553–572. DOI: [10.1137/0904038](https://doi.org/10.1137/0904038). URL: <https://doi.org/10.1137/0904038>.
- [97] T. Chen, H. Ohlsson, and L. Ljung. “On the estimation of transfer functions, regularizations and Gaussian processes—Revisited”. In: *Automatica* 48.8 (2012), pp. 1525–1535. ISSN: 0005-1098. DOI: <https://doi.org/10.1016/j.automatica.2012.05.026>. URL: <https://www.sciencedirect.com/science/article/pii/S0005109812001999>.
- [98] A. Juditsky, H. Hjalmarsson, A. Benveniste, B. Delyon, L. Ljung, J. Sjöberg, and Q. Zhang. “Nonlinear black-box models in system identification: Mathematical foundations”. In: *Automatica* 31.12 (1995). Trends in System Identification, pp. 1725–1750. ISSN: 0005-1098. DOI: [https://doi.org/10.1016/0005-1098\(95\)00119-1](https://doi.org/10.1016/0005-1098(95)00119-1). URL: <https://www.sciencedirect.com/science/article/pii/0005109895001191>.
- [99] M. H. Belae, M. Y. Hagan, and H. B. Deuth. *MATLAB: Neural Network Toolbox User Guide R2018a*. Mathworks, 2018.

- [100] H. Meng, N. Bianchi-Berthouze, Y. Deng, J. Cheng, and J. P. Cosmas. “Time-Delay Neural Network for Continuous Emotional Dimension Prediction From Facial Expression Sequences”. In: *IEEE Transactions on Cybernetics* 46.4 (2016), pp. 916–929. DOI: [10.1109/TCYB.2015.2418092](https://doi.org/10.1109/TCYB.2015.2418092).
- [101] E. A. Wan. “Finite Impulse Response Neural Networks with Applications in Time Series Prediction”. PhD thesis. Stanford University, 1993.
- [102] D. Marquardt. “An Algorithm for Least-Squares Estimation of Nonlinear Parameters”. In: *SIAM Journal on Applied Mathematics* 11.2 (1963), pp. 431–441. URL: <http://www.jstor.org/stable/2098941>.
- [103] D. J. C. MacKay. “A Practical Bayesian Framework for Backpropagation Networks”. In: *Neural Computation* 4.3 (1992), pp. 448–472. DOI: [doi:10.1162/neco.1992.4.3.448](https://doi.org/10.1162/neco.1992.4.3.448). URL: <http://dx.doi.org/10.1162/neco.1992.4.3.448>.
- [104] M. J. Candon, O. Levinski, A. Altaf, R. Carrese, and P. Marzocca. “Aircraft Transonic Buffet Load Prediction using Artificial Neural Networks”. In: *AIAA Scitech 2019 Forum*. DOI: [10.2514/6.2019-0763](https://doi.org/10.2514/6.2019-0763). URL: <https://arc.aiaa.org/doi/abs/10.2514/6.2019-0763>.
- [105] M. J. Candon, M. Esposito, O. Levinski, N. Joseph, S. Koschel, R. Carrese, and P. Marzocca. “On the Application of a Long-Short-Term Memory Deep Learning Architecture for Aircraft Transonic Buffet Loads Monitoring”. In: *AIAA Scitech 2020 Forum*. DOI: [10.2514/6.2020-0702](https://doi.org/10.2514/6.2020-0702). URL: <https://arc.aiaa.org/doi/abs/10.2514/6.2020-0702>.
- [106] ASTM E1049-85(2017). *Standard Practices for Cycle Counting in Fatigue Analysis*. ASTM international. 2017. DOI: [10.1520/E1049-85R17](https://doi.org/10.1520/E1049-85R17).
- [107] E. Turco. “Load distribution modelling for pin-jointed trusses by an inverse approach”. In: *Computer Methods in Applied Mechanics and Engineering* 165.1 (1998), pp. 291–306. ISSN: 0045-7825. DOI: [10.1016/S0045-7825\(98\)80013-3](https://doi.org/10.1016/S0045-7825(98)80013-3). URL: <http://www.sciencedirect.com/science/article/pii/S0045782598800133>.
- [108] C. Hua. “An inverse transformation for quadrilateral isoparametric elements: Analysis and application”. In: *Finite Elements in Analysis and Design* 7.2 (1990), pp. 159–166. ISSN: 0168-874X. DOI: [https://doi.org/10.1016/0168-874X\(90\)90007-2](https://doi.org/10.1016/0168-874X(90)90007-2). URL: <http://www.sciencedirect.com/science/article/pii/0168874X90900072>.

Appendix A

Shape functions

The shape functions for the iQS4 element are the following:

$$N_1 = \frac{(1-s)(1-t)}{4} \quad (\text{A.1})$$

$$N_2 = \frac{(1+s)(1-t)}{4} \quad (\text{A.2})$$

$$N_3 = \frac{(1+s)(1+t)}{4} \quad (\text{A.3})$$

and

$$L_1 = y_{14}N_8 - y_{21}N_5 \quad (\text{A.4})$$

$$L_2 = y_{21}N_5 - y_{32}N_6 \quad (\text{A.5})$$

$$L_3 = y_{32}N_6 - y_{43}N_7 \quad (\text{A.6})$$

$$L_4 = y_{43}N_7 - y_{14}N_8 \quad (\text{A.7})$$

$$M_1 = x_{41}N_8 - x_{12}N_5 \quad (\text{A.8})$$

$$M_2 = x_{12}N_5 - x_{23}N_6 \quad (\text{A.9})$$

$$M_3 = x_{23}N_6 - x_{34}N_7 \quad (\text{A.10})$$

$$M_4 = x_{34}N_7 - x_{41}N_8 \quad (\text{A.11})$$

where

$$N_5 = \frac{(1 - s^2)(1 - t)}{4} \quad (\text{A.12})$$

$$N_6 = \frac{(1 + s)(1 - t^2)}{4} \quad (\text{A.13})$$

$$N_7 = \frac{(1 - s^2)(1 + t)}{4} \quad (\text{A.14})$$

$$N_8 = \frac{(1 - s)(1 - t^2)}{4} \quad (\text{A.15})$$

The shape functions are expressed in terms of the local coordinates of the nodes of the iQS4 element:

$$\left. \begin{array}{l} x_{ij} = x_i - x_j \\ y_{ij} = y_i - y_j \end{array} \right\} \quad (i = 1, 2, 3, 4) \quad (j = 1, 2, 3, 4) \quad (\text{A.16})$$

and the parent space coordinates $s, t \in [-1, 1]$.

Appendix B

Pressure distribution

The pressure distribution is obtained by multiplying a third order polynomial of x and a second order polynomial of y :

$$p(x, y) = p_1(x) \cdot p_2(y) = (a_x x^3 + b_x x^2 + c_x x + d_x) \cdot (a_y y^2 + b_y y + c_y) \quad (\text{B.1})$$

To find the coefficients of the polynomials it is necessary to impose the conditions described in Section 7.2.2. They can be expressed mathematically as follows. The three conditions necessary to find the three coefficients of the $p_2(y)$ polynomial are:

$$\begin{cases} p_2(y = 994) = 0 & p_2 \text{ equal to 0 at the tip section} \\ p_2(y = 0) = 1 & p_2 \text{ is equal to 1 at the root section} \\ p_{2,y}(y = 0) = 0 & p_2 \text{ has a maximum at the root section} \end{cases} \quad (\text{B.2})$$

The four conditions necessary to find the four coefficients of the $p_1(x)$ polynomial are:

$$\begin{cases} p_1\left(x = \frac{528.52}{994}y\right) = 0 & p_1 \text{ equal to 0 at the leading edge} \\ p_1\left(x = \frac{270.52}{994}y + 378\right) = 0 & p_1 \text{ equal to 0 at the trailing edge} \\ p_1\left(x = \frac{618.69}{994}y + 126\right) = 1 & p_1 \text{ equal to 1 at one third of the chord} \\ p_{1,x}\left(x = \frac{618.69}{994}y + 126\right) = 0 & p_1 \text{ has a max. at one third of the chord} \end{cases} \quad (\text{B.3})$$

where $(x = \frac{528.52}{994}y + 378)$ is the equation of the leading edge, $(x = \frac{270.52}{994}y + 378)$ is the equation of the trailing edge and $(x = \frac{618.69}{994}y + 126)$ is the equation of locus of the points at one-third of the chords.

Since the wing box's panel is swept, the leading edge, the trailing edge and the point at one third of the chord have different x values for every y section of the wing panel. Therefore, the coefficients of the $p_1(x)$ polynomial depend on the y coordinate, as expressed in Eqs. B.3, and they have to be computed for each value of y .

Appendix C

Experimental strain measurements

In this appendix the strain measurement from the three performed experiment are reported. For every experiment, the strains from the fibres are compared, if possible, with the one computed with the high fidelity FE model. In the graph that report the sensed strains also the %*ERMS* error between the experimentally measures strains and the simulated ones are noted.

C.1 C-Beam

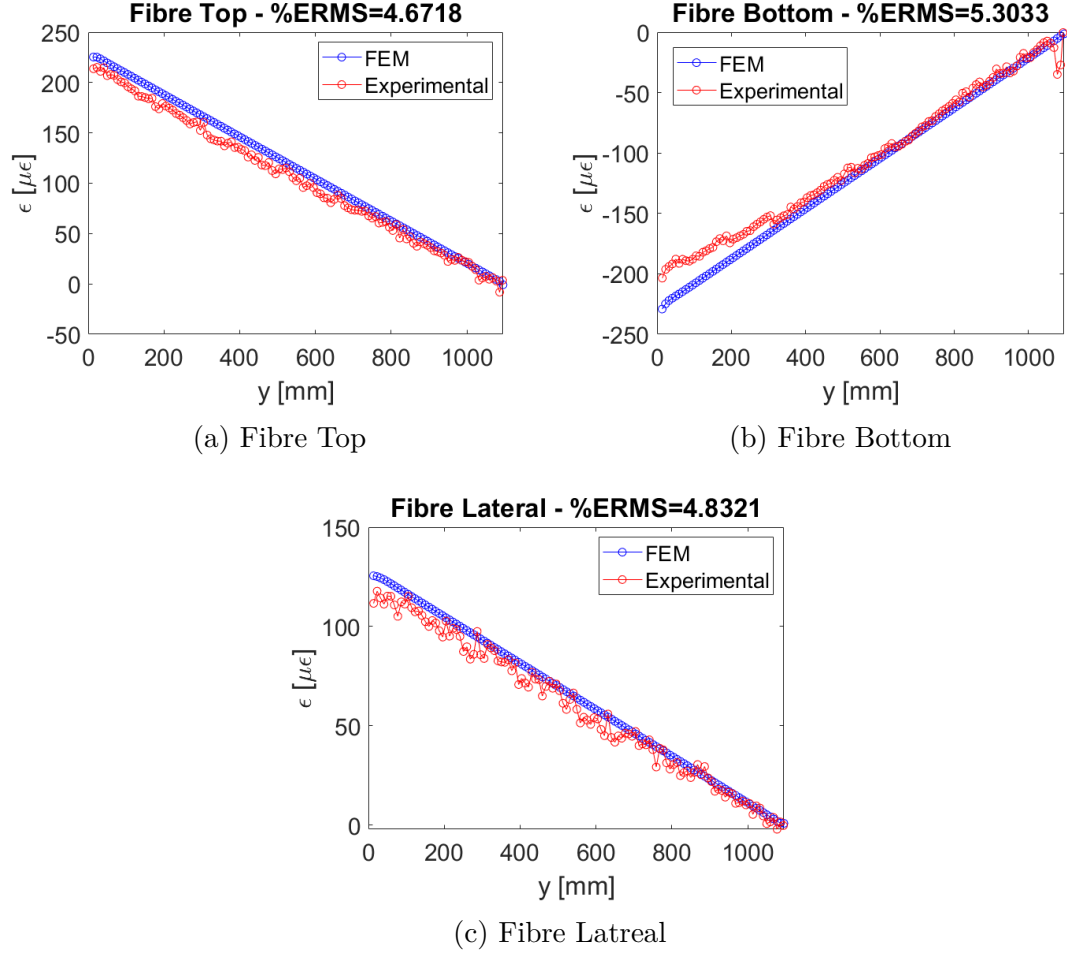


Figure C.1: Experimental strains for Load case 1 - The strains from the fibres and the ones from the refined model are reported.

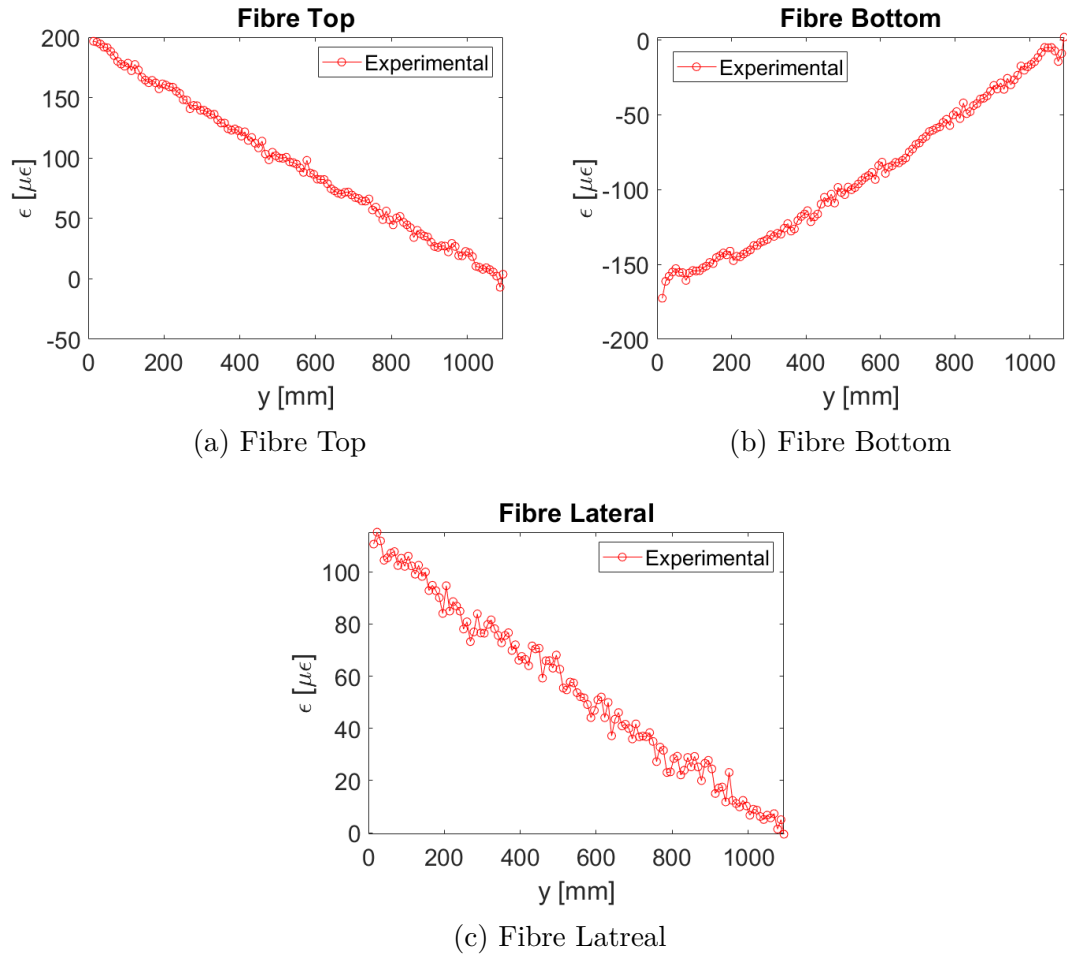


Figure C.2: Experimental strains for Load case 2 - The strains from the fibres are reported. Since in this case no simulation has been performed, the strains from the high-fidelity model are not reported

C.2 Stiffened panel

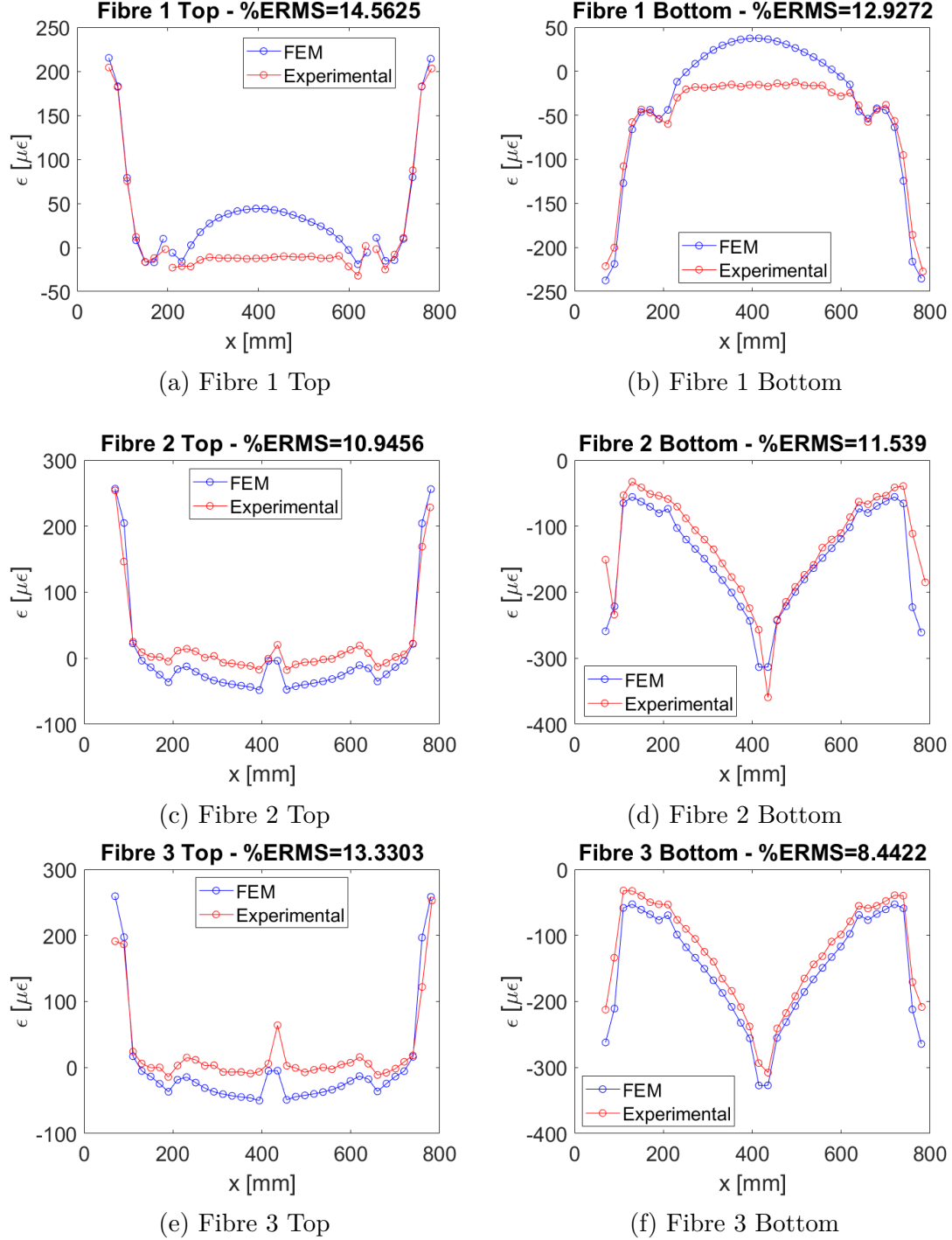


Figure C.3: Experimental strains from the stiffened panel - The numbering of the fibres is the one reported in Figure 8.14.

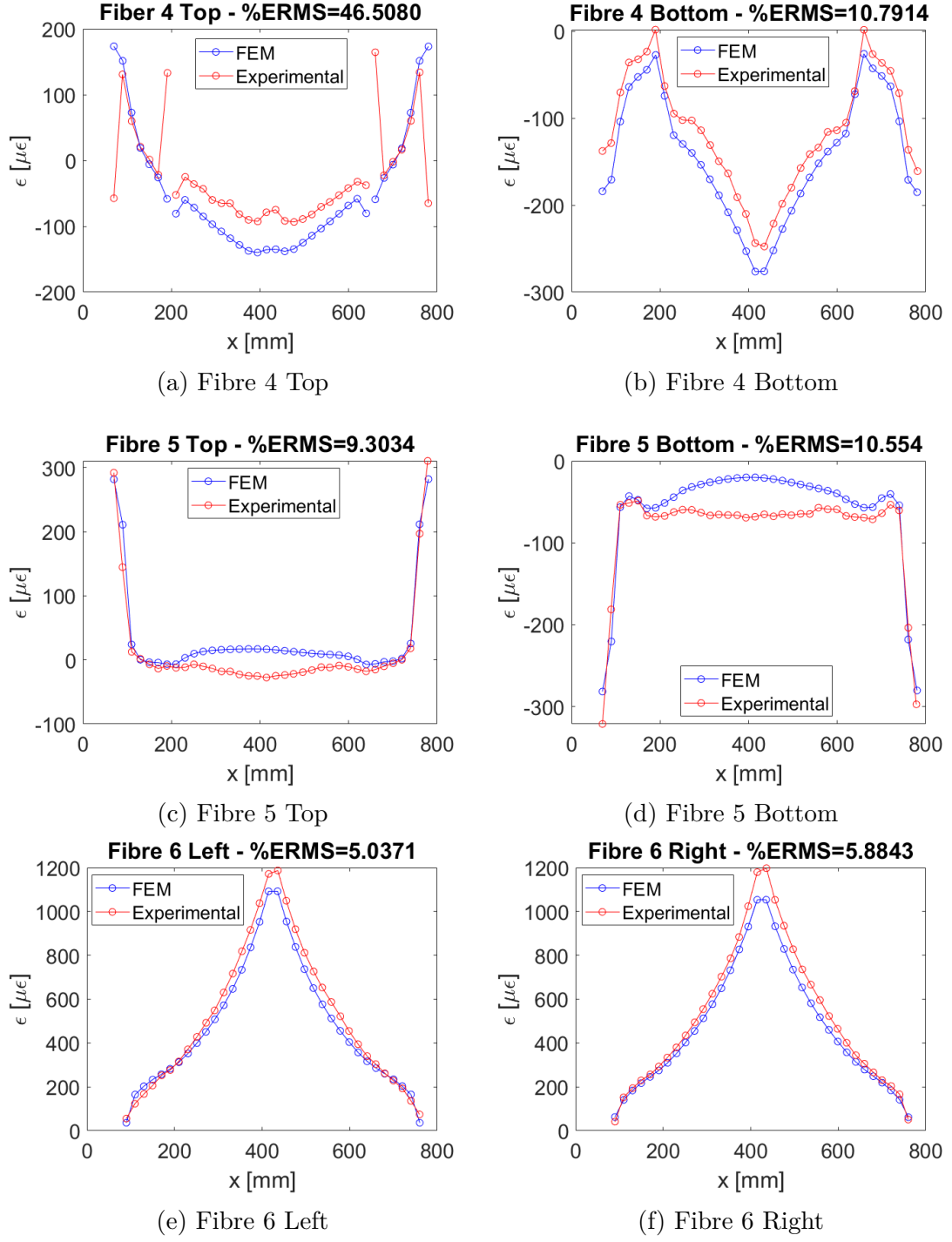


Figure C.4: Experimental strains from the stiffened panel - The numbering of the fibres is the one reported in Figure 8.14.

C.3 Swept aluminium wing box

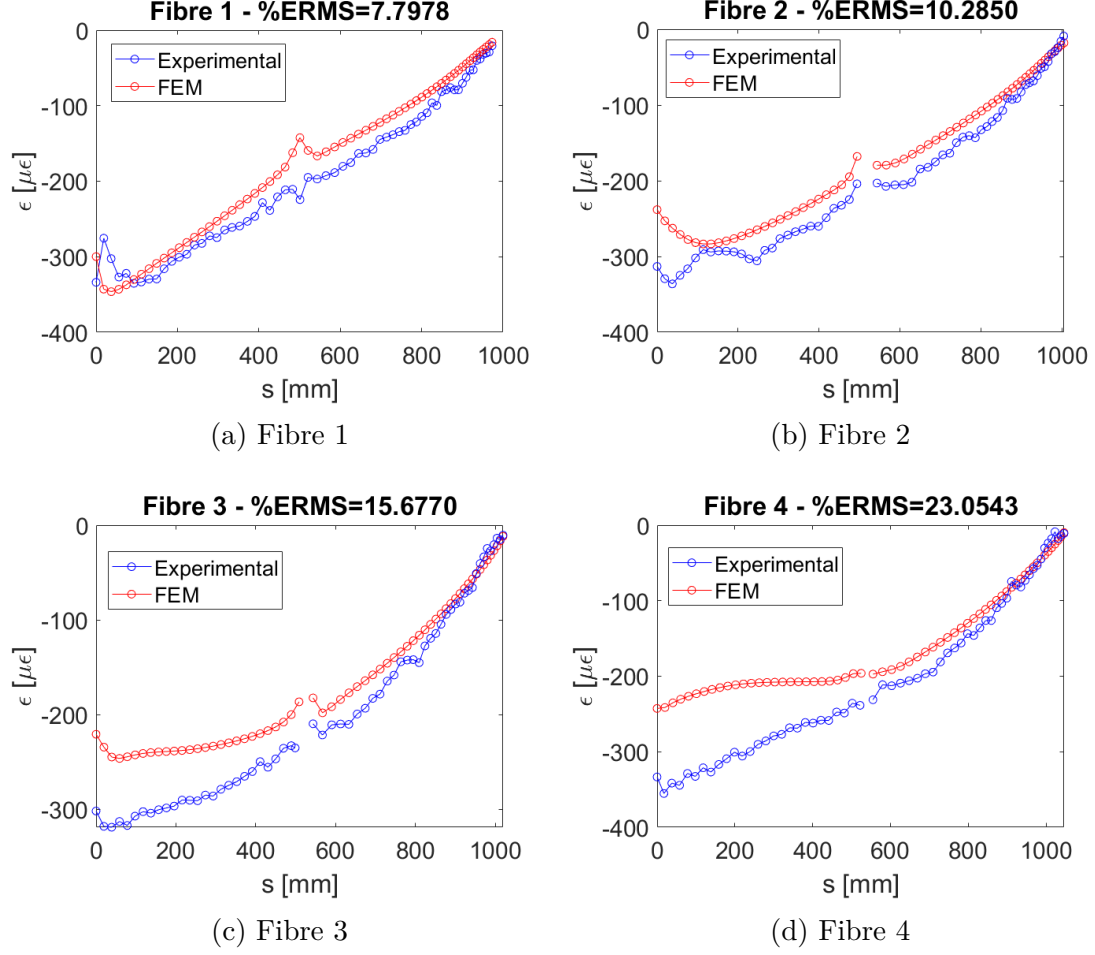


Figure C.5: Experimental strains from the upper panel of the swept aluminium wing box - The numbering of the fibres is the one reported in Figure 8.21 and s is the coordinate along the fibres' length.

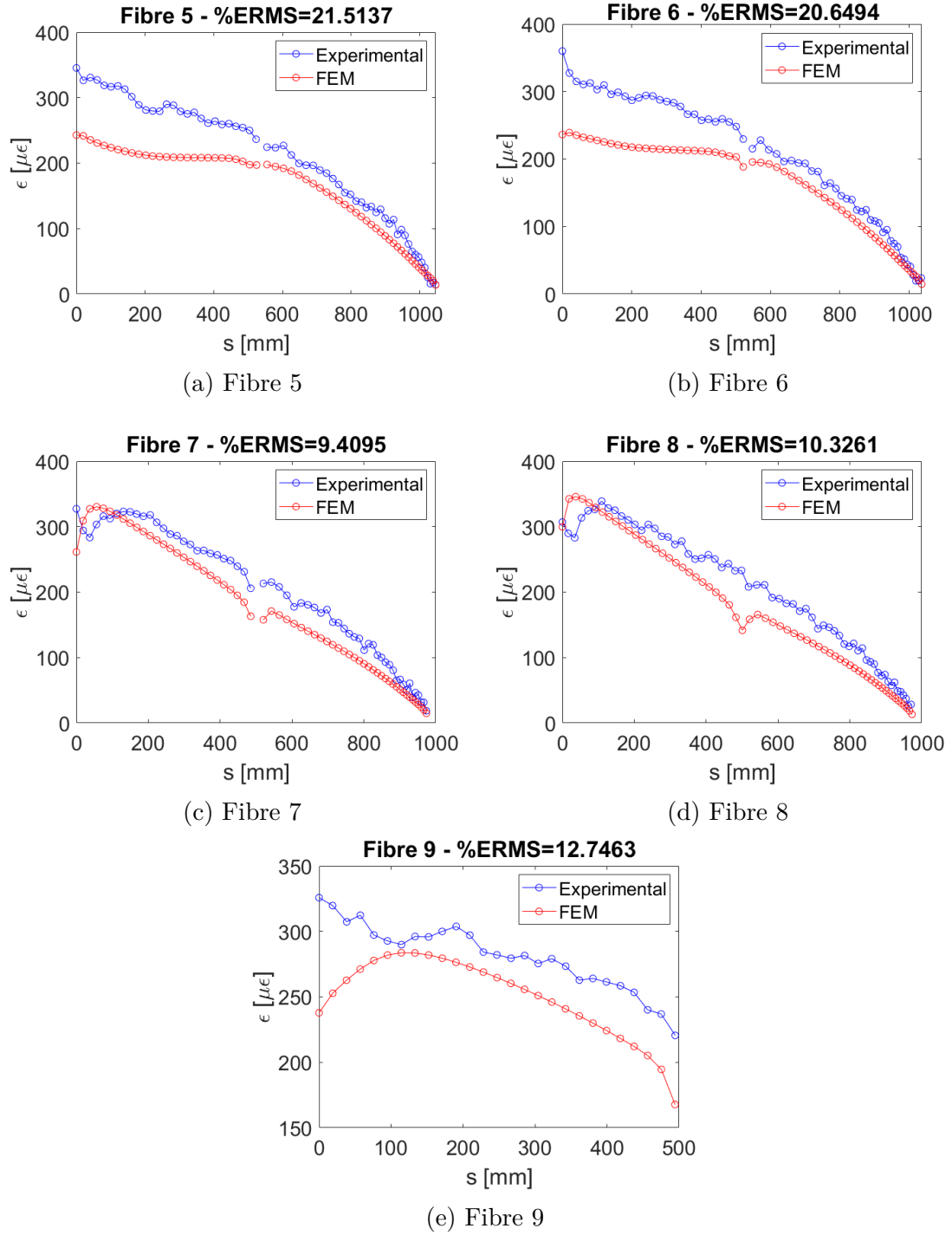
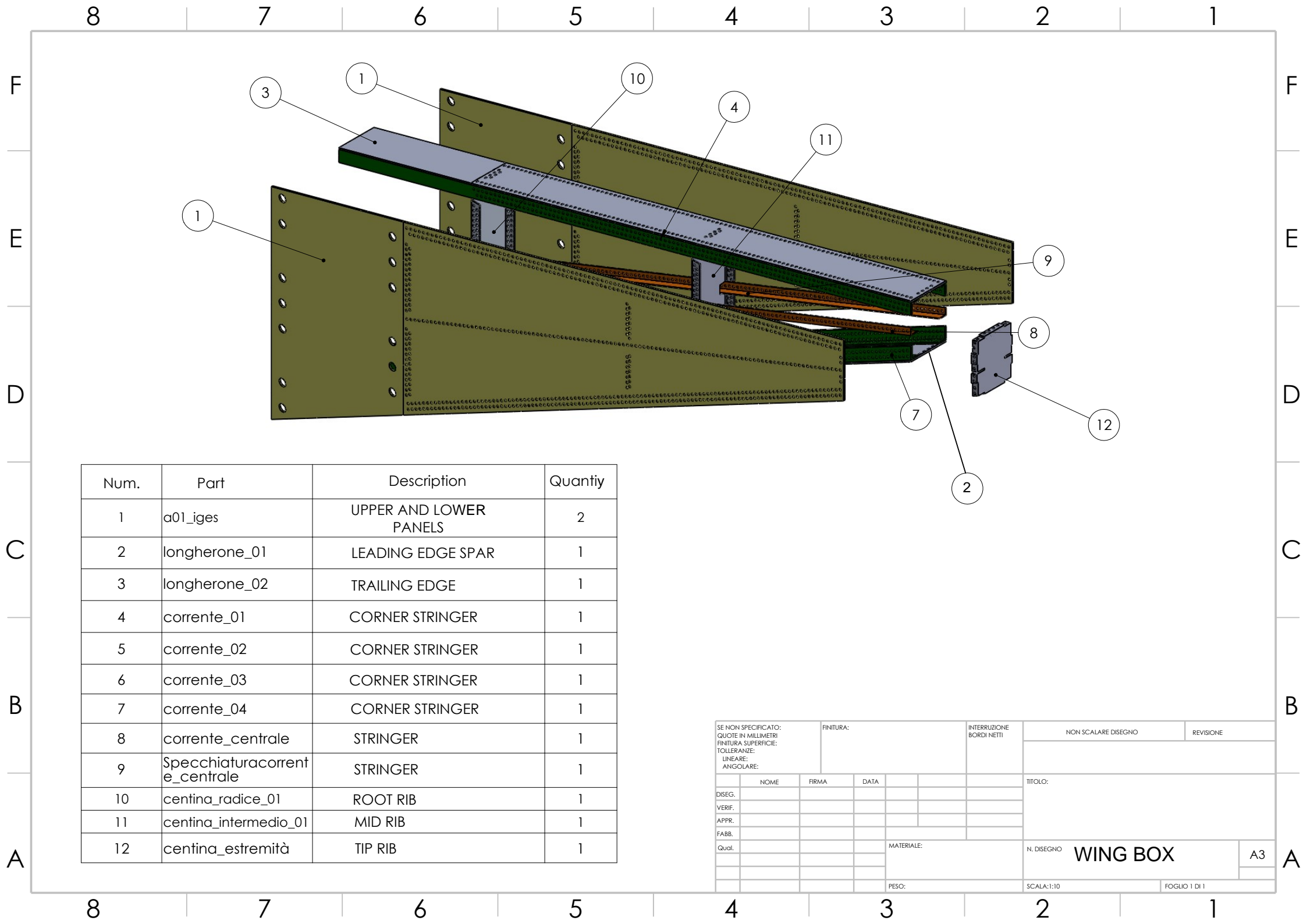


Figure C.6: Experimental strains from the lower panel of the swept aluminium wing box - The numbering of the fibres is the one reported in Figure 8.21 and s is the coordinate along the fibres' length.

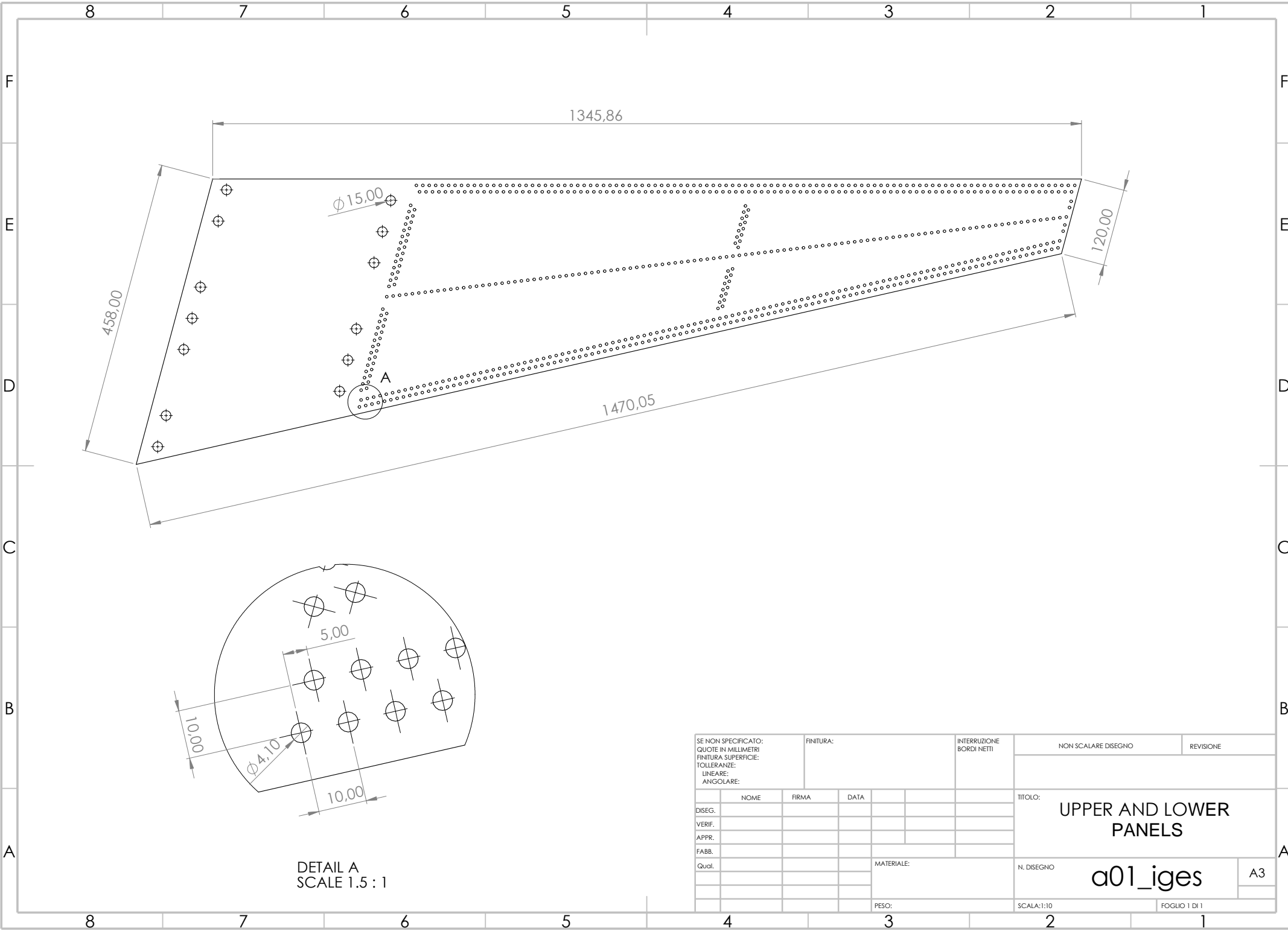
Appendix D

Swept wing box technical drawings

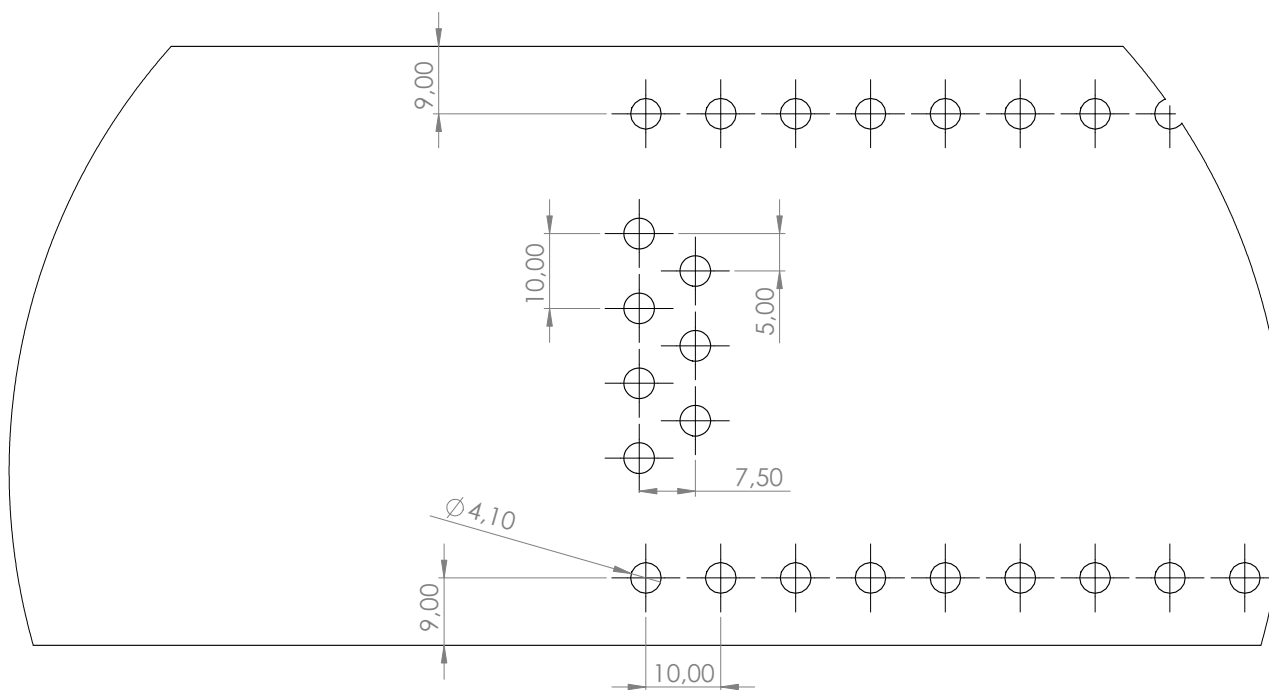


Num.	Part	Description	Quantity
1	a01_iges	UPPER AND LOWER PANELS	2
2	longherone_01	LEADING EDGE SPAR	1
3	longherone_02	TRAILING EDGE	1
4	corrente_01	CORNER STRINGER	1
5	corrente_02	CORNER STRINGER	1
6	corrente_03	CORNER STRINGER	1
7	corrente_04	CORNER STRINGER	1
8	corrente_centrale	STRINGER	1
9	Specchiaturacorrente_centrale	STRINGER	1
10	centina_radice_01	ROOT RIB	1
11	centina_intermedio_01	MID RIB	1
12	centina_estremità	TIP RIB	1

SE NON SPECIFICATO: QUOTE IN MILLIMETRI FINITURA SUPERFICIE: TOLLERANZE: LINEARE: ANGOLARE:		FINITURA:		INTERRUZIONE BORDI NETTI		NON SCALARE DISEGNO		REVISIONE	
NOME		FIRMA		DATA		TITOLO:			
DISEG.									
VERIF.									
APPR.									
FABB.									
Qual.						MATERIALE:		N. DISEGNO	
								WING BOX	
								A3	
						PESO:		SCALA:1:10	
								FOGLIO 1 DI 1	

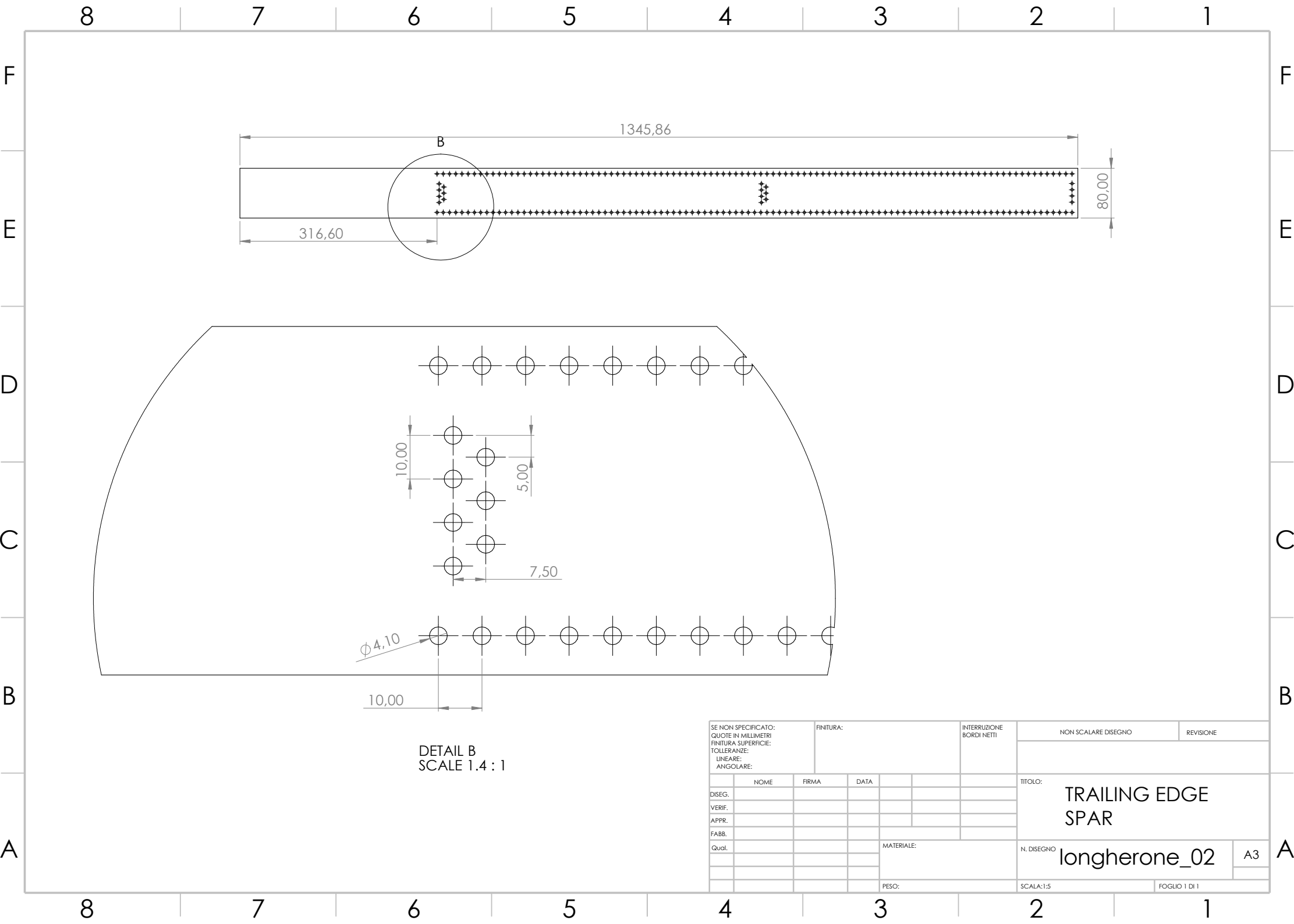


SE NON SPECIFICATO: QUOTE IN MILLIMETRI FINITURA SUPERFICIE: TOLLERANZE: LINEARE: ANGOLARE:				FINITURA:		INTERRUZIONE BORDI NETTI		NON SCALARE DISEGNO		REVISIONE	
		NOME	FIRMA	DATA				TITOLO: UPPER AND LOWER PANELS			
DISEG.											
VERIF.											
APPR.											
FABB.								N. DISEGNO a01_iges			
Qual.					MATERIALE:						
					PESO:			SCALA:1:10		FOGLIO 1 DI 1	

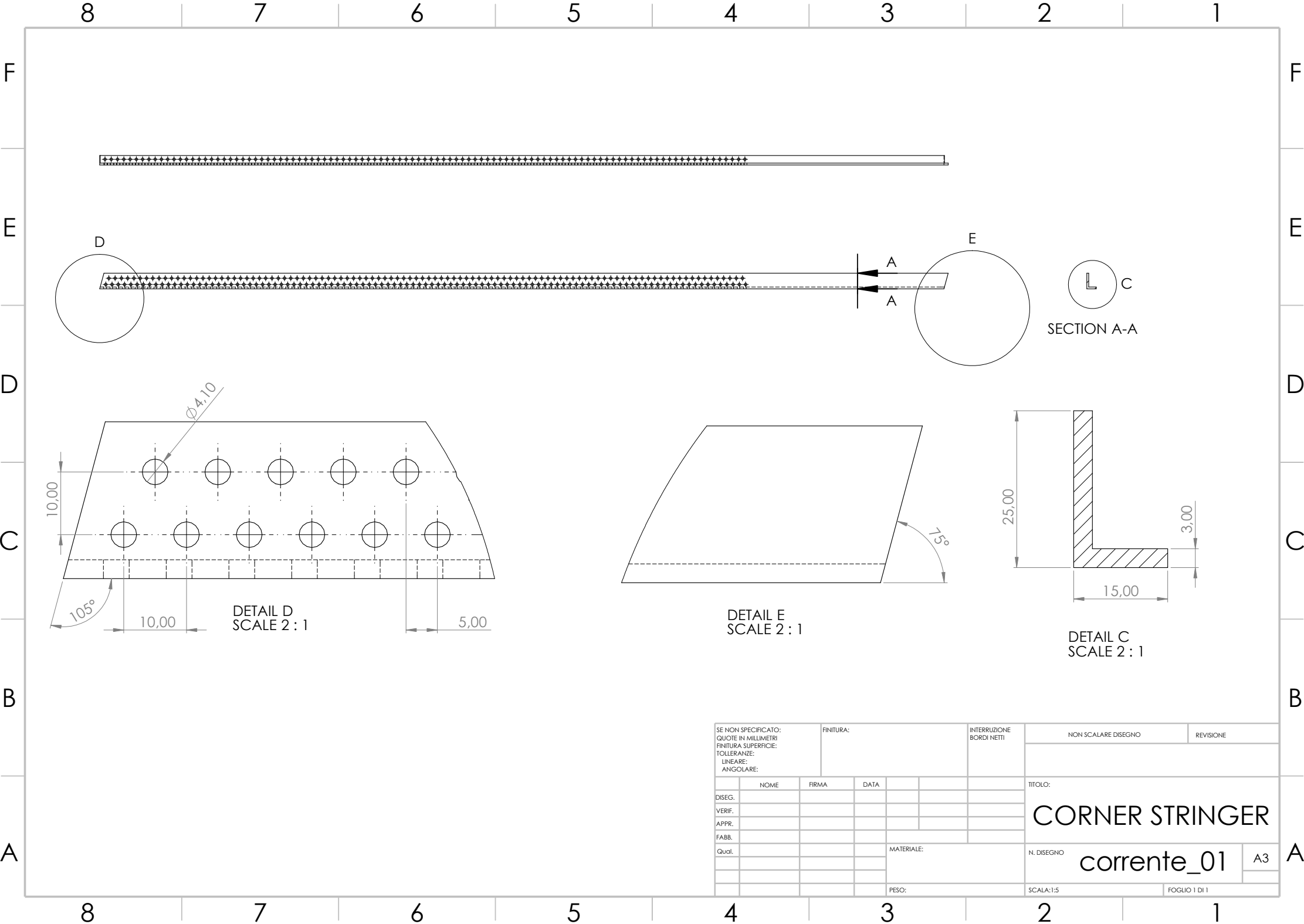


DETAIL A
SCALE 1.4 : 1

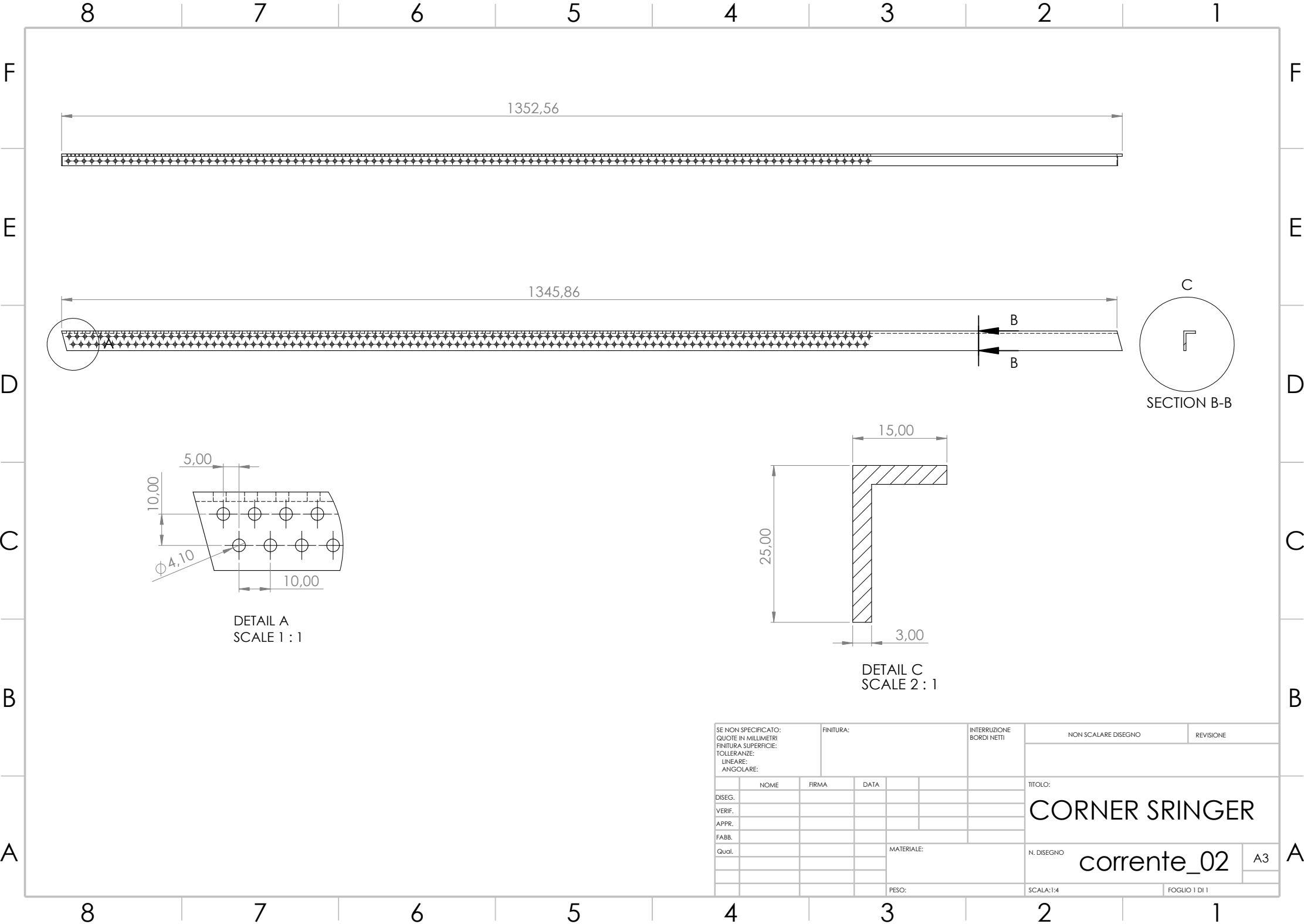
SE NON SPECIFICATO: QUOTE IN MILLIMETRI FINITURA SUPERFICIE: TOLLERANZE: LINEARE: ANGOLARE:		FINITURA:		INTERRUZIONE BORDI NETTI		NON SCALARE DISEGNO		REVISIONE	
						TITOLO: LEADING EDGE SPAR			
DISEG.		NOME		FIRMA		DATA			
VERIF.									
APPR.									
FABB.									
Qual.						MATERIALE:		N. DISEGNO	
								longherone_01	
								A3	
						PESO:		SCALA:1:5	
								FOGLIO 1 DI 1	



SE NON SPECIFICATO: QUOTE IN MILLIMETRI FINITURA SUPERFICIE: TOLLERANZE: LINEARE: ANGOLARE:				FINITURA:		INTERRUZIONE BORDI NETTI	NON SCALARE DISEGNO		REVISIONE		
	NOME	FIRMA	DATA				TITOLO: TRAILING EDGE SPAR				
DISEG.											
VERIF.											
APPR.											
FABB.											
Qual.											
						MATERIALE:	N. DISEGNO	longherone_02		A3	
						PESO:	SCALA:1:5	FOGLIO 1 DI 1			



SE NON SPECIFICATO: QUOTE IN MILLIMETRI FINITURA SUPERFICIE: TOLLERANZE: LINEARE: ANGOLARE:				FINITURA:		INTERRUZIONE BORDI NETTI	NON SCALARE DISEGNO		REVISIONE		
	NOME	FIRMA	DATA				TITOLO:				
DISEG.							CORNER STRINGER				
VERIF.											
APPR.							N. DISEGNO				
FABB.											
Qual.				MATERIALE:			corrente_01				A3
							SCALA:1:5				FOGLIO 1 DI 1
				PESO:							



SE NON SPECIFICATO: QUOTE IN MILLIMETRI FINITURA SUPERFICIE: TOLLERANZE: LINEARE: ANGOLARE:				FINITURA:		INTERRUZIONE BORDI NETTI	NON SCALARE DISEGNO		REVISIONE		
	NOME	FIRMA	DATA				TITOLO:				
DISEG.							CORNER SRINGER				
VERIF.											
APPR.							N. DISEGNO				
FABB.											
Qual.				MATERIALE:			corrente_02		A3		
							SCALA:1:4		FOGLIO 1 DI 1		
				PESO:							

F

E

D

C

B

A

F

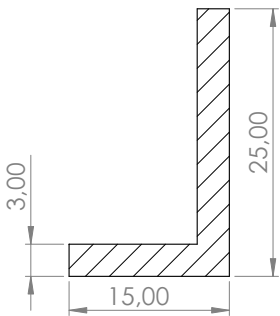
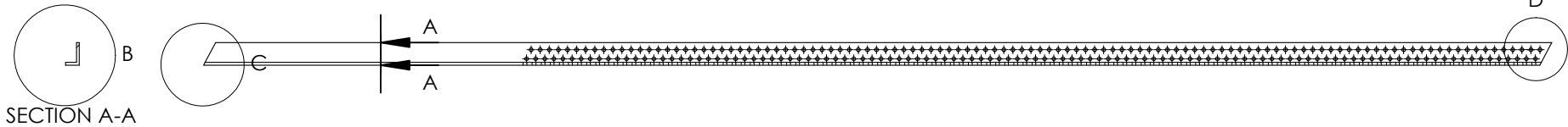
E

D

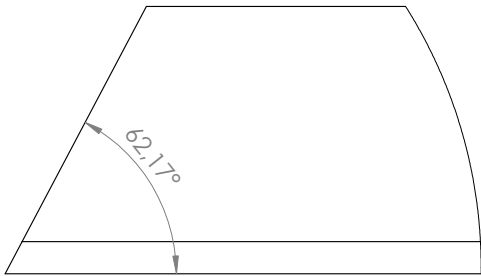
C

B

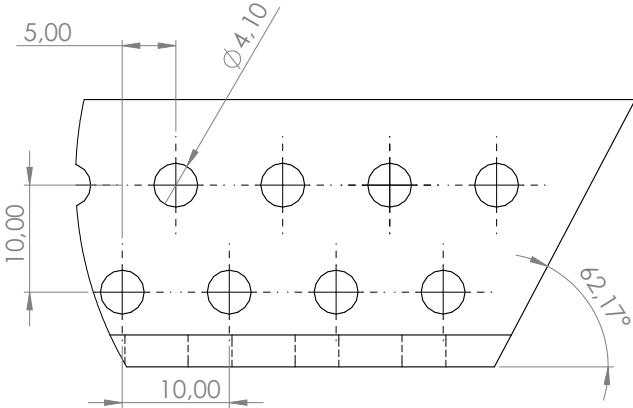
A



DETAIL B
SCALE 2 : 1

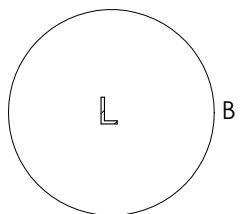


DETAIL C
SCALE 2 : 1

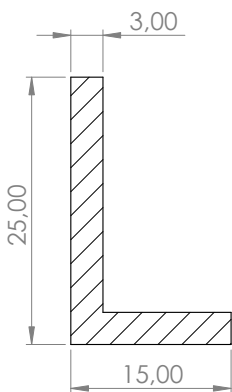


DETAIL D
SCALE 2 : 1

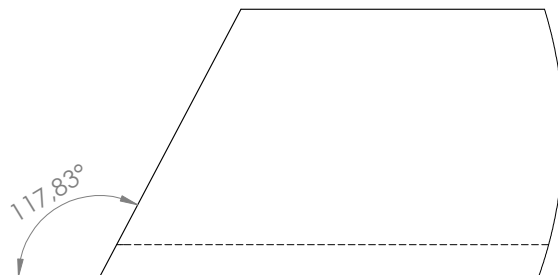
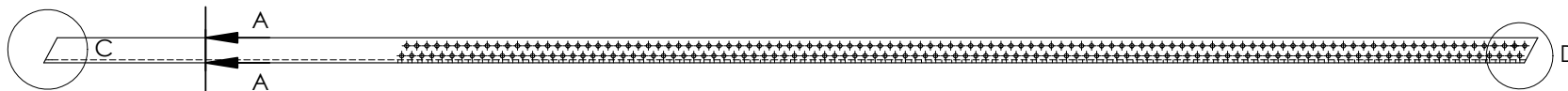
SE NON SPECIFICATO: QUOTE IN MILLIMETRI FINITURA SUPERFICIE: TOLLERANZE: LINEARE: ANGOLARE:			FINITURA:			INTERRUZIONE BORDI NETTI		NON SCALARE DISEGNO		REVISIONE
DISEG.		NOME	FIRMA	DATA				TITOLO: CORNER STRINGER		
VERIF.										
APPR.								N. DISEGNO corrente_03		
FABB.										
Qual.							MATERIALE:	SCALA:1:5		
							PESO:	FOGLIO 1 DI 1		



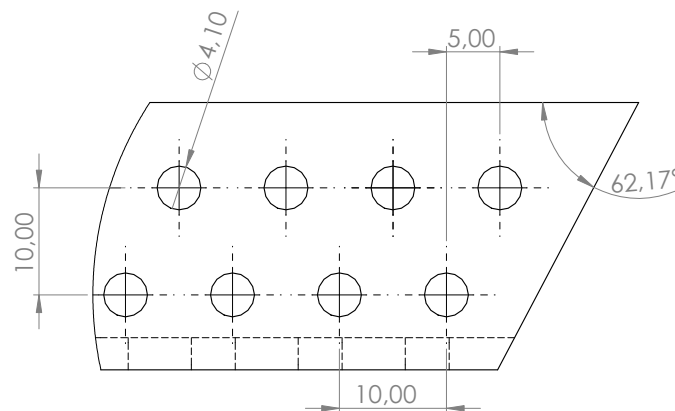
SECTION A-A



DETAIL B
SCALE 2 : 1

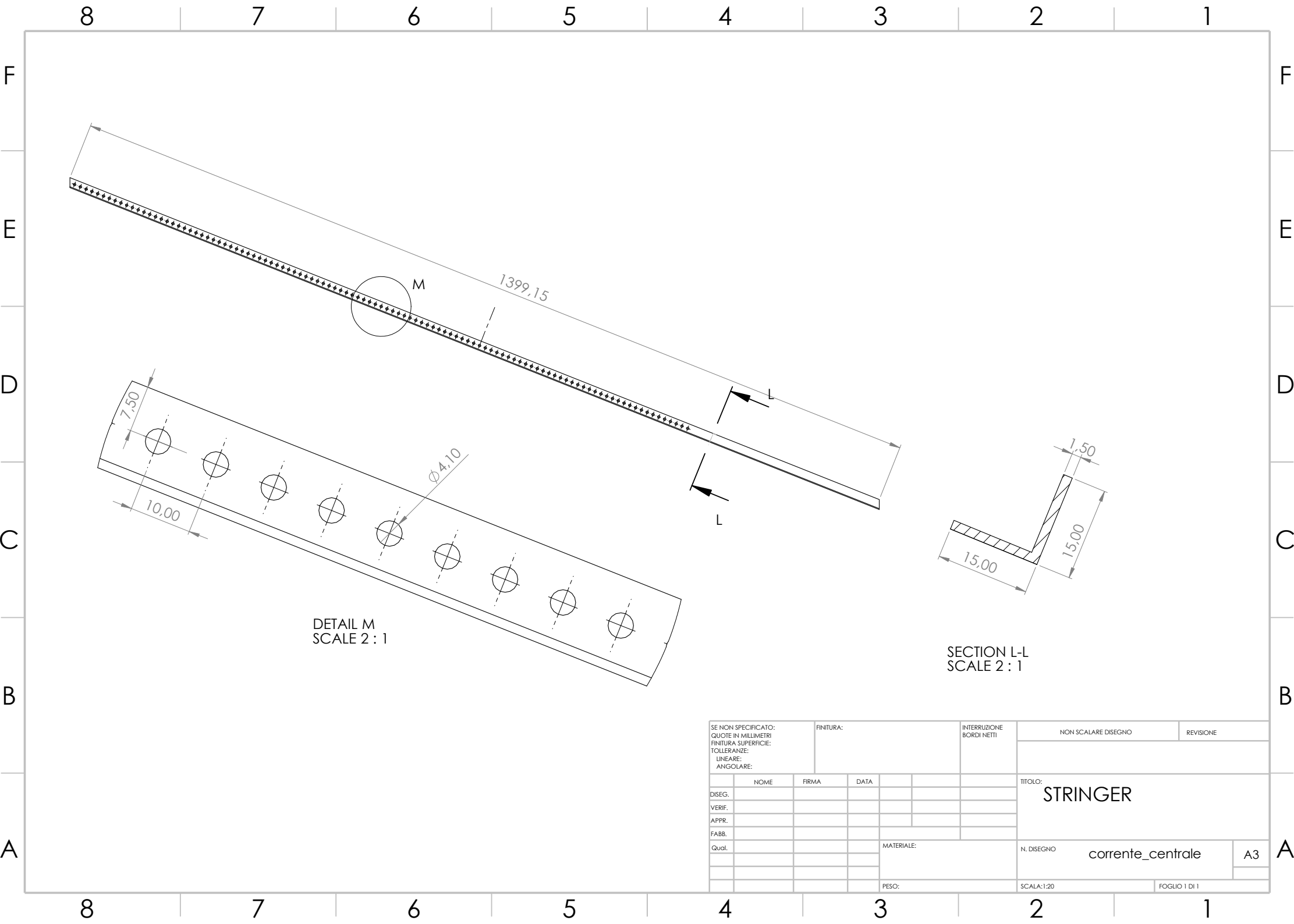


DETAIL C
SCALE 2 : 1

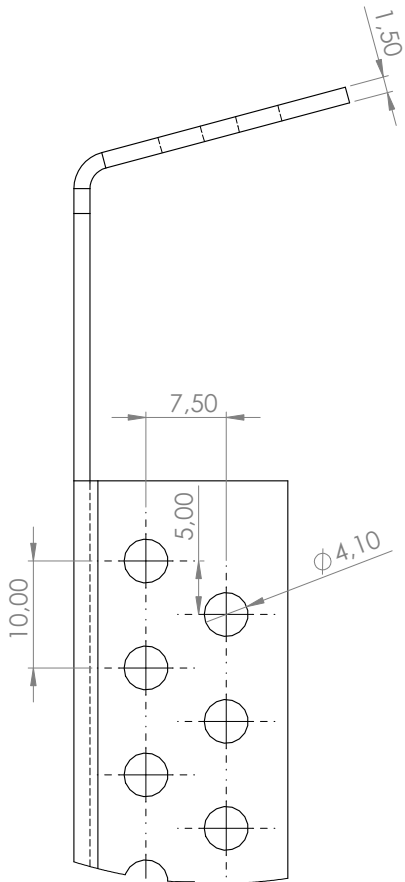


DETAIL D
SCALE 2 : 1

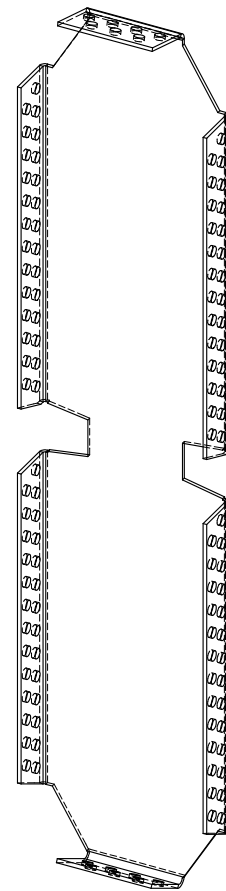
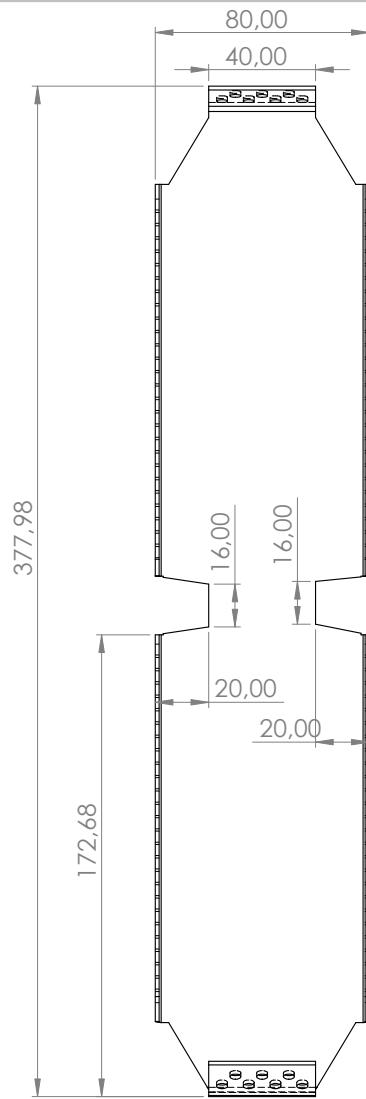
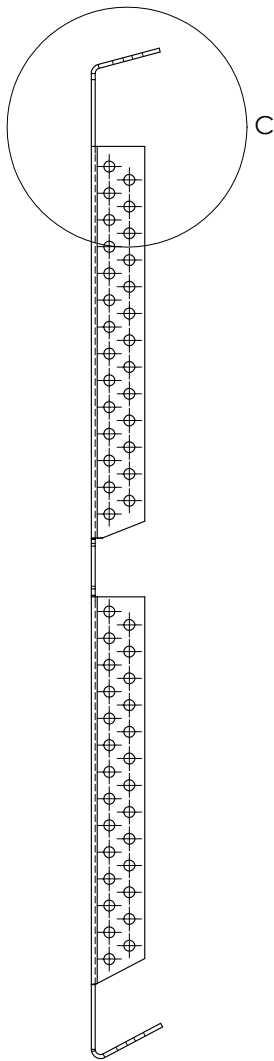
SE NON SPECIFICATO: QUOTE IN MILLIMETRI FINITURA SUPERFICIE: TOLLERANZE: LINEARE: ANGOLARE:				FINITURA:		INTERRUZIONE BORDI NETTI		NON SCALARE DISEGNO	REVISIONE
DISEG.	NOME	FIRMA	DATA					TITOLO:	
VERIF.								CORNER STRINGER	
APPR.									
FABB.									
Qual.						MATERIALE:		N. DISEGNO	
								corrente_04	
								A3	
						PESO:		SCALA:1:5	
								FOGLIO 1 DI 1	



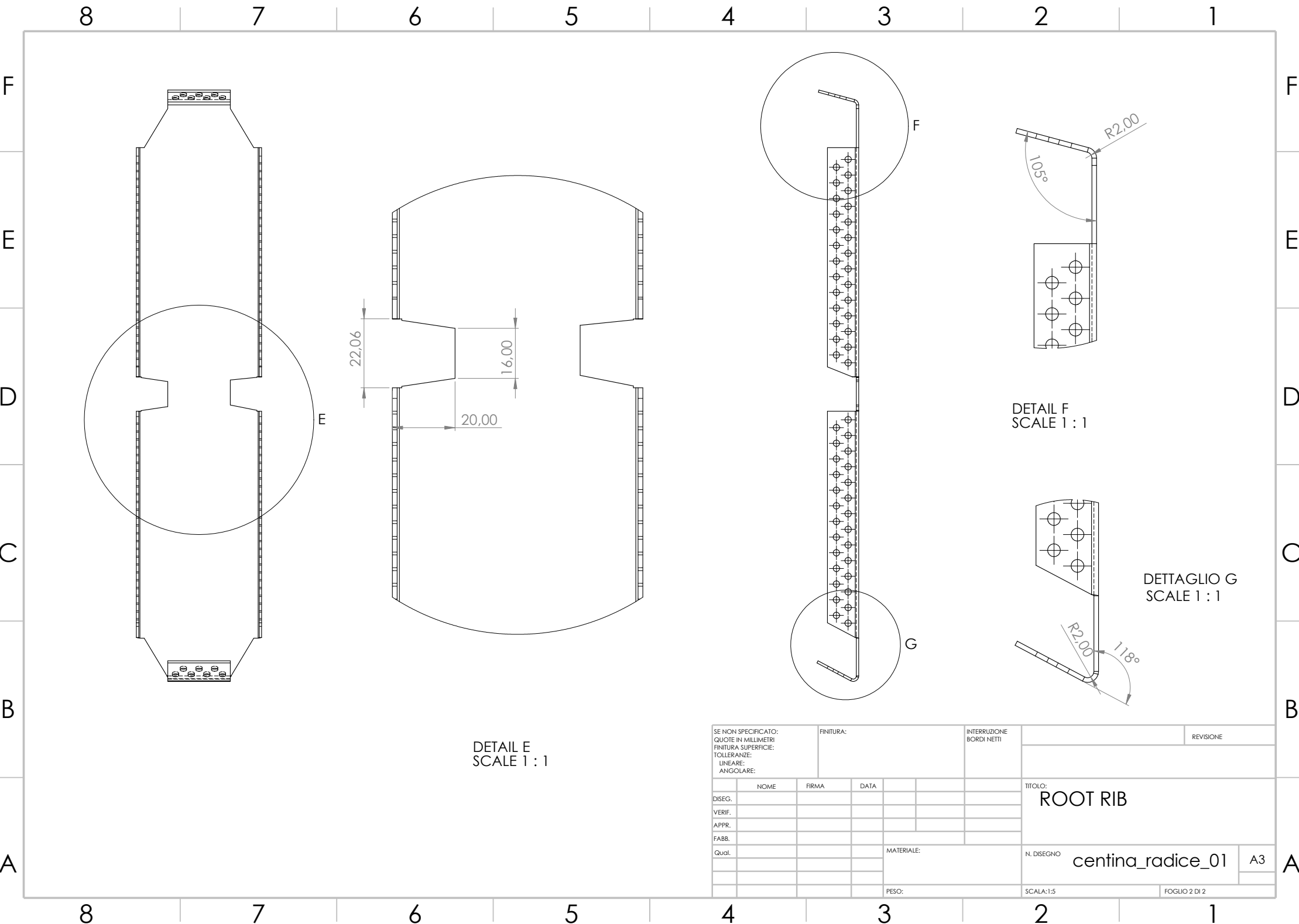
SE NON SPECIFICATO: QUOTE IN MILLIMETRI FINITURA SUPERFICIE: TOLLERANZE: LINEARE: ANGOLARE:				FINITURA:		INTERRUZIONE BORDI NETTI	NON SCALARE DISEGNO	REVISIONE
	NOME	FIRMA	DATA				TITOLO: STRINGER	
DISEG.								
VERIF.								
APPR.								
FABB.								
Qual.				MATERIALE:			N. DISEGNO	corrente_centrale
								A3
				PESO:			SCALA: 1:20	FOGLIO 1 DI 1



DETAIL C
SCALE 2 : 1



SE NON SPECIFICATO: QUOTE IN MILLIMETRI FINITURA SUPERFICIE: TOLLERANZE: LINEARE: ANGOLARE:						FINITURA:		INTERRUZIONE BORDI NETTI		NON SCALARE DISEGNO			REVISIONE	
		NOME		FIRMA		DATA						TITOLO:		
DISEG.												ROOT RIB		
VERIF.												N. DISEGNO centina_radice_01		
APPR.														
FABB.														
Qual.														
								MATERIALE:				A3		
								PESO:		SCALA:1:5		FOGLIO 1 DI 2		

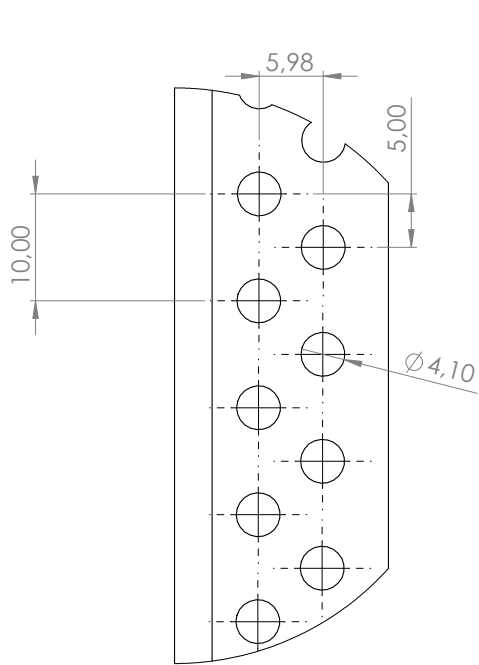


DETAIL E
SCALE 1 : 1

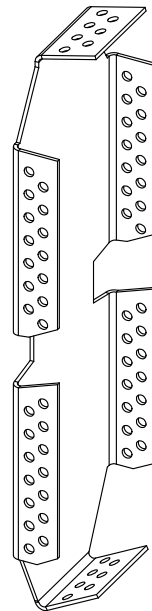
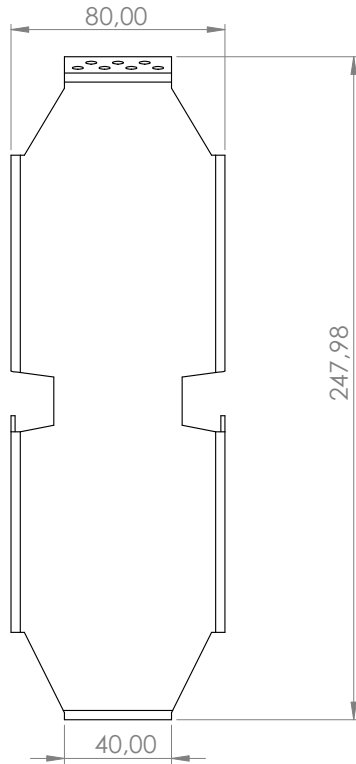
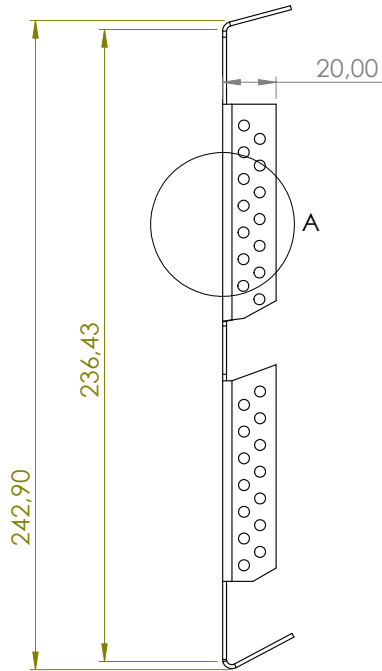
DETAIL F
SCALE 1 : 1

DETTAGLIO G
SCALE 1 : 1

SE NON SPECIFICATO: QUOTE IN MILLIMETRI FINITURA SUPERFICIE: TOLLERANZE: LINEARE: ANGOLARE:				FINITURA:		INTERRUZIONE BORDI NETTI		REVISIONE	
NOME		FIRMA		DATA				TITOLO:	
DISEG.								ROOT RIB	
VERIF.									
APPR.									
FABB.									
Qual.				MATERIALE:		N. DISEGNO		centina_radice_01	
								A3	
				PESO:		SCALA:1:5		FOGLIO 2 DI 2	



DETAIL A
SCALE 2 : 1



SE NON SPECIFICATO: QUOTE IN MILLIMETRI FINITURA SUPERFICIE: TOLLERANZE: LINEARE: ANGOLARE:				FINITURA:		INTERRUZIONE BORDI NETTI	NON SCALARE DISEGNO		REVISIONE		
	NOME		FIRMA		DATA			TITOLO:			
DISEG.								MID RIB			
VERIF.											
APPR.											
FABB.											
Qual.						MATERIALE:		N. DISEGNO		centina_intermedio_01 A3	
						PESO:		SCALA:1:5		FOGLIO 1 DI 1	

F

E

D

C

B

A

F

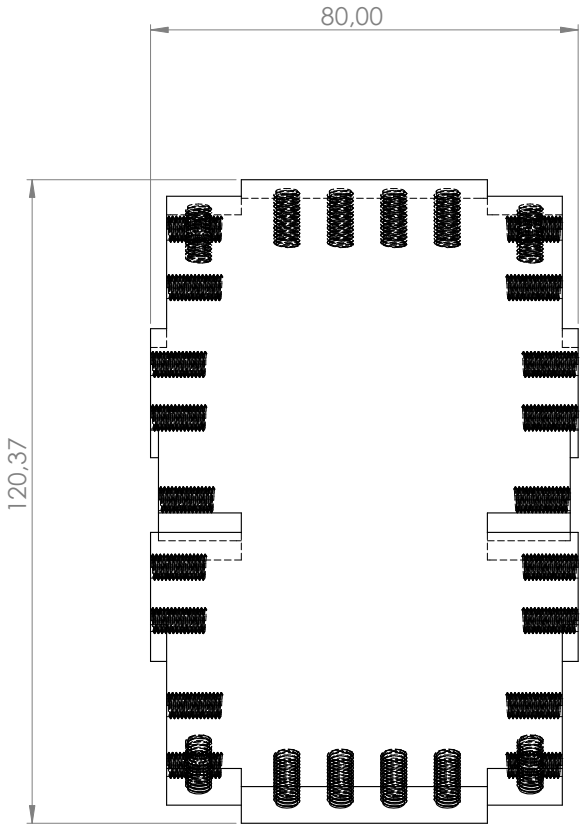
E

D

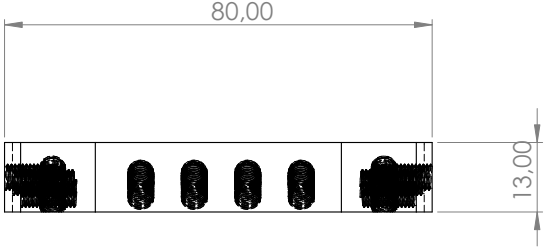
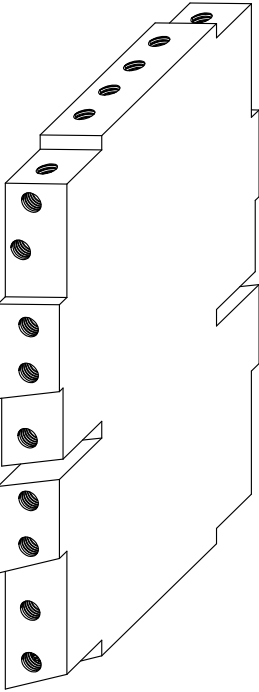
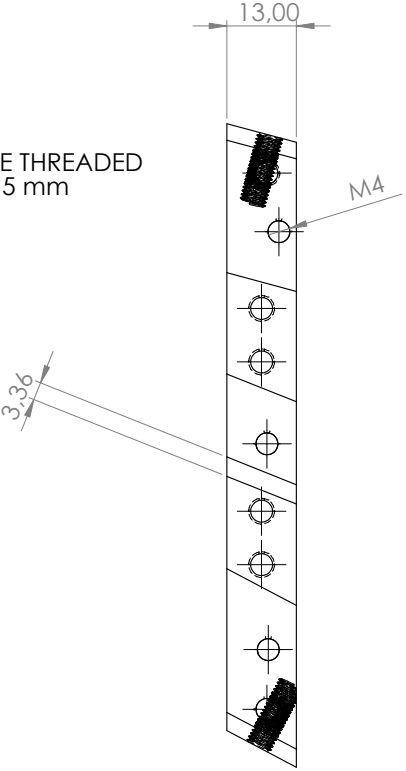
C

B

A



ALL THE HOLES ARE THREADED
M4
DEPTH 15 mm



SE NON SPECIFICATO: QUOTE IN MILLIMETRI FINITURA SUPERFICIE: TOLLERANZE: LINEARE: ANGOLARE:				FINITURA:		INTERRUZIONE BORDI NETTI	NON SCALARE DISEGNO		REVISIONE		
	NOME		FIRMA		DATA			TITOLO: TIP RIB			
DISEG.											
VERIF.											
APPR.											
FABB.											
Qual.					MATERIALE:			N. DISEGNO centina_estremità		A3	
					PESO:			SCALA:1:1		FOGLIO 1 DI 1	

This Ph.D. thesis has been typeset by means of the T_EX-system facilities. The typesetting engine was pdfL^AT_EX. The document class was `toptesi`, by Claudio Beccari, with option `tipotesi=scudo`. This class is available in every up-to-date and complete T_EX-system installation.